QATAR UNIVERSITY

COLLEGE OF ARTS AND SCIENCES

NEW SULFUR-DOPED CARBON FIBER – SUPPORTED ALLOYS FOR ELECTROCATALYTIC REDUCTION OF OXYGEN FOR PEM FUEL CELLS APPLICATIONS

BY

HAMED K. ABUSHAHLA

A Thesis Submitted to the Faculty of

the College of Arts and Sciences

in Partial Fulfillment

of the Requirements

for the Degree of

Masters of Science

in

Material Science and Technology

June 2018

COMMITTEE PAGE

The members of the Committee approve the Thesis of Hamed K. AbuShahla defended on 10/05/2018.

_____
Dr. Ahmed Elzatahry
Thesis/Dissertation Supervisor

_____
Prof. Aboubakr M. Abdullah
Committee Member

_____
Dr. Khalid Abdulla Al-Saad
Committee Member

_____
Name
Committee Member

_____
Add Member

Approved:

_____
Rashid Al-Kuwari, Dean, College of College of Arts and Sciences

ABSTRACT

ABUSHAHLA, HAMED, K., Masters : June : 2018, Material Science and Technology

Title: New sulfur-doped carbon fiber – supported alloys for electrocatalytic reduction of oxygen for PEM fuel cells applications

Supervisor of Thesis: Dr. Ahmed Elzatahry.

The daily increase in the world needs for new sources of energy, the population and economy growth, and the industrial expansions made the demand for new sources of energy a critical request within different societies. Among clean energy sources comes the polymer electrolyte membrane fuel cell (PEMFC), which is used to produce electricity through simple electrochemical reaction process. However, the expensive price of the platinum (Pt) catalyst as one of the main components of fuel cell and considered the most important part responsible for the oxygen reduction reaction (ORR) within the cell, is the main barrier to the commercialization of fuel cells. This thesis deals with the development of novel inexpensive efficient catalysts based on Tri nanostructure metal alloys supported on sulfur doped carbon fibers, which is expected to have high surface area and good conducting properties, the fact that support the electrochemical reaction process within the cell. The synthesized materials was characterized by scanning electron microscope (SEM), Energy-dispersive X-ray spectroscopy (EDX), X-ray photoelectron spectroscopy (XPS), X-ray diffraction (XRD), and FTIR in addition to electrochemical characterization for the catalyst responsible for the ORR. Electrospinning technique was used to produce the sulfur-doped carbon nanofiber, while electrochemical deposition technique was used to load the different metals. The produced sulfur-doped CNF exhibited excellent performance towards ORR in PEM fuel cells via 4-electrons pathway.

Abbreviation

AFC	- Alkaline fuel cell
CB	- Carbon black
CE	- Counter electrode
CNF	- Carbon nanofibers
CNT	- Carbon nanotubes
CV	- Cyclic voltammetry
DMF	- N,N-dimethylformamide
DMFC	- Direct methanol fuel cell
EDX	- Energy-dispersive X-ray spectroscopy
EIS	- Electrochemical impedance spectroscopy
F	- Faraday’s constant
FGIC	- Fluorinated graphite intercalation compounds
GCE	- Glassy carbon electrode
GO	- Graphene oxide
HER	- Hydrogen evaluation reaction
HOR	- Hydrogen oxidation reaction
LSV	- Linear sweep voltammetry
MCFC	- Molten carbonate fuel cell
MWCNTs	- Multi-wall carbon nanotubes
OCP	- Open circuit potential

ORR	- Oxygen reduction reaction
PAFC	- Phosphoric acid fuel cell
PAN	- Polyacrylonitrile
PANI	- Polyaniline
pBDT	- p-Benzanedithiol
PEMFC	- Polymer electrolyte membrane fuel cell
PEO	- Polyethylene oxide
PMMA	- Poly(methylmethacrylate)
PS	- Polystyrene
PSF	- Polysulfone
PtNW	- Platinum nanowires
PTP	- Polythiophene
RDE	- Rotating disk electrode
RE	- Reference electrode
RHE	- Reversible hydrogen electrode
RGO	- Reduced graphene oxide
SEM	- Scanning electron microscopy
SG	- Sulfur graphene
SOFC	- Solid oxide fuel cell
TGA	- Thermogravimetric analysis
WE	- Working electrode
XPS	- X-ray photoelectron spectroscopy
XRD	- X-ray diffraction

ACKNOWLEDGMENTS

First and foremost, I would like to express my honest gratitude to my supervisor, Prof. Ahmed Elzatahry, for his knowledge and continuous support throughout my thesis. The door to Prof. Ahmed's office was always open whenever I had question and his guidance helped me during the research and writing phase of this thesis.

Additionally, I would like to thank the rest of the thesis committee, Prof. Aboubakr Abdullah and Dr. Khalid Al-Saad, for their encouragement, support, and willingness to spare their time. I appreciate their guidance and valued advice enabling me to overcome any issue during my research work.

My sincere thanks too goes to Prof. Talal Altahtamouni and Prof. Khaled Youssef from the Masters in Material Science Program for their support whenever needed.

I am thankful to all the individuals and colleagues who helped me during my research work. Mr. Mostafa Sliem, Mr. Abdullah Al Ashraf, Mr. Abdul Jaleel Naushad from the Center of Advanced Materials (CAM). Mr. Mustafa Zagho at the Material Science Program and to Mr. Jalal Hamdan from the Department of Chemistry and Earth Sciences for his valued comments on this thesis.

Finally, I must thank my family, my wife, and my kids for providing the support and encouragement with all understanding and love during my years of study and through my research and writing of this thesis. Thank you.

Hamed Abushahla

Doha, May 2018

TABLE OF CONTENTS

ACKNOWLEDGMENTS vi
LIST OF TABLES ix
LIST OF FIGURES xi
1. **Chapter 1: Introduction and literature review** 1
1.1 Fuel Cell 3
1.1.1 History of the Fuel Cell 3
1.1.2 Principle of Fuel Cell 5
1.1.3 Advantages and disadvantages of fuel cell: 6
1.1.4 Types of fuel cells 7
1.1.5 Polymer electrolyte membrane fuel cell: 11
1.2 Carbon materials supported Pt and Pt-alloy catalysts 17
1.2.1 Carbon black 18
1.2.2 Nanostructure Carbon Materials: 20
1.2.3 Pt-based alloy catalysts 24
1.2.4 Doped carbon support materials 28
1.2.5 Sulfur Doping 29
1.3 Electrospinning 39
1.3.1 History of Electrospinning 39
1.3.2 The Electrospinning Process 41
1.3.3 Random and aligned fibers 43
1.3.4 Core-shell fibers 45
1.3.5 Effects of Parameters on Electrospinning 46
1.3.6 Polyacrylonitrile (PAN) 53
1.3.7 Electrospinning for oxygen reduction reaction (ORR) applications 58
2 Chapter 2: Experimental Work 68
2.1 Chemicals 68
2.2 Preparation Method of the Polymer Solution: 69
2.3 Fabrication of the fibers using electrospinning technique 71
2.4 Polymer Nanofiber Stabilization Step 75
2.5 Polymer Nanofiber Carbonization Step 75

2.6 Preparation of electrode for electrochemical test 77
2.6.1 Preparation of CNFs ink solution 77
2.6.2 Electrode preparation 77
2.6.3 Electrochemical measurements 77
2.7 SAMPLES CHARACTERIZATION 79
2.7.1 Scanning electron microscopy (SEM) 79
2.7.2 X-ray photoelectron spectroscopy (XPS) analysis 81
2.7.3 X-ray Diffraction analysis 82
2.7.4 Thermal Analysis 83
2.7.5 Fourier Transmittance Infrared (FTIR) Analysis 84
2.7.6 Electrochemical analysis 86
3 Chapter 3: Results and Discussion 87
3.1 Morphological Analysis Results 87
3.1.1 Scanning Electron Microscopy (SEM) Results 87
3.1.2 Energy Dispersive X-ray (EDX) Analysis and Elements Mapping Results: 104
3.2 X-ray Photoelectron Spectroscopy (XPS) analysis Results 120
3.2.1 XPS of the S-doped CNFs 120
3.2.2 Electrode characterization 124
3.3 Structural Analysis Results 126
3.3.1 FTIR analysis Results 126
3.3.2 X-ray Diffraction Analysis (XRD) Results 132
3.4 Thermogravimetric Analysis (TGA) Results 135
3.5 Electrochemical Measurements Results 138
3.5.1 The Cyclic Voltammetry (CV): 138
3.5.2 Linear Sweep Voltammogram (LSV): 140
3.5.3 The electrochemical impedance spectroscopy analysis (EIS) 147
4 Chapter 4: Conclusion and future work 155
REFERENCES 158

LIST OF TABLES

Table 1.1. Various types of carbon black and their physical properties. 18

Table 1.2. Some of the important properties and applications of the different forms of carbon [91]–[98]. 23

Table 1.3. ORR activity of all Co-PAN-x samples with PAN-800 and Pt/C for comparison (vs. Hg/HgO) , Shang et al. [226] 63

Table 2.1. Chemicals used for the polymer solutions preparation..... 69

Table 2.2 The parameters of the electrospinning process..... 73

Table 3.1. EDX results of PAN Sulfur-doped Nanofibers samples..... 113

Table 3.2. EDX results of CNFs samples 118

Table 3.3. Results of the XPS peaks for CNF-3%S-doped sample 121

Table 3.4. Results of the XPS peaks for CNF-5%PTP-doped sample 121

Table 3.5. XPS peak analysis and quantification of Pt-Ni-Co-Cu@CNF-5%PTP/GC-RDE 125

Table 3.6. FTIR peaks for the pristine PTP and the assignment group of each peak..... 128

Table 3.7. FTIR peaks for the pristine PAN and the assignment group of each peak..... 129

Table 3.8. FTIR peaks for the PAN-0%S and the assignment group of each peak..... 130

Table 3.9. FTIR peaks for the PAN-sulfur doped nanofibers and the assignment group of

each peak..... 131

Table 3.10. Onset potentials (E_{onset}), half-wave potentials ($E_{1/2}$), and limiting current densities (LCD) at 0.2 V for different catalysts at 1600 rpm in an alkaline media. 142

Table 3.11. Koutecky–Levich slopes and the calculated average number of electron ... 146

Table 3.12. Dynamic EIS Parameters for CNF-5%PTP and CNF-3%S with electrodeposited Ni-Co-Cu at different deposited time at 1600RPM in presence of nitrogen and oxygen..... 152

Table 3.13. Dynamic EIS Parameters for CNF-5%PTP with electrodeposited Pt-Ni-Co-Cu at different rotation speed in presence of oxygen. 154

LIST OF FIGURES

Figure 1.1. The first practical fuel cell by Sir William Grove[3]. 3

Figure 1.2. The first PEMFC powered passenger green car by Energy Partners, 1993 [4].4

Figure 1.3. A typical PEM fuel cell [5]. 6

Figure 1.4. Main types of fuel cells with their reactions and operation temperature [4]. ... 8

Figure 1.5. Trends in oxygen reduction activity vs oxygen binding energy[41]. 15

Figure 1.6. Trends in the activity of the oxygen reductions vs both the oxygen and hydroxyl binding energy[41]. 16

Figure 1.7. Polarization curves of the different catalysts [113]. 26

Figure 1.8. Fabrication of S-doped graphene from graphene oxide and benzyl disulfide, Yang et al. [147]. 30

Figure 1.9. Fabrication of S-doped graphene via magnesiothermic reduction of CO_3^{2-}, Wang et al. [150]..... 31

Figure 1.10. Linear sweep voltammetry of different samples at 1600 rpm [150]. 32

Figure 1.11. Charge and Spin densities of N and S dual doped graphene. [158]. 35

Figure 1.12. Fabrication process of N/S co-doped graphene, Zhang et al. [160]. 36

Figure 1.13. LSV to compare ORR activity of N/S-G-7d with a) other samples prepared under different reaction conditions, and b) commercial Pt/C and reduced graphene oxide (RGO), Zhang et al. [160]. 37

Figure 1.14. Taylor cone formation with increasing voltage (left to right) [177]. 40

Figure 1.15. The basic electrospinning set-up (a) Vertical and (b) Horizontal [169]..... 42

Figure 1.16. PAN nanofibers with random orientation, Zhang et al.[190]. 43

Figure 1.17. Aligned nanofiber fabricated with high ration drum collector speed, Chew et al. [191]. 44

Figure 1.18. The basic coaxial electrospinning set-up to fabricate core/shell structure fibers [195]. 45

Figure 1.19. SEM of PAN nanofibers (a) 5 wt.% and (b) 7 wt.%, Fang et al. [204]..... 47

Figure 1.20. The fiber dimeter versus the solution viscosity of the PMMA, Gupta et al. [206]. 48

Figure 1.21. Formation of beads on the fibers of 7% PAN at low collecting distance without effect on the fiber diameter, Fang et al. [204]. 50

Figure 1.22. SEM images of the ultrafine PSF fibers with flow rate of 0.4 ml/h (a, b) and 0.66 ml/h (c, d), Yuan et al. [214]..... 51

Figure 1.23. SEM of PS fibers with humidity of: a) less than 25%, b) 31-38%, c) 40-45%, d) 50-59% and e) 60-72%, Casper et al. [215]. 52

Figure 1.24. Structure of Polyacrylonitrile [219]..... 54

Figure 1.25. Ladder structure of PAN [219][221]. 54

Figure 1.26. PAN stabilization process [219]. 56

Figure 1.27. Heat treatment of PAN fibers. First step is stabilization and the second is the

carbonization [141]. 57

Figure 1.28. a) LSV curves in presence of oxygen, and b) The onset and half wave potentials with current density for the three catalysts, Zamani et al [166]. 59

Figure 1.29. SEM images of a) NCNFs, the prepared Fe-N/CN with different concentration of $Fe(NO_3)_3$ b) 0.01 %, c) 0.5 %, and d) 3 %, Qiu et al. [229]..... 60

Figure 1.30. LSV for all Co-PAN-x samples with PAN-800 and Pt/C for comparison, in presence of oxygen, alkaline media, Shang et al. [226]..... 62

Figure 1.31. Cyclic voltammetry curves of ANCNF carbonized at various temperatures in a) 0.1M KOH solution and b) 0.5M H_2SO_4, in presence of oxygen, Wang et al. [139].. 64

Figure 1.32. The production procedure of Fe-S/N-C NFs, Guo et al. [230]..... 65

Figure 1.33. Linear sweep voltammetry of (a) different catalysts, (b) Fe-S/N-C-800 at various rotating speeds, Guo et al.[230]. 66

Figure 1.34. Linear sweep voltammetry of (a) Zn/Co@C-NCNFs at different decomposition temperature; (b) different catalysts, Niu et al.[231]. 67

Figure 2.1. The prepared S-doped of PAN solutions with different sulfur sources..... 70

Figure 2.2. SEM image of PAN-0.5%S with flow rate of 1 ml/h. 72

Figure 2.3. SEM image of PAN-0.5%S working distance of 15 cm. 72

Figure 2.4. Fabrication of the fibers using electrospinning technique. 74

Figure 2.5. The produced fibers collected on the aluminum foil. 74

Figure 2.6. Ceramic tube furnace. 75

Figure 2.7 The carbonization process. 76

Figure 2.8. Electrode preparation steps..... 78

Figure 2.9. The scanning electron microscopy (SEM), model: NOVA NANOSEM 450.79

Figure 2.10. X-ray photoelectron spectroscopy, Model: AXIS Ultra DLD, Kratos..... 81

Figure 2.11. X-ray Diffraction (XRD) diffractometer, Model: PANalytical, Brand: EMPYREAN..... 83

Figure 2.12. PerkinElmer TGA 4000 instrument..... 84

Figure 2.13. FTIR, Model: PerkinElmer Frontier. 85

Figure 2.14. Potentiostat instrument, Model: GAMRY “Reference 3000”. 86

Figure 3.1. SEM of PAN-0%S fibers..... 88

Figure 3.2. SEM of PAN-0%S fibers. 89

Figure 3.3. SEM of PAN-0.5% S fibers..... 90

Figure 3.4. SEM of PAN-0.5% S fibers..... 90

Figure 3.5. SEM of PAN-1% S fibers..... 91

Figure 3.6. SEM of PAN-1% S fibers..... 91

Figure 3.7. SEM of PAN-3% S fibers..... 92

Figure 3.8. SEM of PAN-3% S fibers..... 92

Figure 3.9. SEM of PAN-0.5% PTP fibers. 93

Figure 3.10. SEM of PAN-0.5% PTP fibers. 93

Figure 3.11. SEM of PAN-1% PTP fibers. 94

Figure 3.12. SEM of PAN-1% PTP fibers. 94

Figure 3.13. SEM of PAN-3% PTP fibers. 95

Figure 3.14. SEM of PAN-3% PTP fibers. 95

Figure 3.15. SEM of PAN-5% PTP fibers. 96

Figure 3.16. SEM of PAN-5% PTP fibers 96

Figure 3.17. SEM of CNF-0% S. 97

Figure 3.18. SEM of CNF-0% S. 97

Figure 3.19. SEM of CNF-0.5% S. 98

Figure 3.20. SEM of CNF-0.5% S. 98

Figure 3.21. SEM of CNF-1% S. 99

Figure 3.22. SEM of CNF-1% S. 99

Figure 3.23. SEM of CNF-3% S. 100

Figure 3.24. SEM of CNF-3% S. 100

Figure 3.25. SEM of CNF-1% PTP. 101

Figure 3.26. SEM of CNF-1% PTP. 101

Figure 3.27. SEM of CNF-3% PTP. 102

Figure 3.28. SEM of CNF-3% PTP. 102

Figure 3.29. SEM of CNF-5% PTP. 103

Figure 3.30. SEM of CNF-5% PTP. 103

Figure 3.31. EDX elemental analysis graph of PAN. 105

Figure 3.32. EDX elemental analysis graph of PAN-0.5%S. 105

Figure 3.33. EDX elemental analysis graph of PAN-1%S. 106

Figure 3.34. EDX elemental analysis graph of PAN-3%S. 106

Figure 3.35. EDX elemental analysis graph of PAN-0.5%PTP. 107

Figure 3.36. EDX elemental analysis graph of PAN-1%PTP. 107

Figure 3.37. EDX elemental analysis graph of PAN-3%PTP. 108

Figure 3.38. EDX elemental analysis graph of PAN-5%PTP. 108

Figure 3.39. Elements mapping of PAN nanofibers -0%S. 109

Figure 3.40. Elements mapping of PAN nanofiber-0.5%S. 109

Figure 3.41. Elements mapping of PAN nanofiber-1%S. 110

Figure 3.42. Elements mapping of PAN nanofiber-3%S. 110

Figure 3.43. Elements mapping of PAN nanofiber-0.5%PTP. 111

Figure 3.44. Elements mapping of PAN nanofiber-1%PTP. 111

Figure 3.45. Elements mapping of PAN nanofiber-3%PTP. 112

Figure 3.46. Elements mapping of PAN nanofiber-5%PTP. 112

Figure 3.47. EDX elemental analysis graph of CNF-3%S. 114

Figure 3.48. EDX elemental analysis graph of CNF-5%PTP. 114

Figure 3.49. Elements mapping CNF-0.5%S..... 115

Figure 3.50. Elements mapping CNF -1%S..... 115

Figure 3.51. Elements mapping CNF -3%S..... 116

Figure 3.52. Elements mapping CNF -0.5%PTP..... 116

Figure 3.53. Elements mapping CNF -1%PTP..... 117

Figure 3.54. Elements mapping CNF -3%PTP..... 117

Figure 3.55. Elements mapping CNF -5%PTP..... 118

Figure 3.56. High-resolution XPS C 1s spectra of CNF-3%S-doped sample. 122

Figure 3.57. High-resolution XPS S 2p spectra of CNF-3%S-doped sample. 122

Figure 3.58. High-resolution XPS C 1s spectra of CNF-5%PTP-doped sample..... 123

Figure 3.59. High-resolution XPS S 2p spectra of CNF-5%PTP-doped sample..... 123

Figure 3.60. Wide scan XPS spectrum of the Pt-Ni-Co-Cu@CNF-5%PTP/GC-RDE. . 124

Figure 3.61. FTIR spectra of pristine polythiophene (PTP). 127

Figure 3.62. FTIR spectra of pristine polyacrylonitrile (PAN). 128

Figure 3.63. FTIR spectra of prepared PAN-0%S nanofibers. 129

Figure 3.64. FTIR spectra of prepared PAN-3%S and PAN-5%PTP nanofibers..... 130

Figure 3.65. The XRD for elemental sulfur and powder PAN. 133

Figure 3.66. The XRD patterns of CNF-0%S, CNF-3%S, and CNF-5%PTP. 134

Figure 3.67. The TGA curves for the prepared nanofibers PAN-0%-S, PAN-3%S, and

PAN-5%PTP. 136

Figure 3.68. The TGA curves for the CNF-0%-S, CNF-3%S, and CNF-5%PTP. 137

Figure 3.69. CVs for glassy carbon in 1 M NaOH solution of sulfur doped carbon fiber (PAN-5%PTPCNF) with 30 minutes electrodeposited of Ni-Co-Cu at different scan rate, in A) Nitrogen and B) Oxygen..... 139

Figure 3.70. Anodic and cathodic peak current densities versus scan rate in 1M NaOH solution saturated with oxygen (red) and nitrogen (black). 139

Figure 3.71. Linear sweep voltammograms (LSV) in O_2 saturated 1 M NaOH solution for A) CNF-3%S and B) CNF-5%PTP, with electrodeposited Ni-Co-Cu at different deposition times @1600RPM. 141

Figure 3.72. LSVs of different electrodes in oxygen-saturated 1M NaOH solution at room temperature at (A) 1600 and (B) 1600, 1800, 2500, 3000 and 3500 rpm..... 144

Figure 3.73. K-L plots for different potentials of ORR polarization curves recorded using an RDE in O_2-staurated 1 M NaOH electrolyte at room temperature. To obtain equidistant points, the adopted rpm rates are 1600, 1800, 2500, 3000, and 3500 rpms, respectively. 146

Figure 3.74. Nyquist spectra in 1 M NaOH solution in A) Nitrogen and B) Oxygen, of glassy carbon electrode with sulfur doped carbon fiber (CNF-3%S-CNF) with electrodeposited Ni-Co-Cu at different deposited time at 1600RPM. 150

Figure 3.75. Nyquist spectra in 1 M NaOH solution in A) Nitrogen and B) Oxygen, of glassy carbon electrode with doped carbon fiber (CNF-5%PTP) with electrodeposited Ni-

Co-Cu at different deposited time at 1600RPM. 151

Figure 3.76. Equivalent circuits used for EIS analysis at OCP. 152

Figure 3.77. Nyquist spectra for glassy carbon in 1 M NaOH solution of sulfur doped carbon fiber (PAN+5%PTP-CNF) with electrodeposited Pt-Ni-Co-Cu at different rotation speed. 154

1. Chapter 1: Introduction and literature review

During last decade scientists kept themselves busy searching for new sources of energy in specific clean energy for example solar cells, fuel cells and wind power. The renewable energy or green energy comes with a solution to the drawbacks caused by conventional or fossil fuel such as pollution and greenhouse effect. Among these clean energy sources comes the polymer electrolyte membrane (PEM) fuel cell, which is used to produce electricity through simple electrochemical reaction process. The reaction which takes place at surface of electrode is mainly consisted from platinum material. High interest has been given to PEM fuel cells as an alternative source of energy in many applications especially for portable electronic products and recently in automotive industries. However, different barriers need to be overcome the lack of commercialization of fuel cells. Among these barriers is the high cost of Pt catalyst, which is one of the main components of fuel cells and considered the most important part responsible for oxygen reduction reaction (ORR) within the cell. There have been several attempts to decrease the amount of Pt used in fuel cells with the possibility of replacement with cheaper materials or through a modification process to reduce the amount of platinum used.

Recently, high interest has been given to nanotechnology and its ability to reform ordinary materials in new structures based on atomic scale. Decreasing the diameter of polymeric fibers from micrometers (e.g. 10–100 μm) to sub-microns or nanometers (e.g. 0.01–0.1 μm) leads to the formation of some incredible properties such as an unusual surface area to volume ratio (approximately 10^3 times of that of a microfiber). These materials show completely different properties and will acquire beneficial properties for

example high activity, high optical properties and mechanical properties, which are different from how they behave on a macroscale [1]. One of the advantages of nanotechnology is that it aids in producing material that can be more cost-effective than its traditional counterparts. With the increase in the world's population, the demand for energy increases, this daily growth demand will cause a rapid decrease of the traditional fossil fuel (oil, gas and coal) reserves. The British Petroleum Statistical Review of World of Energy 2017 reported that global primary energy consumption increased by 2.9 % between 2014-2016, and thus, would be enough to supply 50.6 years of worldwide production at 2016 levels [2]. Furthermore, the releases of CO_2 from energy consumption increased by 0.1% in 2016 [2]. On the direction of finding new alternative energy sources other than fossil fuels, any approach that can produce clean energy with high efficiency, minimum pollution output and simple operation and lower the overall cost would be very advantageous. Such processes can be achieved and improved by using nanomaterials designed through nanotechnology [1].

1.1 Fuel Cell

1.1.1 History of the Fuel Cell

The concept of the fuel cell was discovered in 1839 by Christian Friedrich Schönbein during his research on the electrolysis of dilute sulfuric acid and other matters [3]. Later, Sir William Grove, set-up the first practical fuel cell referred to as “a gaseous voltaic battery”[3], as he used two platinum strips as electrodes and diluted sulfuric acid as the electrolyte, encompassed by tubes of hydrogen and oxygen (Figure 1.1) [3].

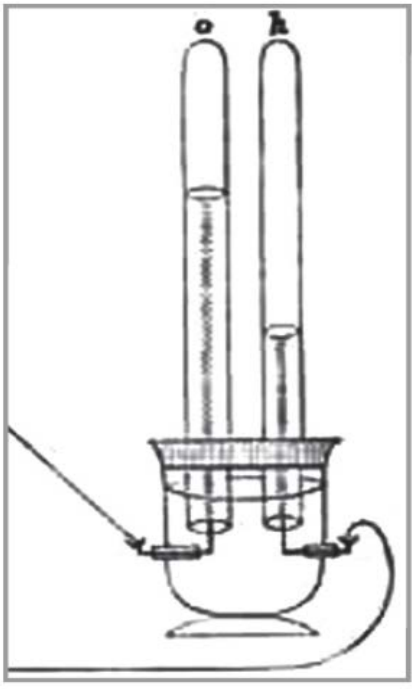

Figure 1.1. The first practical fuel cell by Sir William Grove[3].

In 1937, Francis T. Bacon presented his patent of a working 6 kW fuel cell [4]. This

patent was used later by Pratt and Whitney from the Apollo space program in 1960s to build and use a fuel cell to generate electricity, and as a matter of fact is still used in the U.S. space programs to this day [4]. In 1989, Perry Energy Systems and Ballard Power Systems, established a PEM fuel cell, and later in 1993 Energy Partners demonstrated the first green car using a PEM fuel cell (Figure 1.2), which then opened the door for all car manufacturer to develop their own fuel cell-powered vehicle [4].

Figure 1.2. The first PEMFC powered passenger green car by Energy Partners, 1993 [4].

1.1.2 Principle of Fuel Cell

The fuel cell is simply a device able to generate electricity through a simple electrochemical process. The reaction process uses input materials such as hydrogen and oxygen to generate electricity with byproducts of only water and heat with no moving parts or burning within the fuel cell [5]. The fuel cell system composes of two electrodes of platinum as catalysts, separated by an electrolyte [6].

The first electrode is the anode where the fuel decomposes into ions and electrons in an oxidation process:

$$H_2 \rightarrow 2H^+ + 2e^- \qquad \textit{Equation 1}$$

The ionic species traveling from the anode towards cathode across the electrolyte membrane or inversely, based on the type of the fuel cell and the electrons, moving toward the cathode via an external circuit where a reduction process of oxygen occurs producing water as product [3]–[5]:

$$½\, O_2 + 2H^+ + 2e^- \rightarrow H_2O \qquad \textit{Equation 2}$$

Figure 1.3 shows the typical PEM fuel cell:

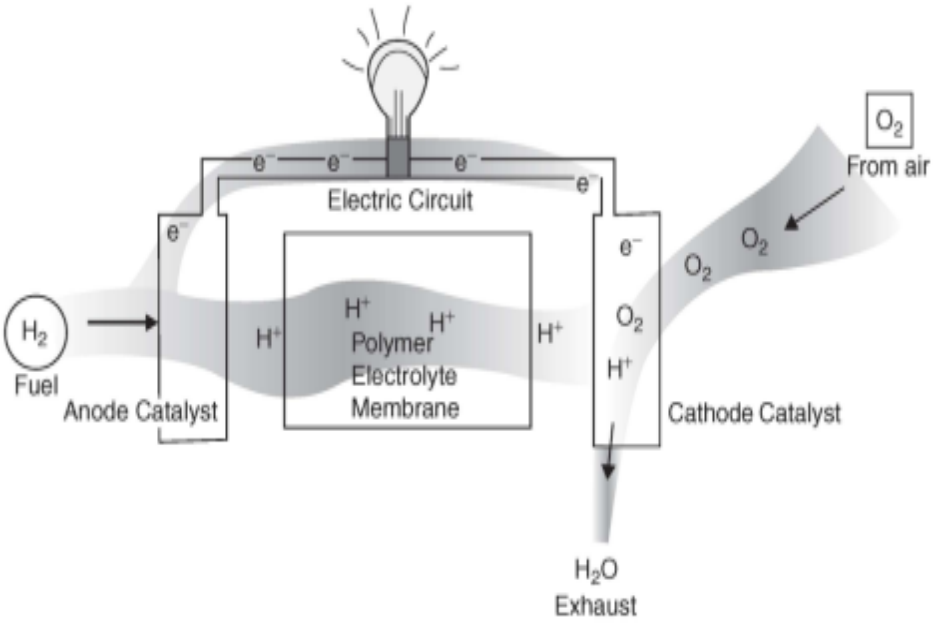

Figure 1.3. A typical PEM fuel cell [5].

1.1.3 Advantages and disadvantages of fuel cell:

Fuel cells have many advantages [5]–[7] as an electrochemical energy conversion device including:

- Unlike batteries, fuel cells can keep generating electricity as long as there is a steady source of fuel and oxidants to the system.
- The process is a very clean operation and environment friendly, as the input is only hydrogen and oxygen and the byproducts are water and heat with no CO_2 emission or other pollutants.

- Fuel cells have shown high efficiency even more than the combustion engines, for example the high temperature fuel cells have efficiency in the range of 32-47% and 25-60% in low temperature fuel cells.
- No moving parts within the fuel cells, this makes it a quiet system.
- Many applications use fuel cell including automotive transportation and portable electronic products.
- Fuel cell can operate independently in remote locations.

Although fuel cells have many advantages, they also have some disadvantages, the manufacturing cost due to the price of component materials within the fuel cell especially the use of platinum catalysts in the anode and cathode [8]. In fact due to intensive efforts by scientist to find low cost materials and to improve the manufacturing process, some applications using fuel cell are already in the market [3], [4], [9].

1.1.4 Types of fuel cells

There are numerous types of fuel cells such as proton exchange fuel cell (or polymer electrolyte membrane fuel cell) (PEMFC), direct methanol fuel cell (DMFC), molten carbonate fuel cell (MCFC), alkaline fuel cell (AFC), phosphoric acid fuel cell (PAFC), and solid oxide fuel cell (SOFC) [5]. All types follow the same concept of the electrochemical principles, but characterized by the electrolyte and materials used in the fuel cell and/or by the operating temperature [4]–[7], [10]. Figure 1.4 summarizes the most used fuel cells with their reactions and operation temperature.

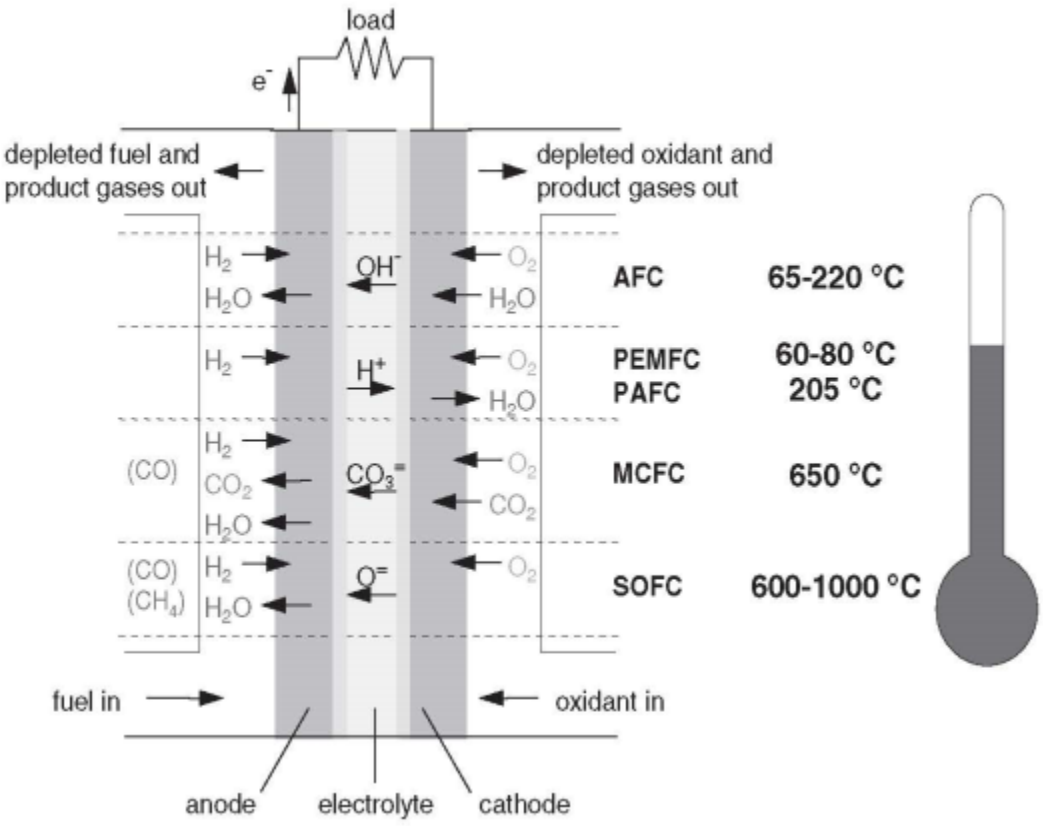

Figure 1.4. Main types of fuel cells with their reactions and operation temperature [4].

1.1.4.1 Alkaline fuel cells (AFC) [4], [6], [7], [10], [11]:

Developed and used in 1960s for Apollo space programs, the used electrolyte was concentrated potassium hydroxide (KOH ~ 85 wt.%) when operated at high temperature (250 °C), but a diluted KOH (35-50 wt.%) at the low operating temperature (<120 °C). However, the fuel cell is mostly operated at low operation temperatures. It is a relatively low cost fuel cell as it can operate with non-platinum catalysts electrodes such as nickel. The reactions as follows:

Oxidation reaction at the anode:

$$2H_2 + 4OH^- \rightarrow 4H_2O + 4e^- \qquad \textit{Equation 3}$$

Reduction reaction at the cathode:

$$O_2 + 4e^- + 2H_2O \rightarrow 4OH^- \qquad \textit{Equation 4}$$

Very pure gases should always be used within the fuel cell to avoid electrolyte poisoning by CO_2 from the fuel or oxidant.

1.1.4.2 Phosphoric acid fuel cells (PAFC) [4], [6], [7], [10], [12]:

This type of fuel cell is widely commercialized. In this type, the electrolyte is concentrated phosphoric acid (H_3PO_4) (100%) and the electrodes are platinum supported on carbon black, which is used to reduce the platinum loading. PAFC can produce an output of up to 1MW. The operating temperature for this PAFC is about 200 ^oC. The anode and cathode reactions are as the following:

At the anode:

$$H_2 \rightarrow 2H^+ + 2e^- \qquad \textit{Equation 5}$$

At the cathode:

$$½\ O_2 + 2H^+ + 2e^- \rightarrow H_2O \qquad \textit{Equation 6}$$

1.1.4.3 Molten carbonate fuel cell (MCFC) [4], [6], [7], [10], [13]:

The Molten carbonate fuel cell is a high temperature fuel cell, where it operates between 600 and 700 °C. This type does not require noble metal catalysts, it uses nickel as catalyst, which makes it an inexpensive type of fuel cell. The electrolyte is typically molten salt of Li^+/Na^+ or Li^+/K^+ carbonates in a $LiAlO_2$ matrix. The electrochemical half reactions are:

At the anode:

$$2H_2 + 2CO_3^{2-} \rightarrow 2H_2O + 2CO_2 + 4e^- \qquad \textit{Equation 7}$$

At the cathode:

$$O_2 + 2\,CO_2 + 4e^- \rightarrow 2CO_3^{2-} \qquad \textit{Equation 8}$$

The CO_3^{2-} ions produced at the cathode side are the charged carriers in MCFC, these ions travel toward the anode where they convert back to CO_2, which in turn is recycled back to the cathode side.

1.1.4.4 Solid oxide fuel cell (SOFC) [3], [4], [6], [7], [10], [14]:

SOFC is another type of a high temperature fuel cell. It usually operates at 800-1000 °C using an electrolyte of "nonporous metal oxide of Y_2O_3 (8%) doped with ZrO_2"[4]. This type of fuel cell is still under demonstration and development. The anode in SOFC is Ni/YSZ and the cathode is usually a ceramic composite of $LaMnO_3$-based perovskite oxides. The charge carrier in SOFC is O^{2-} as shown in the electrochemical half reactions

below:

At the anode:

$$H_2 + O^{2-} \rightarrow H_2O + 2e^- \qquad \textit{Equation 9}$$

At the cathode:

$$\tfrac{1}{2} O_2 + 2e^- \rightarrow O^{2-} \qquad \textit{Equation 10}$$

1.1.5 Polymer electrolyte membrane fuel cell:

The polymer electrolyte membrane fuel cell (PEMFC) also known as a proton exchange membrane fuel cell [15], it is considered one of the best cells in terms of efficiency [16]. PEMFC is characterized by a simple structure, high-energy efficiency, efficient fuel storage and low emissions. This makes it fairly common in portable applications [17]. The operation temperature of PEMFC is low in the range of 80-200 °C, making it suitable for the quick start-up applications.

Typical H_2/air PEMFCs operation simply occurs by oxidation of hydrogen at the anode and reduction of oxygen at the cathode side using Pt catalyst supported by carbon material [17], [18]. The Pt is the efficient catalyst material and considered to be most active, selective and stable catalyst for both the anode and cathode[18], [19]–[21]. The electrodes squeezed between a thin layers (~50µm) of polymer membrane acting as an electrolyte. The most commonly used membrane is Nafion® because of its high proton conductivity, stability and durability [7], [8], [10], [22], [23]. However, different membranes could be used in the high temperature PEMFCs which show good conductivity and mechanical stability under elevated temperatures [24]–[27], [22]. Each

cell can produce less than 1 V and efficiency of up to 83%, therefore, more than one cell can be stacked together in series using bipolar plates in order to generate more useful voltage for different applications [4], [22], [28]–[31] [32].

1.1.5.1 The Process

At the anode (the negative side of the cell), the hydrogen is fed in as a fuel. Hydrogen atoms adsorb onto the catalyst (Pt) surface, the H-H bond breaks and each hydrogen atom loses one electron and leaves the surface as a H^+ proton (equation 11). The protons move over the polymer membrane towards the cathode, whereas the electrons move through an outside circuit performing useful work and back to the cathode side. This step is called "the hydrogen oxidation reaction (HOR)"[33] and the kinetics of this step are very fast, hence, the voltage losses are very small even with a very small loading of Pt [20].

$$2H_2 \rightarrow 4H^+ + 4e^- \qquad \textit{Equation 11}$$

1.1.5.2 Oxygen Reduction Reaction (ORR)

At the cathode (the positive side of the cell), the oxygen is fed into the system as an oxidant. Oxygen is the most common oxidant for most fuel cell cathodes, because of its availability in the atmosphere [34]. The oxygen atoms adsorb onto the Pt catalyst surface and meet the hydrogen protons coming from the membrane and the electrons from the external circuit, this step is called "the oxygen reduction reaction (ORR)"[33]. In this step, the O=O bond breaks and reduction takes place, producing water (equation 12). The

produced water is pushed out of the cell by the hydrophobic nature of the surroundings and by the flow of air as fuel [4].

$$O_2 + 4H^+ + 4e^- \rightarrow 2H_2O \qquad \textit{Equation 12}$$

The kinetics of the ORR are sluggish compared to HOR. ORR is six times slower than the kinetics of HOR due to the strength of the oxygen double bond [35], [36]; therefore, the ORR at the cathode is a reason for over 50% of the voltage loss in the PEMFC [20], [35], [36]. There are two possible pathways on how ORR can process [37]:

A. In acidic media:

(i) The 4-electrons pathway (dissociative pathway), where the catalyst is active enough to break the O=O bond and directly produce water:

$$O_2 + 4H^+ + 4e^- \rightarrow 2H_2O \qquad (E_o = 1.229\ V)\text{[38]} \qquad \textit{Equation 13}$$

(ii) The 2-electrons pathway (associative pathway), where hydrogen peroxide is produced and adsorbed onto the catalyst surface to give water:

$$O_2 + 2H^+ + 2e^- \rightarrow H_2O_2 \qquad (E_o = 0.670\ V)\text{[38]} \qquad \textit{Equation 14}$$

$$H_2O_2 + 2H^+ + 2e^- \rightarrow 2H_2O \qquad (E_o = 1.77\ V)\text{[38]} \qquad \textit{Equation 15}$$

B. In Alkaline media:

(i) The 4-electrons pathway:

$$O_2 + 2H_2O + 4e^- \rightarrow 4OH^- \qquad (E_o = 0.401\ V)\text{[38]} \qquad \textit{Equation 16}$$

(ii) The 2-electrons pathway:

$O_2 + H_2O + 2e^- \rightarrow HO_2^- + OH^-$ $(E_o = -0.065\ V)$[38] *Equation 17*

$HO_2^- + H_2O + 2e^- \rightarrow 3OH^-$ $(E_o = 0.87\ V)$[38] *Equation 18*

The 4-electrons pathway is preferred to avoid the generation of the hydrogen peroxide as the reaction intermediate, which may degrade the membrane and the carbon support as a result of the formation of the $HO^{\bullet}$ radicals. This depends on the chosen catalyst material, choosing a poor catalyst may not be active enough to reduce the oxygen directly and lead to generation of H_2O_2 instead of water [18], [35], [36], [39]. According to Sabatier Principle, the interaction between the substrate and the catalyst should be balanced, neither too strong nor too week. If the interaction is too week, the catalyst will not be able to make bonds with the substrate, and thus, the reaction will be sluggish or not happen. In contrast, if the interaction is very strong, the intermediates or products will not leave the catalyst surface, and hence, block the catalyst surface for any further reaction[40][18]. Nørskov et al.[41], used the concept of Sabatier principle and "Density Functional Theory (DFT)"[41] calculations to get the bond energies of oxygen and hydroxyl species with some metals. The activities of those metals plotted as a function of the oxygen binding energies named volcano plot. Figure 1.5 displays the volcano plot for binding between oxygen and those metals, and Figure 1.6 displays the activity versus both oxygen and hydroxyl binding energies. In both, Platinum (Pt) observed the best active ORR catalyst with optimum binding energies. Metals such as Ag and Au, show week binding with oxygen, thus, low oxygen adsorption limited the rate. In contrast, metals such as Cu and Ni, bind oxygen strongly, and thus, limit the activity by the desorption of

oxygen and hydroxyl. However, platinum-based materials are the best choice for the more desirable 4-electrons pathway [18], [39], [42], [43].

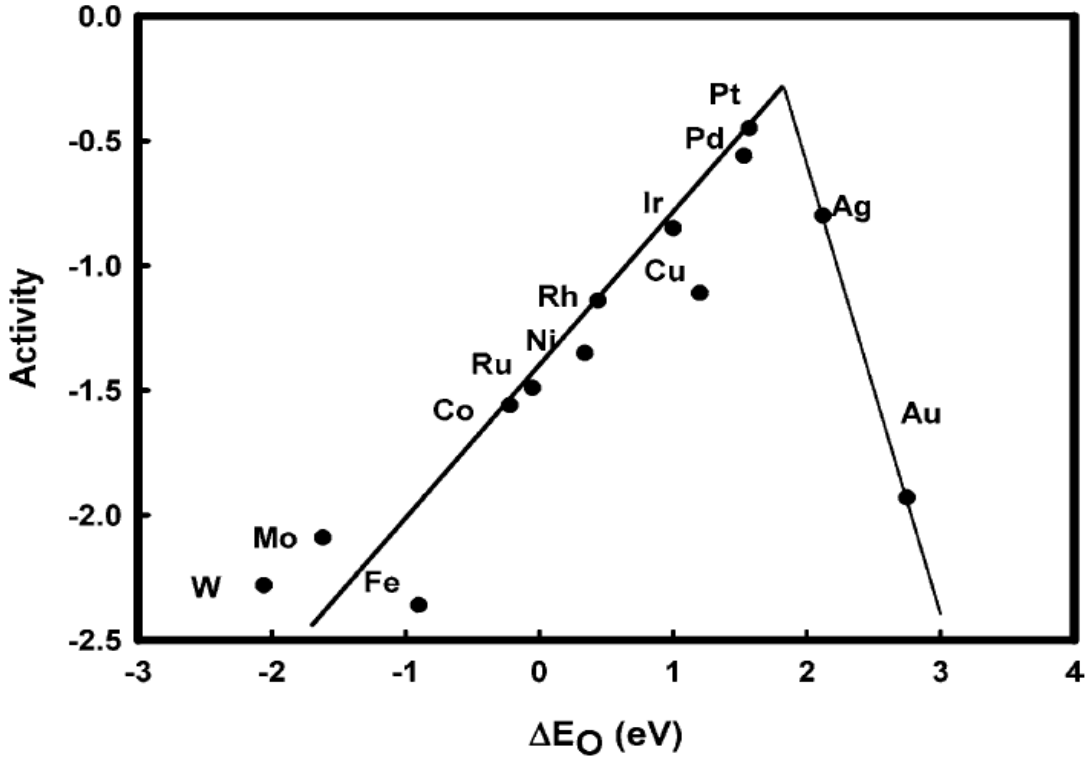

Figure 1.5. Trends in oxygen reduction activity vs oxygen binding energy[41].

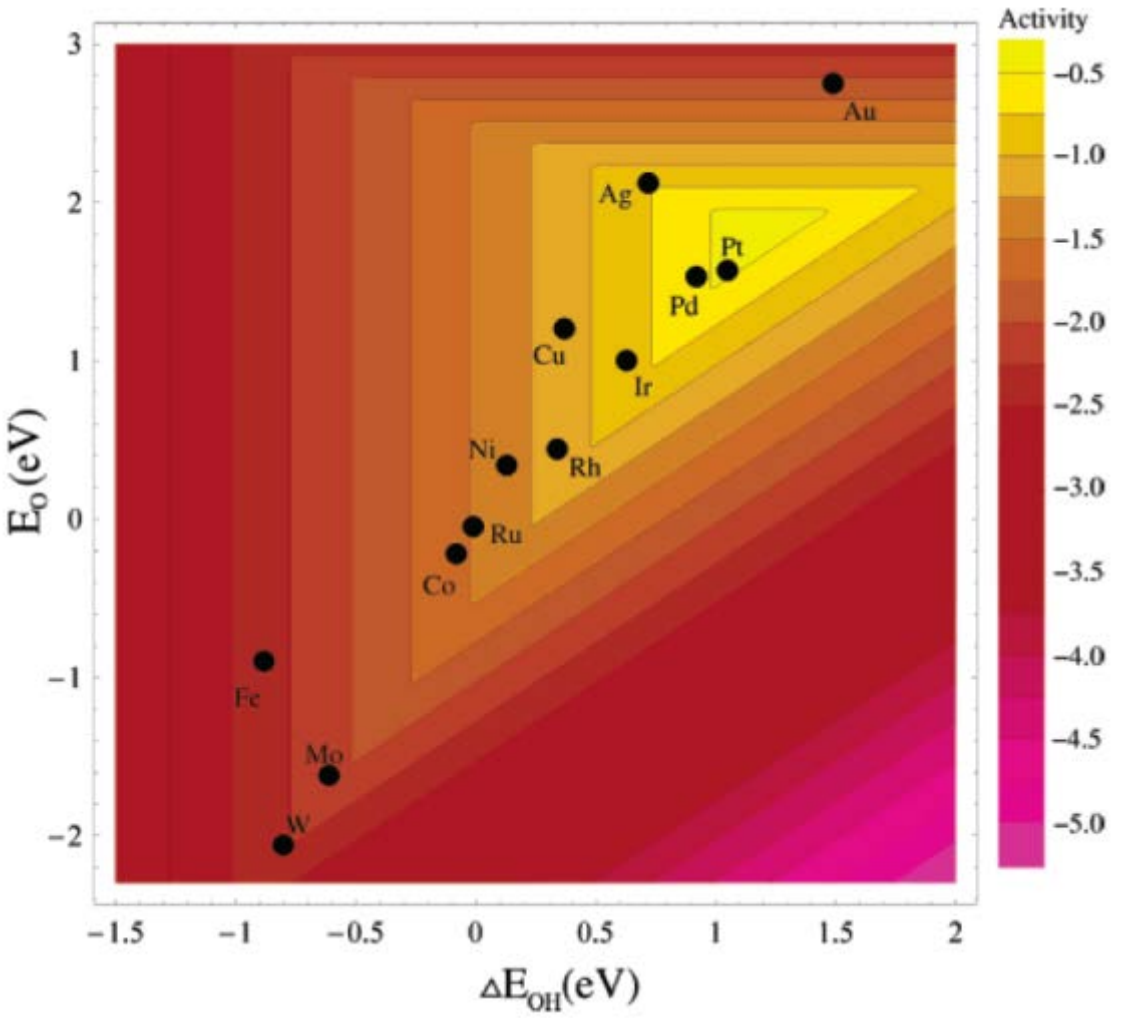

Figure 1.6. Trends in the activity of the oxygen reductions vs both the oxygen and hydroxyl binding energy[41].

Since the major drawback of fuel cells is the cost of its components in specific catalysts, which are used in the oxygen reduction reactions (ORR) such as Pt, it is an important to design new family of relatively inexpensive ORR catalysts with high efficiency and more durability.

1.2 Carbon materials supported Pt and Pt-alloy catalysts

Day by day, the improvement of high performance energy storage devices has been increasing to allow effective usage of clean and renewable energy sources [44]. The most important issues that manage the performance of such devices are the features of electrode materials. In PEMFCs, platinum is the most efficient catalyst material used for both cathode and anode supported on carbon material. However, the high cost, durability and stability are the main challenges for wide-scale commercialization.

Currently, 0.4 mg/cm^2 of Pt nanoparticle is used in the fuel cell, which cost about 50% of the PEMFCs total cost. However, the Pt loading should reduce to less than 0.1 mg/cm^2 to reach the commercialization target [17], [45]. Improving the activity of the carbon support materials by enhancing their properties is one of the strategies to increase the carbon support performance, decrease the Pt loading, and therefore, reduce the cost of the fuel cell [45].

Presently, the excellent electrical conductivity and chemical stability of carbon materials in addition to their large surface area make it the most commonly used materials in electrodes [44], [46]. Carbon materials work as a substrate with large surface area for well dispersion of Pt nanoparticles, and therefore, decrease the quantity of the platinum loading in the fuel cell electrodes [17]. In addition to their main work as electrode materials, carbon materials can also work as a conductive additive [47], [48] and as a substrate for supporting metals in fuel cells [49]–[51]. The characteristics of the support plays an important role in the performance and durability/stability of the catalyst [45].

1.2.1 Carbon black

Carbon black (CB) is the most commonly used material as catalyst support for Pt and Pt-alloy as Pt/C and Pt-alloy/C since 1990s [17], [45], [52], [53]. They are manufactured by "pyrolysis of hydrocarbons using a furnace black process"[36] as one of the most important production method [36], [52], [54] . The materials are characterized by their large surface area to well dispersion of Pt nanoparticles with low loading [53], [55], high electrical conductivity (>1 S/cm) which is important to meet the need of the electrons flow between catalyst and electrode [53], [55], porous structure and low cost [17], [45], [52], [53]. The most common types of carbon black materials with their properties are listed in Table 1.1.

Table 1.1. *Various types of carbon black and their physical properties.*

Carbon Support	**Supplier**	**Surface area (m^2/g)**	**Partial Size (nm)**	**Conductivity (S/cm)**	**Reference**
Vulcan XC-72R	Cabot	250	30	2.77	[17], [53], [54]
Black pearls 2000	Cabot	1500	15	>1	[17], [53], [54]
Denka black	Denka	65	40	4	[17], [53], [54]
Ketjen	Ketjen Black	800	30-40	4	[17], [53],

EC300J	international				[54], [56]
Ketjen EC600JD	Ketjen Black international	1270	35-40	10-100	[17], [53], [54], [57]

Among these types of carbon black, Vulcan XC-72R is commonly used as a support by 80% of electrocatalysts according to its high conductivity, high surface area, and availability with cost effective [52], [54]. Commonly, Pre- chemical or physical activation is needed for carbon black materials before their use as catalyst support to increase the dispersion of metals on carbon black and to enhance the catalytic activity [36], [52]. However, although carbon black materials have many advantages, they also suffer from some disadvantages when used as catalyst supports. The two main problems of these materials, firstly, the dense structure of the carbon leads to a very low amount of Pt nanoparticles to deposit, due to the small average pore diameter of less than 2 nm of carbon black, this small pore size limits the interaction between Nafion ionomer and the catalyst nanoparticles and prevents the fuel from moving smoothly, and thus, limiting the mass transfer [17], [36], [45]. Tang et al. [58] published a review studying the effect of pore size, morphology and structure of using carbon support materials on improvement of high-performance electrodes for fuel cells.

The second problem is the corrosion of the carbon as a result of the formation of CO_2 on the cathode surface during the electrochemical oxidation as the following:

$$C + 2H_2O \rightarrow CO_2 + 4H^+ + 4e^- \qquad \text{Equation 19}$$

As the carbon corrodes, Pt nanoparticles dissolute and migrate from the carbon surface and tend to agglomerate into larger particles, and thus, to decrease in the Pt high surface area and subsequently lowering the durability and performance of the fuel cell [45], [59]–[61]. Many publishers studied the influence of corrosion on the fuel cells when using carbon black as a support [62]–[67]. Consequently, researchers gave more attention to develop other novel carbon-support materials with large surface area, better stability, high conductivity and mesoporosity instead of Vulcan XC-72R and other types of carbon black materials. In this regard, nanostructure materials like graphene, carbon nanotubes (CNTs), and carbon nanofibers (CNFs) have attracted the focus of intensive research in recent to use as supports because of their unique properties [17], [54]–[56], [68], [69].

1.2.2 Nanostructure Carbon Materials:

The effect of nanotechnology on proton exchange fuel cell as a new source of alternative energy has been shown in many directions such as; high surface area support materials, purification of input fuel, and high performance membranes [70], [71]. Nanotechnology also affords the possibility to introduce new nanomaterials to work as catalysts in order to replace the highly expensive platinum catalyst [70]. On the other hand, different supporting materials other than carbon black have exhibited an interesting influence on the catalytic activity of the prepared catalyst. Commercial carbon, which is normally used as supporting materials for the catalyst, showed low dispersion ability because of its low surface area of less than 300 m^2/g especially with high loading catalyst [72]. In addition

to carbon black, various nanostructure materials have been developed over time to be used as catalyst supports in PEMFCs. These include graphene, carbon nanofibers (CNFs), and carbon nanotubes (CNTs) [72]–[74]. They are characterized by their mesoporous structure and average pore diameter of 2-50 nm which favors smooth mass transport [58], [75], high purity, high surface area, high chemical stability in acid and alkaline media due to their "high graphitic nature (e.g. CNTs and CNFs)"[75], large energy conservation and high conductivity, has been used as a support for different metals [70], [76]. With the revolution of graphene technology, due to the high specific surface area of graphene, it has been used as a support for a catalyst in fuel cell [72], [77], [78]. Graphene will solve the problem of low surface area of commercial carbon, which is normally used as a support for catalysts in manufacturing fuel cells [78]. In addition, graphene has a lower cost, similar conductivity and higher surface area than CNT [78]. On the other hand, scientists recently have given high interest to the use of carbon nanofibers (CNFs) as a catalyst support for fuel cells [70], [79], [80]. CNF is characterized by having good electrical conductivity, high surface area and micro/meso-porous structure [70], [81]. The different arrangement of graphite sheets gives the advantage of having hollow cavities in the case of CNF compared to CNT [70].

However, various publications described the use of metal free carbon materials as catalyst and potential electrodes in fuel cells such as nitrogen doped graphene [82]–[84], where results proved better performance and high stability compared to Pt/C for ORR in alkaline electrolyte [78], [84]. Additionally, researchers reported the effect of nitrogen doped carbon fibers on the conductivity [81] and electrocatalytic activity of NiOx for the oxidation of methanol in alkaline medium [80].

Among the various forms of carbon, the one dimensional (1D) carbon nanotubes (CNTs) and carbon nanofibers (CNFs) are preferred for fuel cells due to their advantages compared to the other forms of carbon. One of these advantages is the low percolation conductivity because of the high aspect ratio of over a few hundred [85], [86]. The other advantage is that the large surface area help to accept high concentrations of metals and metal oxides when they are used as substrates[87]. Also the flexibility and the mechanical properties makes CNTs and CNFs a preferred choice in fuel cells over other carbon forms[88], [89] and makes it possible to use CNTs and CNFs as electrode materials in fuel cells.

Although CNFs generally exhibit less electrical conductivity and less surface area than CNTs, CNFs are still prioritized for use in such devices ahead of CNTs. This is primarily due to the flexibility of fabricating different morphological features, such as hierarchical pores and core shell structures with low crystallinity of the CNFs compared to CNTs. This helps to in as it has “defects and functional groups” working as active sites for reactions for “charge storage” and improving the “energy density”[46], [90], as well as the easy dispersion and low production cost. Table 1.2 presents some of the important properties and applications of the different forms of carbon.

.[91]–[98].

Table 1.2. *Some of the important properties and applications of the different forms of carbon* [91]–[98].

Carbon	**Properties**				**Applications**
	Specific gravity (g. cm^{-3})	**Electrical conductivity (S.cm^{-1})**	**Thermal conductivity (W/mK)**	**Surface area (m^2/g)**	
Carbon black	0.13- 2	5- 30	0.4	10- 1443	Conductive additives, electrodes
CNTs	0.8- 1.8	10^2- 10^6	2000-6000	50- 1315	Conductive additives, electrodes, substrates
CNFs	1.5- 2.0	10^{-7}- 10^3	5-1600 (graphitic CNFs)	20- 2500	Conductive additives, electrodes, substrates
Graphite	1.9- 2.3	4000 (in plane), 3.3 (*c*-axis)	298^p, 2.2^c	1- 20	Anodes in LIB
Graphene	2.3	10^6	600-5000	500- 2630	Conductive additives, electrodes, substrates

Carbon nanofibers (CNFs) show many features such as high conductivity, stability, and good mechanical properties[98]. Therefore, CNFs are preferred in several applications like fuel cells, batteries, sensors, nanocomposites, and tissue engineering [99]. Andersen et al. [100] published a study comparing the durability of CNTs, CNFs and Vulcan XC-72. The results show that the high crystalline CNFs presented better stability over CNTs. The study also reported that CNFs have the best durability relative to CNT and Vulcan XC-72 in the order of CNF > CNT > Vulcan XC-72 when used as catalyst support for PEMFCs. Park et al. [101] mentioned the production of high porosity polyacrylonitrile PAN-based carbon nanofiber with high surface area and rough surface, using the electrospinning technique and studied the performance of the produced CNFs as catalytic support in PEMFCs. The results presented that the morphology of the produced CNF enhanced the catalytic activity due to the increased Pt utilization of the Pt/CNF electrode 69%, while that of Pt/XC-72R was 35%. Thus, the produced CNFs exhibited better performance over Vulcan XC-72R as a Pt support.

1.2.3 Pt-based alloy catalysts

Although Pt supported carbon is considered the main catalyst responsible for both ORR at the cathode and HOR at anode, its high cost is also the main barrier for the wide distribution and commercialization of fuel cells [102]. Scientists have invested a lot of effort to reduce the cost of these electrodes by decreases the amount of platinum used [79], [80], [103]–[108]; bimetals such as Pt-Au, Pt-Pd,Pt-Co, Pt-Cu, Pt-Ir, Pt-V, Pt-Mn, Pt-Ru and Pt-Ni [8], [103], [104], [108], [109], tertiary metals such as Pt-Co-Cr [105], and quaternary metals such as Pt-Ru-Rh-Ni [70]. Also non Pt catalysts such as Pd, and

NiOx, Ni-CoOx [79], [80], [106]. It has been reported that the Pt alloys with non-noble transition metals had a great ability to decrease the catalyst cost and enhance the ORR activity [110] [19][111]. Among different metals, the CuCoNi ternary nanostructure showed good activity and stability [110], [112]–[115]. In addition to that, many synthetic method have been reported for the preparation of platinum alloys. One example beings colloidal methods, where agglomeration is inhibited by using polymeric substance, which act as protective agents in the reaction medium [107], [108]. This is better than the conventional impregnation method including high heat treatment leading to particle size growth and low surface area [116]. Also, a microwave synthetic method has been reported as a unique technique for preparation of catalysts in fuel cell applications [106], [117], [118]. This method is characterized over the last two methods by a uniform and fast heating process, which avoids temperature gradient leading to very narrow particle size distribution [108]. Furthermore, electrodeposition method is a promising technique to prepare Pt alloy catalysts [119]. It is considered as an effective, low cost, and simple technique [119]. This method has been reported in many studies [109], [119]–[127]. Hakemy et al. [119] and Li et al. [128], reported in separate studies the use of electrodeposition method to fabricate cobalt oxide modified carbon nanotubes and a low platinum content of Pt-Ni-Co ternary alloy catalyst, respectively. The fabricated catalysts exhibited obvious enhancement of ORR activity. Earlier, Tang et al.[128] and Kim et al. [122] proposed in their studies the high dispersion and adhesion of the Pt nanoparticles on CNFs when using the electrodeposition technique, and thus reduce the Pt loading. Liu et al. [113] prepared a quaternary PtCuCoNi nanotube via one step direct electrodeposition technique. A porous anodic aluminum oxide (AAO) membrane

template has been used, which removed later by immersed the AAO membrane into 10 wt% H_3PO_4 solution for 5 hours at 45 ^oC. The study showed that the fabricated PtCuCoNi nanotube exhibited better ORR activity than the commercial Pt black and Pt/C catalysts. The ORR activity was evaluated by rotating disk electrode (RDE) voltammetry. The polarization curve of the fabricated PtCuNiCo/NT, Pt black, and Pt/C are presented in Figure 1.7. The scan rate was 10 mVs^{-1} with a rotating speed of 1600 rpm in 0.1 M $HClO_4$ saturated with O_2. The half wave potential of the three catalysts were 0.74 V, 0.84 V, and 0.87 V for Pt black, Pt/C, and PtCuCoNi, respectively. As shown, although the prepared PtCuCoNi/NT has low content of Pt, but it exhibited better ORR activity over the commercial Pt black and Pt/C.

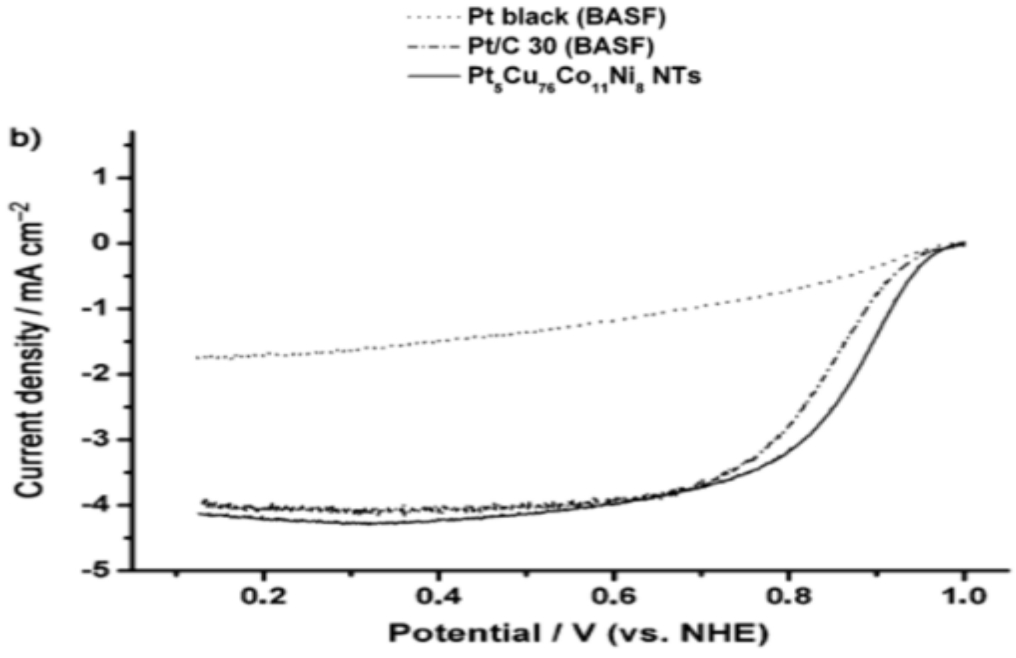

Figure 1.7. Polarization curves of the different catalysts [113].

The author suggested this enhancement of the ORR activity is due to the multimetallic alloy consisting of Cu, Co, and Ni, and also due to the hollow structure of the material, and thus could be used to fabricate a high effective ORR electrocatalyst with low Pt content in fuel cells. Moreover, Wang et al. [114] reported the influence of such metallic structure towards hydrogen evaluation reaction (HER) on their work of fabrication 3D CoNiCu nanostructure by a facile electrochemical method. The results proposed good electrocatalytic performance and excellent activity in HER compared with other non-noble alloys. Rostami et al. [115] published a study about the activity of a modified ternary alloy graphite electrode (G/NiCuCo) for the methanol oxidation in alkaline media in DMFCs. The deposition of the ternary alloy was achieved by repetitive scanning the electrode to a soluble solution of the metals salts over cathodic potential range of 0 V to -1 V vs Ag/AgCl for 40 cycles. Consequently, a scanning of 60 cycles over anodic potential range of 0 V to 1 V in alkaline solution with scan rate of 100 mVs^{-1} for both processes. The results proposed that the addition of Co and Cu to the Ni-based modified graphite electrode enhanced the methanol oxidation performance in alkilne medium comparing with the pure metals or the binary alloys. In a similar work, A. Hamza et al. [112] used the electrodeposition technique to fabricate a ternary nanostructure of CuCoNi modified CNT on glassy carbon electrode (GCE). The activity of the fabricated ternary catalyst has been examined towards methanol oxidation in alkaline medium. In the study, a constant electrolysis potential of -0.9 V has been applied for several times in the potentiostatic deposition of the metals on CNT/GCE. A 0.1 M sodium sulfate solution was prepared including 1mM of the sulfate salt of each metal ion. The passivation of the

metallic deposition carried out using 1M NaOH at scan rate of 100 $mV.s^{-1}$, and the potential has been cycling in the range of -0.2 V-0.55 V for 15 cycles. The results exhibited better stability and activity towards methanol oxidation for the $CuCoNiO_x$@CNT/GCE of about 2.5 times comparing with the mono catalysts depending mainly on the deposition time.

1.2.4 Doped carbon support materials

Doping carbon support materials with heteroatoms can enhance their physical and electrochemical properties like the electrical conductivity, mechanical properties and chemical binding between the Pt and the support leading to enhance the dispersion of the Pt on the support and therefore more catalytic activity and durability [129]–[131].

The incorporation of a heteroatom into a carbon skeleton serving secondary phases within the carbon framework and enhance the ORR performance by adding more catalytic active sites favor for O_2 adsorption and the $4e^-$ pathway reaction mechanism of catalysts [17], [42], [132].

The most common dopants are nitrogen, boron, sulfur and phosphorus. These materials are relatively cheap and environmental friendly [133], [134]. Among all of these dopants, N-doping with carbon has been widely used and studied to improve the nature and properties of the support material [42], [84], [90], [133]–[141]. Nitrogen has a large electronegativity (N: 3.04) comparing to carbon (C: 2.55) with an excessive valence, providing more defects in the graphitic plane due to the π-electrons, and also decrease the crystallinity, and thus, create more chemically active to Pt nanoparticles deposition [42], [133]–[135]. The positive charge density on adjacent carbon atom make it favorable for O_2 adsorption and, therefore, weaken O-O bonding and drive the ORR via the $4e^-$

pathway, and as a result, has excellent catalytic activity towards ORR [134], [142], [143]. Moreover, doping carbon materials with boron (B) and phosphorus (P) have been studied [144], [145]. Unlike Nitrogen which is strongly bonded with Pt with covalent bonds because of the high electronegativity, boron and phosphorus have smaller electronegativity (B: 2.04 and P: 2.19 respectively) than carbon, nevertheless, they also showed good catalytic activity toward ORR by forming ionic bonds with Pt and therefore increased the Pt dispersion on the carbon material [17], [144], [145].

1.2.5 Sulfur Doping

Sulfur-doped (S-doped) carbon materials have recently been investigated for catalytic applications [146]–[148]. In the case of using sulfur as dopant material, the electronegativity between sulfur (electronegativity of S: 2.58) and carbon (electronegativity of C: 2.55) is relatively the same. As many researches study the effect of doping carbon materials with atoms having larger electronegativity such as nitrogen or smaller electronegativity such as boron and phosphorus than carbon. It was interesting to study the doping with elements of similar electronegativity (e.g. Sulfur). Only few reports have been published to study the sulfur doping effect on the ORR performance [149], [150]. Antonietti et. al [151] reported that the large atomic size of sulfur plays an important role to create stain and defect sites in the carbon lattice more than nitrogen which is smaller in its atomic size than sulfur, and also sulfur can easily interact with the surrounding electrolyte molecules more than nitrogen, due to lone pairs of sulfur in the polarizable d-orbitals than those of nitrogen [151], [152]. Kicinski et al. [153] reported the important effect of the lone electrons pairs of sulfur, which make sulfur plays as a

donor of electrons, and thus, increase the electronic density when using as a dopant. Yang et al. [147] published a study about producing a metal free ORR catalyst of S-doped graphene through “annealing graphene oxide and benzyl disulfide under argon” (Figure 1.8). The electrochemical activity of the fabricated S doped graphene was investigated at different temperature from 600 to 1050 ^{O}C.

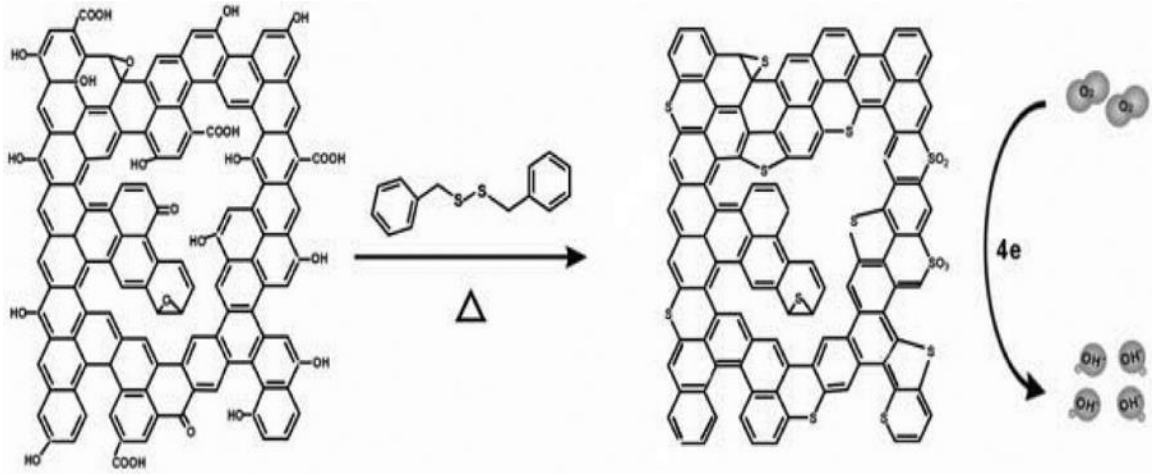

Figure 1.8. Fabrication of S-doped graphene from graphene oxide and benzyl disulfide, Yang et al. [147].

All the samples had limiting current density and onset potentials higher than pristine graphene. The results show better catalytic activity for ORR with the fabricated S-graphene compared with commercial Pt\C catalysts. The study as well suggested that the small change in the atomic charge distribution is most probably due to the creation of C-bonds at the edge of the defect sites. Wang et al. [150] published a fabrication way of

sulfur doped graphene using a Na_2SO_4 as a source for sulfur and Na_2CO_3 as a source for carbon in the presence of magnesium metal under high temperature (Figure 1.9). The Mg act as a reducing agent from both CO_3^{2-} to produce graphene and SO_4^{2-} to supply sulfur which is employed to the carbon sp^2 structure.

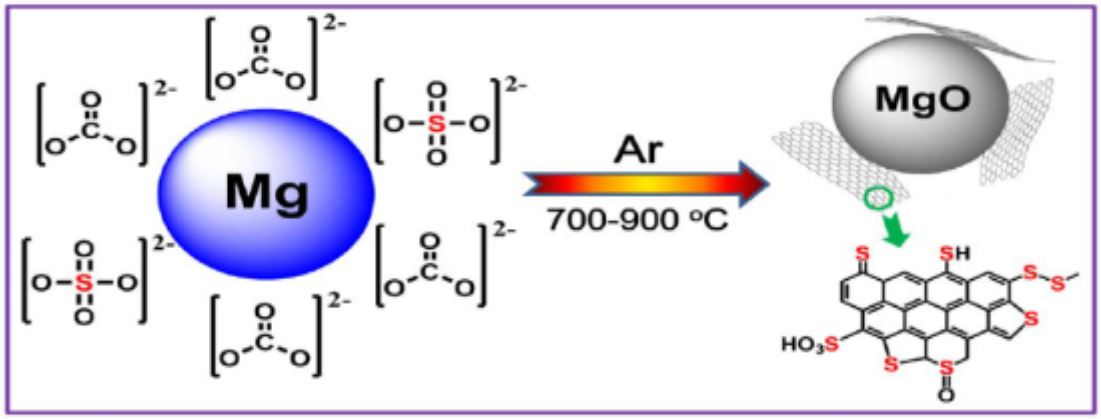

Figure 1.9. Fabrication of S-doped graphene via magnesiothermic reduction of CO_3^{2-}, Wang et al. [150].

The produced S doped graphene samples show less ORR onset potentials and more limiting current density compared with pure graphene as confirmed by the LSV results in Figure 1.10 for the different samples. Furthermore, the XPS results confirm direct doped of sulfur atoms into the carbon as thiophene-like (-C-S-C-). The produced S doped graphene show enhancement of the electrocatalytic activity and stability for ORR through 4-e^- reaction pathway than the commercial Pt/C.

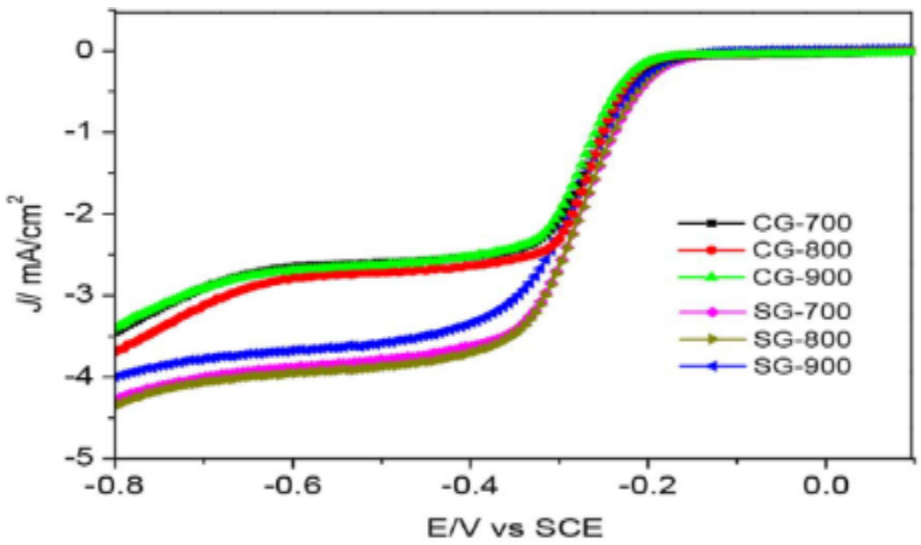

Figure 1.10. Linear sweep voltammetry of different samples at 1600 rpm [150].

Li et al. [154] published a new and cost effect method of dopant p-benzenedithiol (pBDT) to produce S-doped CNTs after heating oxidized CNTs and pBDT in presence of N_2 directly to get pSCNT with good electrocatalytic efficiency and stability as well as long durability and better selectivity in case they used for ORR in alkaline fuel cells. The resulting sulfur-doped CNTs show that sulfur be can doped inside the network of CNT as thiophene-like sulfur in addition to the oxidized sulfur groups.

Hoque et al.[155] provides a study about how the sulfur concentration can effect ORR activity of sulfur graphene support platinum nanowires. The morphologies, structural and electrical properties of sulfur graphene doped platinum nanowires (PtNW/SG) with various concentrations of sulfur, followed by electrochemical kinetic study with different

parameters like Tafel slope, exchange current density and activation energy in respect of ORR. This study clearly showed that the ORR kinetics of nanowire catalysts affected by the amount of sulfur dopants in sulfur graphene (SG). The XRD outcomes show that the graphene layers increase with the increase of sulfur content and the ratio of SP^2 and SP^3 carbon decreases showing lower graphitic character of SG. Furthermore, the UV-vis and LPR technique results indicate that with the increasing sulfur content in graphene, the band gab increases and the electrical conductivity decreases. Among the different concentrations of sulfur content of SG (0.35, 1.40, 2.70 and 3.95 at.%), the 1.40 at.% sulfur provide the best electrokinetic activity, with a 1852 mA/mg_{pt} of mass activity and 662 $\mu A/cm^2_{pt}$ of specific activity at 0.9V vs. RHE. It also shows high exchange current density and low activation energy. The higher sulfur contents interrupt the growth of well-defined PtNWs which reduces the ORR performance and stability, while the lower concentration of sulfur content (0.35 at.% sulfur) shows a similar ORR performance with pure graphene. Park et al. [152] studied the preparation of sulfur-doped graphene using pristine graphene which was prepared based on "fluorinated graphite intercalation compounds (FGIC)-derived graphene with heat treatment at 600-900 °C in presence of carbon disulfide (CS_2) vapor under argon (Ar) gas". In addition, nitrogen-doped graphene was also prepared in the same way at 850 °C under ammonia (NH_3) gas for comparison. In results, it found that the sulfur content influenced the catalytic activity of S-doped graphene, and hence, the current density and onset potential toward ORR. Moreover, the prepared s-doped graphene exhibited higher electrocatalytic and durability than N-doped graphene which, however, enhanced the onset option. The XPS results

showed that the S has “thiophene-like structure”. Earlier, Inamdar et al. also mentioned the effect of how the sulfur bonding with carbon structure [156]. In the study, the thiophene used as a sulfur and carbon source after burning using “flame pyrolysis method”. The XPS results suggested that the thiophene structure (-C-S-C-) is an active site for ORR, as the electrochemical results showed that the ORR peak potentials shifted to less negative values with sulfur content, indicating that sulfur has a role as an active site for ORR by effectively drive the oxygen reduction process towards the 4-electron pathway.

Domínguez et al.[157] reported the integration of nitrogen or sulfur and nitrogen by urea or thiourea as a sources of both S and N, inside multiwalled carbon nanotubes after it was physically treated to enhance defects for the integration of N and S in those defects sites in the C-C structure of CNTs. Co-doping with S helped increase the amount of N into C-C structure after the CNTs graphitic structure collapses. This increase of the N amount in the catalyst and enhanced the activity of N/CNT towards ORR in acidic media as well as alkaline media. Furthermore, the co-doping with S enhanced the catalytic activity towards ORR in acid media. A fabrication of N and S dual-doped mesoporous graphene by a single step reported by Liang et al. [158] to create an ORR electrocatalyst with a high performance to replace Pt/C. It mentioned that enhanced mesoporosity helps the diffusion of reactants in the ORR process and synergistic effects forming by multiple-element doping. By comparison to commercial Pt/C or even only S or only N, the dual-doped carbon catalyst showed excellent ORR performance. Furthermore, the redistribution of spin and charge densities from dual-doping leads to more active sites of carbon atoms as sulfur forms a double bond with C on the edge of graphene clusters.

With S only doped graphene, charge transfer originates from the difference on the elements orbitals. The charge transfer on N only doped graphene is because of the difference between C and N electronegativity, thus the ORR originates from all around C atoms with high positive charge density. Sulfur loss and an electron on the 3s orbitals as its embedding into the carbon texture with sp^2 hybridization, lead the sulfur atom to be positively charged and work as the catalytic center of ORR. In N/S dual-doped, no paired electrons insert into the graphene cluster and the density of atomic charge/spin is highly changed. (Figure 1.11)[158].

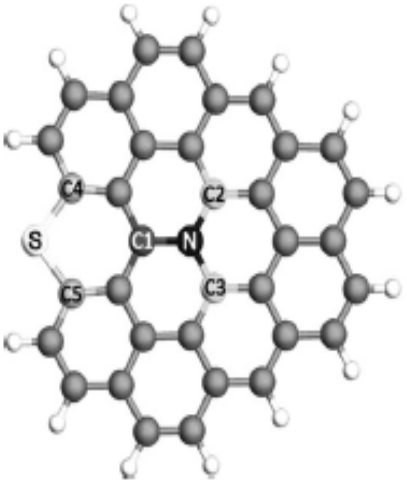

Atom Number	Spin Density	Charge Density
C1	0.43	0.23
C2	-0.03	0.28
C3	-0.03	0.28
C4	0.16	-0.22
C5	0.16	-0.22
N	0.06	-0.88
S	0.09	0.21

Figure 1.11. Charge and Spin densities of N and S dual doped graphene. [158].

However, many studies reported the role of spin density in the case of S-doping to catalytic activity [147], [152], [158], [159]. Recently, Zhang et al. used Cysteine as a

sulfur source to produce nitrogen/sulfur-doping graphene [160]. The fabrication process (Figure 1.12) started with modifying the graphene oxide (GO) with cysteine as a N/S source by mixing together and stirring the mixture for 7days, followed by heating at 900 ^{o}C under Argon.

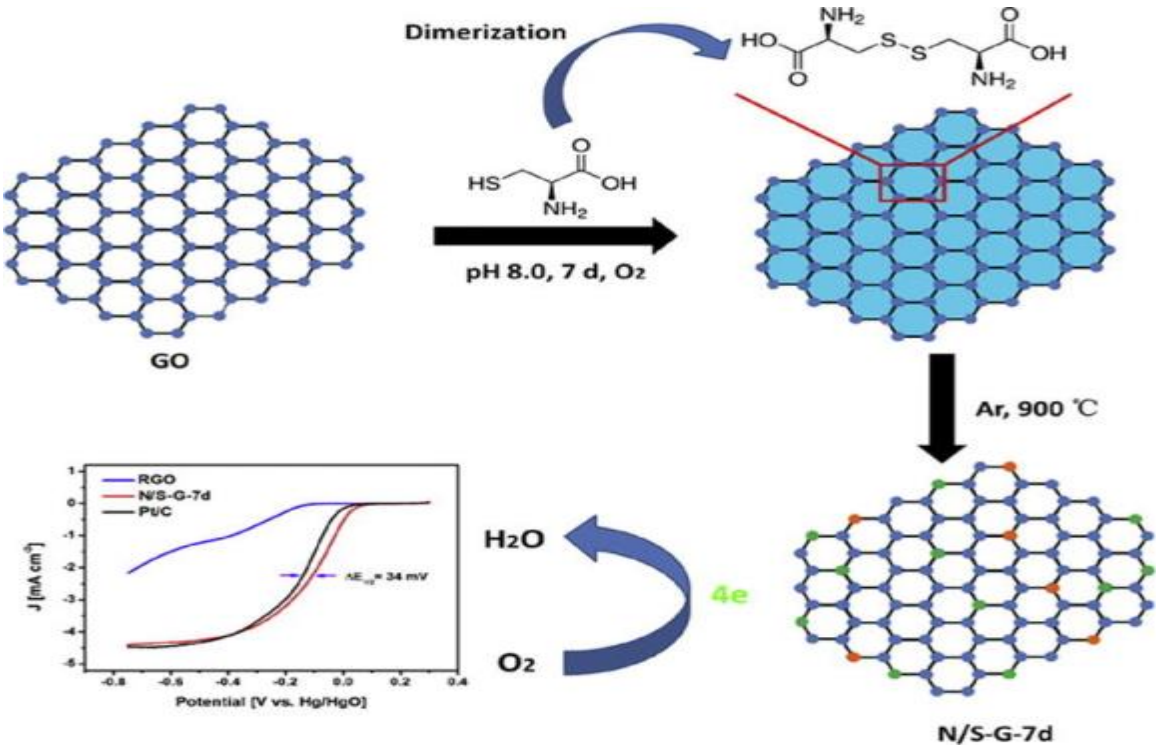

Figure 1.12. Fabrication process of N/S co-doped graphene, Zhang et al. [160].

The produced catalyst was denoted as N/S-G-7d. The ORR activity measured using glassy carbon electrode for linear scanning voltammetry (LSV) and cyclic voltammetry (CV) measurements. The results showed excellent ORR performance and durability in

alkaline electrolyte. From the LSV results presented in Figure 1.13a, the N/S-G-7d sample has more positive onset potential and the highest limiting current density not just to the other samples which had less or more stirring days, but also over the commercial Pt/C (Figure 1.13b). However, the current density and the 4-electron reaction selectivity was very near to that of Pt/C. The study obviously indicates the importance of the heteroatom source and the reaction conditions as a main factor in getting dopant materials with good ORR performance.

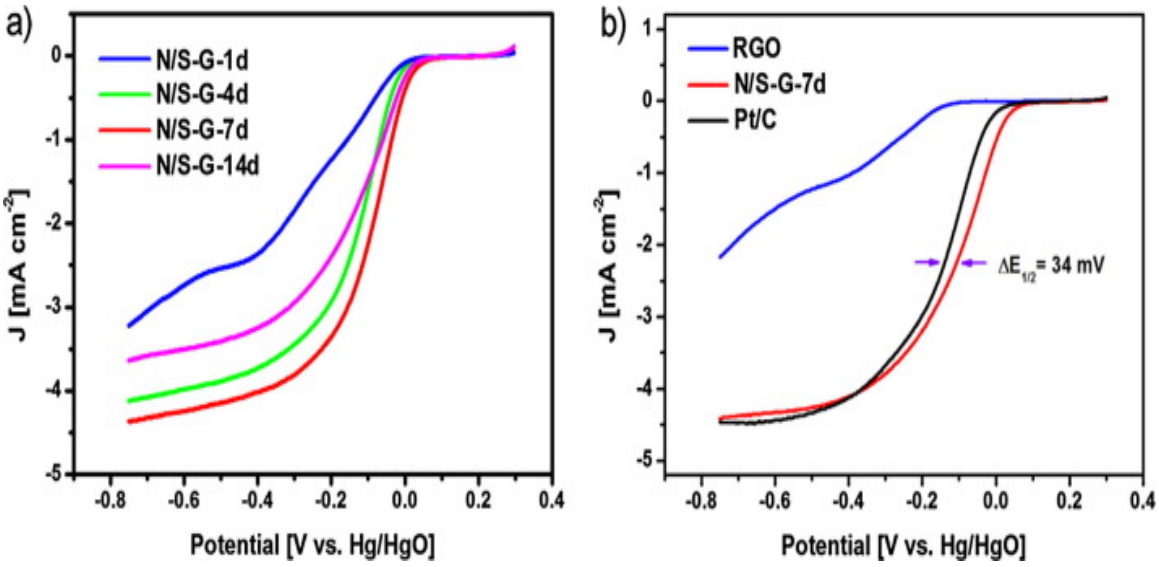

Figure 1.13. LSV to compare ORR activity of N/S-G-7d with a) other samples prepared under different reaction conditions, and b) commercial Pt/C and reduced graphene oxide (RGO), Zhang et al. [160].

Theoretically, Tavakol and Keshavarzipour studied the influence of sulfur doped carbon

nanotubes in 4-eletron ORR by employing DFT theory method [149]. They calculated all possible energies of all pathways in addition to energy gaps and chemical potentials. When doping the carbon nanotube with sulfur, unpaired electrons were introduced leading to local high density and smaller gap energy, and thus, higher ORR performance than none doped carbon nanotubes.

1.3 Electrospinning

The electrospinning technique is considered to be the most effective, easy and cost effective technique to fabricate CNFs with small diameters in the range of tens micrometers down to a few nanometers, which makes it suitable to use with many applications including the energy storage devices[138], [161]–[166]. Furthermore, the variability of the materials (organic and inorganic materials) that can be used to produce nanofibers by electrospinning add greater advantage to this technique for energy device uses, especially the use of metal oxides which help to enhance the conducting properties of the produced nanofibers [99].

1.3.1 History of Electrospinning

In 1745 Bose studied the effect of electrostatics on liquids as he "produced aerosols by applying a high electric potentials to drops of liquids"[167]. Later in 1882, Lord Rayleigh studied the charge amount that can overcome the surface tension of a drop, which opened the door for electrodynamic researchers to understand the effect of electric change on dielectric liquids.[167]. This led to the fundamentals of electrospinning technique, firstly reported in 1934 [168][169] by Anton Formhals who published several patents between 1934 to 1944 where a polymer filament of cellulose acetate was formed as an effect of electrostatic force [170]–[174] with the term "electrostatic spinning". He used an apparatus consisting of two electrodes of different electrical charges, one connected to a collector while the other immersed in solution to form fiber effected with many factors like the viscosity and the distance between the spinnerets and the collector. In 1952, Vonnegut and Neubauer created a simple high-voltage uniform electrified method using a

glass tube filled with water or other liquids and an electric wire attached to a source of high voltage (5-10 kV) [175]. In 1955, Drozin used a similar tube to that used by Vonnegut to produce an aerosol of uniform size of different liquids under high electrical potentials [176]. Taylor in 1964, reported the formation of jet from liquid drop on the needle forming a conical shape when applying an electric field (Figure 1.14) [177], which was later named after him; the 'Taylor cone' [178]. Taylor in 1969 also introduced the first model of the electrospinning process named the "leaky dielectric model", which is usable if the fluids conductivity is finite [169][179].

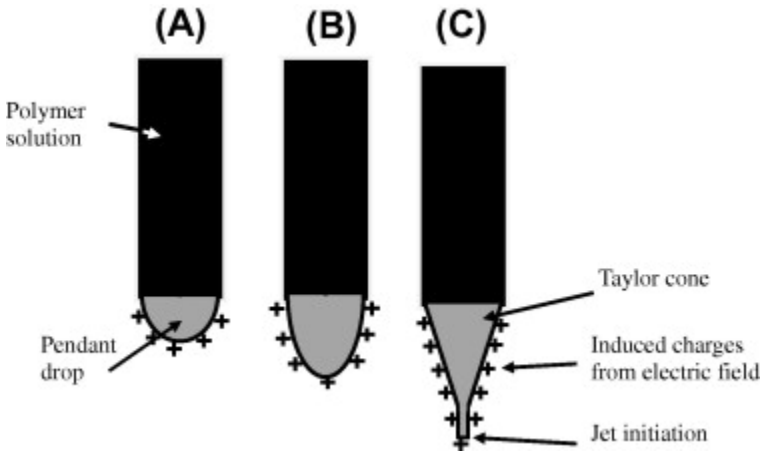

Figure 1.14. Taylor cone formation with increasing voltage (left to right) [177].

In 1966, Simons patented a technique using electrical spinning to get short, fine, and non-woven fabrics of lightweight ultra-thin textiles from low viscosity solutions [180]. Baumgarten in 1971, reported how he had successfully produced acrylic fiber with

micrometer diameter of 0.05-1.1 microns using stainless steel capillary tube attached with a source of high voltage current and used a grounded metal screen to collect the produced fibers [181]. Years after, the electrospinning technique attracted researchers yet further. Larrondo and Manley in 1981, Reneker and Chun in 1996, Fong and Reneker in 1999, Chen et al. in 2001, Huang et al. in 2003, Yang et al. in 2005 among many others [182].

1.3.2 The Electrospinning Process

Although many improvements have been made, the main principle and the classic device setup of the electrospinning is the same. In 1993 Doshi and Reneker published their study of the typical electrospinning process. They successfully produced fibers with a diameter range of 0.05 to 5 microns [183]. In the electrospinning technique, the typical setup of the device (Figure 1.15) is composed of three major components to achieve the process [183] [184] [185]:

1- A power supply as a source of high voltage electric current between the spinneret and the collector.

2- A pump with syringe which have a small metallic needle at its, to control the flow rate.

3- A collector.

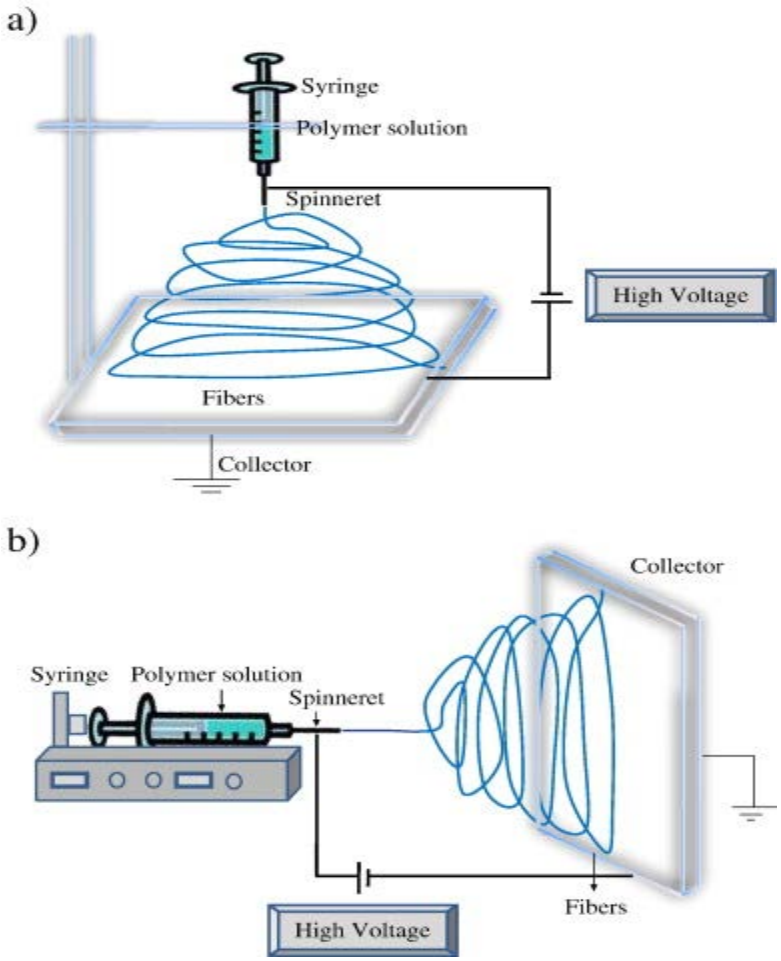

Figure 1.15. The basic electrospinning set-up (a) Vertical and (b) Horizontal [169].

Firstly, the syringe is filled with polymer solution, then connected to a high voltage source at the metallic needle tip, while the other electrode is attached to a collector. A high voltage is applied to the syringe needle containing the polymer solution causes the polymer drop to be charged and generation of an electrostatic force. At a critical amount of the charge, the electrostatic force and the surface tension cause the polymer solution drop to deform in the direction of the collector, and thus take a conical shape called a

"Taylor cone" (Figure 1.14) due to the eruption from the formed droplet [178] [184][186]. The deformed drop elongates and becomes long and thin then forms a jet from the polymer solution which attracts to the charged collector, the solvent evaporates during its travels in the air and when it reaches the collector, results in solid nanofibers on the collector [187] [188].

1.3.3 Random and aligned fibers

Many kinds of fibers can be produced via electrospinning, however the fiber alignment can change with the change of the collector type and its rotation speed [189]. Also, changing the single syringe to a multi-system syringe with different polymer solutions can be used to produce core-shell nanofibers [189]. Zhang et al. [190] used a rotating drum collector at low rotation speed to fabricate uniform thickness of PAN nanofibers with random orientation (Figure 1.16).

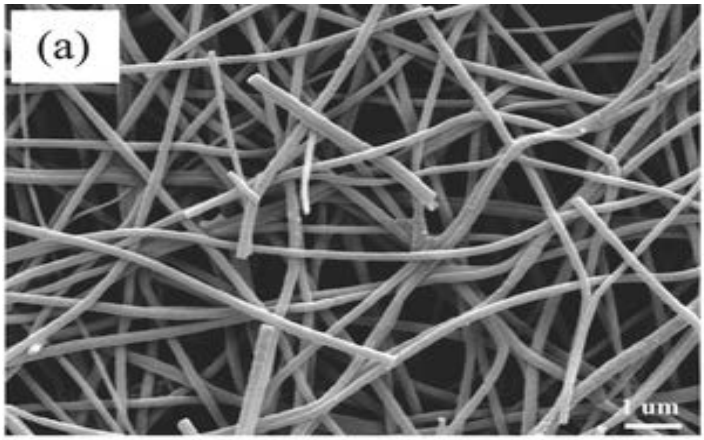

Figure 1.16. PAN nanofibers with random orientation, Zhang et al.[190].

Increasing the rotation speed leads to increase drawing force which causes the production of aligned fibers. Chew et al. [191] successfully produced aligned nanofibers when rising the rotation speed of the drum collector to a high speed (2200 rpm) resulting long aligned nanofibers. (Figure 1.17). Also Zhou et al. got aligned fibers when using a metal disk collector with a high rotation speed instead of the drum collector [192]. It is important to note that the very high rotation could lead to breaks and non-continues fibers [177]. The aligned fibers are important in that engineering applications such as tissue engineering and nanocomposites, because of its high mechanical properties compared with random fibers, while random orientation is more popular in electrochemical energy storage applications [177].

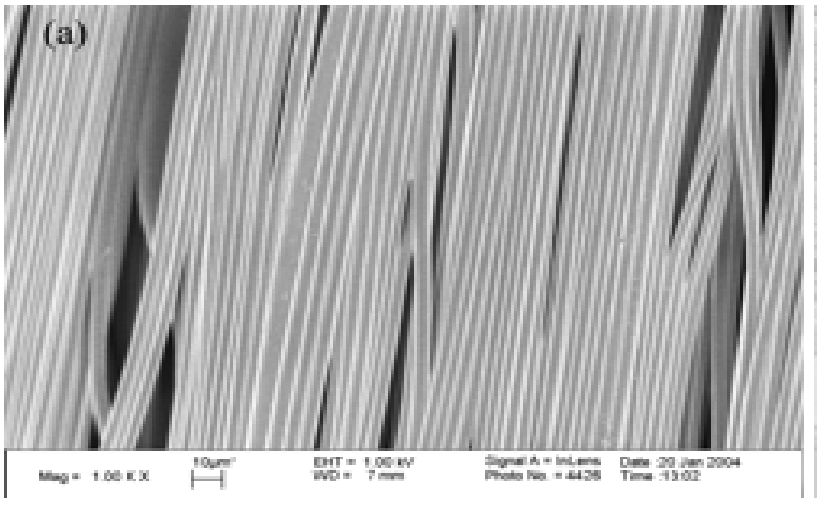

Figure 1.17. Aligned nanofiber fabricated with high ration drum collector speed, Chew et al. [191].

1.3.4 Core-shell fibers

The core/shell fibers are used in many applications, such as, “drug delivery system”[193]–[195] and as “electrode materials in electrochemical energy storage devices”[98], [196], [197]. To fabricate core/shell structures, a co-electrospinning (or coaxial electrospinning) is used as shown in Figure 1.18, with two different polymer solutions filled into the inner and outer nozzles. Generally, the shell works as support to protect the core materials. This structure is very useful to use with drugs and their delivery system, and can be used for loading two different drugs in a single fiber at the same time [168] [193]–[195], [198]–[201].

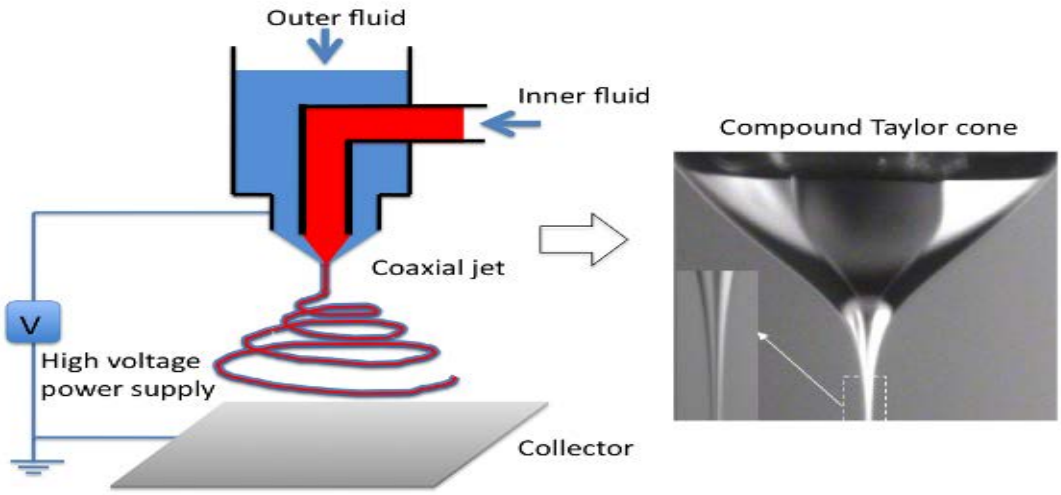

Figure 1.18. The basic coaxial electrospinning set-up to fabricate core/shell structure fibers [195].

1.3.5 Effects of Parameters on Electrospinning

There are many parameters effecting on the electrospinning process, those parameters are very important on the quality, morphology and proprieties of the produced fibers. Doshi and Reneker [183] summarized those parameters and classified them into three categories: polymer solution parameters, process parameters and ambient parameters. The polymer solution parameters including polymer concentration, conductivity, viscosity, and surface tension, while the current voltage used, the flow rate, and distance from the needle to the collector are the process parameters. Finally, the humidity and the temperature during the electrospinning process are the ambient parameters.

1.3.5.1 The Polymer Solution Parameters

1.3.5.1.1 Polymer concentration and viscosity

The molecular weight and the concentration of the polymer is the main factor to control the viscosity of the polymer solution [202]. Fong et al. [203] studied, in 1999, the effect of viscosity on forming beads with polyethylene oxide (PEO) polymer. They used a polymer concentration of 1 to 4 wt.% during the experiment. The results show that a high viscosity was needed in order to get bead free fibers, as the beads decrease with the increase of the polymer solution viscosity. Identical conclusion was mentioned by Fang et al. [204] in his study of PAN polymer in DMF solvent, the low concentration (5 wt.%) formed more beads comparing with the higher concentration (7 wt.%) of the PAN

polymer solution (Figure 1.19).

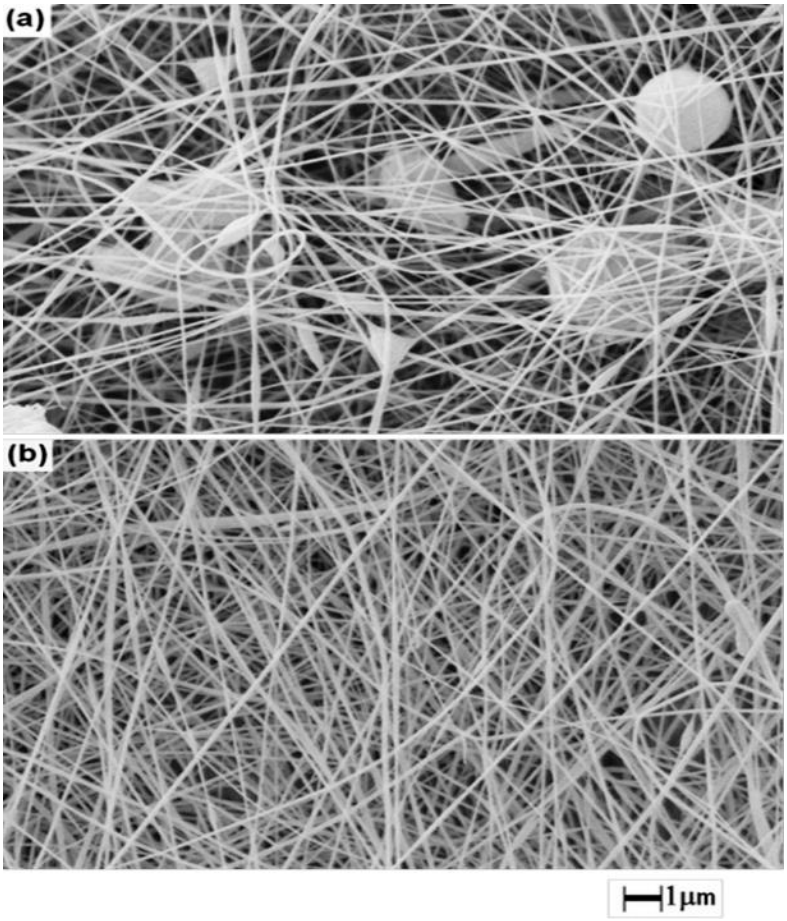

Figure 1.19. SEM of PAN nanofibers (a) 5 wt.% and (b) 7 wt.%, Fang et al. [204].

The study also showed that the fiber diameter is effected by viscosity, which increased with the increasing viscosity. This was mentioned earlier in 2005 by Mit-uppatham et al. [205] and in 2005 by Gupta et al. [206] In his study of viscosity and concentration on the

fiber formation of poly(methylmethacrylate), the PMMA fiber increased with the increase of the polymer solution viscosity (Figure 1.20).

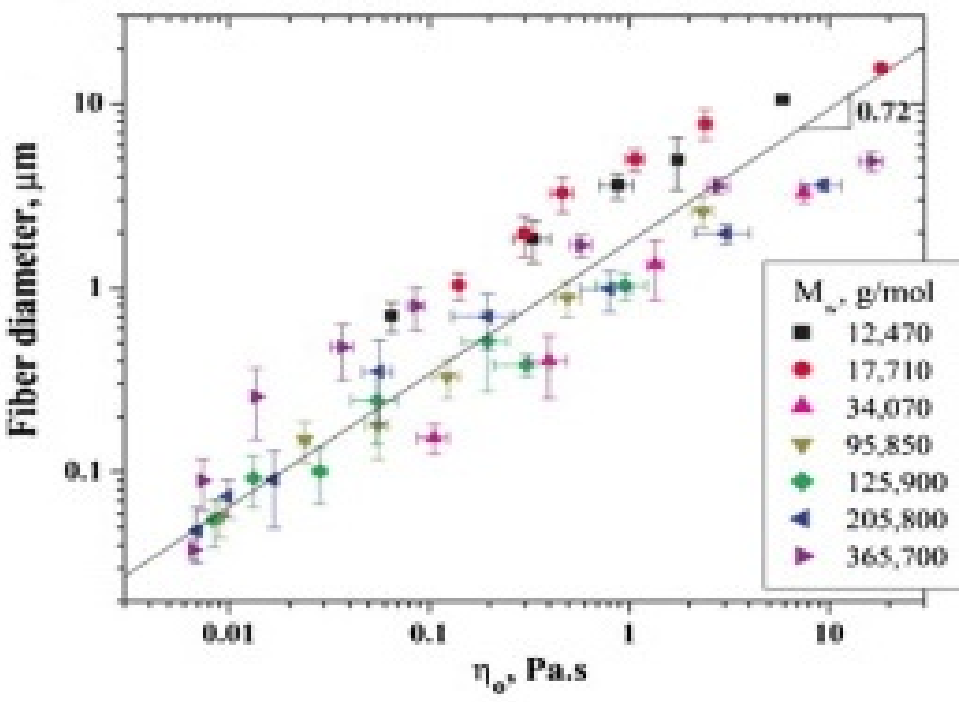

Figure 1.20. The fiber dimeter versus the solution viscosity of the PMMA, Gupta et al. [206].

1.3.5.1.2 Surface tension

Lowering the surface tension of the polymer solution reduces the formation of the beads and reduces the applied electric field that is needed to overcome the surface tension in order to eject the charged droplet [183] [204]. The surface tension mainly depends on the

solvent used, Wang et al. [207] mentioned the importance of using a solvent with low surface tension in the electrospinning process. Fong et al. [208] described the use of ethanol as a solvent to produce smooth fibers, while Zeng et al. [209] reported the addition of surfactants to reduce the surface tension and get uniform fibers.

1.3.5.1.3 The conductivity

The polymer solution must have enough charges that make it able to overcome the surface tension and stretching the jet during the electrospinning process. Meaning if the polymer solution conductivity is low, the elongation of the jet because of the electric force and results in more beads [187]. One way to increase the conductivity is by adding an ionic salt (such as NaCl) to the solution [208], [210] to produce uniform fibers with less beads and small diameter.

1.3.5.2 The Process Parameters

1.3.5.2.1 The electric field

The electrospinning process needs electric field with a specific value to generate the required charges on the polymer solution and overcome the surface tension then elongate the polymer jet to produce the fibers [178]. However, this critical value is dependent on the surface tension and the viscosity of the polymer solution. Generally, the higher molecular weight of the polymer, the higher the viscosity of its solution and so the higher electric field voltage needed [211].

1.3.5.2.2 The distance from the tip to the collector

The distance between the needle tip and the collector should be enough to give the fibers enough time to evaporate the solvent and dry before collected. A very short distance might cause beads to form on the formation fibers, [212] [213]. Fang et al. [204] again, reported the effect of the collecting distance on the formation of beads with PAN 7 wt. %, he mentioned the formation of beads with a distance less than 8 cm, while formation of bead-free fibers when increasing the collecting distance without changing the fiber diameter (Figure 1.21).

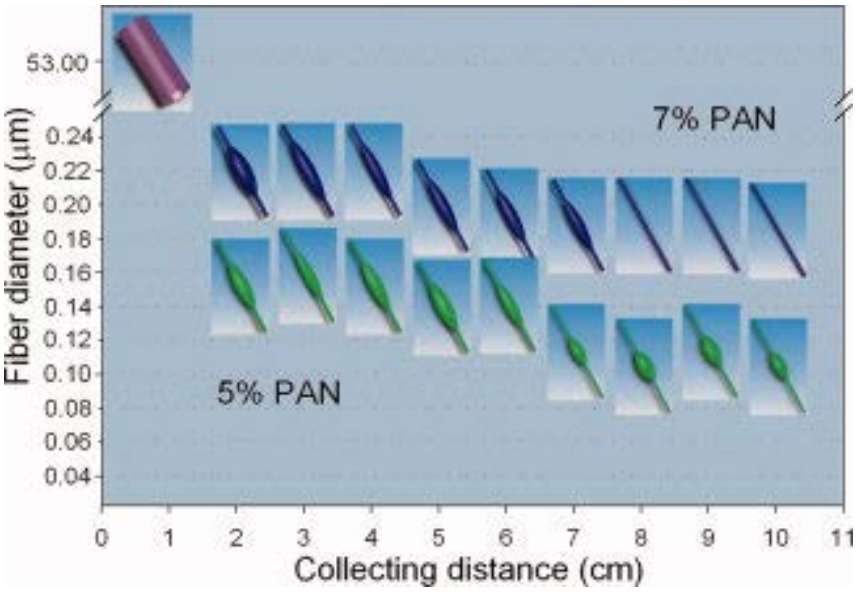

Figure 1.21. Formation of beads on the fibers of 7% PAN at low collecting distance without effect on the fiber diameter, Fang et al. [204].

1.3.5.2.3 The flow rate

The flow rate is an important factor to determine the produced nanofiber during the electrospinning process. Yuan et al. [214] published a study to fabricate ultrafine fibers of polysulfone (PSF), mentioned that increasing of the flow rate will lead to form fibers with larger diameter and also forming beads within the fibers as observed in the SEM images in Figure 1.22 of two different samples prepared at flow rate of 0.4 ml/h and 0.66 ml/h.

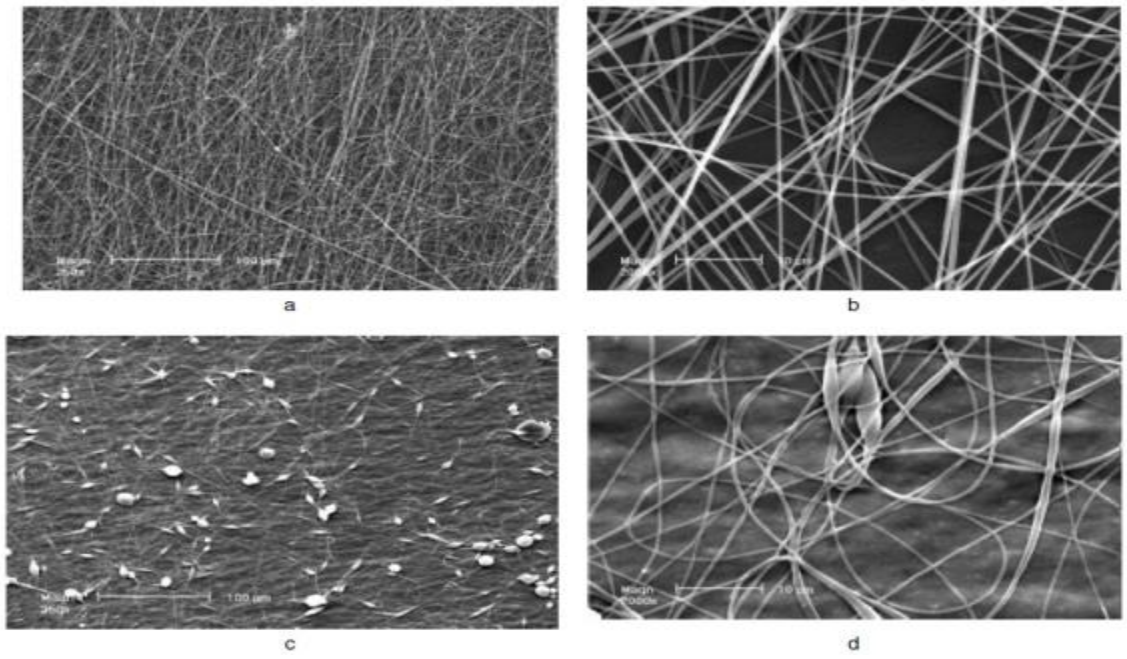

Figure 1.22. SEM images of the ultrafine PSF fibers with flow rate of 0.4 ml/h (a, b) and 0.66 ml/h (c, d), Yuan et al. [214].

1.3.5.3 The ambient parameters

The temperature and the humidity are the ambient parameters that must consider about during the electrospinning process because they can affect the fiber morphology and the whole process of electrospinning. Casper et al. [215] reported on his study in 2004 the possible effect of humidity during the electrospinning process on polystyrene nanofibers., He found that with the increase of the humidity creates a porous structure of the fiber that forms on the surface of the produced fiber (Figure 1.23).

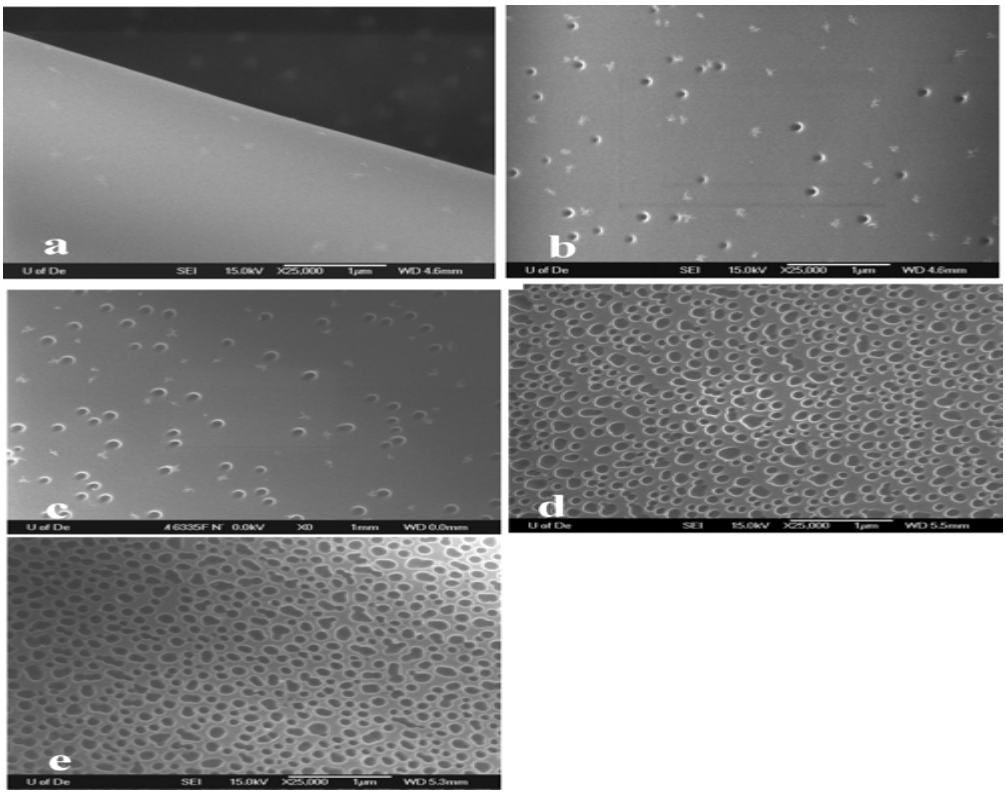

Figure 1.23. SEM of PS fibers with humidity of: a) less than 25%, b) 31-38%, c) 40-45%, d) 50-59% and e) 60-72%, Casper et al. [215].

The number and the size of the pores increased with the increase in humidity. He recommended that the electrospinning process should take place at 25% humidity or less in order to get smooth fibers (Figure 1.23a).

Furthermore, Mit-uppatham et al. [205] published a study to produce ultrafine polyamide-6 fibers and reported the effect of temperature on the produced fiber. He found that when increasing the temperature, the fiber morphology was not affected and still shows some beads with the smooth fiber, nevertheless, he reported that the increase of the temperature causes to reduce the viscosity of the polymer solution and therefore, decreases the fiber diameter.

1.3.6 Polyacrylonitrile (PAN)

Polyacrylonitrile (PAN) is one of the most common polymers used as precursor to produce carbon nanofiber by electrospinning technique, "using N,N-dimethylformamide (DMF) as a solvent"[216]. To date, Polyacrylonitrile (PAN) based material meets 90% of the total world's manufacture of carbon nanofibers [217]. PAN is characterized by its good spinability [218]. It is able to produce CNF with high carbon yield of more than 50% of the main mass and its content of N atoms, due to its chemical formula $(C_3H_3N)_n$ (Figure 1.24) [219], [220]. This gives it excellent mechanical properties, ability for modifying the structure of the produced CNFs and the simplicity of locating stabilized as a result of the creation of a ladder structure (Figure 1.25) through nitrile polymerization [219].

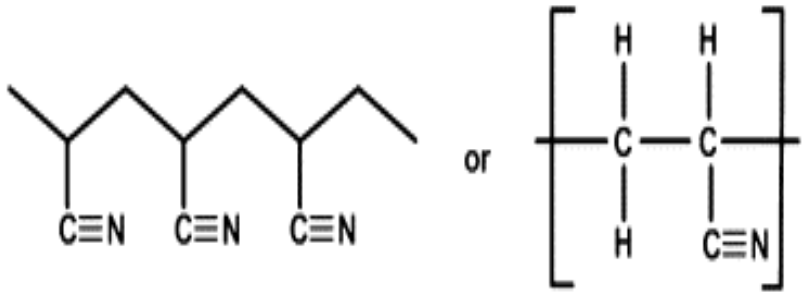

Figure 1.24. Structure of Polyacrylonitrile [219].

They consist of nitrogen in the PAN structure, they have role as a nitrogen source within the produced fiber, which is useful to the ORR [141].

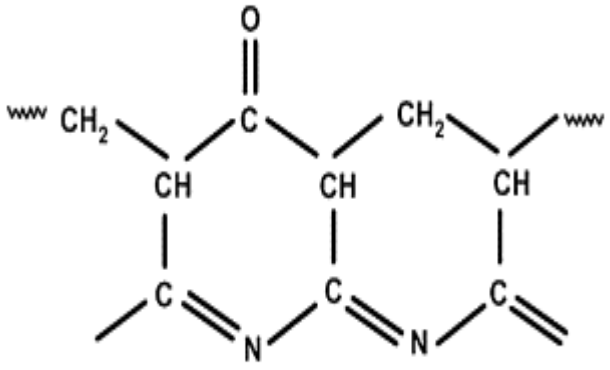

Figure 1.25. Ladder structure of PAN [219][221].

1.3.6.1 Heat Treatment

In order to convert the electrospun PAN nanofiber into CNFs, further heat treatment is required consisting of two sequential steps: a stabilization followed by a carbonization step. Through stabilization and carbonization of PAN nanofibers, the fibers show major weight loss and shrinkage, causing a reduction of the fiber diameter [218][219].

1.3.6.1.1 Stabilization

During the stabilization process, the chemical structure of the fibers change to form ladder structures by oxidation, dehydrogenation and cyclization reactions [219]. The process achieved in an atmosphere of air as an oxidizing medium at 180-300 ^{O}C [222] [219]. This process is very important to make the carbon fiber structure thermally stable and ready for the carbonization process [219]. During the dehydrogenation process, a double bond is formed because of the elimination of water. Consequently, a cyclization reaction of the nitrile groups take place converting the triple bond of C≡N to a double bond C=N and makes a bond with other nearby carbon atoms resulting in the change of the aliphatic structure to a cyclic ring structure [217] [219] as shown in Figure 1.26 below.

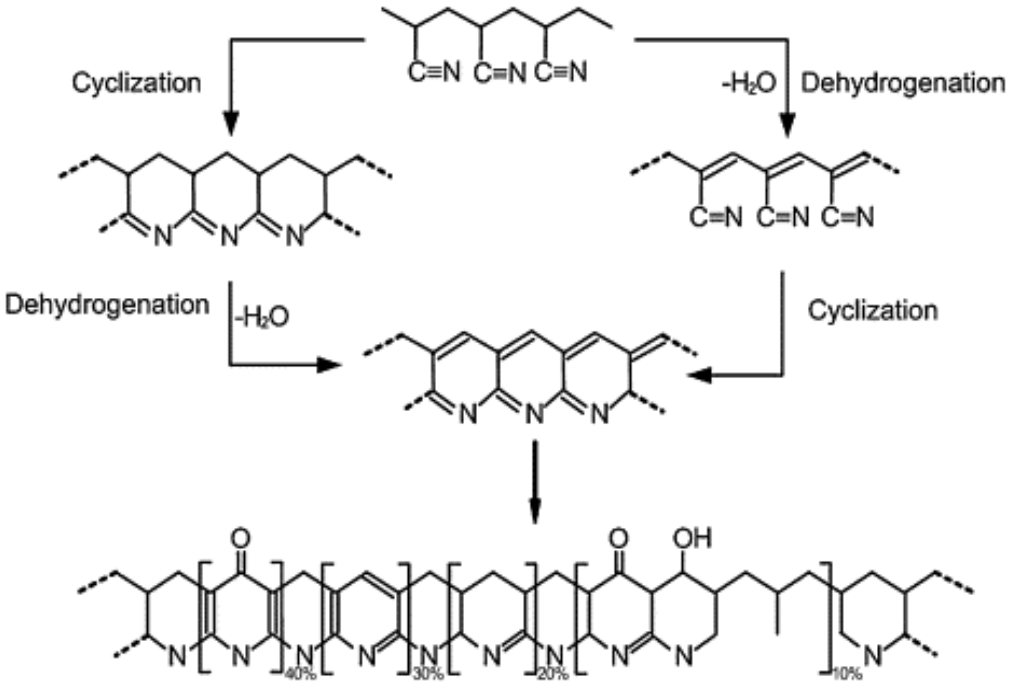

Figure 1.26. PAN stabilization process [219].

The fibers color change from white to brown then black at the end. Many research papers reported the ideal temperature for the stabilization process. For example, Fitzer et al. [223] reported that 270 °C is the best stabilized temperature, while Mathur et al. [224] reported the need of a temperature up to 400 °C for complete stability. However, overheating may burn the fibers while low temperatures may result in incomplete stabilization. Recently studies achieved this process in the range of 150-300 °C [225] [226][164].

1.3.6.1.2 Carbonization

After the stabilization step, the carbonization step takes place. Unlike the stabilization process which needs oxygen for the oxidation reaction, the carbonization process is achieved in an inert atmosphere under nitrogen or argon [219]. During the process, aromatic growth and polymerization occur. When the temperature rises up to 800 °C, the cyclic structure opens and a carbon chains begins to form in order to build graphitic carbon structure. Figure 1.27 represent the carbonization step which start after the stabilization step. With this process, the amount of nitrogen and hydrogen atoms decrease with shrinkage of the fibers diameter size, as a result of the elimination of nitrogen and hydrogen as (HCN) and NH_3 gases [217] [227] .

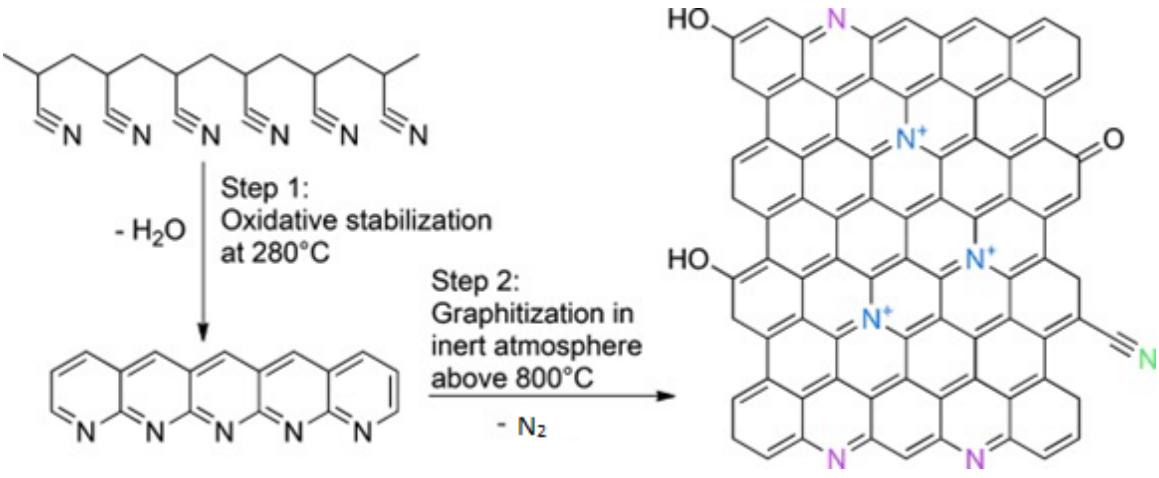

Figure 1.27. Heat treatment of PAN fibers. First step is stabilization and the second is the carbonization [141].

A further increase of the temperature above 800 °C leads to the formation of more graphitic phase but decreases the nitrogen content within the CNF structure. However, the existence of nitrogen atoms into CNF is favorable for ORR applications [141].

1.3.7 Electrospinning for oxygen reduction reaction (ORR) applications

As discussed above, electrospinning is a simple, easy and cheap method used to produce fibers with small size of diameter in the nanoscale range[228]. Reducing the polymer fiber size from micrometers to micrometers and nanometers gives the fibers unique properties relative to other fibers, increasing the surface area, high porosity, high permeability, light weight, and all with cost effectiveness[228]. Furthermore, the use of precursors rich in nitrogen (i.e. PAN), can add more benefits to the produced fiber as a N-doped CNF, and is favorable for the ORR applications [141][226].

Zamani et al.[166] studded the combination of polyaniline (PANI) with Fe-PAN as a blend to fabricate Fe–PANI-PAN nanofibers by electrospinning for the first time. The pyrolysis leading to creation of catalysts of M-N-C nanofiber to enhance the ORR performance in acidic media. Choosing the PANI was based on its perfect nitrogen precursor to give effective M-N-C catalysts due to its structure of aromatic ring with rich nitrogen in orderly distribution, which can produce nitrogen-doped graphitic carbon structures while heating. Moreover, PAN can be a cheap polymer carrier to improve the solubility of PANI in solution as well as being another source of nitrogen. From the polarization curves in Figure 1.28a, he noticed that adding 10 wt. % PANI to the Fe-PAN solution can improve the ORR performance of the nanofiber produced for fuel cell applications compared with Fe-PAN without PANI with 100 mV improvement of the

onset potential and 70 mV of half-wave potential, with a high selectivity of the 4-electron pathway (Figure 1.28b).

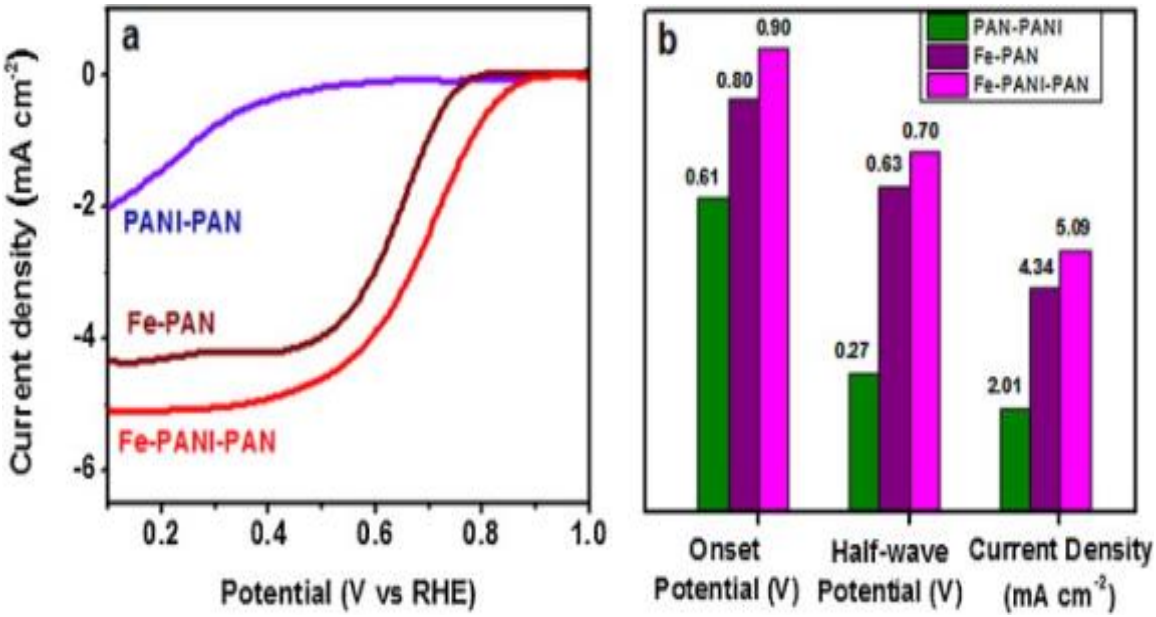

Figure 1.28. a) LSV curves in presence of oxygen, and b) The onset and half wave potentials with current density for the three catalysts, Zamani et al [166].

He proposed the role of high nitrogen content within the fabricated fiber to enhance the ORR activity. This study presented a unique method to produce an effective 1D inexpensive catalysts via electrospinning for ORR. In similar work, Qiu et al. [229] prepared an electrocatalyst based on PAN via electrospinning in the form of (Fe-N/CNF). The prepared electrospun PAN fibers stabilized at 250 °C and then doped with Fe using different concentrations of $Fe(NO_3)_3$ solution, subsequently with carbonization process.

The SEM images of the prepared Fe-N/CNF showed broken fibers with porous structure (Figure 1.29), unlike the NCNF prepared earlier without Fe doping for comparison, which showed smooth, uniform and continuous fibers (Figure 1.29a).

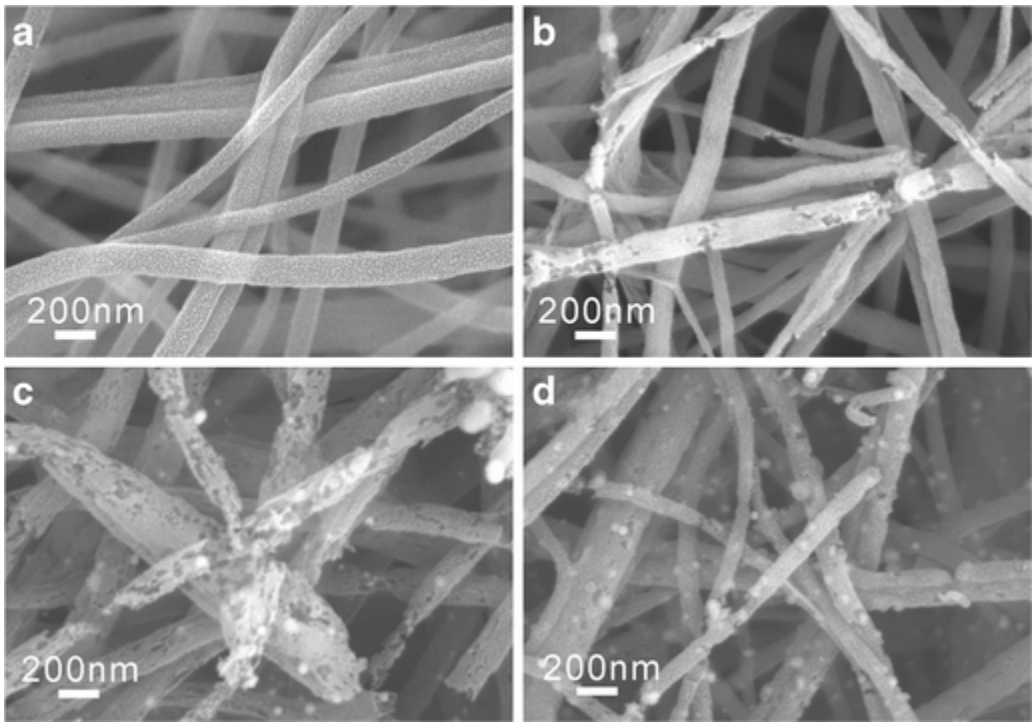

Figure 1.29. SEM images of a) NCNFs, the prepared Fe-N/CN with different concentration of $Fe(NO_3)_3$ b) 0.01 %, c) 0.5 %, and d) 3 %, Qiu et al. [229].

The ORR activities of the produced samples were studied in both alkaline and acidic media. The prepared electrocatalyst exhibited better ORR activity and stability than the catalyst without Fe specially in the acidic media. The author proposed that the existence

of Fe within the CNF enhanced the graphitization of the polymer to carbon and thus, improved the anti-oxidation ability, and therefore enhanced the lifetime of the catalyst.

Recently, Shang et al. [226] used PAN as precursor with its benefit as a nitrogen and carbon source, to prepare a nitrogen-doped nanofiber encapsulated in cobalt nanoparticles (Co-PAN) as an ORR catalyst by electrospinning technique. The polymer solution consisted of both PAN and cobalt acetylacetonate, 0.8 g and 0.35 g respectively. They then dissolved in 10 ml of DMF as a solvent after heating to 75 ^{o}C for 30 minutes. The electrospinning parameters were sited-up as 15 cm distance between needle tips and collector, the voltage was 22 kV, and 1.5 ml feeding rate. The collected samples stabilized at 150 ^{o}C and then carbonized at various temperatures 700, 800, 900 and 1000 ^{o}C donated as Co-PAN-700, Co-PAN-800, Co-PAN-900 and Co-PAN-1000 respectively. The ORR activity was investigated for the four samples and compared with commercial Pt/C and PAN-800, without Co doping. Linear sweep voltammetry (LSV) in Figure 1.30, was carried out in alkaline media in presence of oxygen at scan rate of 10 mVs^{-1} and 1600 rpm rotation rate. Figure 1.30 exhibits that Co-PAN-800 has the highest positive onset potential, the best limiting current density and more positive half-wave potential over the other samples. The ORR performance for the samples is listed in Table 1.3. Moreover, Co-PAN-800 catalyst showed high stability after 5000 CV cycles at 1600 rpm.

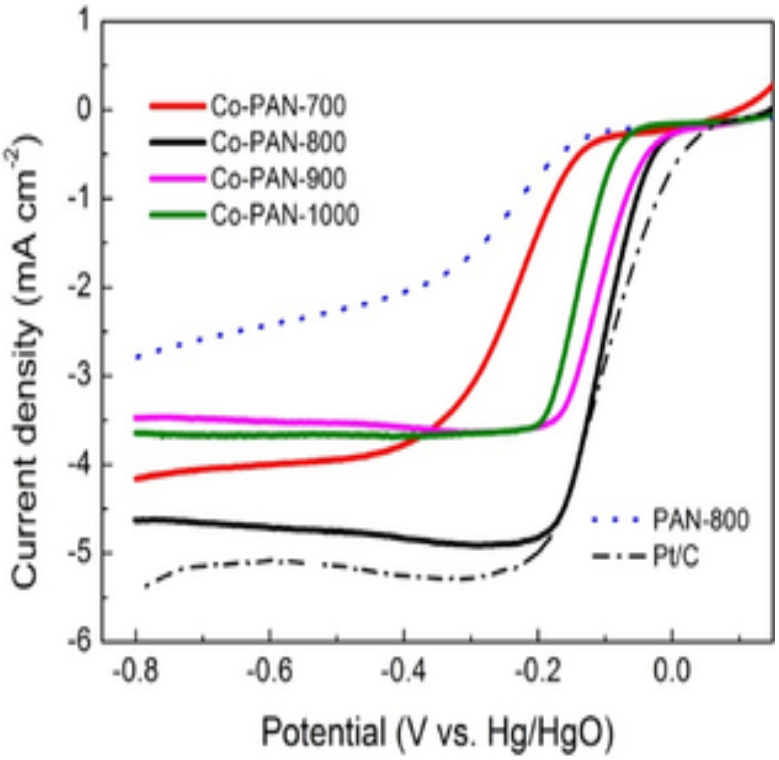

Figure 1.30. LSV for all Co-PAN-x samples with PAN-800 and Pt/C for comparison, in presence of oxygen, alkaline media, Shang et al. [226].

The author proposed the influence of nitrogen on the ORR activity as an active sites. However, the introduction of Co had an important effect in changing the N species from pyridinic-N to pyrrolic-N which decrease with the increasing of the high pyrolysis temperature (900 and 1000 °C), and thus, reduce the ORR activity. Furthermore, the fabricated nanofibers with its high surface area and mesoporous structure had a positive effect in the ORR process.

Table 1.3. *ORR activity of all Co-PAN-x samples with PAN-800 and Pt/C for comparison (vs. Hg/HgO) , Shang et al.* [226]

Sample	**Onset potential (V)**	**Limiting Current ($mAcm^{-2}$)**	**Half-wave potential (V)**
Co-PAN-700	-0.15	4.16	-0.221
Co-PAN-800	-0.02	4.91	-0.092
Co-PAN-900	-0.03	3.64	-0.094
Co-PAN-1000	-0.08	3.65	-0.127
PAN-800	-0.17	2.79	-0.242
Pt/C	0.06	5.42	-0.092

Furthermore, Wang et al. [139] studied how the source of dopant material used can influence the catalytic properties of produced doped carbon nanofibers for ORR. In the study, nitrogen from different sources including urea, melamine, polyaniline and aniline, were added to PAN solution dissolved in DMF for electrospinning to produce N-doped carbon nanofiber from the above nitrogen sources denominated as UNCNF, MNCNF, PNCNF, and ANCNF, respectively. The prepared samples stabilized at 250 °C, and were then carbonized in NH_3 atmosphere. The SEM images of the samples showed that the use of solid nitrogen source (i.e. melamine, urea, and polyaniline) produced nanofibers with larger average diameter compared with the use of a liquid source of nitrogen (i.e. aniline). This change of the diameter is due to the increased of the solution viscosity in case of using solid source of nitrogen, and thus increase the produced nanofiber diameter.

Among all the prepared samples, ANCNF carbonized at 1000 °C with a 20:3 mass ratio of aniline/Pan, had the best electrocatalytic activity. The cyclic voltammetry curves (Figure 1.31), showed ORR peaks at -0.047 V and 0.426 V (vs. Hg/Hg_2Cl_2) in alkaline and acidic media respectively.

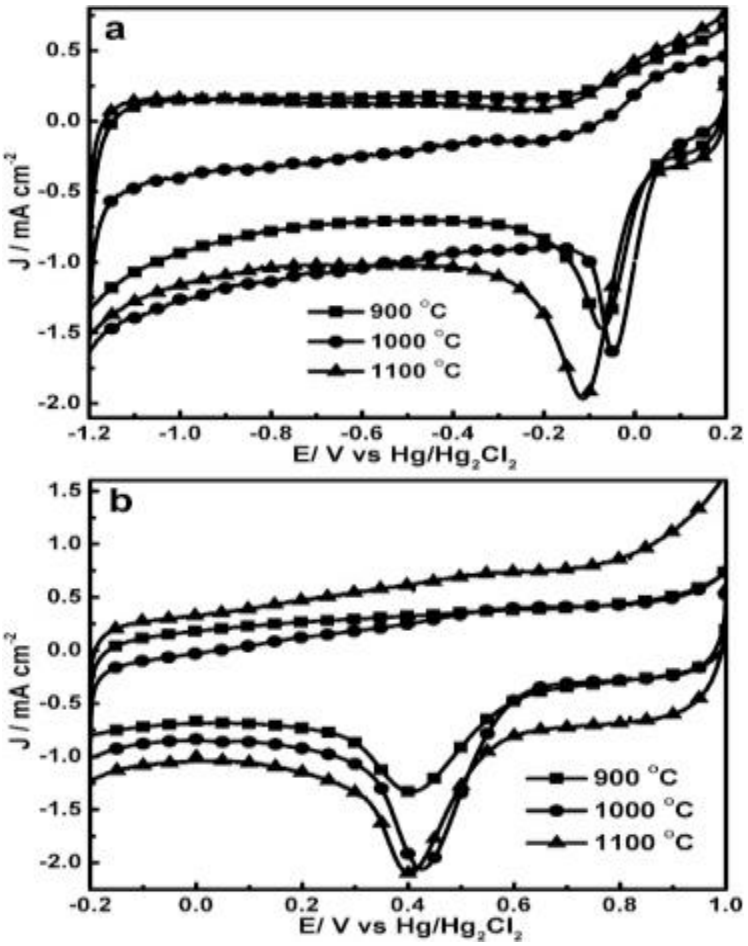

*Figure 1.31. C*yclic voltammetry curves of ANCNF carbonized at various temperatures in a) 0.1M KOH solution and b) 0.5M H_2SO_4, in presence of oxygen, Wang et al. [139].

Recently, Guo et al. [230] fabricated a composite nanofiber consisting of PAN, melamine as a nitrogen source, and ferric chloride (PAN/ $C_3N_6H_6/FeCl_3$) dissolved in DMF via electrospinning technique. Then, a sulfur-doped source of polythiophene (PT) was applied on the surface of the fabricated fibers using a photopolymerization method to get PAN/ $C_3N_6H_6/FeCl_3$@PT core-shell nanofibers. consequently, a pyrolysis process takes place, starting with stabilization step in air at 280 °C for 2 hours, subsequently carbonization step in nitrogen atmosphere at different temperatures (700, 800, 900 and 1000 °C) for 1 hour in order to get a core-shell nanofibers as Fe-S/N-C-*x*, which *x* is the carbonized temperature used. Figure 1.32 represent the fabrication process.

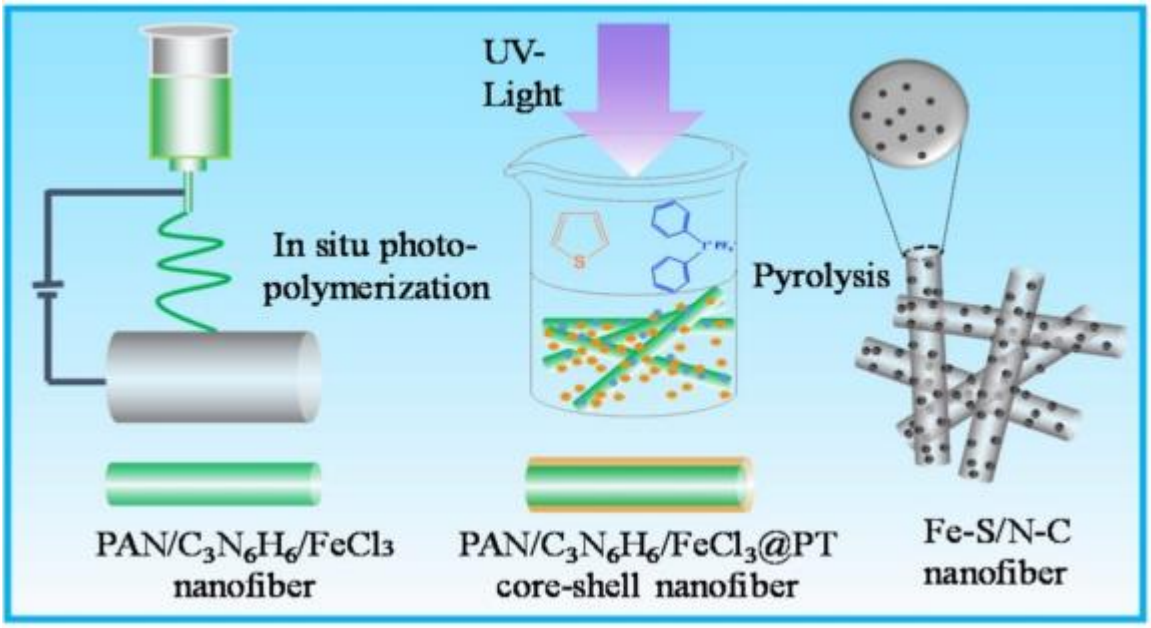

Figure 1.32. The production procedure of Fe-S/N-C NFs, Guo et al. [230].

The energy-dispersive spectrometry (EDS) results confirmed the presence of Fe, S, and N with a content of 2.79, 2.45, and 10.22%, respectively within the final product. The

fabricated Fe-S/N-C-*x* was used as an ORR catalyst to investigate its performance and stability toward ORR electrocatalytic activity. The linear sweep voltammetry (LSV) analysis (Figure 1.33a) proved the excellence of Fe-S/N-C-800 among the other prepared samples, which had onset potential of -0.03 V and half-wave potential of -0.14 V. Moreover, the fabricated Fe-S/N-C-800 exhibited more stability (Figure 1.33b) even than the 20 wt. % Pt/C. The study proposed that the ORR catalytic performance is due to the influence of the S/N-codoped, the high degree graphitized and the connected structure of the electrospun nanofibers.

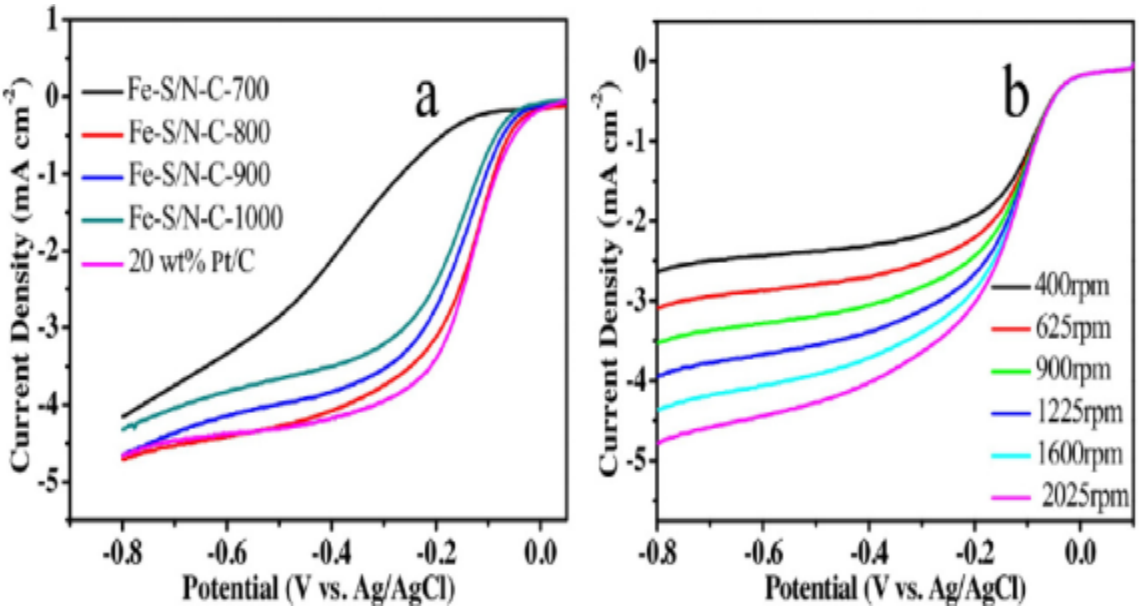

Figure 1.33. Linear sweep voltammetry of (a) different catalysts, (b) Fe-S/N-C-800 at various rotating speeds, Guo et al.[230].

In a similar work, Niu et al. [231] prepared Zn/Co@C-NCNFs composite using the electrospinning technique to produce nitrogen-doped CNFs based on PAN. The core layer was PAN and the shell layer was Zn/Co bimetal nanoparticles coated with graphitic carbon (Zn/Co@C). The product showed superior electrocatalytic activity towards ORR (Figure 1.34).

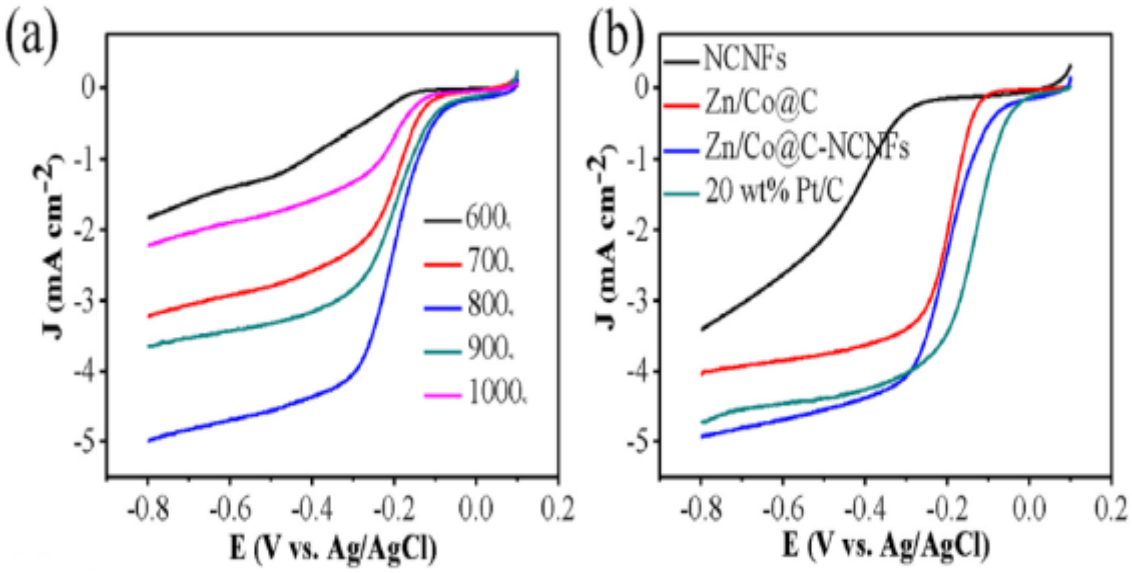

Figure 1.34. Linear sweep voltammetry of (a) Zn/Co@C-NCNFs at different decomposition temperature; (b) different catalysts, Niu et al.[231].

2 Chapter 2: Experimental Work

2.1 Chemicals

- Polyacrylonitrile (PAN), SIGMA-ALDRCIH, USA, average molecular weight ~ 150,000.
- N, N-Dimethylformamide (DMF), (Riedel-deHaen, Germany).
- Sulfur Roll, (BDH, England, S= 32.06).
- Poly(thiophene-2,5-diyl) (PTP), (Aldrich, USA).
- Nafion 5%, SIGMA-ALDRICH, USA.
- Isopropyl alcohol, ACS reagent, ≥ 99.7%, BDH, England.
- Sodium Sulfate, SIGMA-ALDRICH, USA, Mw = 142.04.
- Nickel Sulfate, SIGMA-ALDIRICH, USA, Mw = 280.86.
- Copper Sulfate, SIGMA-ALDRICH, USA, Mw = 159.60.
- Cobalt Sulfate, BDH, England, Mw = 280.10.
- Potassium tetrachloro-platinate (II), SIGMA-ALDRICH, USA, average Mw ~ 415.09
- Nitrogen high purity, grade 99.999%, (Bozwaier local Liquid Company).
- Oxygen high purity, grade 99.999%, (Bozwaier local Liquid Company).
- Ethanol (Assay 96%, SIGMA- ALDRICH, USA)
- Deionized water.

2.2 Preparation Method of the Polymer Solution:

Prepare 30 ml of 10% polyacylonitrile solution, using DMF as the solvent with different percentage of different sulfur source (wt. % to wt. %) as given in the Table 2.1 below:

Table 2.1. *Chemicals used for the polymer solutions preparation*

PAN weight (gm)	**Sulfur source**	**Sulfur weight (gm)**	**Sulfur loading %**	**DMF weight (gm)**	**Abbreviation**	**Abbreviation (After Carbonization)**
3.000	-	0	0	27	PAN-0%S	CNF-0%S
2.985	Pure sulfur	0.015	0.5	27	PAN-0.5%S	CNF-0.5%S
2.970	Pure sulfur	0.030	1	27	PAN-1%S	CNF-1%S
2.910	Pure sulfur	0.090	3	27	PAN-3%S	CNF-3%S
2.850	Pure sulfur	0.150	5	27	Failed to prepare	-
2.985	Polythiophene	0.015	0.5	27	PAN-0.5%PTP	CNF-0.5%PTP
2.970	Polythiophene	0.030	1	27	PAN-1%PTP	CNF-1%PTP
2.910	Polythiophene	0.090	3	27	PAN-3%PTP	CNF-3%PTP
2.850	Polythiophene	0.150	5	27	PAN-5%PTP	CNF-5%PTP

First, we dissolved the sulfur amount as shown in the table above in 27 g DMF as a solvent using a dry beaker at the room temperature, then we used bath sonication for 30 minutes to dissolve and completely disperse the sulfur in the DMF solvent. After that, we added the amount of PAN as shown above in Table 2.1 to the solution slowly with continuous stirring. We left the solution on a hot plate at 60 °C under vigorous stirring for 5 hours to completely dissolve and homogenize all the materials into the polymer solution to get uniform yellowish clear solution with the pure sulfur source and brown-red color with the PTP as a sulfur source. The beaker was covered all the time with aluminum foil and parafilm during the preparation process to prevent the DMF from evaporating due to heating. The polymer solution will is ready to use and can be stored in clean dry small sealed bottle (Figure 2.1). Unfortunately, the preparation of PAN-5%S did not achieved. The sulfur was not able to dissolve if the sulfur concentration increases more than 3%.

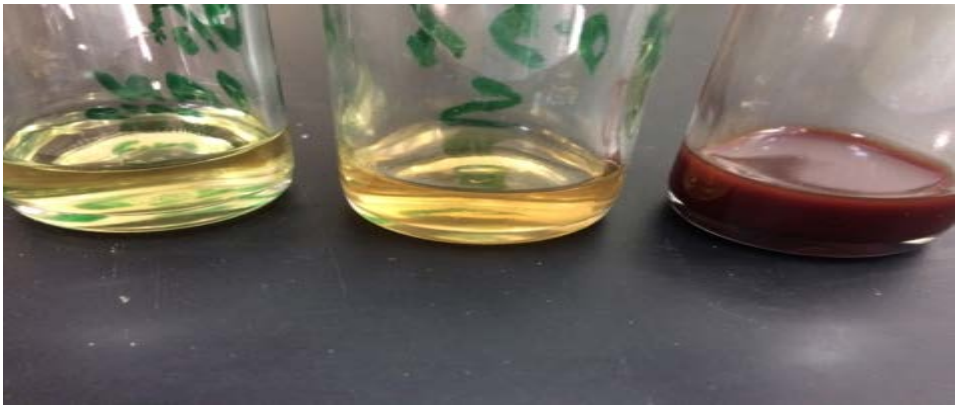

Figure 2.1. The prepared S-doped of PAN solutions with different sulfur sources.

2.3 Fabrication of the fibers using electrospinning technique

The preparation of the nanofibers was achieved by electrospinning technique. Several parameters control the morphology and properties of the nanofiber produced by electrospinning technique such as the voltage used, the flow rate, the needle diameter and the collector rotation speed. It is important to setup suitable parameters to get beads free, continuous and fine diameter fibers.

The viscosities of the prepared sulfur-doped polymer solutions were high, which as we noticed blocked the needle from time to time when setting up the flow rate to less than 1.5 ml/h as the polymer solution not flow smoothly through the needle, and thus, the produced fiber was broken, not continuous, and full of beads as shown from the SEM image in Figure 2.2 below. Furthermore, the distance between the needle tip and the collector had an important effect on the fabricated fibers. The distance less than 20 cm leaded to produce fiber full of beads as shown in the Figure 2.3 below. Therefore, we set the parameters conditions as given in Table 2.2 below.

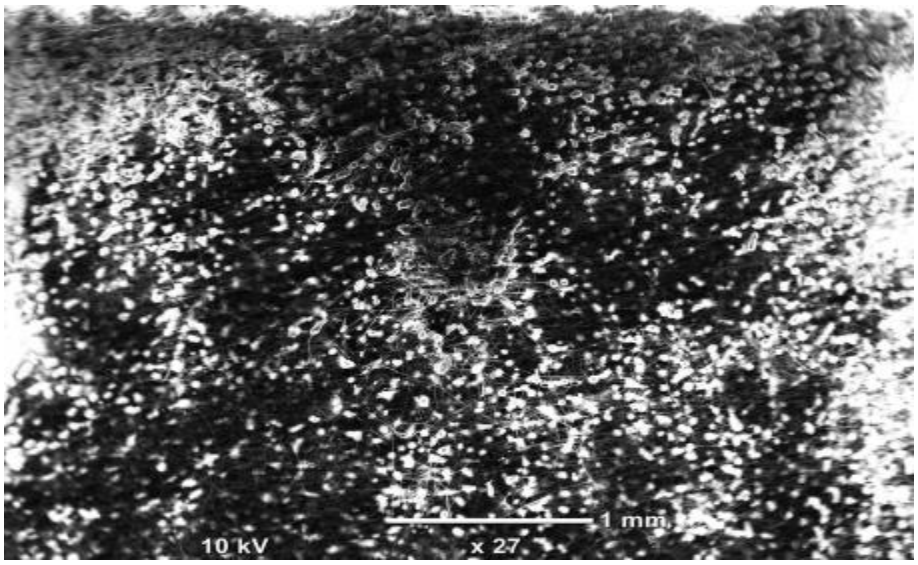

Figure 2.2. SEM image of PAN-0.5%S with flow rate of 1 ml/h.

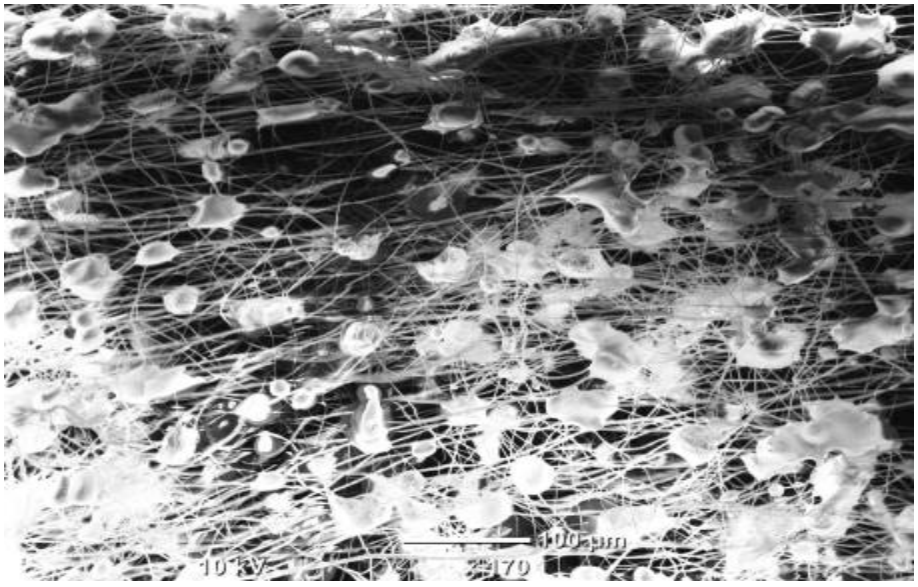

Figure 2.3. SEM image of PAN-0.5%S working distance of 15 cm.

Table 2.2 *The parameters of the electrospinning process*

Parameter	**Condition**
Solution Flow Rate	1.5 ml/hour
Voltage	15-kV
Working Distance	20-cm
Collector Drum Speed	230 rpm
Needle Diameter Size	0.08 mm

The procedure was as the follow:

1- Setup the electrospinning conditions as mentioned in Table 2.2 above.

2- Fill the syringe with the polymer solution and make sure to remove any air bubbles from the solution.

3- Fix the syringe and set the flow rate.

4- Adjust the distance and the rotating drum speed.

5- Start.

6- After a few minutes, we noticed the fiber start to form on the collector (Figure 2.4).

7- When all the polymer solution transferred to fiber, we switched off the electrospinning and remove the aluminum foil with the fiber from the collector (Figure 2.5).

8- The prepared collected nanofibers dried under vacuum for 6 hours at 40C° to take off any possible moisture on the fabricated nanofiber mats.

Figure 2.4. Fabrication of the fibers using electrospinning technique.

Figure 2.5. The produced fibers collected on the aluminum foil.

2.4 Polymer Nanofiber Stabilization Step

The prepared nanofibers was removed from the aluminum foil and then stabilized in air at 200 °C for 2 hours. The heating rate was 5 °C/min.[81]

2.5 Polymer Nanofiber Carbonization Step

After the stabilization step, the carbonization step took place in order to transfer the nanofibers to CNFs through a pyrolysis step at 800 °C for 5 hours and heating rate of 5 °C/min under a high purity nitrogen atmosphere (99.999%) [81] using a ceramic tube furnace (Figure 2.6).

Figure 2.6. Ceramic tube furnace.

The nanofiber sample was put in ceramic crucible and was then placed inside the tube furnace and closed at both ends. The left side of the tube was connected to a nitrogen gas cylinder and the other side outlet in water to monitor the bubbles of the nitrogen flow during the process. The tube was purged of oxygen by applying the nitrogen to flow through it for 30 minutes. After heating for 5 hours, the prepared CNFs are allowed to cool and then collected in clean dry bottle (Figure 2.7).

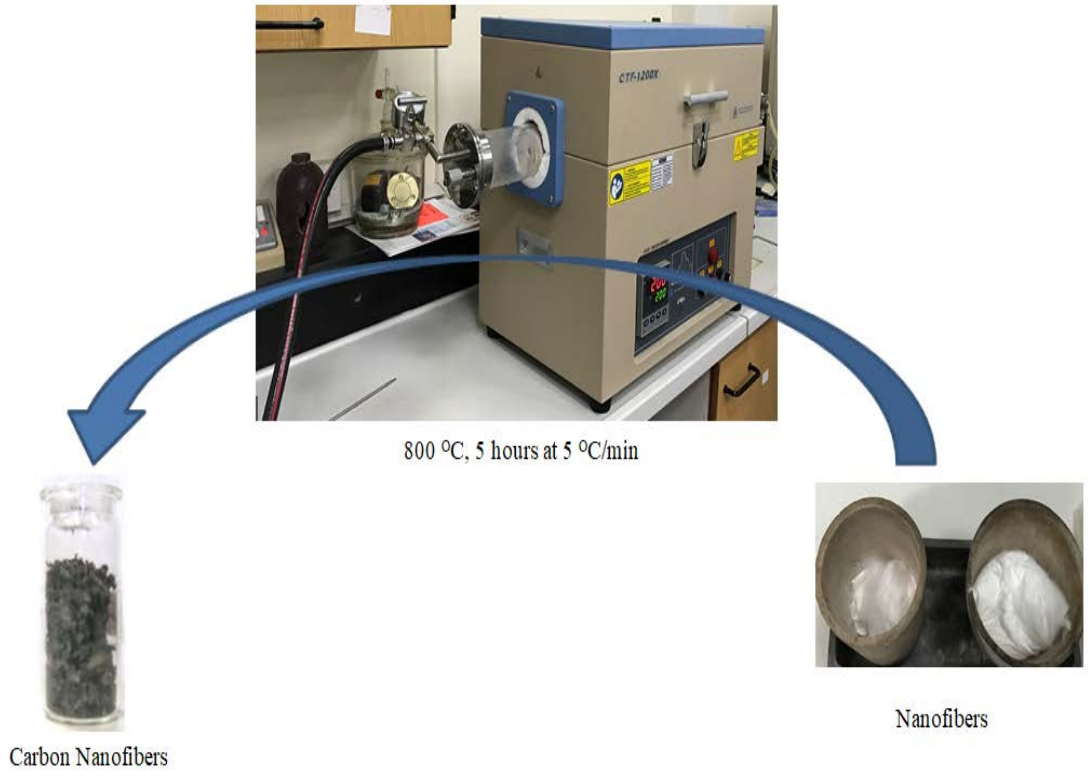

Figure 2.7 The carbonization process.

2.6 Preparation of electrode for electrochemical test

2.6.1 Preparation of CNFs ink solution

CNF-3% S and CNF-5%-PTP inks were prepared using 1% Nafion and isopropanol as a solvent. The 1% of Nafion was prepared by dilution of the 5% Nafion with isopropanol, then 1 mg of CNFs was dispersed in 1 mL of the 1% Nafion and sonicated the solution for 2 h.

2.6.2 Electrode preparation

First, casting a 5 μL of the ink dispersion onto the RDE GC and allowing the ink to dry for 2 hours. To assure the surface wettability, the same electrolyte was used to flush the surface of the electrode before immersion it into the electrolytic cell. Second, applying of a one-step potentiostatic deposition of the metals ions (Cu^{2+}, Co^{2+}, Ni^{2+}) from 1 mM sulphate salt of each ion dissolving in 0.1 M sodium sulphate (Na_2SO_4) on the working electrode (i.e. CNFs/GC-RDE) at potential of -1 V for 600, 1200, 1800, and 2400 seconds of deposition time. Similarly, Pt was deposited from 1 mM of PtK_2Cl_4 as Pt source, then applying a constant electrolysis potential of -1 V for 600, 1200, 1800, and 2400 seconds. The third step is the passivation of the metallic deposit in 1 M NaOH by cycling the potential between 0.2 V and 0.55 V for 15 successive cycles at a scan rate of 100 mVs^{-1}[112]. Figure 2.8 summarize the electrode preparation steps.

2.6.3 Electrochemical measurements

The Electrochemical behavior of the ORR is tested in a 1 M NaOH aqueous solution. The test takes place using a working rotating electrode (RDE), which was prepared by

mechanical polishing for its surface using aqueous slurries of finer alumina powder (down to 0.06 μm) following by well rinse with deionized water. The applied reference electrode was Ag/AgCl electrode (3 M KCl) and the counter electrode was a platinum wire.

The cyclic voltammetry and linear sweep curves were acquired at 50 mV s^{-1} from 0 to -1.0 V (vs Ag/AgCl) at 1600 rpm electrode rotation in N_2 saturated 1 M NaOH then repeating the same experiments in O_2 saturated 1 M NaOH.

The EIS analysis were performed under an open circuit potential (OCP) condition within a frequency range of 0.1 Hz to 100 kHz with an AC amplitude of 10 mV.

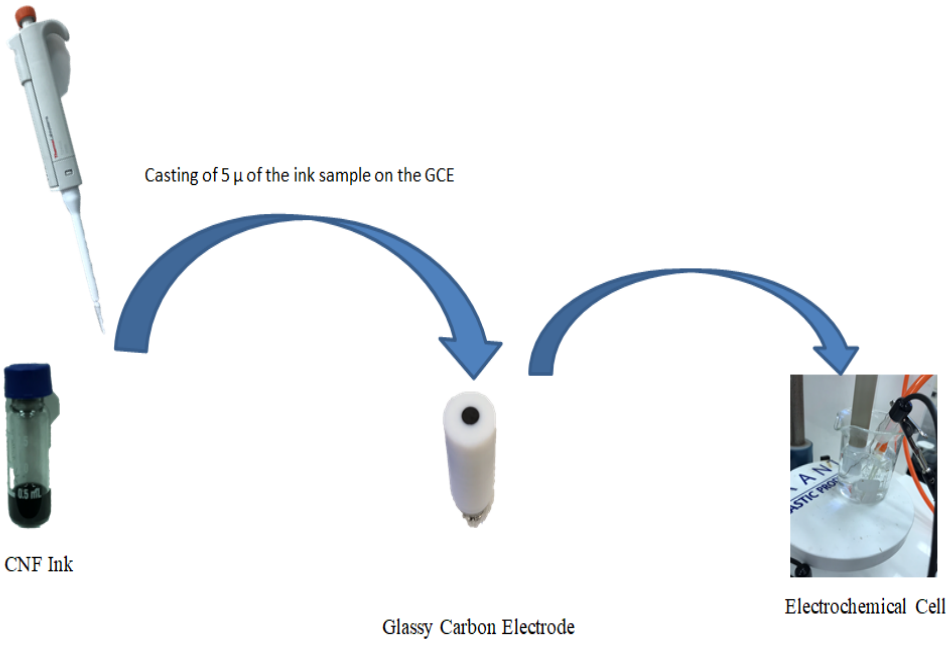

Figure 2.8. Electrode preparation steps.

2.7 SAMPLES CHARACTERIZATION

Many advanced characterization techniques were used. Herein, a number of those techniques used for this thesis work are described.

2.7.1 Scanning electron microscopy (SEM)

The morphological characterization and the fiber diameter of the prepared nanofibers were explored by scanning electron microscopy (SEM), model: NOVA NANOSEM 450, FEI instrument, (Figure 2.9) which engaged with Energy dispersive X-ray (EDX). A Powder sample of the fabricated nanofibers and carbon nanofibers were used direct without need to any additional preparation after sputter coating with Gold.

Figure 2.9. The scanning electron microscopy (SEM), model: NOVA NANOSEM 450.

A powerful of electrons is used to illuminate the sample to attain an ultra-high resolution imaging of the sample's morphology based on the secondary or back-scattered electrons collected by the detector after scanning. The instrument can operate at high or low-vacuum modes. The instrument is available in the Central laboratory Unit, Qatar University.

2.7.2 X-ray photoelectron spectroscopy (XPS) analysis

X-ray photoelectron spectroscopy Model: AXIS Ultra DLD, Kratos (Figure 2.10), was used to investigate the elemental composition as one of the most effective spectroscopy technique that quantitatively inspect the elemental composition of a material and their oxidation states. An X-ray photon is focused at the sample which cause emission of electrons from one of the atom's core shells according to the photoelectric effect with specific kinetic energies reflecting their binding energies measured by the instrument and used to detect the elements that are existing in the sample. Full survey has been done at 160 eV passing energy based on use of monochromatic X-ray Source Al Kα source, also high resolution at 20 or 40 eV passing energy. The X-ray Power was: 15 kv, 20 mA.

Figure 2.10. X-ray photoelectron spectroscopy, Model: AXIS Ultra DLD, Kratos

2.7.3 X-ray Diffraction analysis

The crystallographic structure investigation was achieved by X-ray Diffraction (XRD) diffractometer, Model: PANalytical, Brand: EMPYREAN, with a Cu Kα (λ= 1.5406 Å) radiation source, operated at 45 kV and 40mA in a 2Θ range from 0 to 100 with a 2Θ step size of 2^{O} min-1. The X-ray beams are emitted from the radiation source and focused on the sample which interact with the atoms of the materials causing and emission of high energy photons that knows as x-rays. The output of the XRD Scan is a spectrum with 2Θ on the x-axis and intensity on the y-axis, where Θ is the angle of incident X-rays on the sample. Diffraction pattern of the crystal structure based on the diffraction of the X-ray and the interlayer spacing of the atomic planes in the crystalline and polycrystalline materials is obtained. The instrument is available in Center of Advanced Materials, Qatar University (Figure 2.11).

Figure 2.11. X-ray Diffraction (XRD) diffractometer, Model: PANalytical, Brand: EMPYREAN

2.7.4 Thermal Analysis

Thermal Gravimetric Analysis (TGA) is an effective technique to characterize the thermal stability of polymers and fibers. In the TGA analysis, the sample is heating to a certain temperature and determine the change of its weight versus time. The results can give useful information about the rate of degradation the practical temperature range without degradation for the material. The analysis was carried out using PerkinElmer TGA 4000 instrument at 25–1000 ^{O}C with a heating rate of 5 ^{o}C/min under nitrogen. The

instrument is located in Center of Advanced Materials, Qatar University (Figure 2.12).

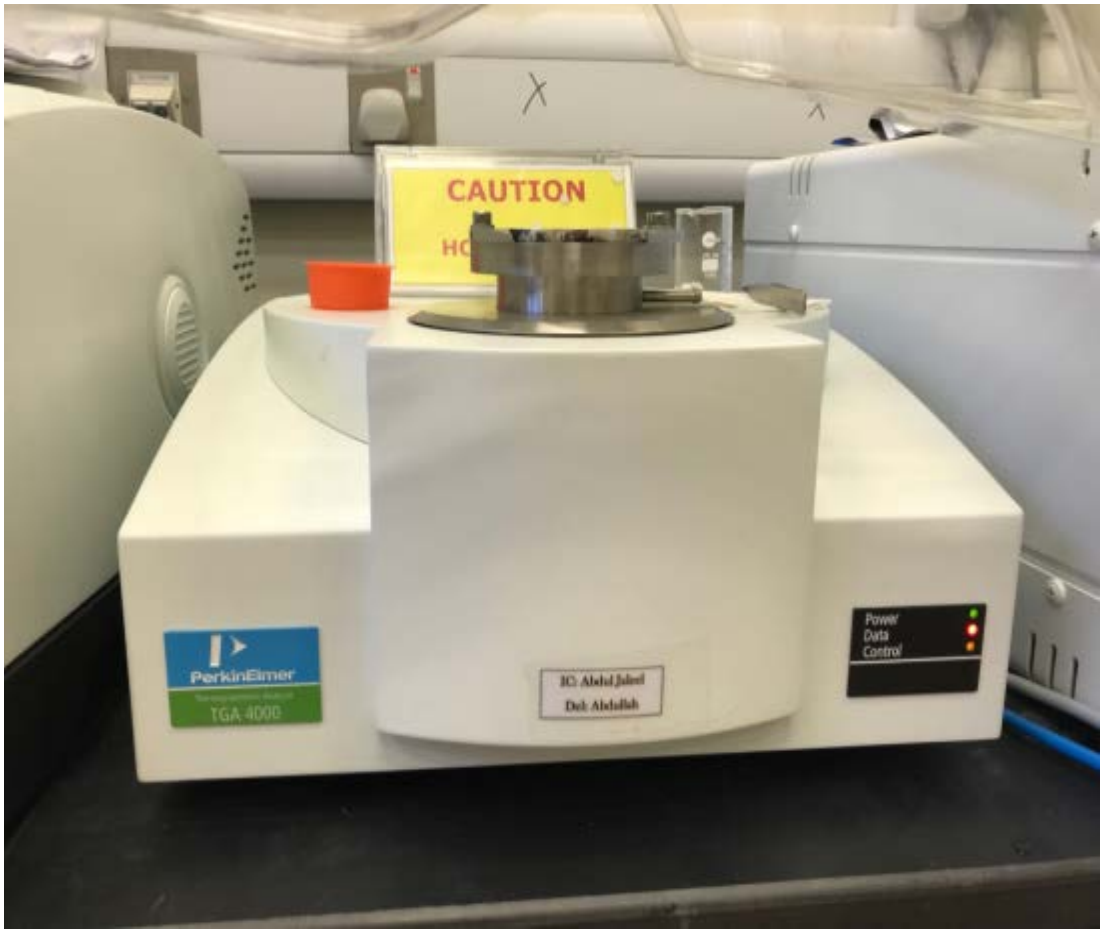

Figure 2.12. PerkinElmer TGA 4000 instrument.

2.7.5 Fourier Transmittance Infrared (FTIR) Analysis

FTIR spectroscopy is a technique for qualitative analysis. The IR radiation is generally limited to the range of 4000-400 cm^{-1} where most application happen in this range. In

FTIR, the sample molecule absorb the IR radiation and convert it to energy molecular vibration. The frequency of absorption spectra obtained from the FTIR instrument can give useful information about structure and functional groups of the sample. FTIR instrument by PerkinElmer Frontier located at the Center of Advanced Materials, Qatar University (Figure 2.13), was used for the FTIR analysis in this thesis.

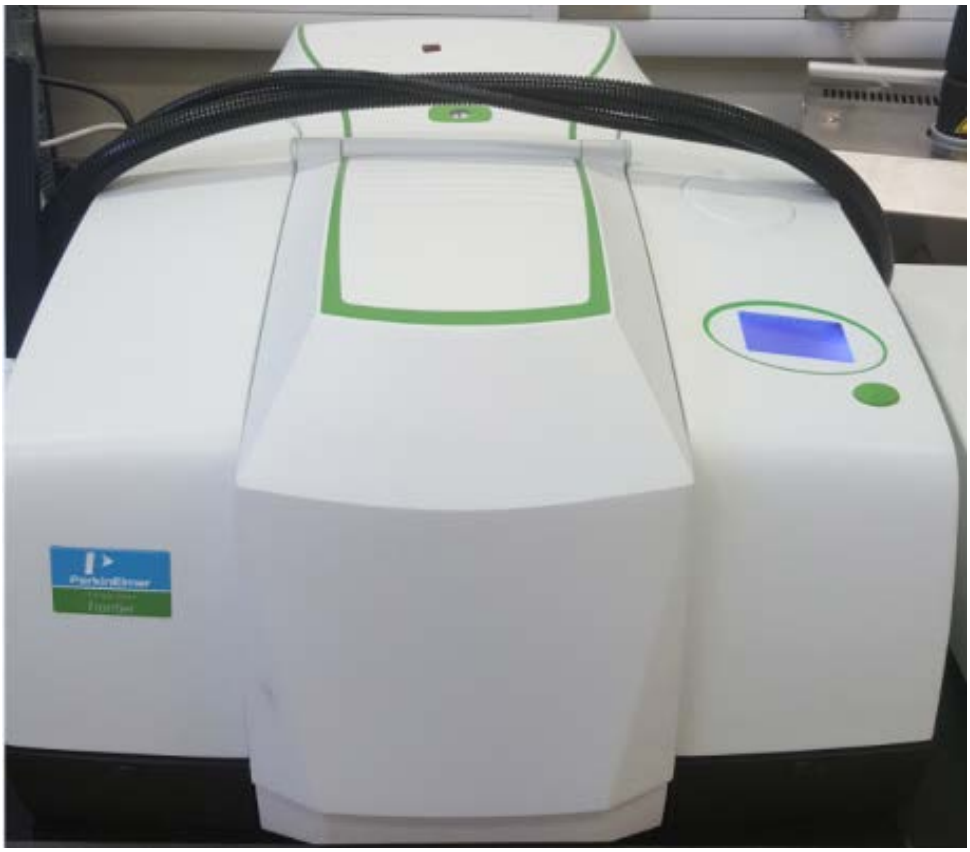

Figure 2.13. FTIR, Model: PerkinElmer Frontier.

2.7.6 Electrochemical analysis

The electrochemical measurements were done using a Reference 3000 GAMRY potentiostat (Warminster, USA), a single compartment glass cell, a reference electrode of Ag/AgCl electrode (GAMRY), platinum wire as counter electrode, and a glassy carbon electrode (GCE) (0.2 cm^2 area) as working electrode. Figure 2.14, shows the potentiostat instrument.

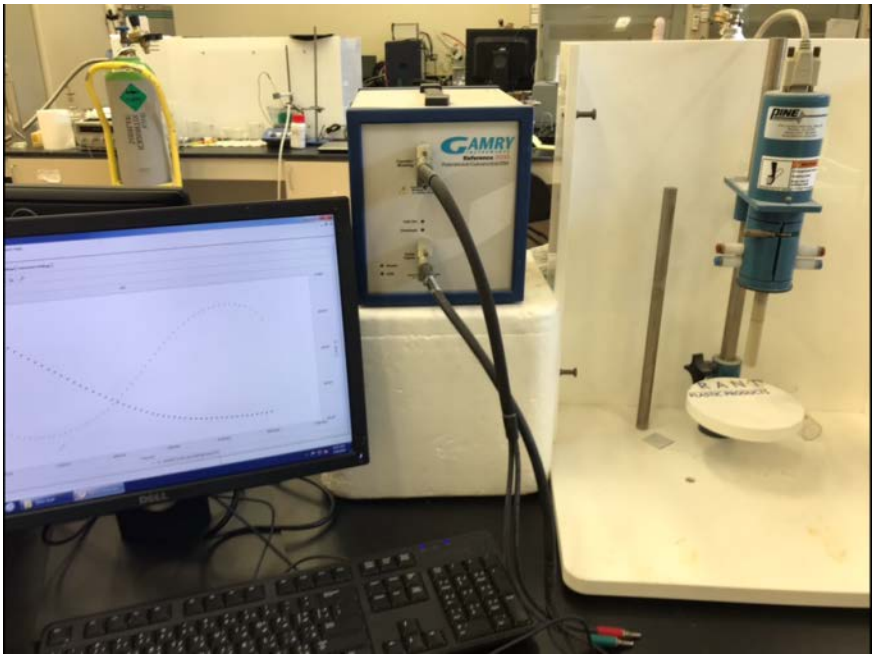

Figure 2.14. Potentiostat instrument, Model: GAMRY "Reference 3000".

3 Chapter 3: Results and Discussion

3.1 Morphological Analysis Results

3.1.1 Scanning Electron Microscopy (SEM) Results

Scanning electron microscopy (SEM) was utilized to investigate the morphological characterization and the fiber size of the successfully prepared nanofibers. Figure 3.1 and Figure 3.2 below shown the SEM images of pristine PAN nanofibers, Figure 3.3 to Figure 3.8 display the PAN nanofibers doped with powder sulfur source, and PAN nanofibers doped with polythiothene (PTP) as a sulfur source are shown in Figure 3.9 to Figure 3.16.

As observed from images, the prepared nanofibers are randomly oriented with smooth and uniform surface, bead free and interlinked in some points to form a network structure. The average diameter of 423 nm- 661 nm, 1924 nm- 898.4 nm, and 436.6 nm - 826.9 nm for pristine PAN, PAN doped with powder sulfur, and PAN doped with polythiophene (PTP), respectively.

Figures 3.17 and Figure 3.18 below show the carbonized fibers of pristine PAN nanofibers, Figures 3.19 to Figure 3.24 are for carbonized PAN nanofibers doped with powder sulfur, and carbonized PAN nanofibers doped with polythiophene (PTP) are show in Figure 3.25 to Figure 3.30. The images of the CNFs preserved continuous nanofibers morphology and a network structure.

Moreover, it is noticed that the average diameters of the fibers decreased to 349.7 nm- 408.2 nm, 391.5 nm- 1010 nm, and 320.9 nm- 457.3 nm for pristine PAN CNFs, PAN CNFs doped with powder sulfur, and PAN CNFs doped with polythiophene (PTP),

respectively. This decrease in diameter is expected as a result of the shrinkage during the pyrolysis process caused by elimination of nitrogen and hydrogen as (HCN) and NH_3 gases [217] [227]. It is observed that larger diameter size of nanofibers resulted when using powder sulfur source than in case of using polytiophene as a sulfur source. This is possibly due to the higher dispersion and homogenous polymer solution when using polytiophene with PAN than using sulfur powder. However, Wang et al. [139] reported how the source of dopant material used for doping can affect the produced fibers diameter size and properties.

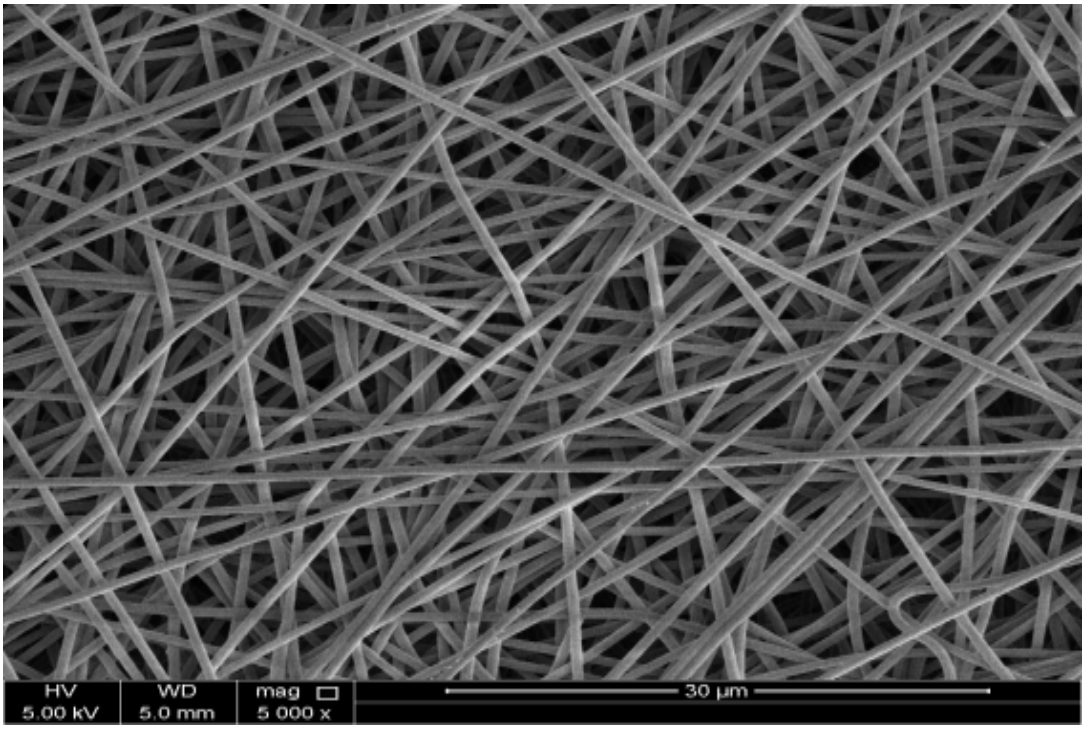

Figure 3.1. SEM of PAN-0%S fibers.

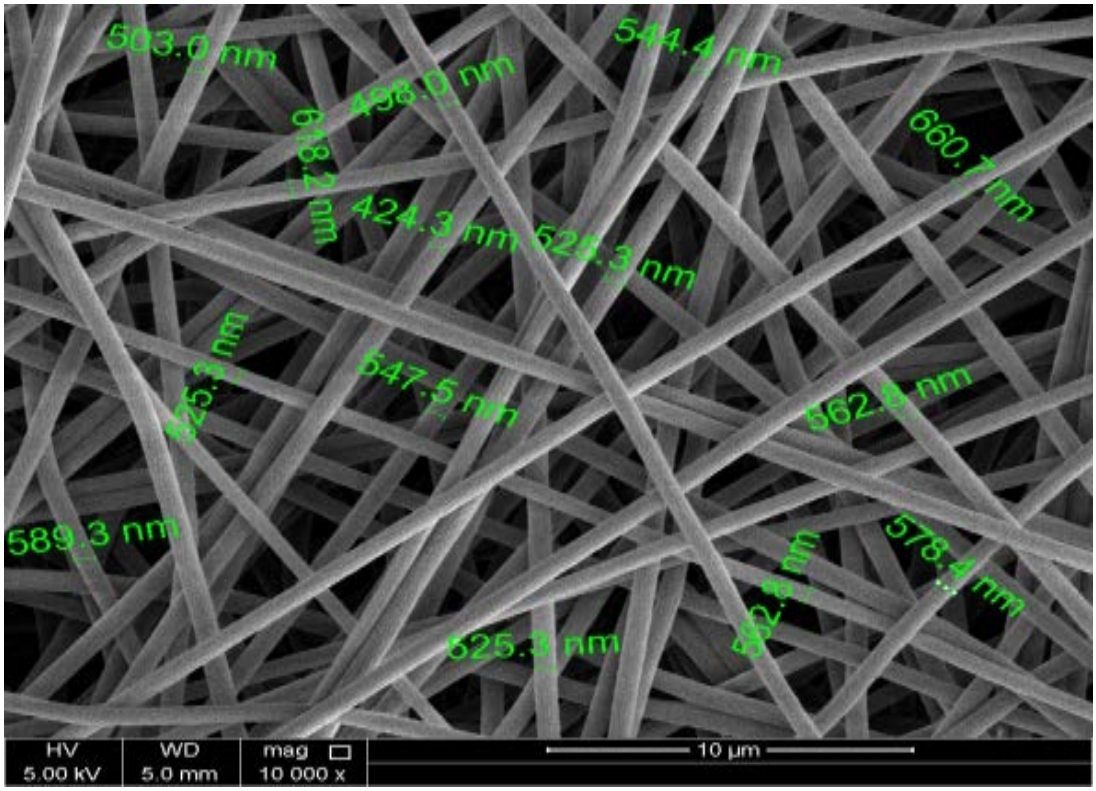

Figure 3.2. SEM of PAN-0%S fibers.

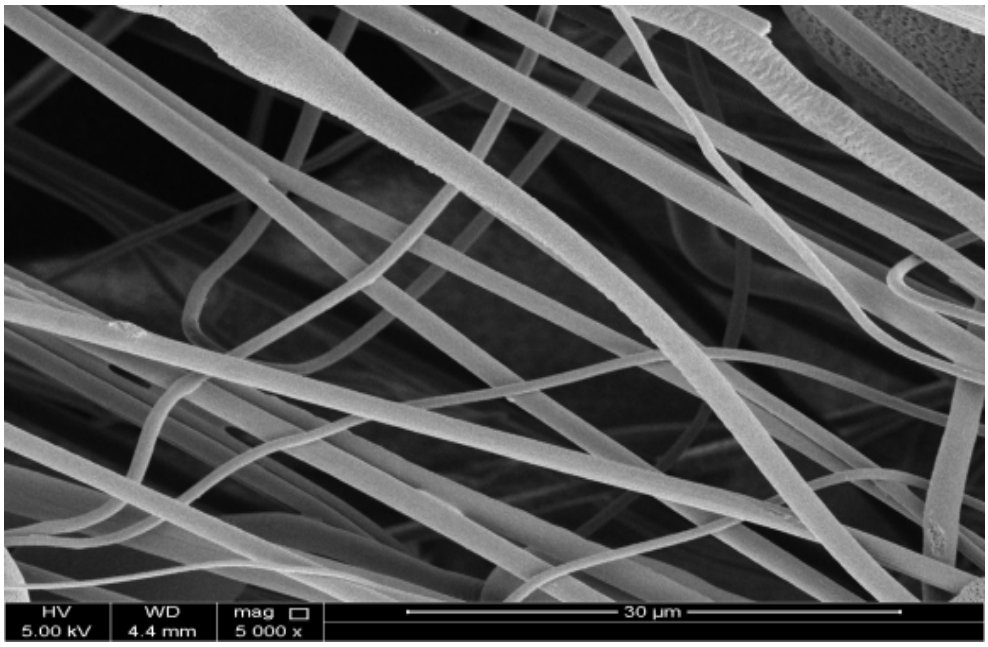

Figure 3.3. SEM of PAN-0.5% S fibers.

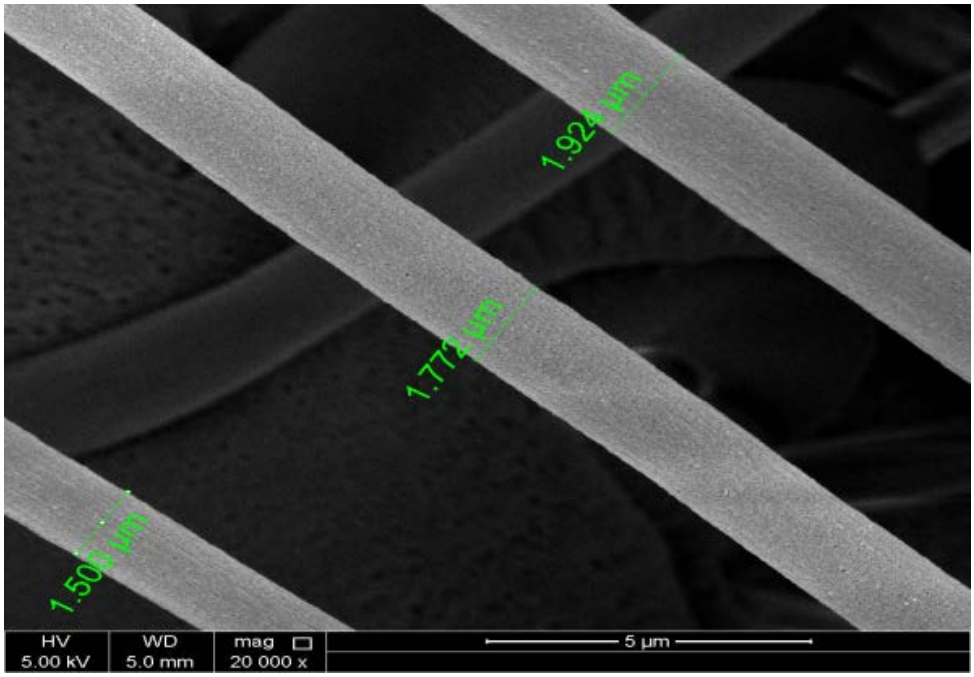

Figure 3.4. SEM of PAN-0.5% S fibers.

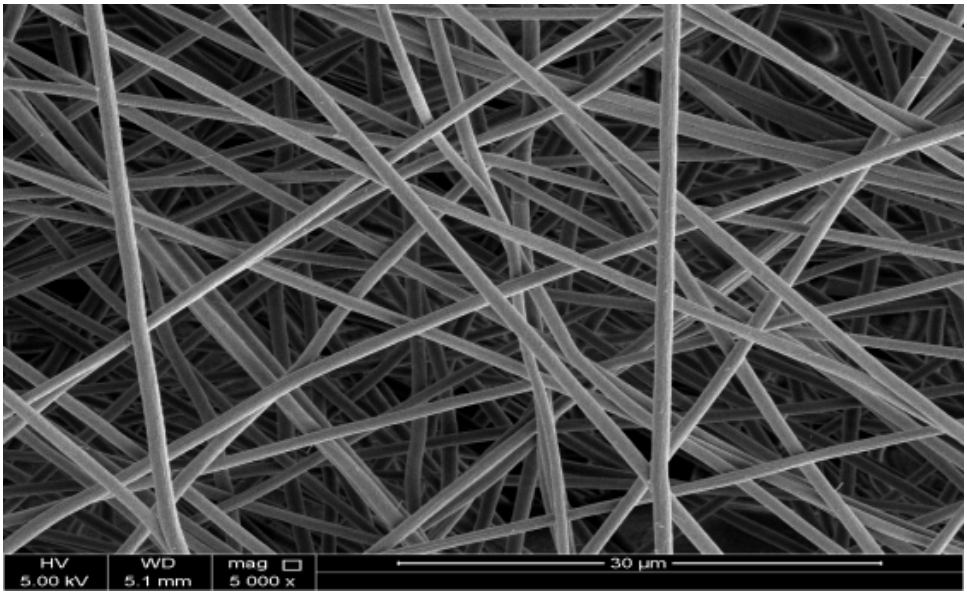

Figure 3.5. SEM of PAN-1% S fibers.

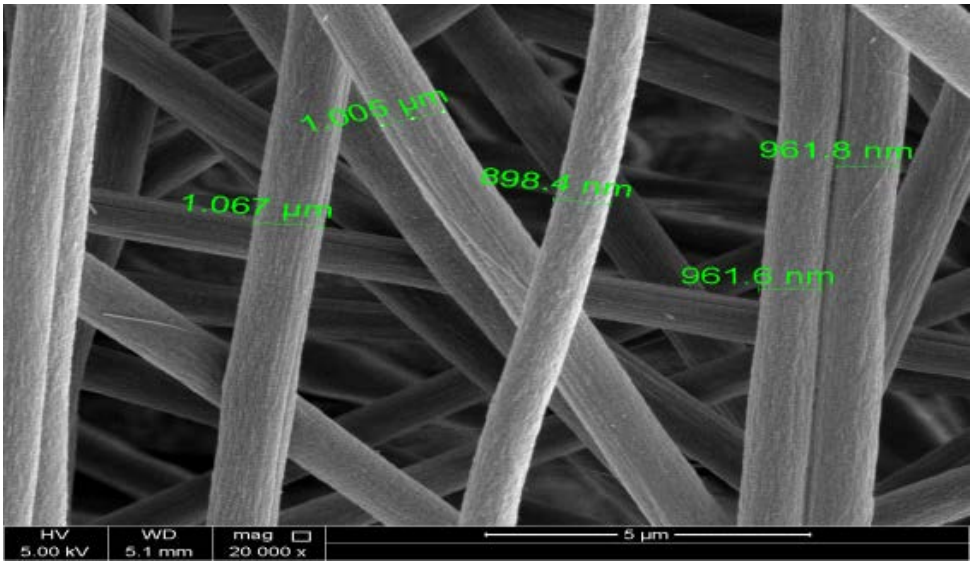

Figure 3.6. SEM of PAN-1% S fibers.

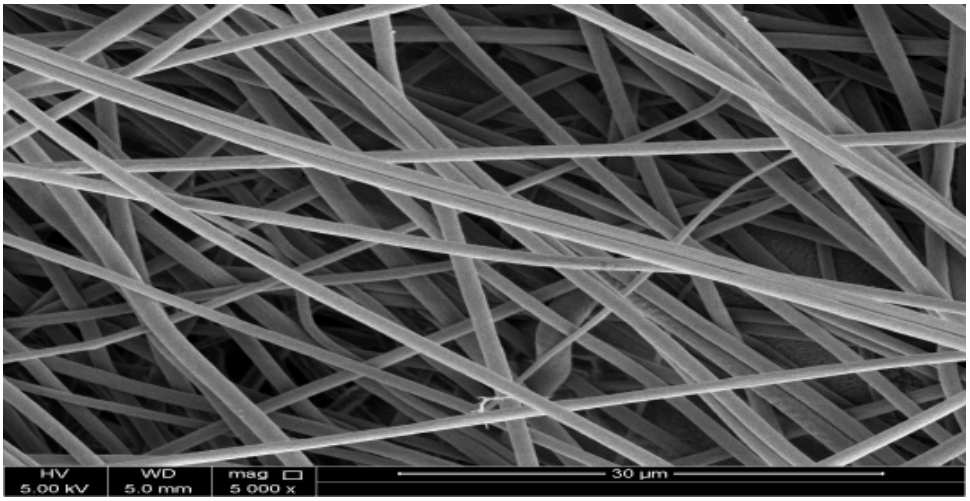

Figure 3.7. SEM of PAN-3% S fibers.

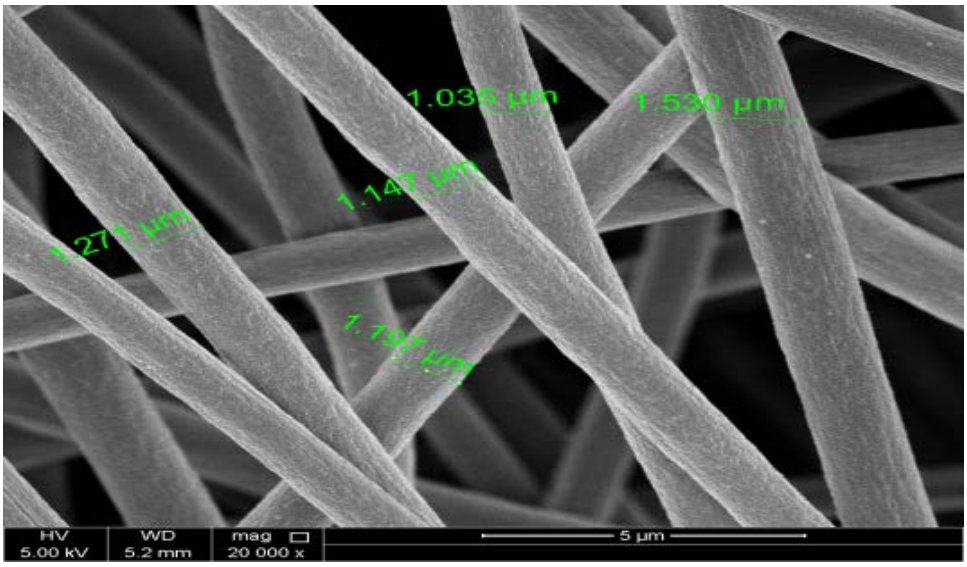

Figure 3.8. SEM of PAN-3% S fibers.

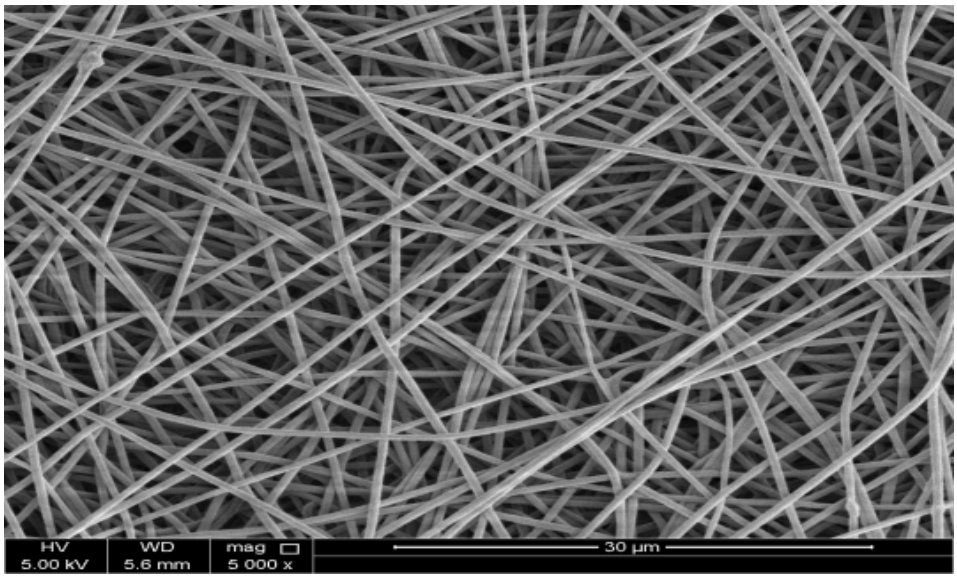

Figure 3.9. SEM of PAN-0.5% PTP fibers.

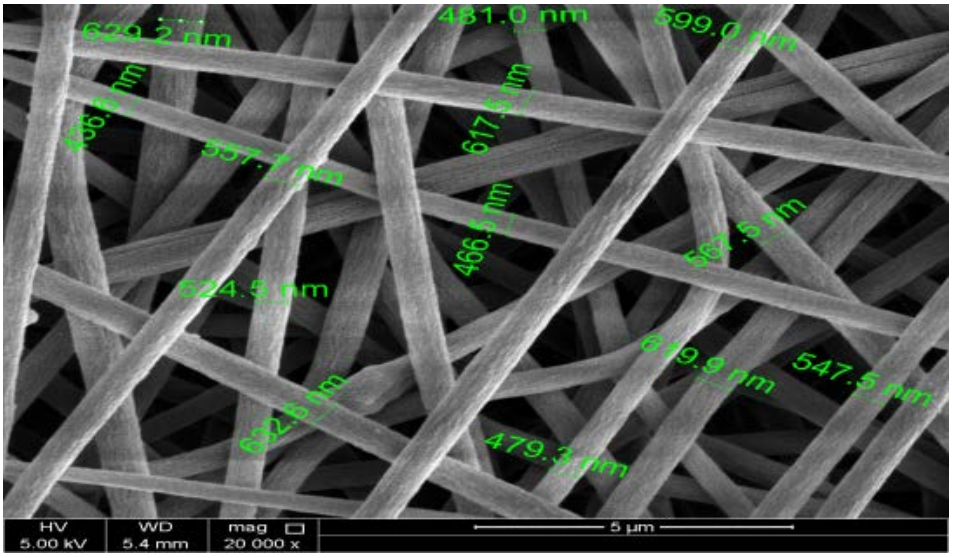

Figure 3.10. SEM of PAN-0.5% PTP fibers.

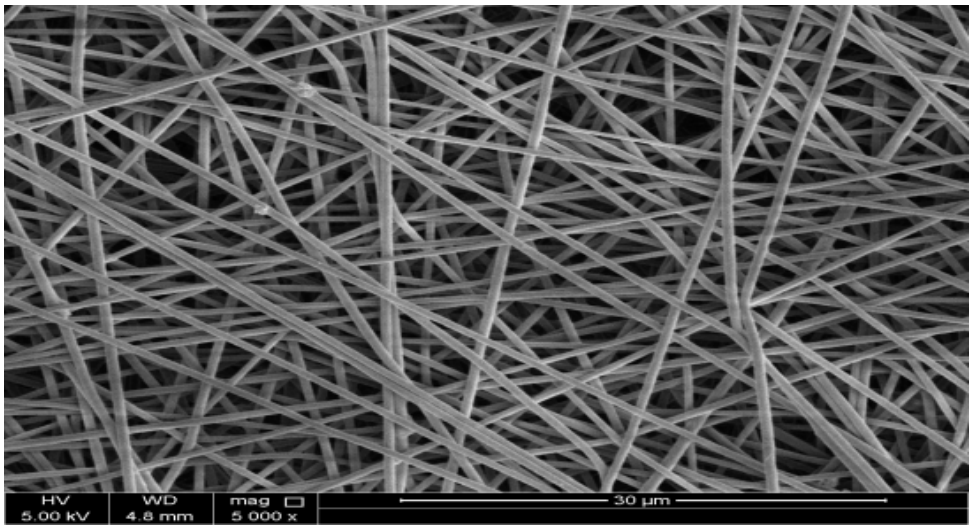

Figure 3.11. SEM of PAN-1% PTP fibers.

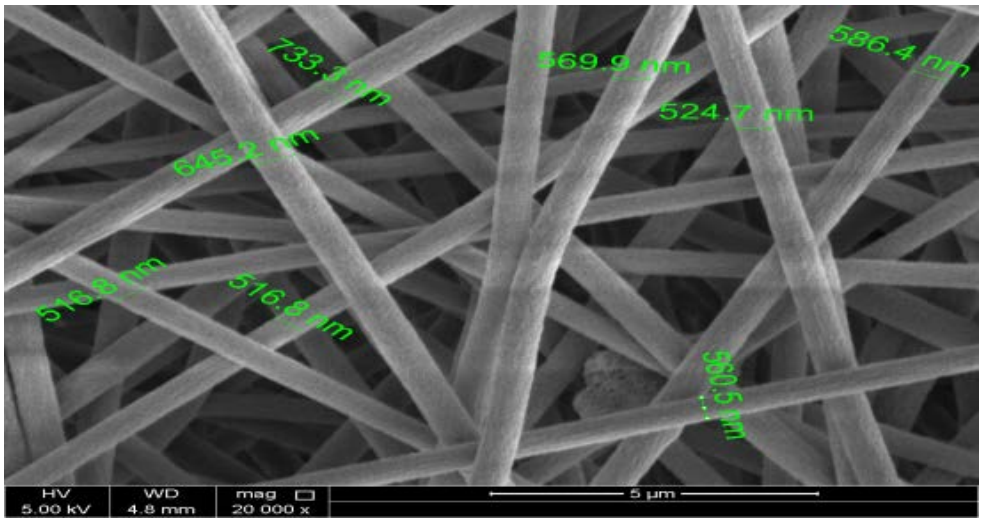

Figure 3.12. SEM of PAN-1% PTP fibers.

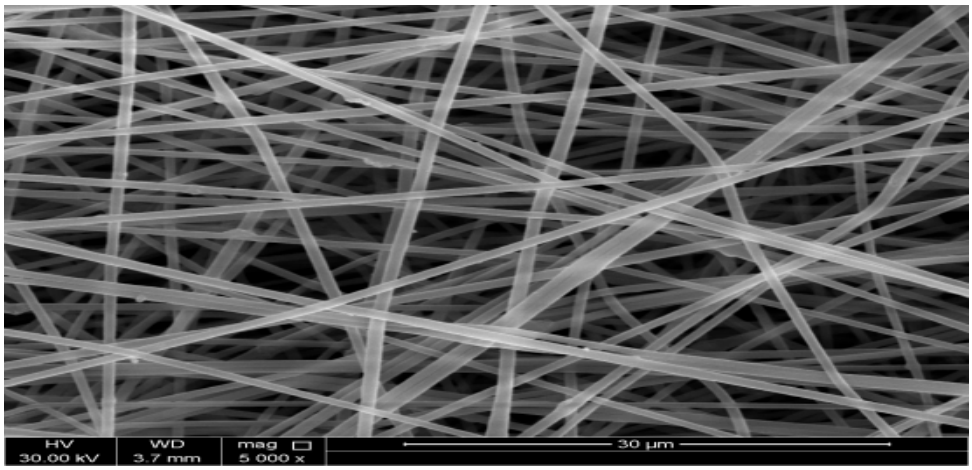

Figure 3.13. SEM of PAN-3% PTP fibers.

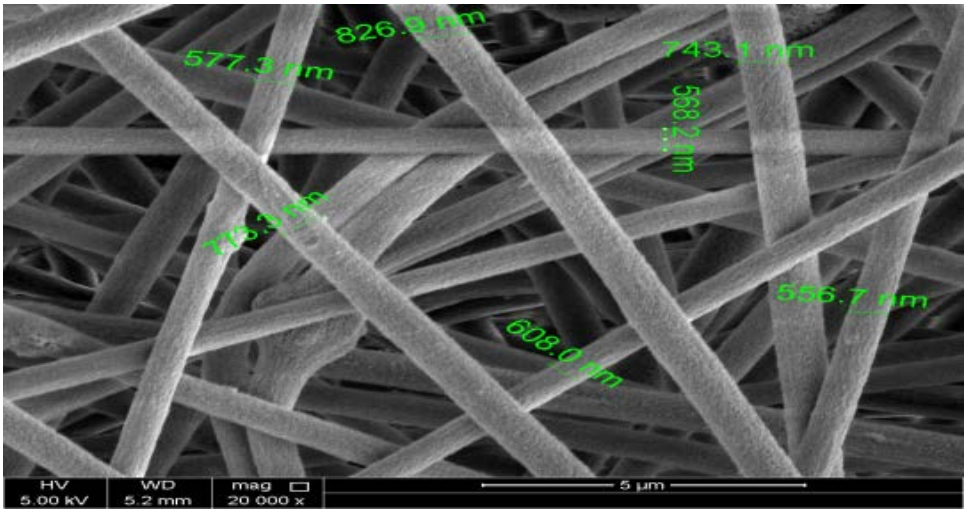

Figure 3.14. SEM of PAN-3% PTP fibers.

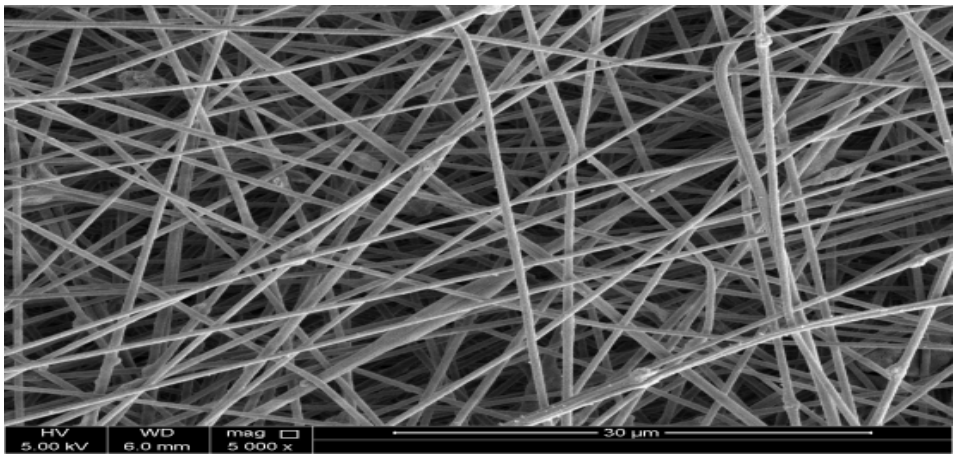

Figure 3.15. SEM of PAN-5% PTP fibers.

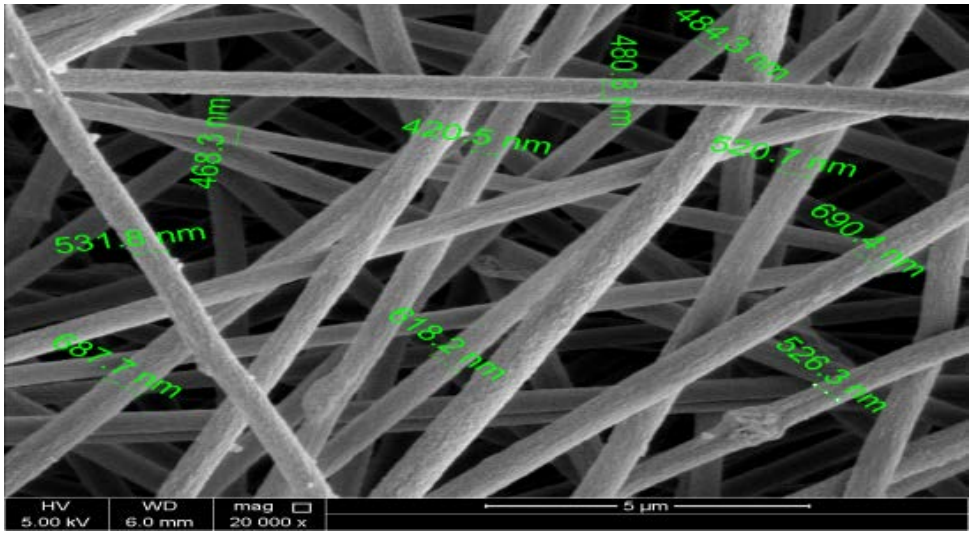

Figure 3.16. SEM of PAN-5% PTP fibers

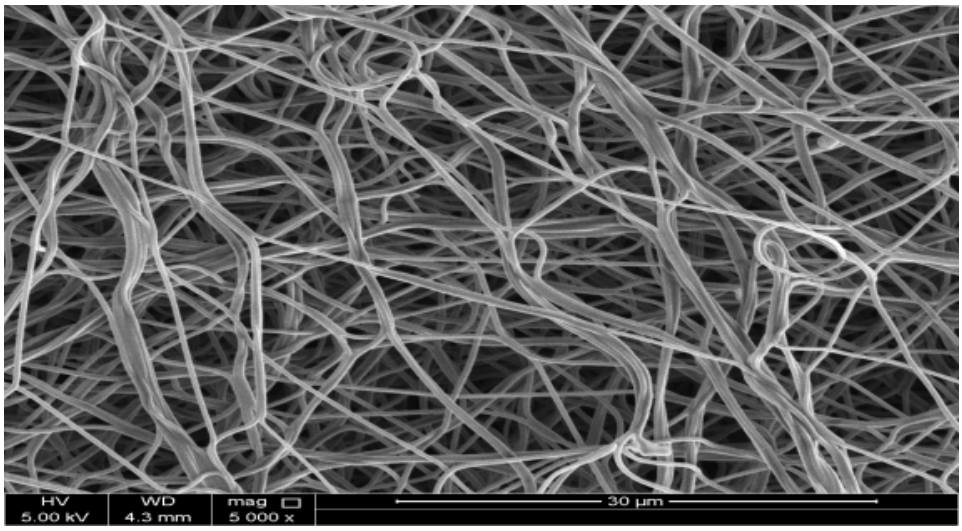

Figure 3.17. SEM of CNF-0% S.

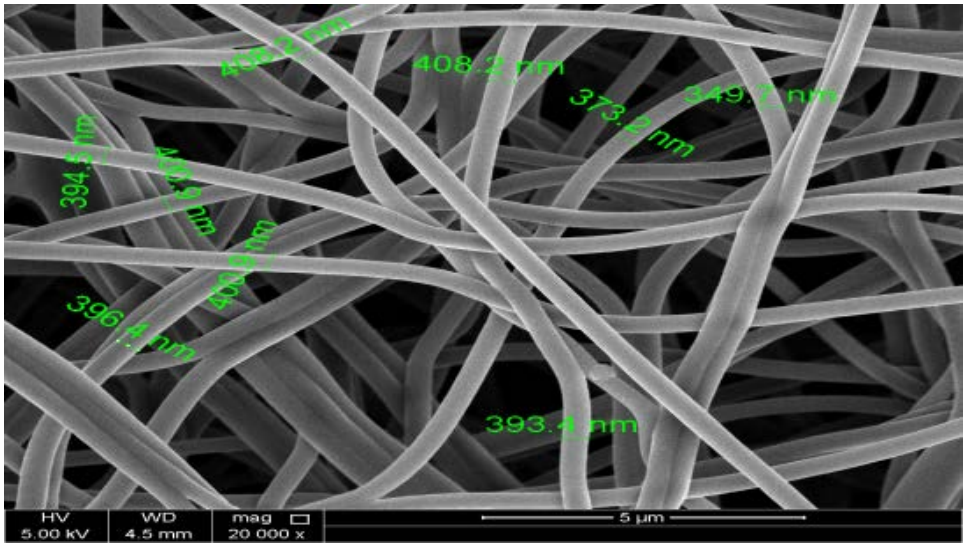

Figure 3.18. SEM of CNF-0% S.

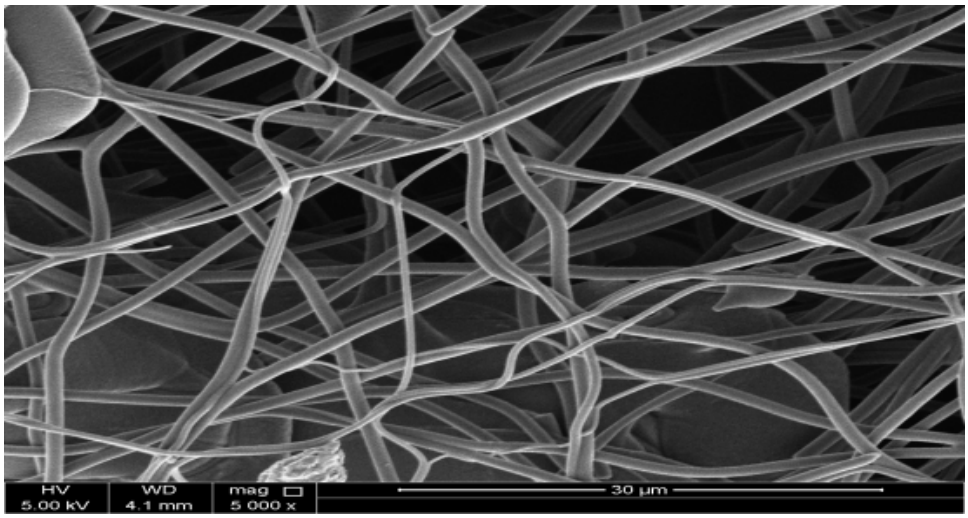

Figure 3.19. SEM of CNF-0.5% S.

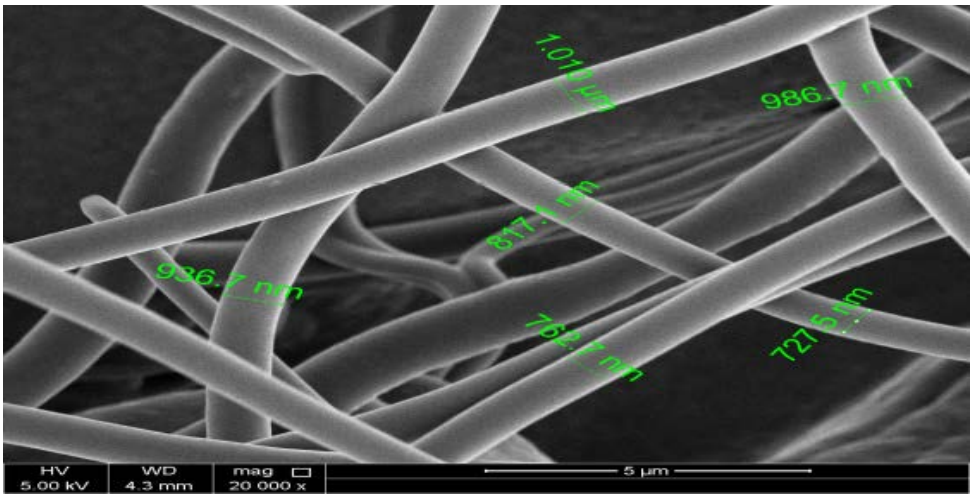

Figure 3.20. SEM of CNF-0.5% S.

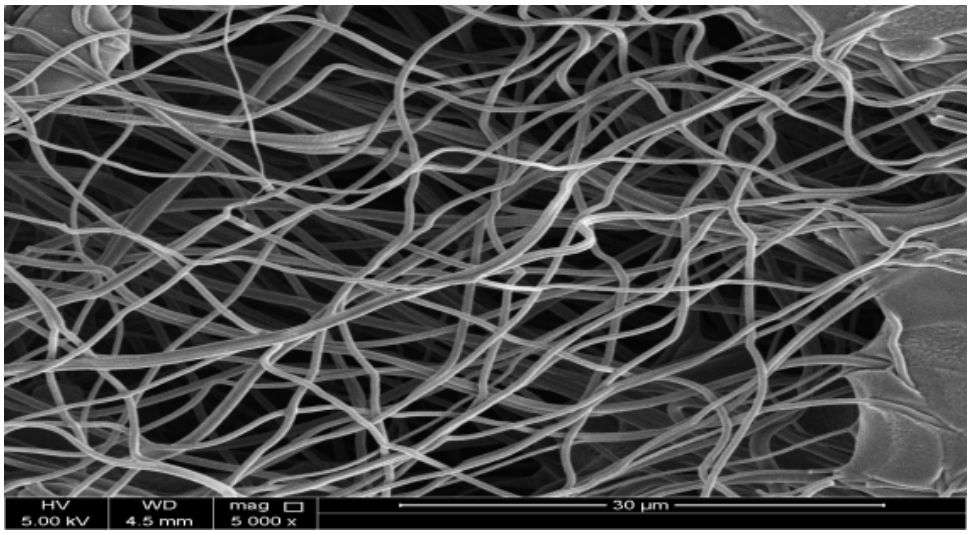

Figure 3.21. SEM of CNF-1% S.

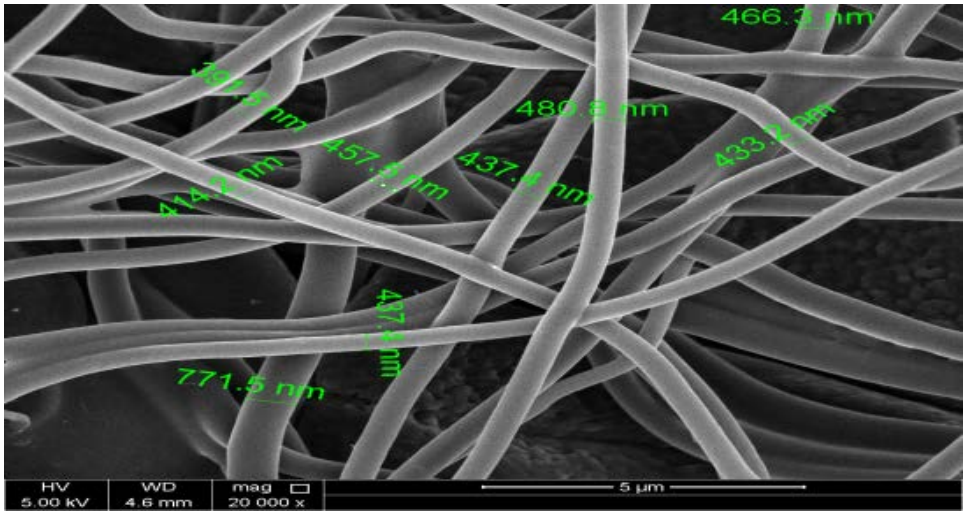

Figure 3.22. SEM of CNF-1% S.

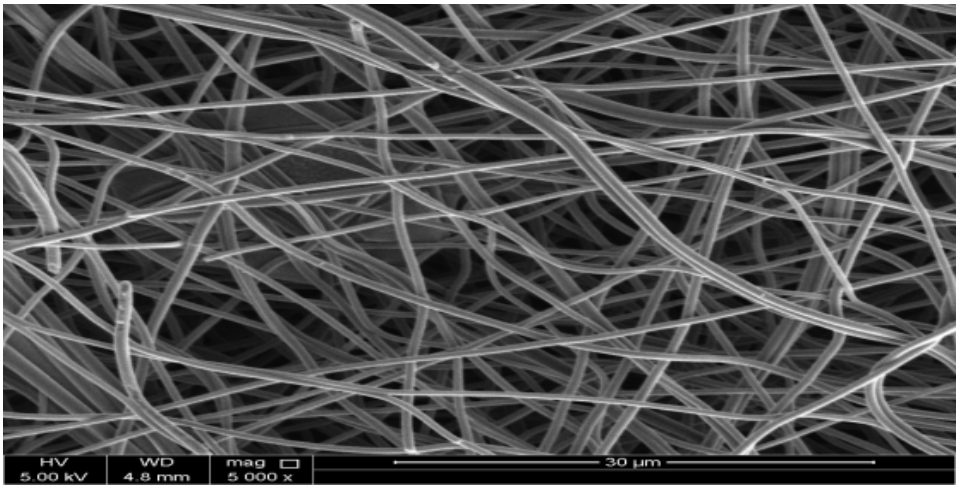

Figure 3.23. SEM of CNF-3% S.

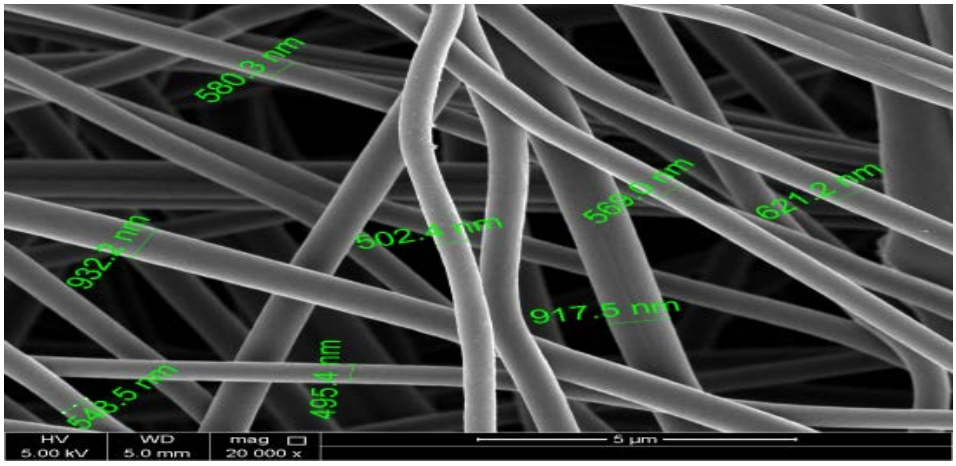

Figure 3.24. SEM of CNF-3% S.

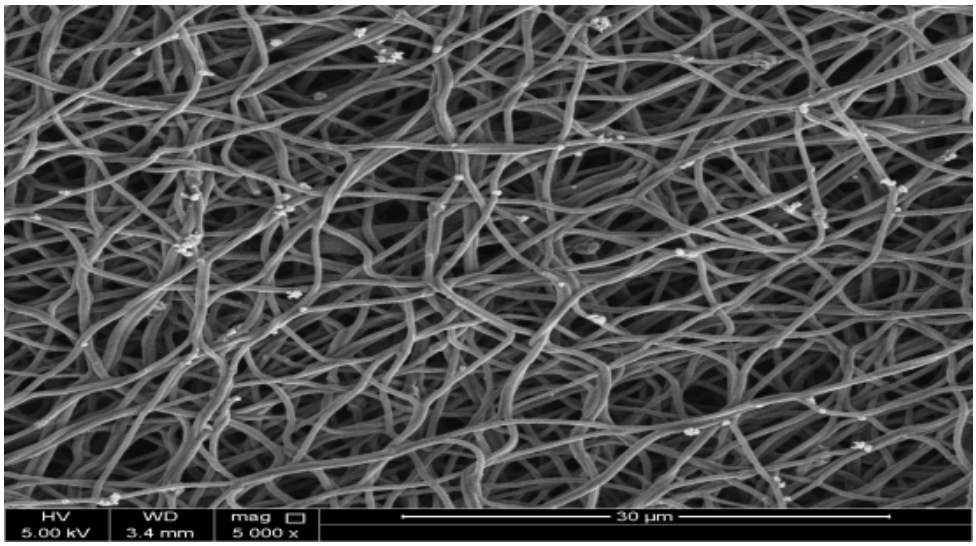

Figure 3.25. SEM of CNF-1% PTP.

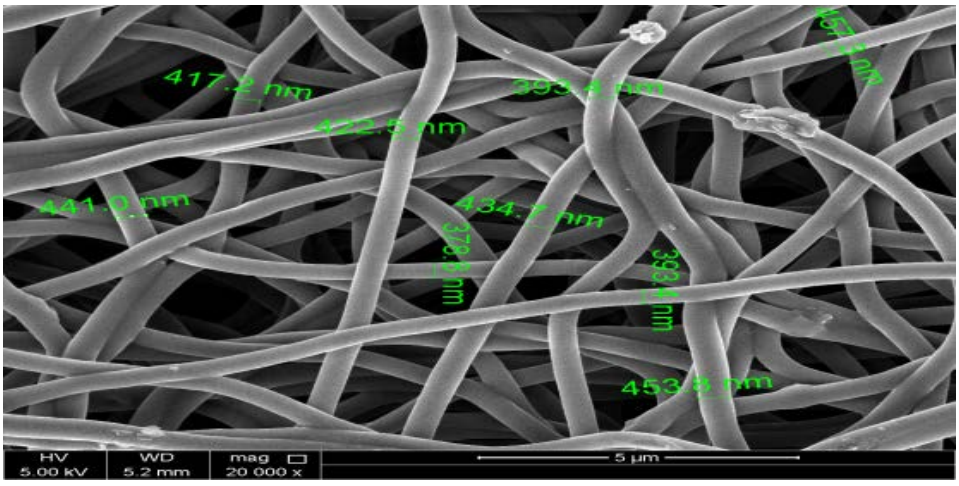

Figure 3.26. SEM of CNF-1% PTP.

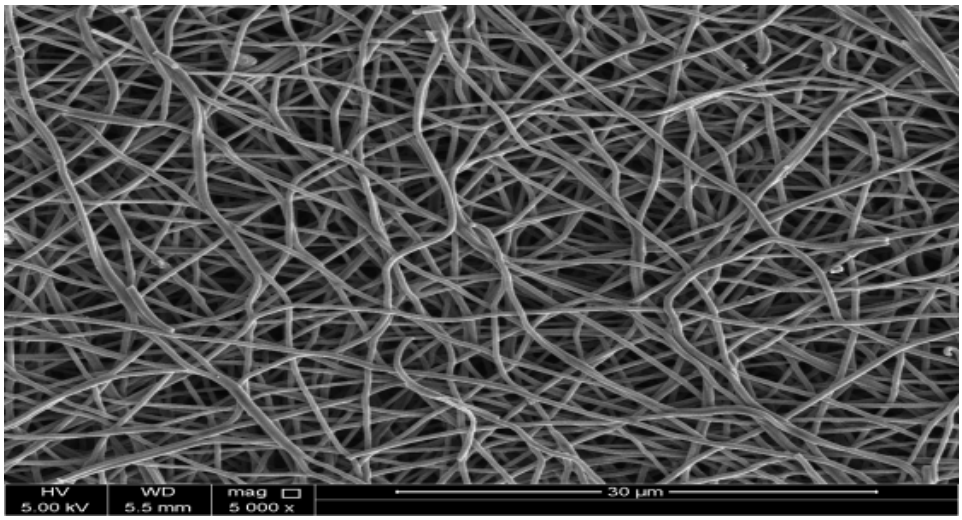

Figure 3.27. SEM of CNF-3% PTP.

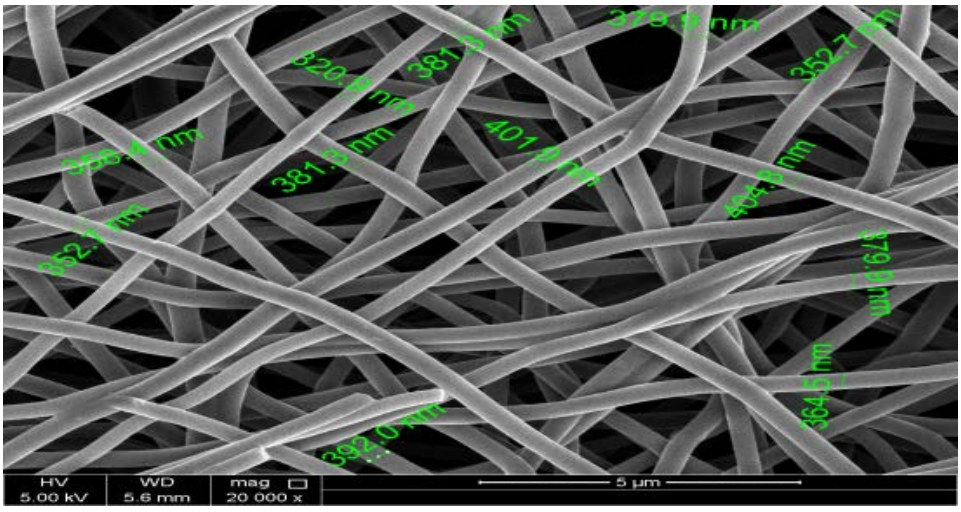

Figure 3.28. SEM of CNF-3% PTP.

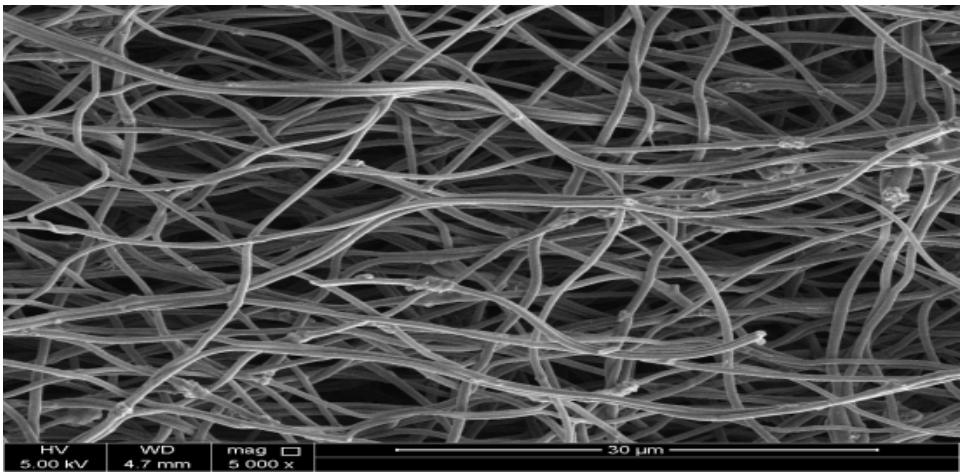

Figure 3.29. SEM of CNF-5% PTP.

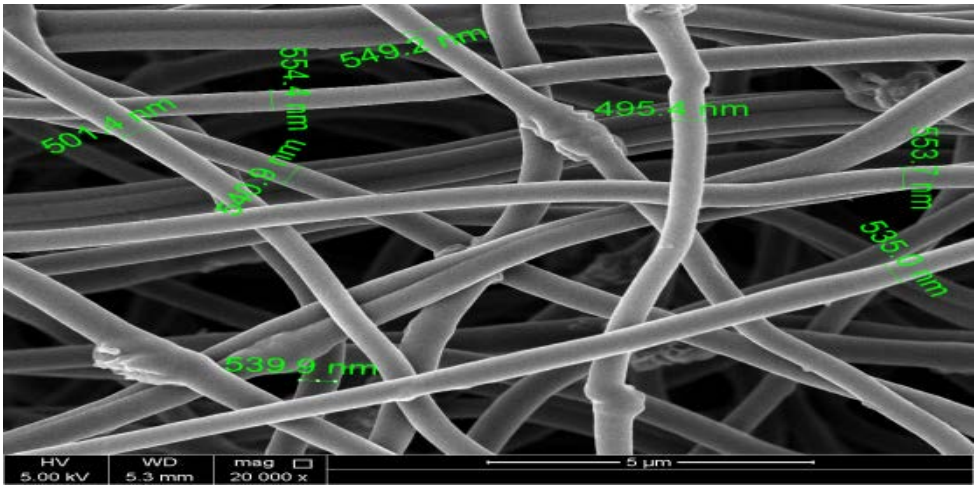

Figure 3.30. SEM of CNF-5% PTP.

3.1.2 Energy Dispersive X-ray (EDX) Analysis and Elements Mapping Results:

Energy dispersive X-ray (EDX) analysis was utilized to approve the existence of carbon, nitrogen, oxygen, and sulfur on the prepared nanofibers and estimate their percentage. Moreover, elements mapping was used to inspect the distribution of elements within the produced nanofibers. The results Figure 3.31 to Figure 3.38 confirmed the presents of carbon, nitrogen, oxygen and sulfur in the produced nanofibers with different percentage. The Figures 3.49 and Figure 3.48 confirmed the presents of carbon, nitrogen, oxygen and sulfur with less amounts in the carbonized nanofibers with different percentage for the samples CNF-3%S and CNF-5%PTP, respectively. The elemental mapping images (Figure 3.39 to Figure 3.46) observed a random distribution of the elements within the nanofibers and within the CNFs (Figure 3.49 to Figure 3.55). Tables 3.1 and 3.2, represent the different percentage of each element within the nanofibers and CNFs, respectively. From the tables, we notice the decrease in the nitrogen and sulfur amounts during the pyrolysis process as expected. In contrast, the results show the increase in the carbon content which confirm the success of converting the nanofibers to carbon nanofibers during the pyrolysis process. However, the samples CNF-3%S and CNF-5%PTP represent the highest sulfur content from each sulfur source of 1.05 wt. % and 0.77 wt. % respectively (Table 3.2). Thus, those two samples had been selected to continue the rest of the work and investigation in this thesis.

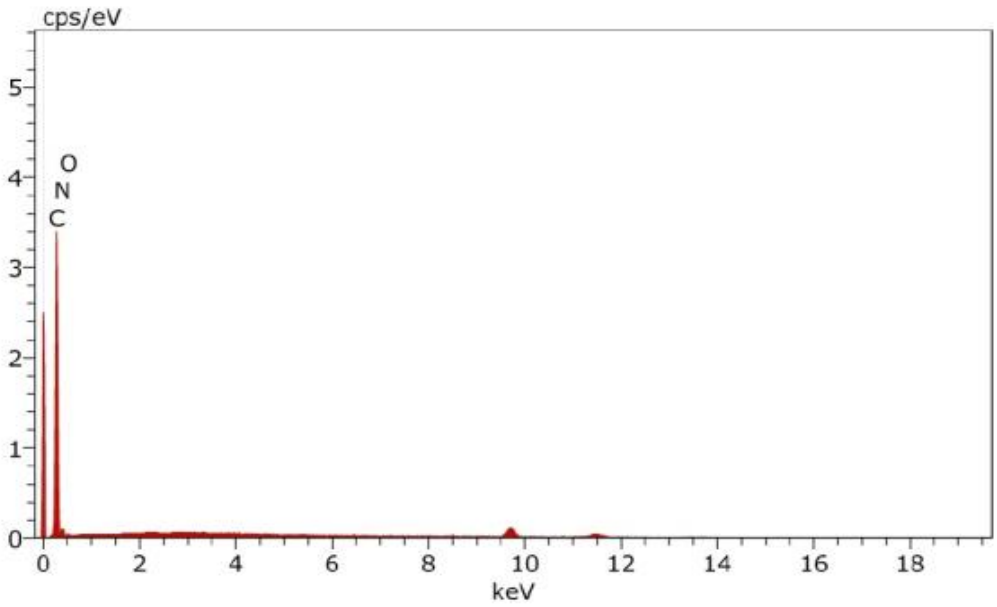

Figure 3.31. EDX elemental analysis graph of PAN.

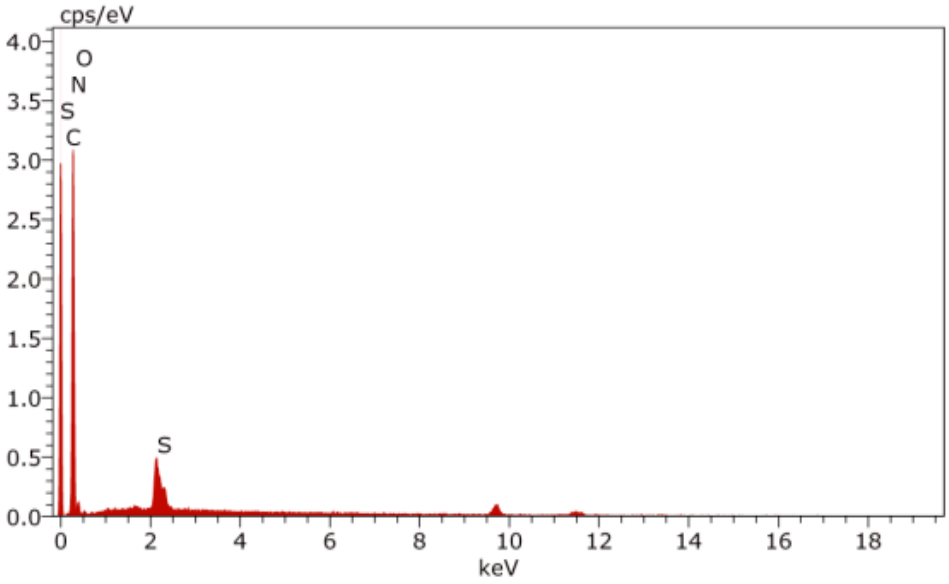

Figure 3.32. EDX elemental analysis graph of PAN-0.5%S.

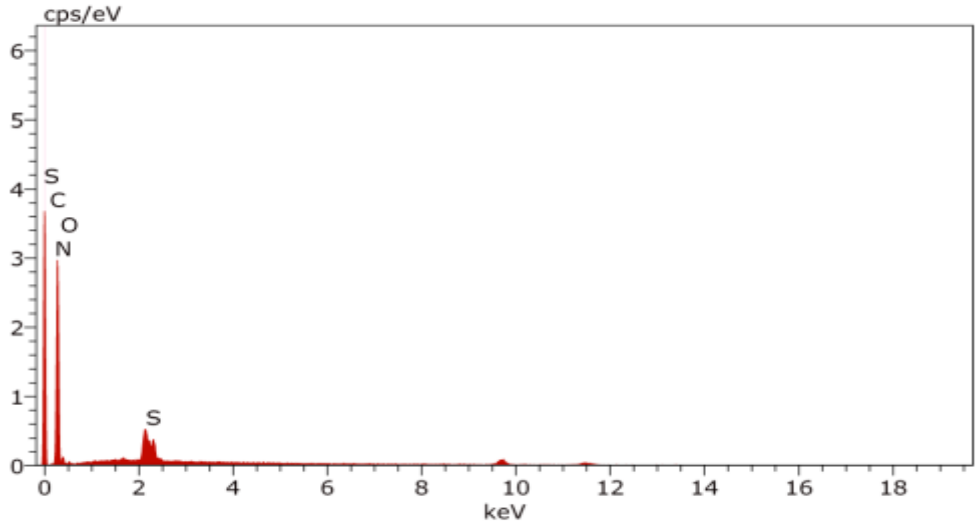

Figure 3.33. EDX elemental analysis graph of PAN-1%S.

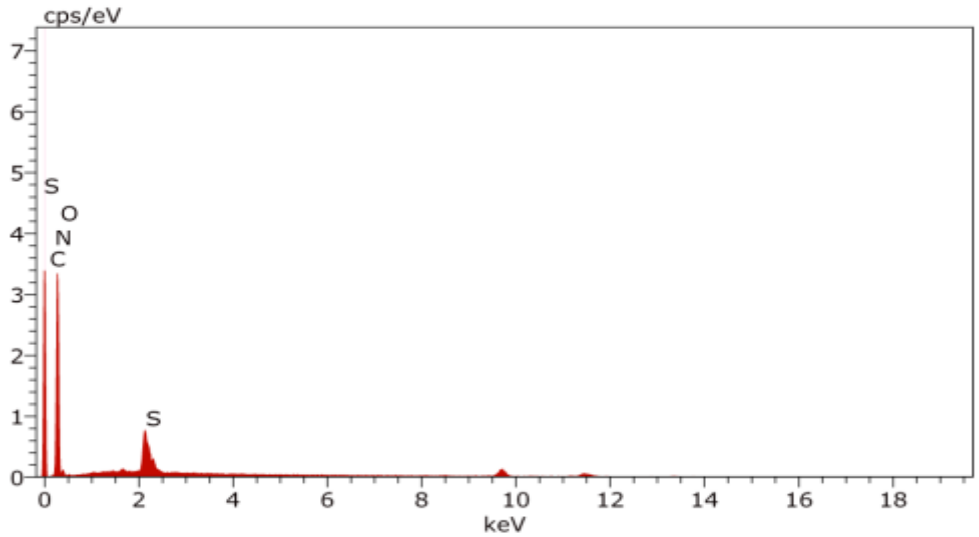

Figure 3.34. EDX elemental analysis graph of PAN-3%S.

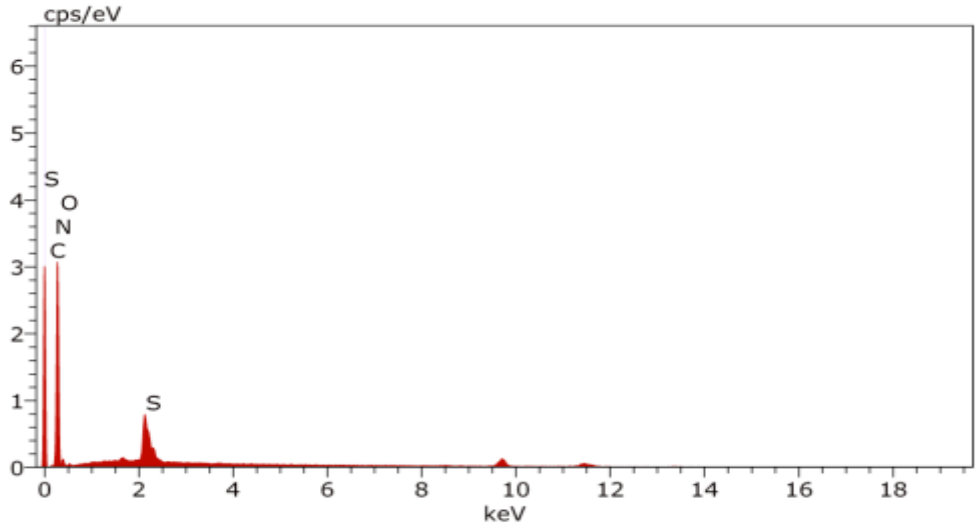

Figure 3.35. EDX elemental analysis graph of PAN-0.5%PTP.

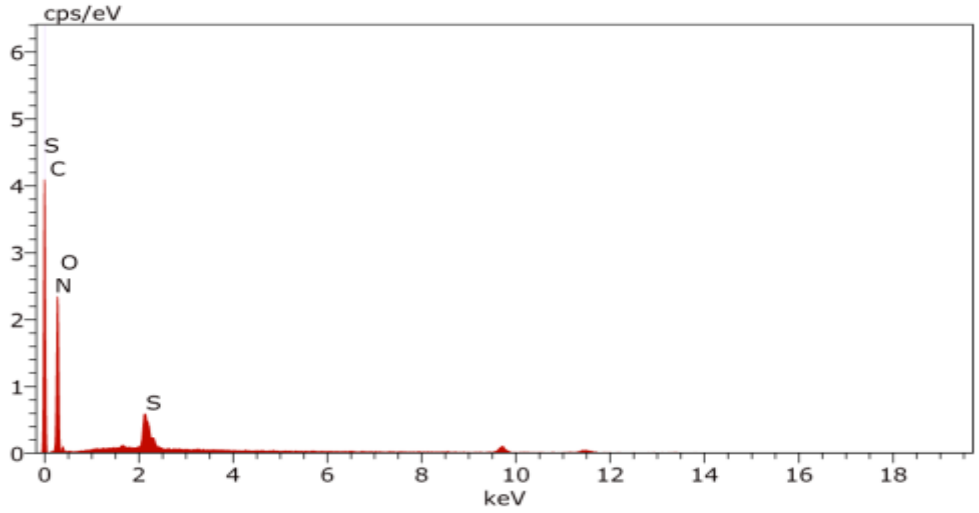

Figure 3.36. EDX elemental analysis graph of PAN-1%PTP.

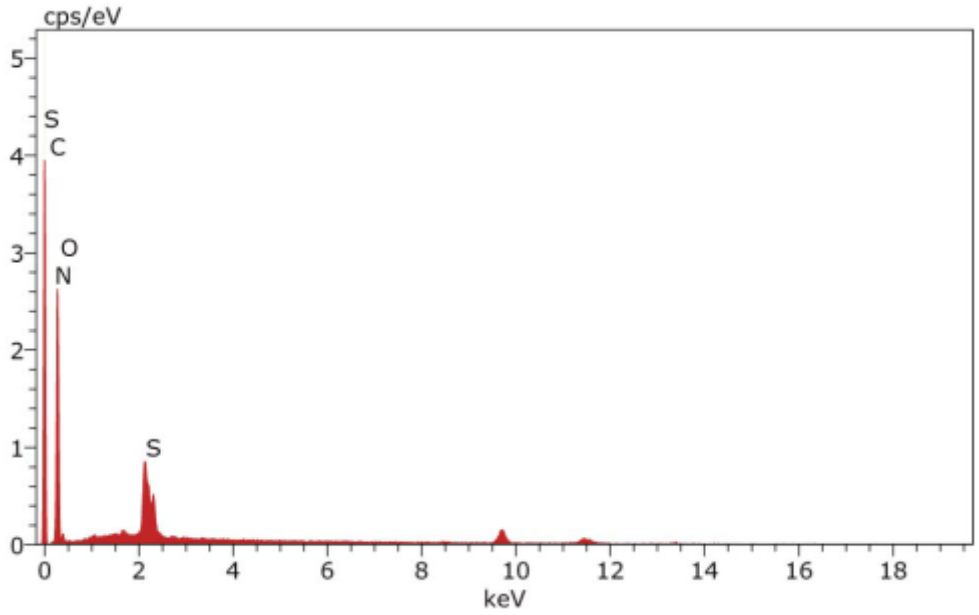

Figure 3.37. EDX elemental analysis graph of PAN-3%PTP.

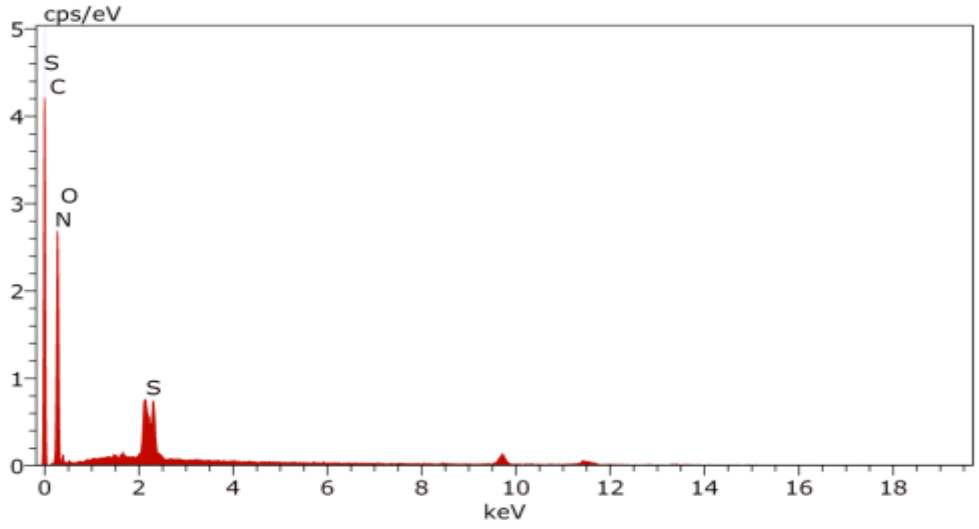

Figure 3.38. EDX elemental analysis graph of PAN-5%PTP.

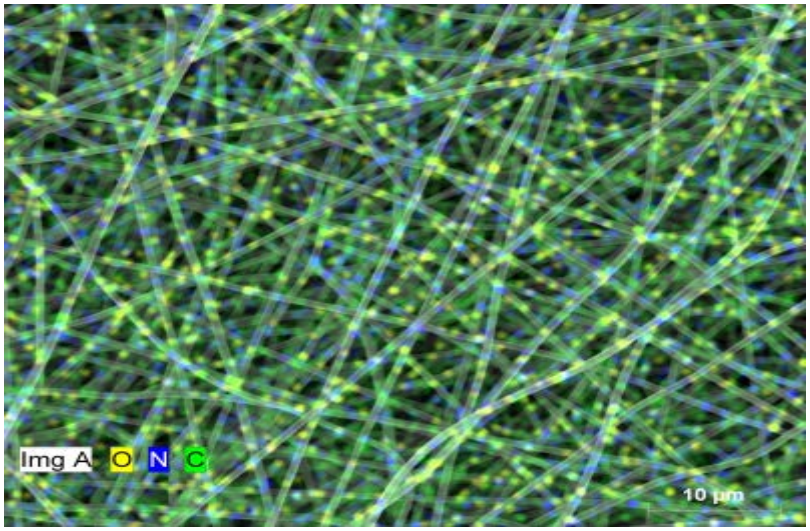

Figure 3.39. Elements mapping of PAN nanofibers -0%S.

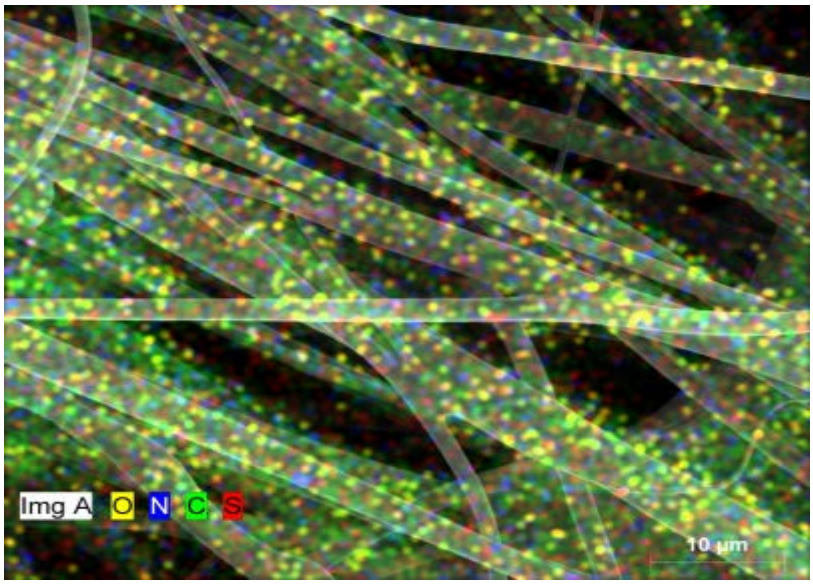

Figure 3.40. Elements mapping of PAN nanofiber-0.5%S.

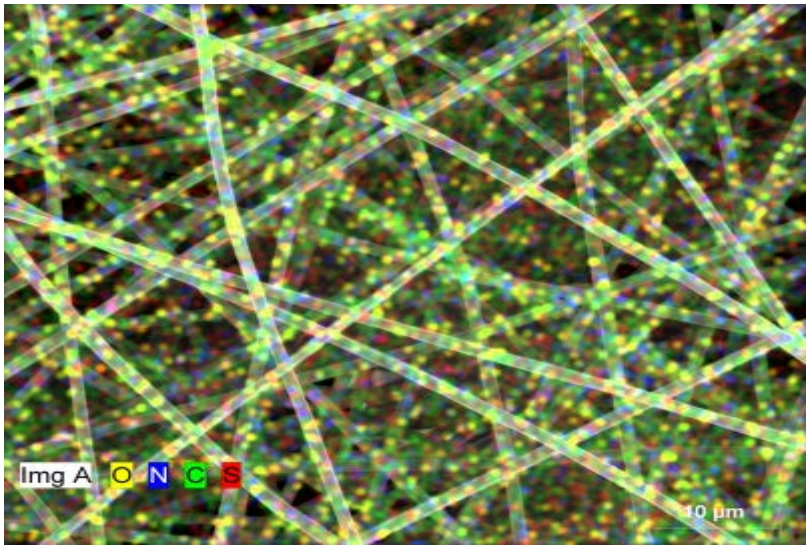

Figure 3.41. Elements mapping of PAN nanofiber-1%S.

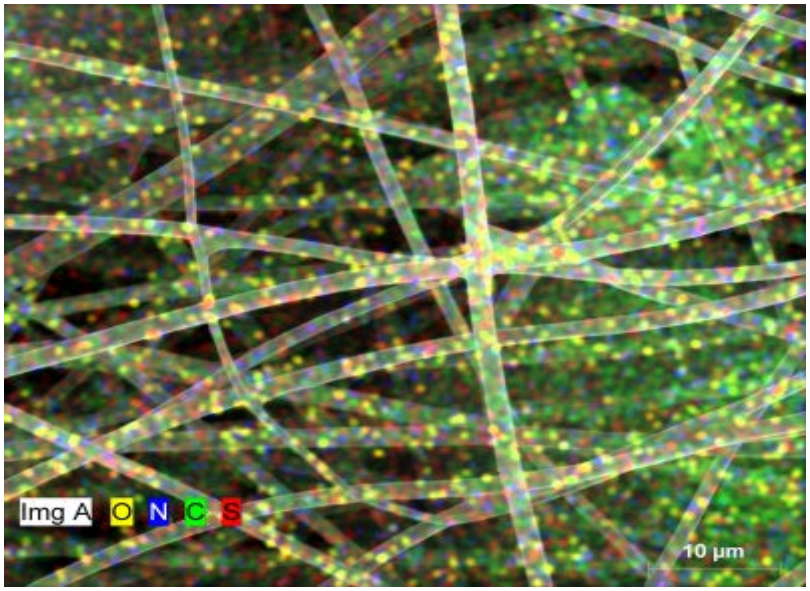

Figure 3.42. Elements mapping of PAN nanofiber-3%S.

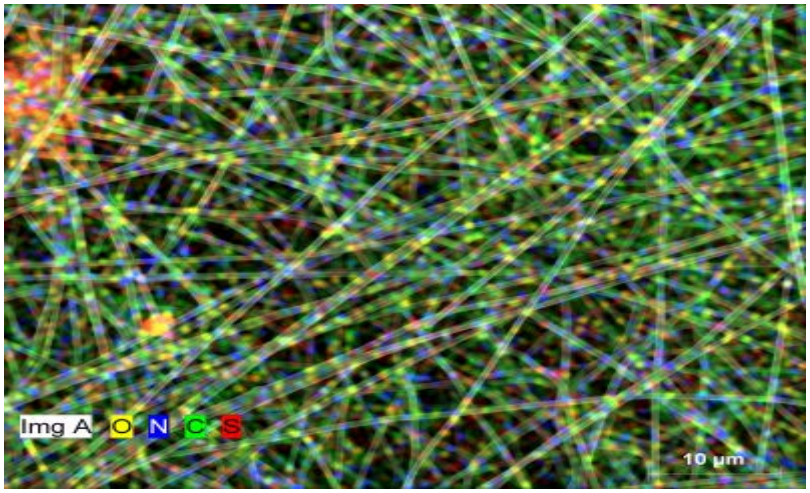

Figure 3.43. Elements mapping of PAN nanofiber-0.5%PTP.

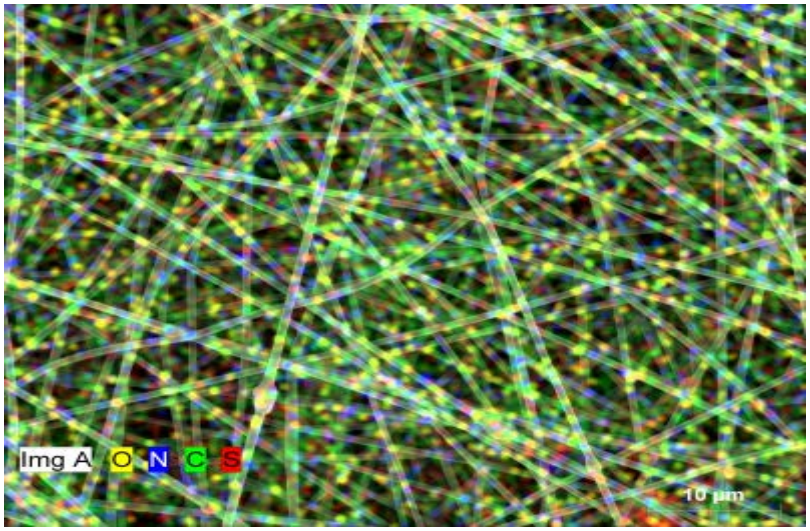

Figure 3.44. Elements mapping of PAN nanofiber-1%PTP.

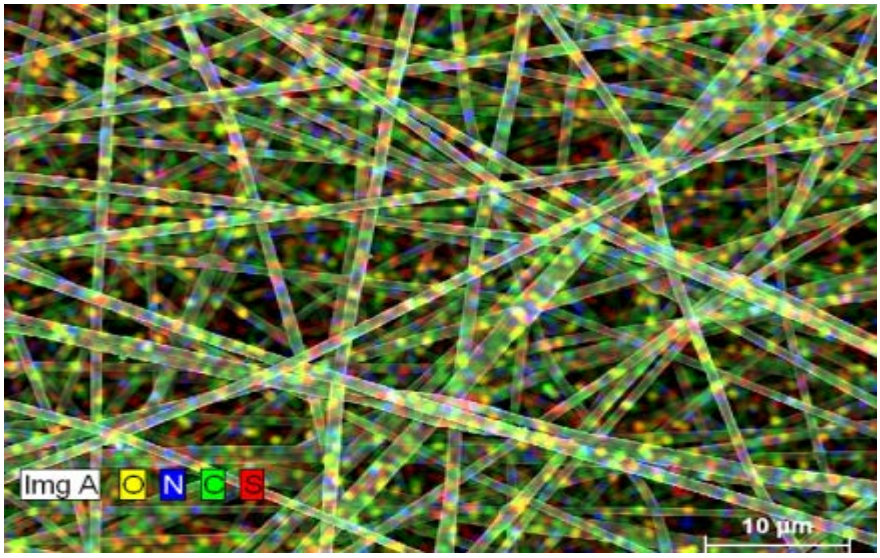

Figure 3.45. Elements mapping of PAN nanofiber-3%PTP.

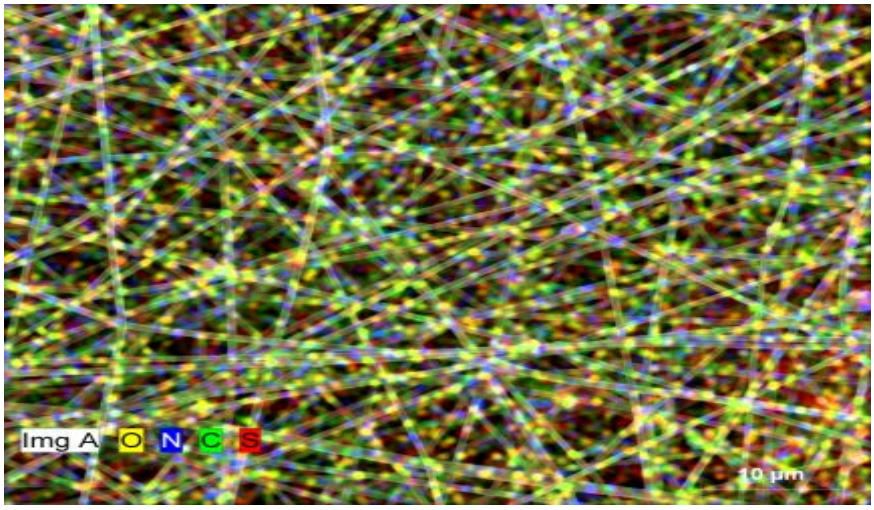

Figure 3.46. Elements mapping of PAN nanofiber-5%PTP.

Table 3.1. *EDX results of PAN Sulfur-doped Nanofibers samples*

Sample	**C**		**N**		**O**		**S**	
	wt.%	**at.%**	**wt.%**	**at.%**	**wt.%**	**at.%**	**wt.%**	**at.%**
PAN	73.02	76.33	22.13	20.00	4.67	3.66	0	0
PAN-0.5%S	71.39	75.08	23.70	21.37	4.08	3.22	0.83	0.33
PAN-1%S	71.50	75.43	22.44	20.30	4.71	3.73	1.34	0.53
PAN-3%S	73.94	77.49	21.27	19.11	3.84	3.02	0.95	0.37
PAN-0.5%PTP	71.79	75.55	22.67	20.67	4.56	3.60	0.98	0.39
PAN-1%PTP	73.27	76.92	21.52	19.37	4.19	3.31	1.02	0.40
PAN-3%PTP	72.32	76.45	21.17	19.19	4.49	3.56	2.03	0.8
PAN-5%PTP	73.83	78.16	18.86	17.12	4.57	3.64	2.73	1.08

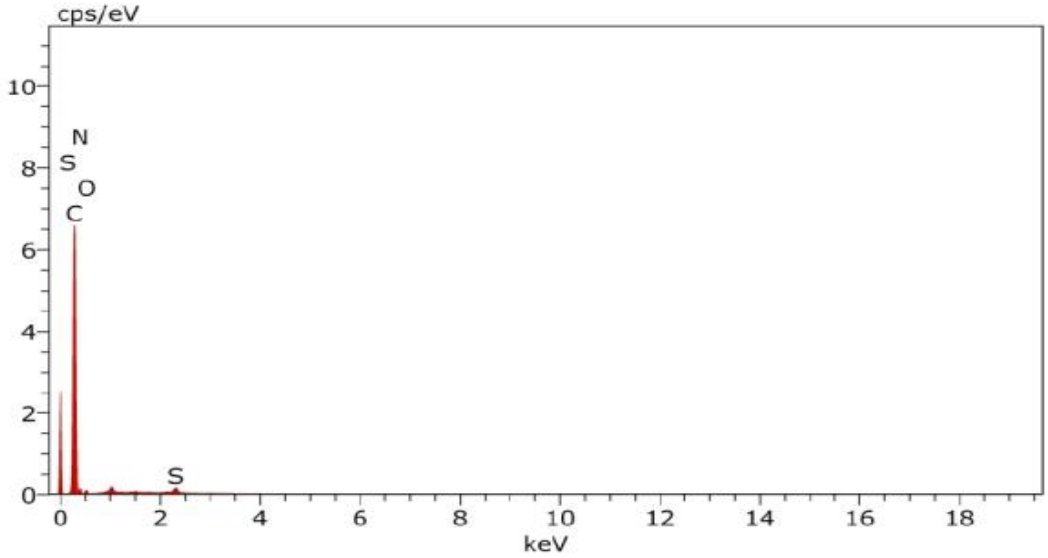

Figure 3.47. EDX elemental analysis graph of CNF-3%S.

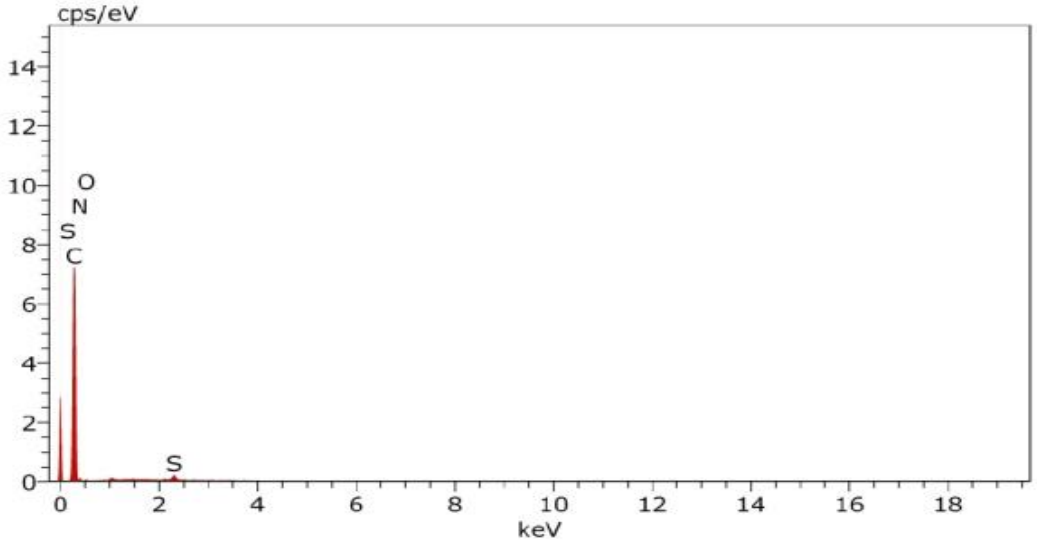

Figure 3.48. EDX elemental analysis graph of CNF-5%PTP.

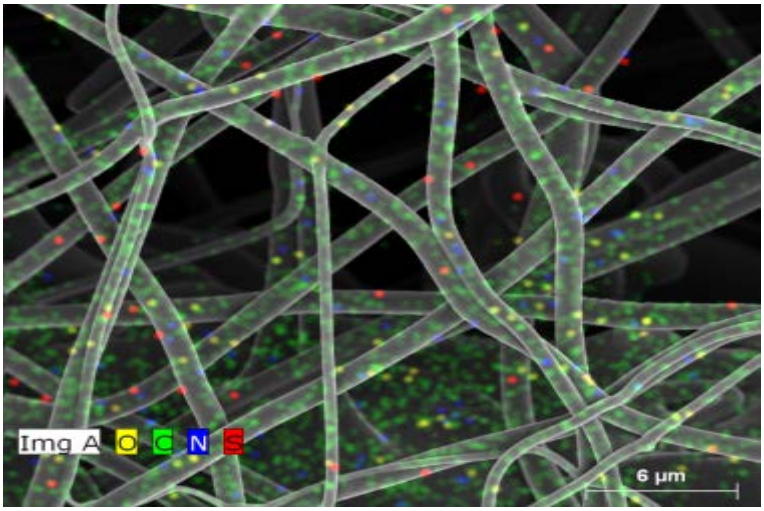

Figure 3.49. Elements mapping CNF-0.5%S.

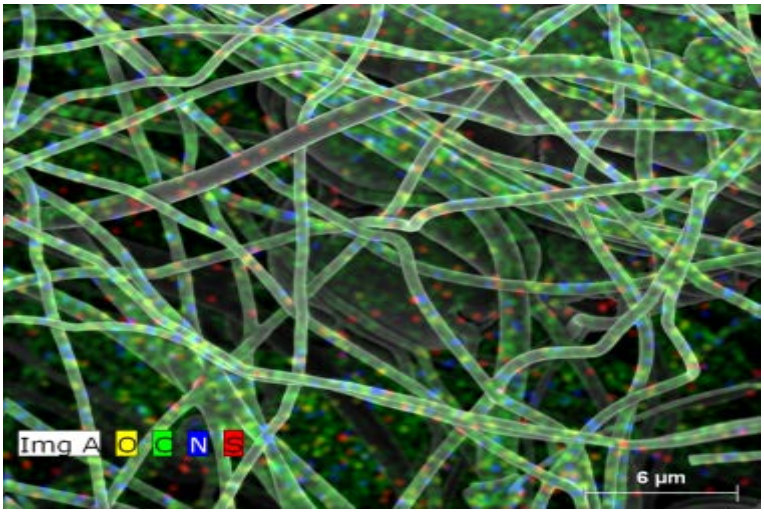

Figure 3.50. Elements mapping CNF -1%S.

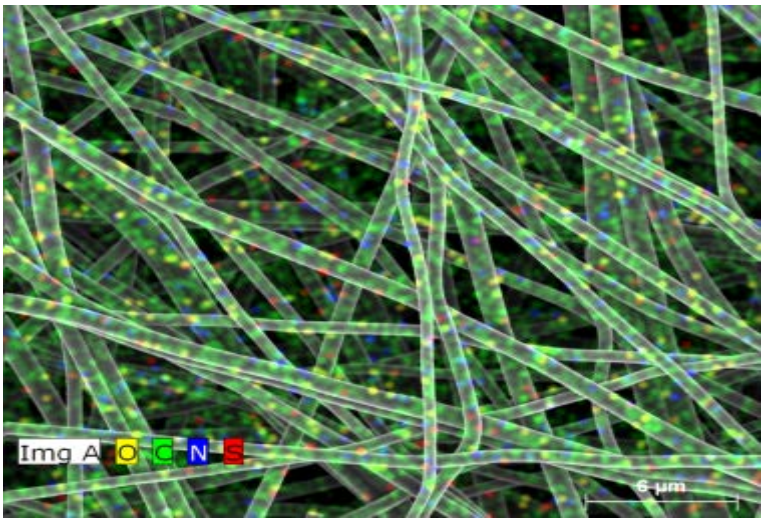

Figure 3.51. Elements mapping CNF -3%S.

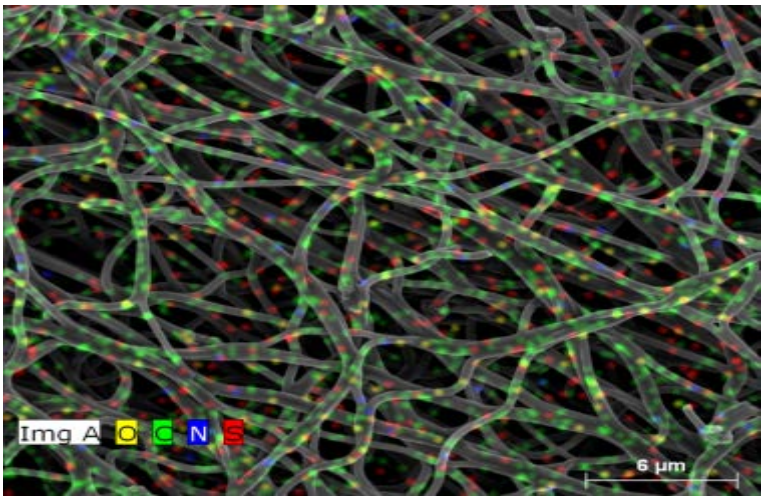

Figure 3.52. Elements mapping CNF -0.5%PTP.

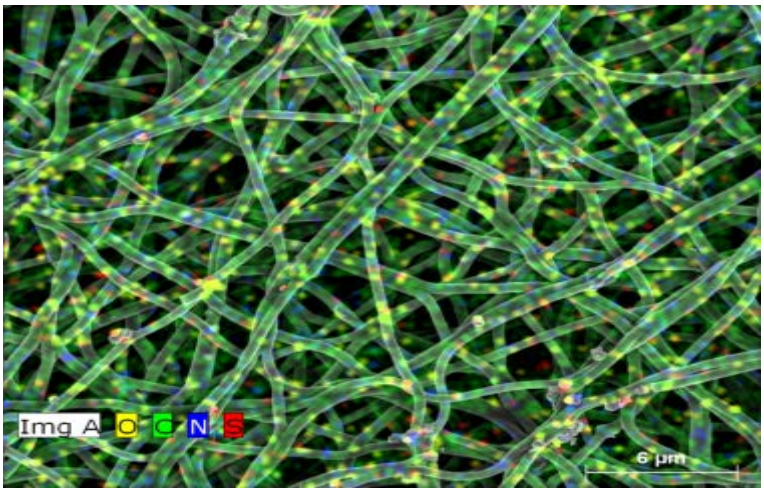

Figure 3.53. Elements mapping CNF -1%PTP.

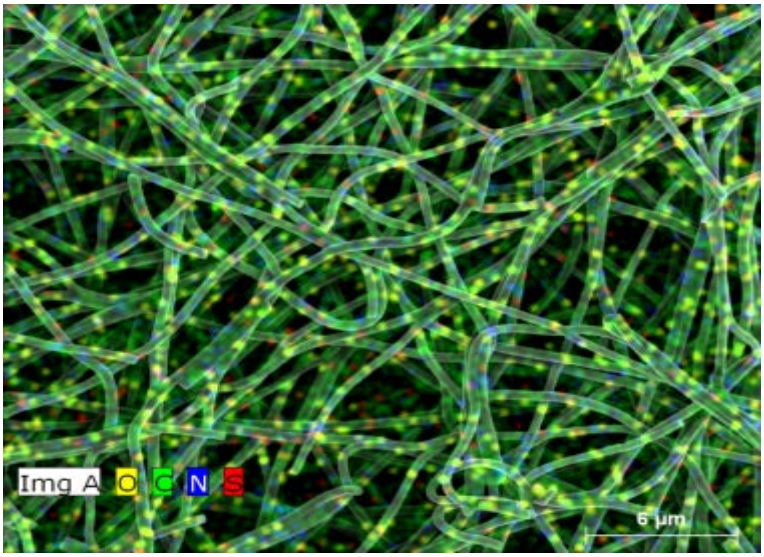

Figure 3.54. Elements mapping CNF -3%PTP.

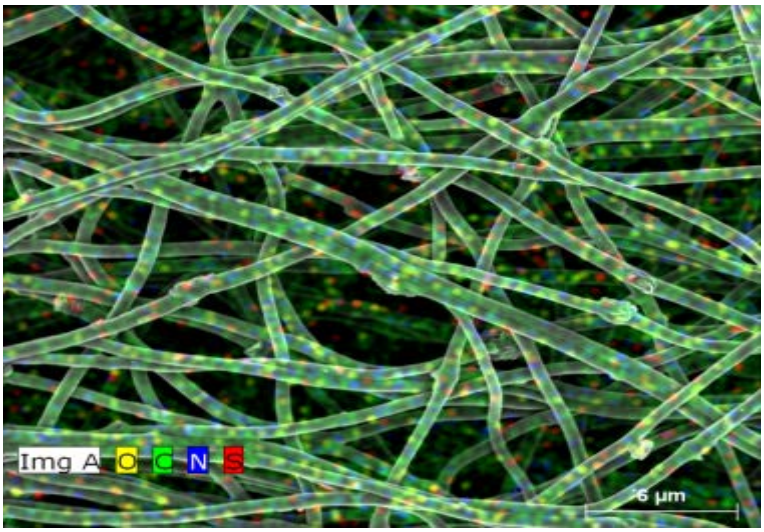

Figure 3.55. Elements mapping CNF -5%PTP.

Table 3.2. *EDX results of CNFs samples*

Sample	**C**		**N**		**O**		**S**	
	wt.%	**at.%**	**wt.%**	**at.%**	**wt.%**	**at.%**	**wt.%**	**at.%**
CNF-0%S	83.70	85.70	13.30	11.71	2.98	2.30	0	0
CNF-0.5%S	81.25	83.95	13.79	12.22	4.92	3.82	0.03	0.01
CNF-1%S	82.97	85.97	12.17	10.76	4.74	3.67	0.12	0.05
CNF-3%S	79.28	82.53	15.19	13.56	4.49	3.51	**1.05**	**0.41**
CNF-0.5%PTP	82.08	84.54	15.21	13.44	2.54	1.96	0.17	0.06

CNF-1%PTP	85.88	88.01	11.70	10.28	2.02	1.56	0.40	0.16
CNF-3%PTP	85.12	87.36	11.23	9.89	3.49	2.69	0.16	0.06
CNF-5%PTP	83.66	86.25	12.80	11.31	2.77	2.15	**0.77**	**0.30**

3.2 X-ray Photoelectron Spectroscopy (XPS) analysis Results

3.2.1 XPS of the S-doped CNFs

X-ray Photoelectron Spectroscopy (XPS) analysis was performed to further investigate the chemical composition of the CNF-3%S and CNF-5%PTP. The XPS peak analysis data and quantification of CNF3%S-doped and CNF5%PTT samples are listed in Table 3.3 and Table 3.4, respectively. The broad scan of both samples presented the peaks related to C, S, N, and O. These results agree with the previous EDX analysis. Figures 3.56 and 3.58 shows the high-resolution C 1s XPS peaks of CNF-3%S-doped and CNF-5%PTP samples, respectively. In the XPS spectra for both samples, the major peak at 284.9 eV corresponds to the C=C graphene sp^2carbon. The peak at 286.8 eV assigned to carbon atoms bond the sulfur and/or oxygen (i.e. C-O and/or C-S), on the surface. Moreover, the minor peak at 289.3 eV relates to O-C-O sp^2 carbon structures [155][225][150]. On the other hand, the S 2p XPS spectra for CNF-3%S and CNF-5%PTP are shown in Figures 3.57 and 3.59, respectively. In both, a major peak was observed at 163.8 eV assigned to –C-S-C-, which suggest the existence of thiophenic sulfur dopant. The other peak at 165.9 eV corresponds to conjugated –C=S-C- [160] [232] [233] [155]. However, the existence of thiophenic sulfur species indicate that the sulfur are mainly doped at the edges or on the surface of graphene [234]. The –C-S-C- probably work as ORR catalytic site which has a significant influence on the ORR performance [233] [235]. Furthermore, the minor peak centered at 168.5 eV in Figure 3.57 of CNF-3%S sample is assigned to –C-SO_x-C- type. This sulfate species most probably formed by the oxidation of elemental sulfur during the preparation process [148] [155] [225].

Table 3.3. *Results of the XPS peaks for CNF-3%S-doped sample*

Peak	**Position** **Binding energy (ev)**	**Atomic %**	**Mass %**
C 1s	284.6	86.48	82.49
S 2p	163.6	1.22	3.12
N 1s	399.6	7.77	8.64
O 1s	531.6	4.52	5.75

Table 3.4. *Results of the XPS peaks for CNF-5%PTP-doped sample*

Peak	**Position** **Binding energy (ev)**	**Atomic %**	**Mass %**
C 1s	284.6	86.66	83.73
S 2p	163.6	0.28	0.73
N 1s	399.6	7.90	8.90
O 1s	531.6	5.16	6.65

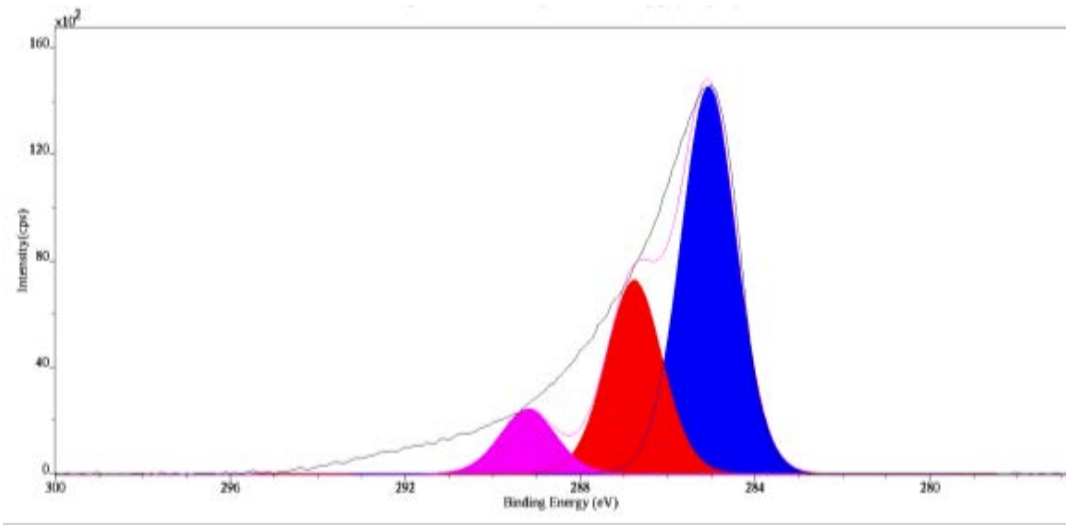

Figure 3.56. High-resolution XPS C 1s spectra of CNF-3%S-doped sample.

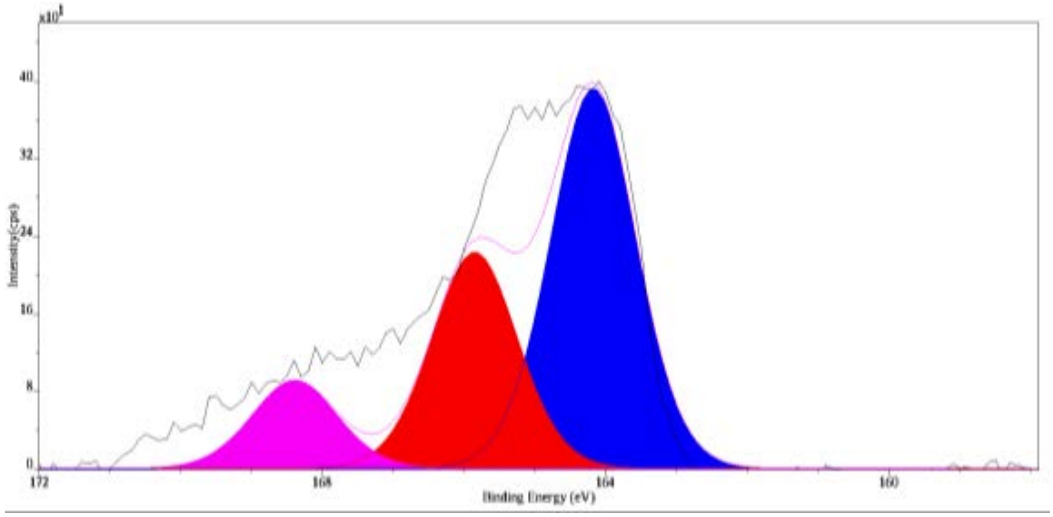

Figure 3.57. High-resolution XPS S 2p spectra of CNF-3%S-doped sample.

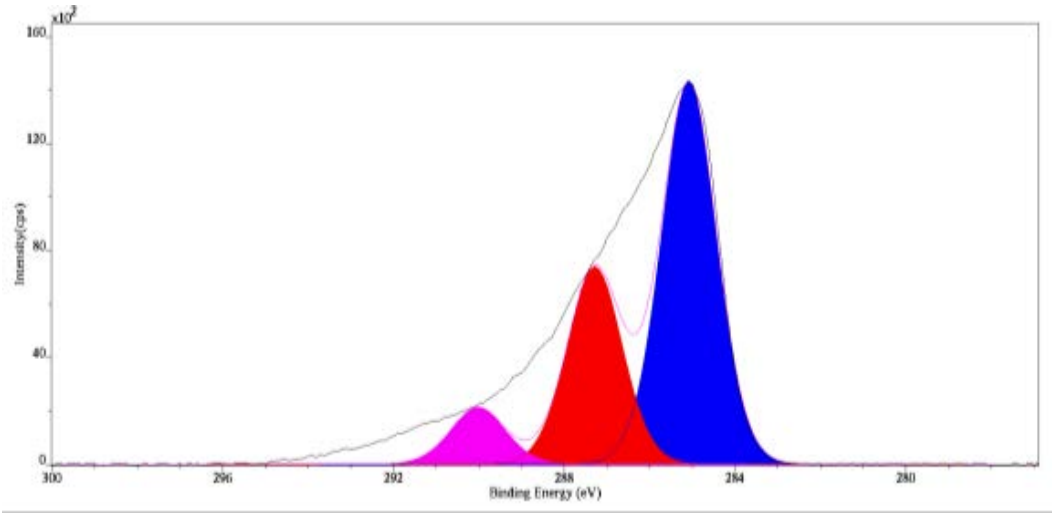

Figure 3.58. High-resolution XPS C 1s spectra of CNF-5%PTP-doped sample.

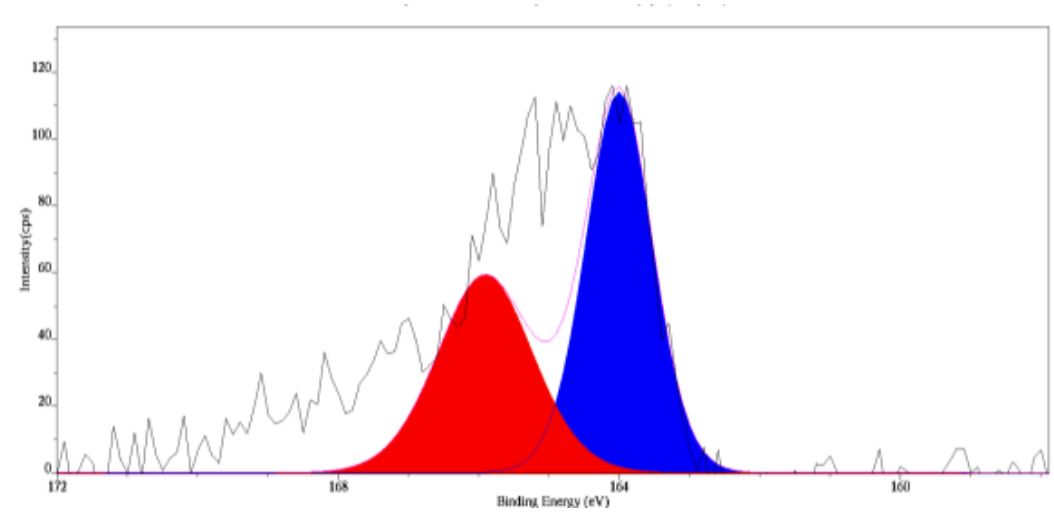

Figure 3.59. High-resolution XPS S 2p spectra of CNF-5%PTP-doped sample.

3.2.2 Electrode characterization

X-ray photoelectron spectroscopy was measured to inspect the alloy composition. Figure 3.60 represents the wide scan XPS spectrum of the Pt-Ni-Co-CuCNF-5%PTP/GC-RDE The characteristic peaks of C 1s at 281.6 eV, O 1s at 528.6 eV, N 1S at 401.6 eV, S 2p at 166.6 eV, Pt 4f at 71.6 eV, Ni 2p at 858.6 eV, Co 2p at 781.6 eV, and Cu 2p at 929.6 eV, confirm evidence the successfully deposition of the metals on the CNF-5%PTP surface. The XPS peak analysis data and quantification of Pt-Ni-Co-Cu@CNF-5%PTP/GC-RDE are shown in Table 3.5.

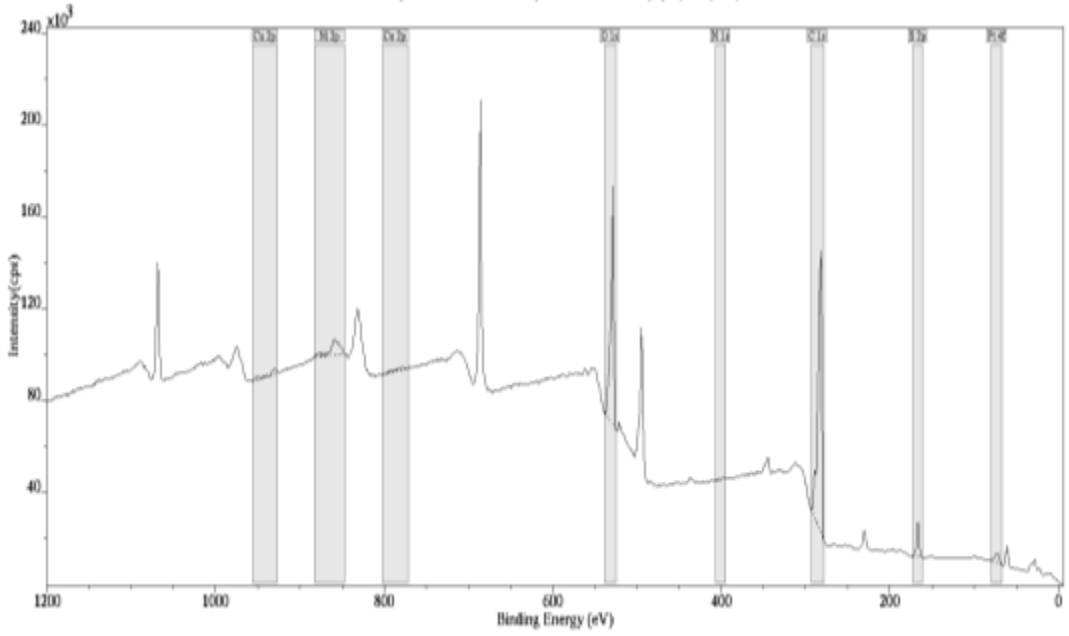

Figure 3.60. Wide scan XPS spectrum of the Pt-Ni-Co-Cu@CNF-5%PTP/GC-RDE.

Table 3.5. *XPS peak analysis and quantification of Pt-Ni-Co-Cu@CNF-5%PTP/GC-RDE*

Peak	Position Binding energy (eV)	Atomic %	Mass %
Pt 4f	71.6	0.15	2.14
Ni 2p	858.6	0.79	3.32
Co 2p	781.6	0.15	0.64
Cu 2p	929.6	0.15	0.69
N 1s	401.6	0.17	0.17
S 2p	166.6	2.58	5.89
C 1s	281.6	77.79	66.44
O 1s	528.6	18.20	20.71

3.3 Structural Analysis Results

3.3.1 FTIR analysis Results

Figure 3.61 and Figure 3.62 displays the FTIR spectra of pristine polythiophene (PTP) and pristine polyacrylonitrile (PAN), respectively. Table 3.6 and Table 3.7 list the assignment group of each peak for the pristine PTP and pristine PAN, respectively. For the PTP, the most distinctive peaks were detected in the low wavenumber region of 600-1500 cm^{-1}. The peaks at 689 cm^{-1} and 788 cm^{-1} correspond to C-S-C ring deformation and stretching C-S respectively [236] [237] [238]. The sharp peaks at 830 cm^{-1} and 1067 cm^{-1} are attributed to the C-H out of plane and C-H in plane respectively [236] [237][239]. Moreover, the peaks of 1439 cm^{-1} and 1492 cm^{-1} are corresponding to symmetric C=C and asymmetric C=C stretching, respectively [237][239]. The last peak is relatively weak observed at 3063cm^{-1}, corresponding to C-H aromatic stretching [239][240][241][237]. Furthermore, Figure 3.62 displays the FTIR spectra of pristine polyacrylonitrile (PAN). The C≡N stretching of acrylonitrile unit in the polymer chain is observed at 2241 cm^{-1}. The other peaks appeared at 1358, 1450, 1628, 2941 cm^{-1} are corresponding to C-H bending, CH_2 stretching, C=C stretching and C-H stretching, respectively [190] [219] [199]. In contrast, the FTIR spectra of prepared PAN-0%S nanofibers (Figure 3.63) showed the same peaks of that of the pristine PAN, expect the appearance of another peak at 1690 cm^{-1} which corresponds to C=O formed in the hydrolyzed PAN nanofibers and the stretching vibration of the C=O bonds in remaining solvent DMF [242][199] and/or existence of oxygen on the fiber surface[239]. A broad peak at 3548 cm^{-1} also appeared, which assigned to O-H of the absorbed water on the fiber surface [242][237]. However, spectrum of the prepared S-doped of PAN nanofibers

in Figure 3.64, also show the same peaks of PAN nanofibers and both pristine PTP and PAN nanofibers for PAN-3%S and PAN-5%PTP, respectively. Moreover, a new weak peak appear at 875 cm^{-1} for the PAN-3%S nanofibers, which may be contributed for C-S stretch as a result of the doped sulfur [238]. Table 3.8 and 3.9 summarize the assignmet group of each peak for the PAN nanofibers befor and after doped with sulfur, respectively.

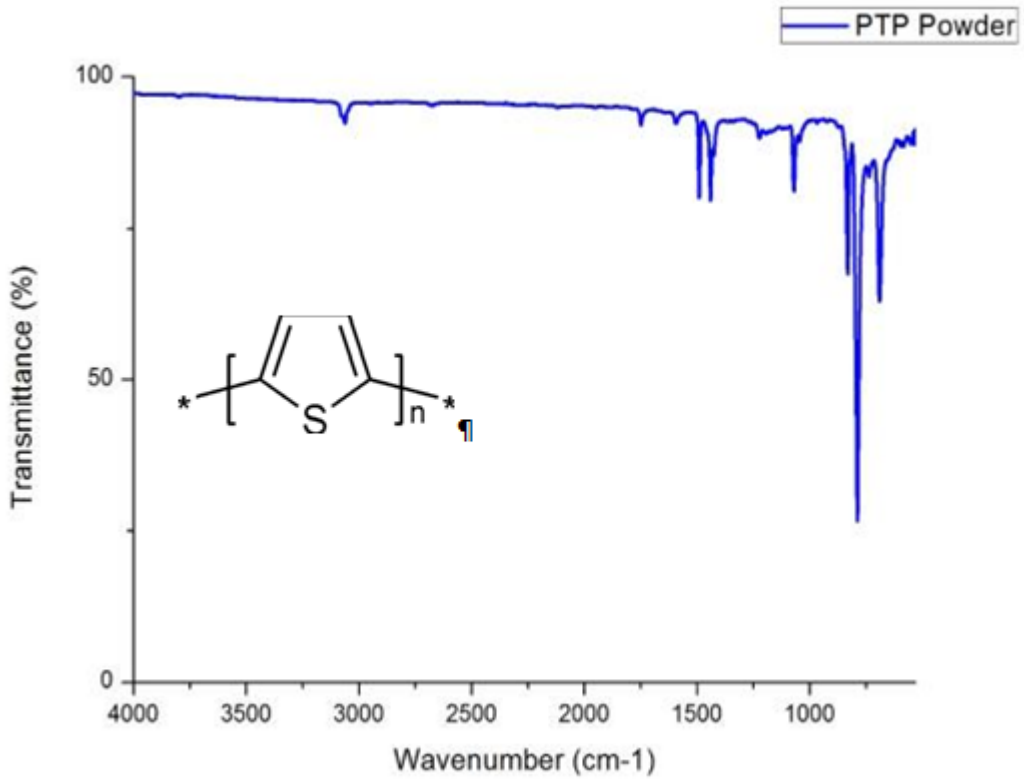

Figure 3.61. FTIR spectra of pristine polythiophene (PTP).

Table 3.6. *FTIR peaks for the pristine PTP and the assignment group of each peak*

Wavenumber (cm^{-1})	**Assignment**
689	C-S-C ring deformation
788	C-S stretching
830	C-H out of plane
1067	C-H in plane
1439	symmetric C=C
1492	asymmetric C=C stretching
3063	C-H aromatic stretching

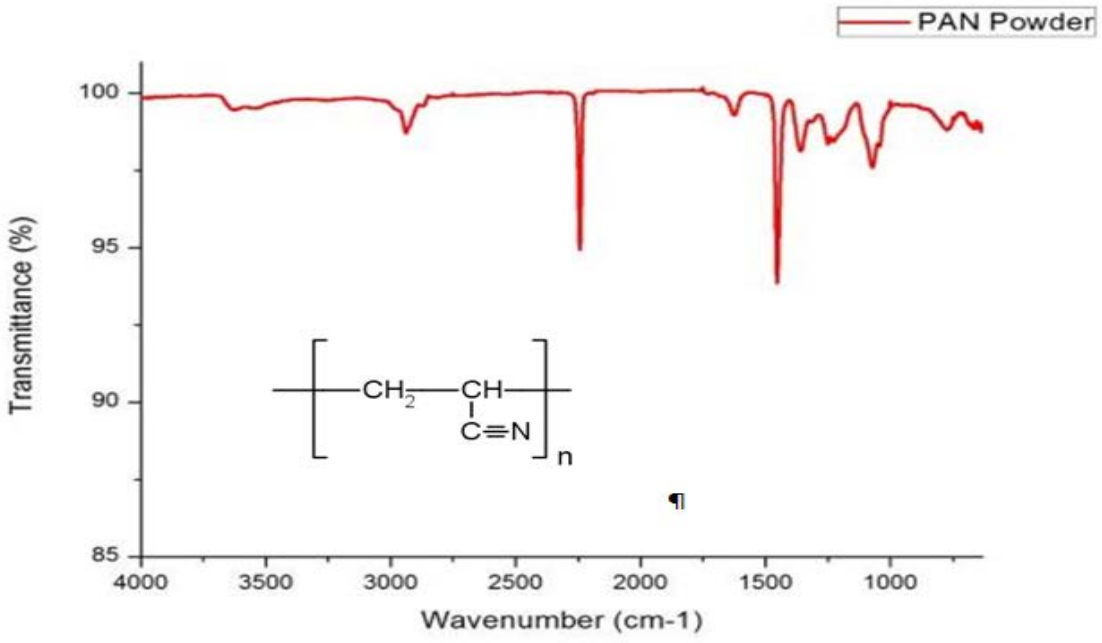

Figure 3.62. FTIR spectra of pristine polyacrylonitrile (PAN).

Table 3.7. *FTIR peaks for the pristine PAN and the assignment group of each peak*

Wavenumber (cm^{-1})	**Assignment**
1358	C-H bending
1450	CH_2 stretching
1628	C=C stretching
2241	C≡N stretching
2941	C-H stretching

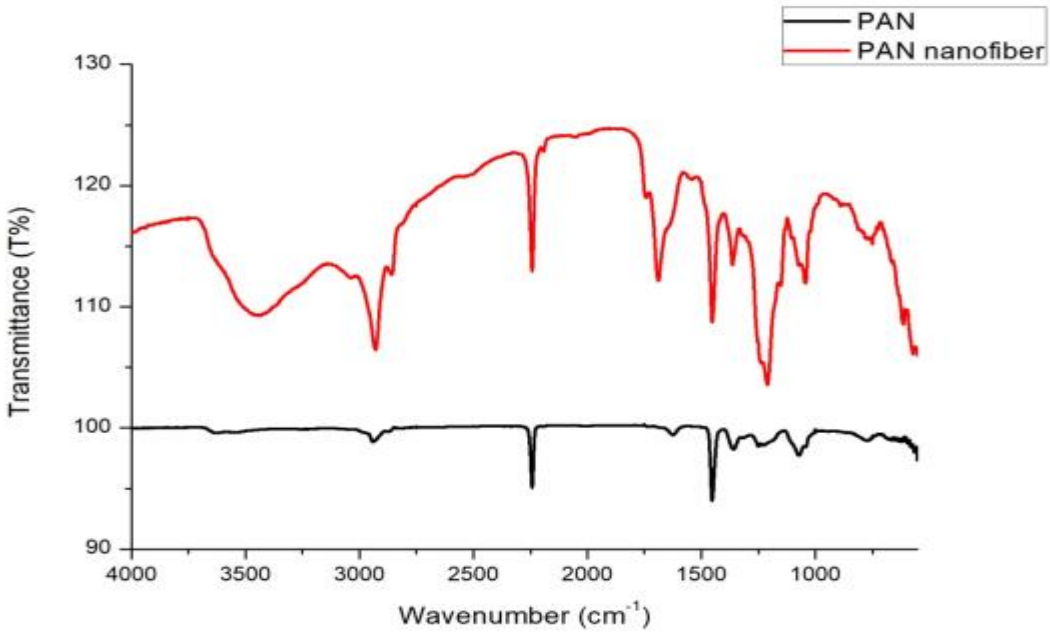

Figure 3.63. FTIR spectra of prepared PAN-0%S nanofibers.

Table 3.8. *FTIR peaks for the PAN-0%S and the assignment group of each peak*

Wave-number (cm^{-1})	**Assignment**
1358	C-H bending
1450	CH_2 stretching
1628	C=C stretching
1690	C=O stretching
2241	C≡N stretching
2941	C-H stretching
3548	O-H stretching

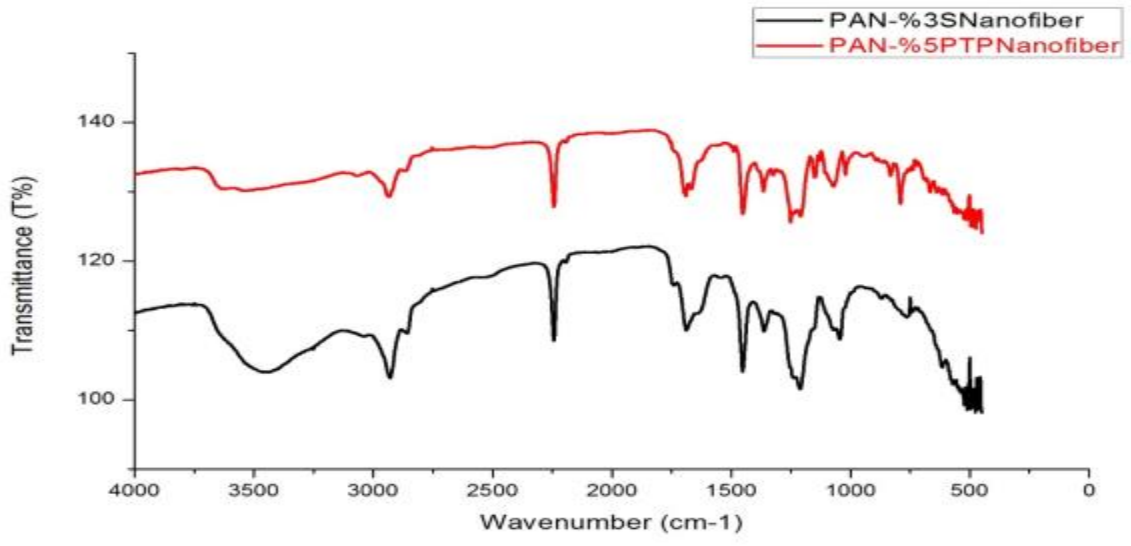

Figure 3.64. FTIR spectra of prepared PAN-3%S and PAN-5%PTP nanofibers.

Table 3.9. *FTIR peaks for the PAN-sulfur doped nanofibers and the assignment group of each peak*

Wave-number (cm^{-1})	**Assignment**
875	C-S stretch
1358	C-H bending
1450	CH_2 stretching
1628	C=C stretching
1690	C=O stretching
2241	C≡N stretching
2941	C-H stretching
3548	O-H stretching

3.3.2 X-ray Diffraction Analysis (XRD) Results

The XRD for elemental sulfur and powder PAN are presented in Figure 3.64. The pattern of the powder PAN show a major strong diffraction peak at 2Θ angel of 16.8° representing the X-ray reflection of (100) plane and a wide weak diffraction peak at 2Θ angel of 28.8° corresponding the X-ray reflections of (110) plane in PAN [243]. The interlayer spacing for the (100) plane d_{100} calculated was about 5.27 Å using Bragg's law:

$$n\lambda = 2d\sin\Theta \qquad \textit{Equation 20}$$

d: interlayer spacing in angstroms.

λ: wavelength in angstroms (1.54 Å for copper)

Θ: the diffraction angel in degree.

n: the order of the diffraction.(n=1 for the first order)

The XRD patterns of CNF-0%S, CNF-3%S, and CNF-5%PTP are displayed in Figure 3.65. The XRD spectrum obviously shows the disappearance of the PAN signature peak, which proposes the complete destruction of the PAN crystal structure [244][245][238]. In contrast, a new broad diffraction peak appeared at 2Θ angel of 24.9° corresponding to the (002) plane of the graphitic carbon [134][245][238][190], and a broader weaker peak at 2Θ angel of 43.5° corresponding to the (101) plane of graphitic carbon structure [190] for the three CNF samples. The interlayer spacing for the (002) plane d_{002} calculated by applying the Bragg's equation (Equation 20) was about 3.57 Å, which is close to that of graphite [134]. The broad peaks of the produced CNF samples reveals an amorphous

phase is obtained after the carbonization process [244][246][238]. However, the amorphous highly graphitized CNFs can work as a pathway for the charge carrier, and thus enhance the electric conductivity, which is beneficial for the ORR [134]. On the other hand, the absence of the signature peaks of elemental sulfur indicates the embedding of sulfur into the heterocyclic structure of dehydrogenated polyacrylonitrile [247][248][246][238].

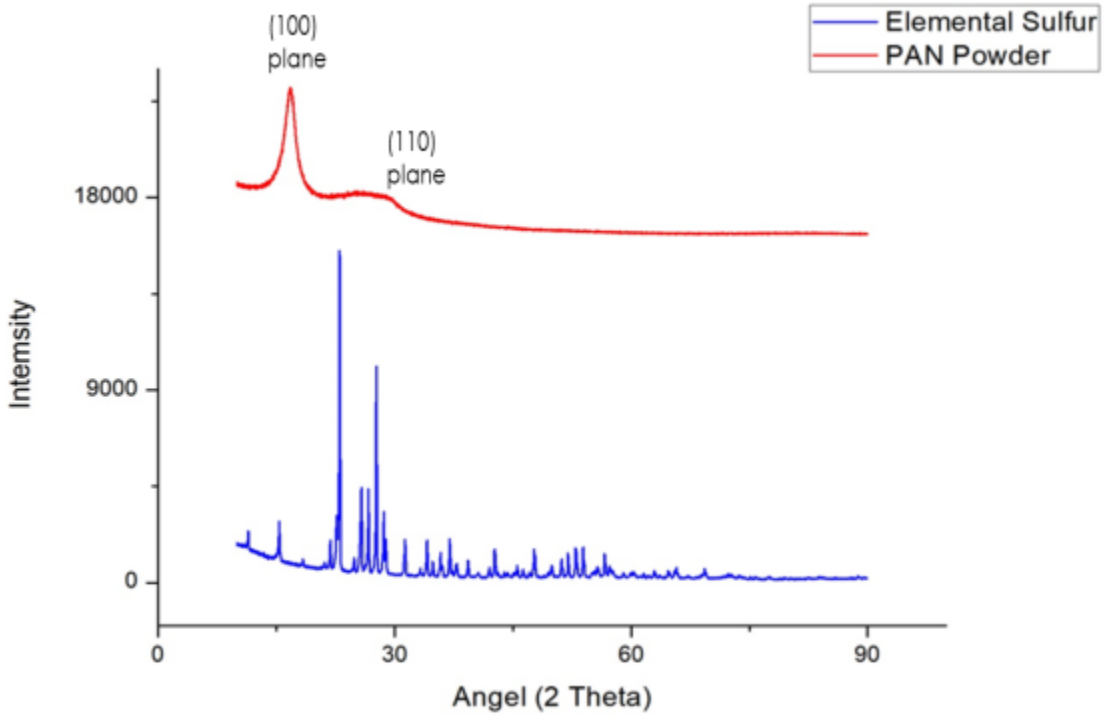

Figure 3.65. The XRD for elemental sulfur and powder PAN.

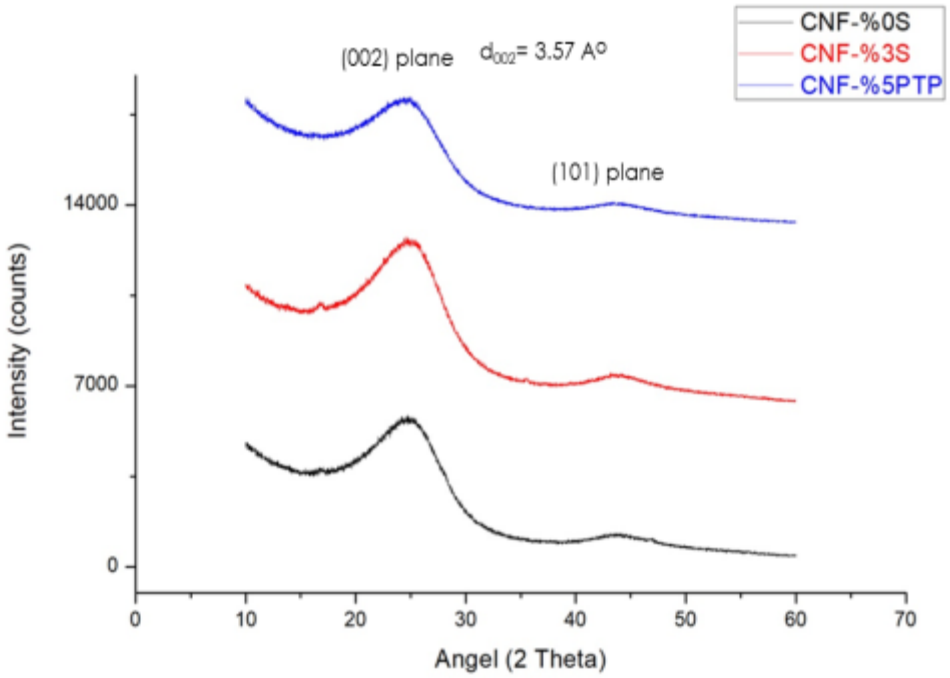

Figure 3.66. The XRD patterns of CNF-0%S, CNF-3%S, and CNF-5%PTP.

3.4 Thermogravimetric Analysis (TGA) Results

It is important to understand the thermal behavior of electrospun PAN before converting the nanofibers to carbon nanofibers and to know the suitable temperature for the nanofiber, which can withstand during the carbonization process. Therefore, thermal properties and weight loss of nanofibers were studied by Thermogravimetric analysis (TGA) in nitrogen atmosphere. Figure 3.66 shows the TGA curves for the prepared nanofibers PAN-0%-S, PAN-3%S, and PAN-5%PTP nanofibers. The TGA graph displays four different weight loss regions. The initial weight loss step between 25-297 ^{o}C with a little weight loss of only about 3% for the PAN-0%S and PAN-3%S samples, while the weight loss of the PAN-5%PTP was just over 8%. This negligible weight loss may be due to evaporation of the absorbed water and moisture from the samples [249]. The higher weight loss in the PAN-5%PTP can be explained as it consists of rich polymer of PAN and PTP, and thus more easily degrades [250]. The second step is a small temperature range between 297-330 ^{o}C. Although the temperature change is so small the nanofibers exhibited rapid weight loss of about 25% at this stage, due to the thermal decomposition of PAN chains and chemical reactions taking place with volatiles being evolved [251]. After that, the nanofiber samples displayed stable behavior in the third region between 330-550 ^{o}C with only a further 10% weight loss. The weight loss was due to the elimination of gaseous compounds and evacuation of water from the cyclization condensation reaction of the adjacent ladder structures [245][219] It was noticed that the PAN-5%PTP sample also had a further weight loss of about 5% more relative to the other two samples, this could be due to the fact it consists of more sulfur which melt at this temperature range [247][244]. The last region was from 550 ^{o}C

through to the maximum decomposing temperature of 950 °C. At 800 °C, the nanofiber samples lost almost 75% of their total weight as a side gas evolved and resulted in the release of HCN and NH_3, in addition to water and N_2 [219]. It is noticed that the S-doped samples showed less weight loss at 800 °C with 25% residues of the nanofiber weight comparing with the 0%S-doped sample, which had 19% residues of the nanofiber weight. This evidenced that the interaction between sulfur and PAN produces a more stable structure of nanofibers [244]. On the other hand, the TGA result for the carbonized CNF of the three samples in Figure 3.67 represent a stable structure of the CNFs. Even at very high temperature of 900 °C, the CNF samples had more than 60% residues of the weight [238].

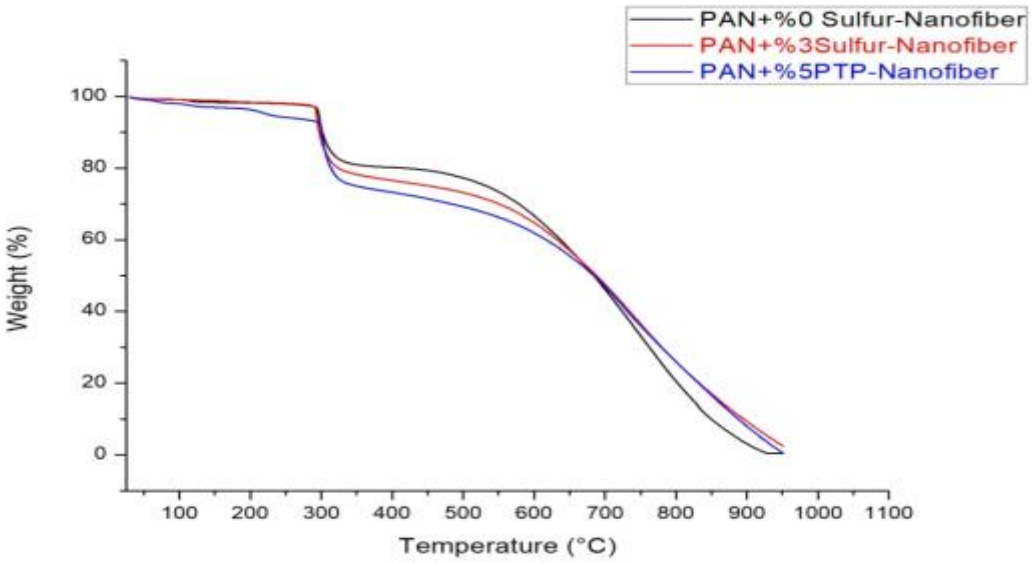

Figure 3.67. The TGA curves for the prepared nanofibers PAN-0%-S, PAN-3%S, and PAN-5%PTP.

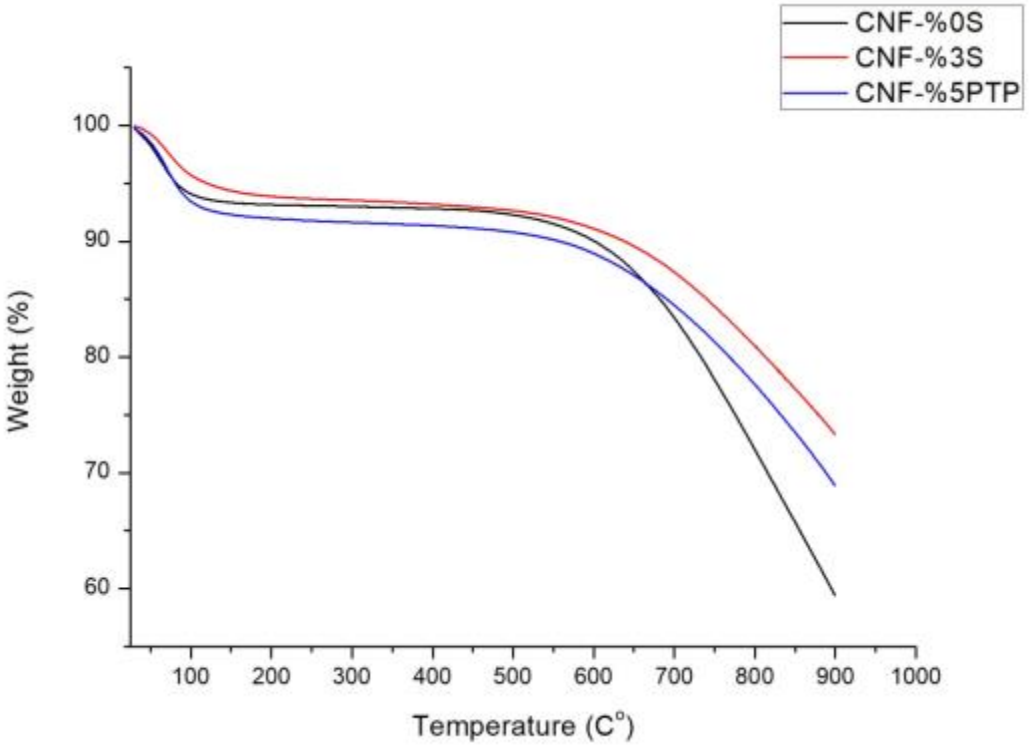

Figure 3.68. The TGA curves for the CNF-0%-S, CNF-3%S, and CNF-5%PTP.

3.5 Electrochemical Measurements Results

3.5.1 The Cyclic Voltammetry (CV):

Figure 3.69 displays the effect of scan rate on the cyclic voltammogramsof the Ni-Co-Cu@CNF-5%PTP/GCE electrode in 1 M NaOH solution saturated with (A) nitrogen and (B) oxygen. It is worthy to mention that the Ni-Co-Cu alloy was deposited potentiostatically for 30 minutes at different scan rates. It can be noticed that the higher the scan rate is, the higher the measured peak currents are. Figure 3.70 displays the relation of both cathodic and anodic peak currents with the scan rate. The relation is found to be linear which confirms that the peaks are due to a surface redox reaction [112].

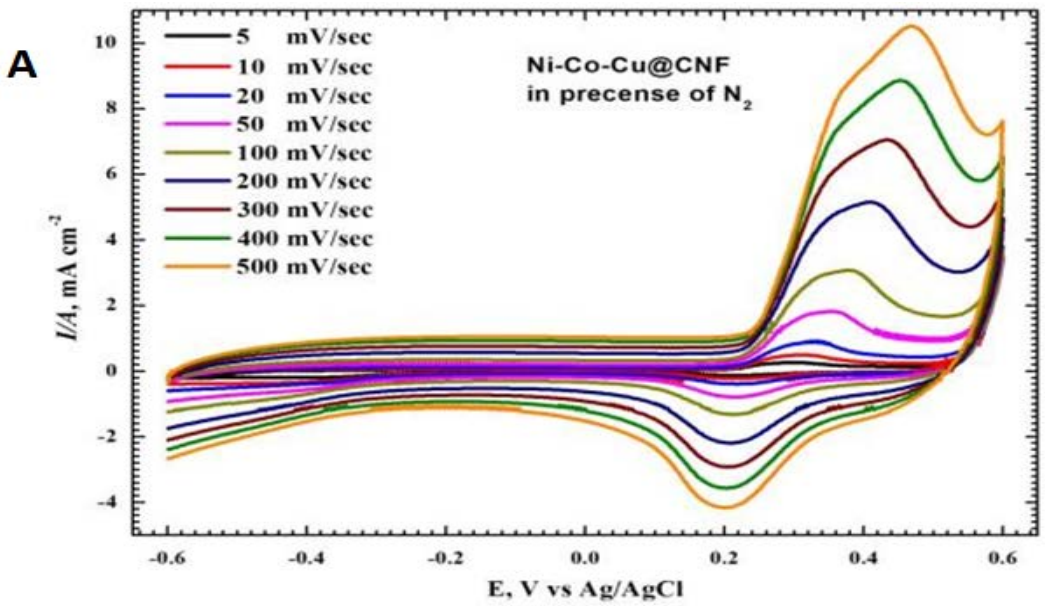

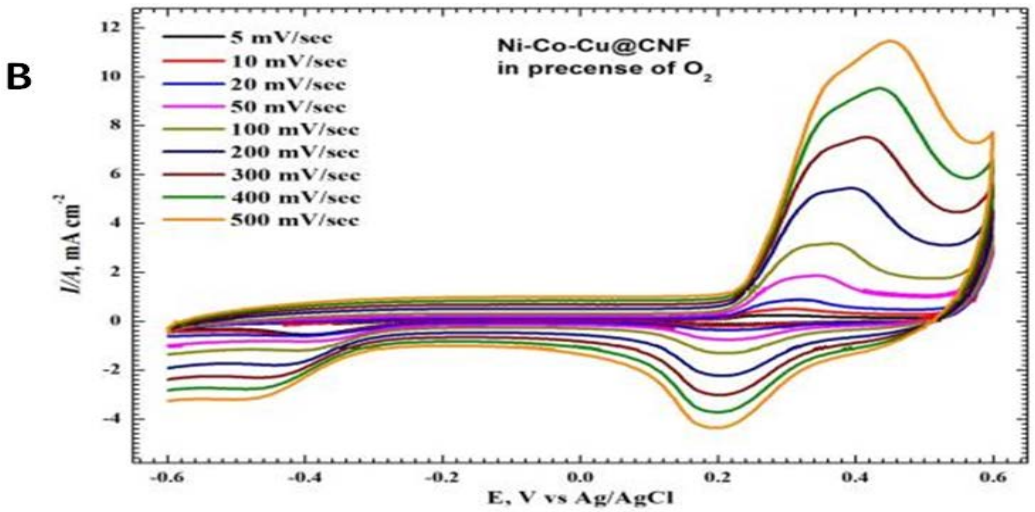

Figure 3.69. CVs for glassy carbon in 1 M NaOH solution of sulfur doped carbon fiber (PAN-5%PTPCNF) with 30 minutes electrodeposited of Ni-Co-Cu at different scan rate, in A) Nitrogen and B) Oxygen.

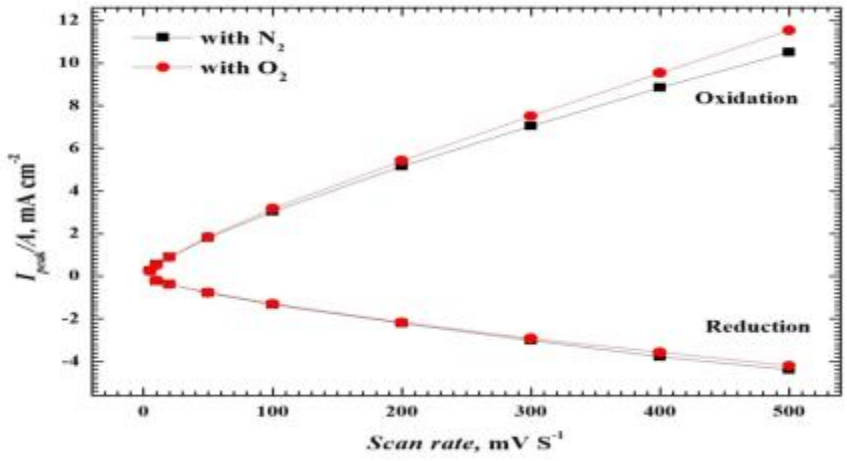

Figure 3.70. Anodic and cathodic peak current densities versus scan rate in 1M NaOH solution saturated with oxygen (red) and nitrogen (black).

3.5.2 Linear Sweep Voltammogram (LSV):

Linear sweep voltammograms (LSVs) of glassy carbon electrode (RDE) in 1 M NaOH saturated with oxygen to compare the ORR activity for both CNF-3%S and CNF-5%PTP, with and without electrodeposited Ni-Co-Cu at different deposition time were measured. In terms of onset potential and half- wave potential, LSV results exhibit that the activity and current density of the catalyst increase with the increase of the deposition time for both samples. The potentials of the Ag/AgCl reference electrode were adjusted to the reversible hydrogen electrode (RHE) by applying the equation:

$$E_{(RHE)} = E_{Ag/AgCl} + 0.198 + 0.059pH \qquad \textit{Equation 21}$$

In the catalysts based on CNF-3%S (Figure 3.71A), the highest onset potential was 0.73 V (vs RHE) at 30 minutes of deposition and half-wave potential of 0.66 V. In the catalysts based on CNF-5%PTP (Figure 3.71B). The onset potential and half-wave potential were of 0.76 V and 0.67 V respectively, showing that the ORR activity of CNF-5%PTP is higher than that of the CNF-3%S.

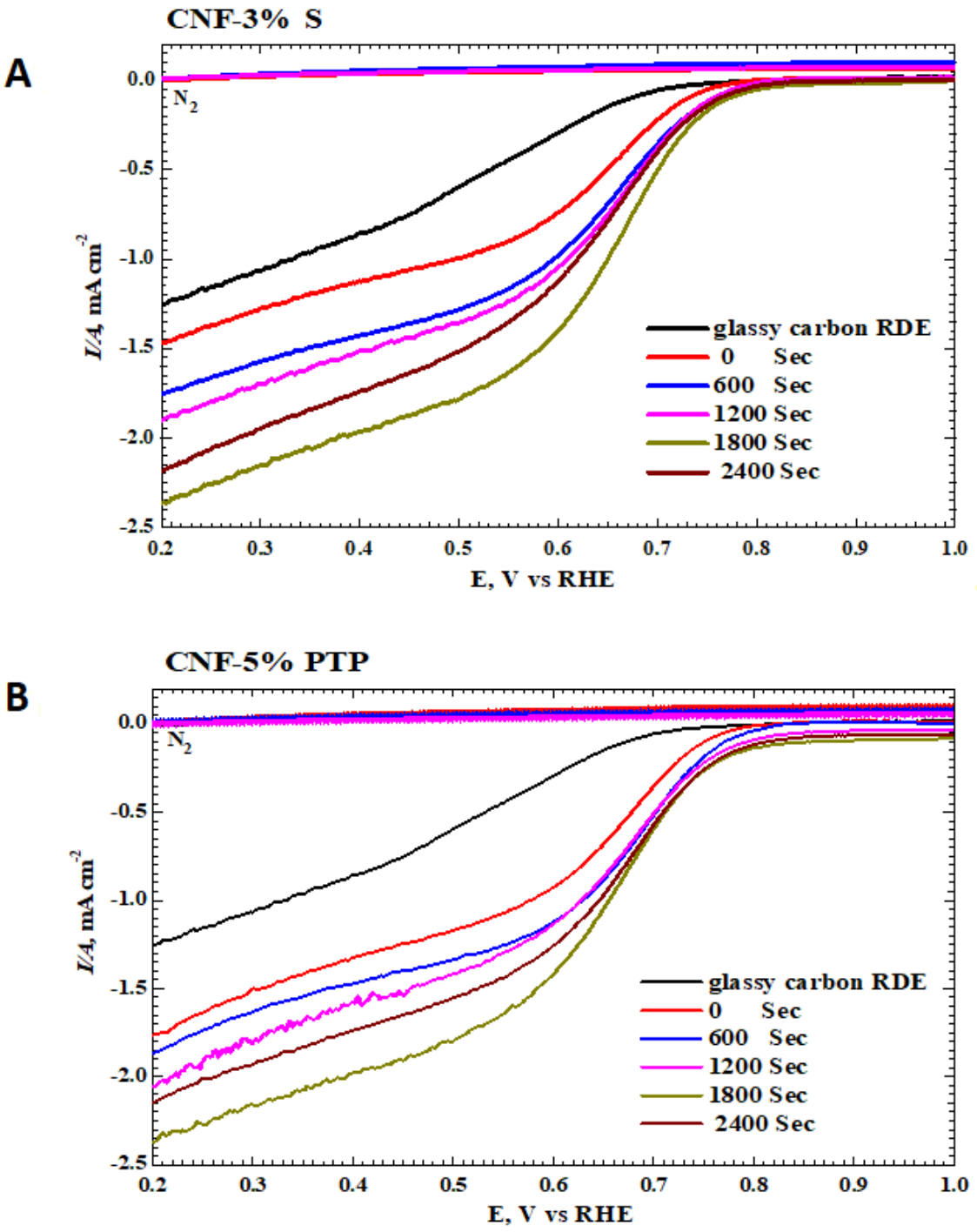

Figure 3.71. Linear sweep voltammograms (LSV) in O_2 saturated 1 M NaOH solution for A) CNF-3%S and B) CNF-5%PTP, with electrodeposited Ni-Co-Cu at different deposition times @1600RPM.

In order to enhance the electrocatalytic activity, a 1mM of PtK_2Cl_4 was added to the 1mM of the metals electrodeposition solution. LSVs were used to compare the kinetics of ORR in oxygen-saturated 1M NaOH solution at room temperature for the different electrodes at (A) 1600 and for the Pt-Ni-Co-Cu@CNF-5%PTP/GCE (B) at 1600, 1800, 2500, 3000 and 3500 rpm. As can be seen in Figure 3.72A, Ni-Co-Cu@CNF-5%PTP/GCE shows higher electrocatalytic activity toward ORR with a more positive onset potential than Ni-Cu-Co@CNF-3%S/GCE [252]. Moreover, the addition of Pt to the alloy enhances the kinetics of the ORR as the onset potential (E_{onset}), was shifted to more noble direction and the measured current is higher at any potential. The half-wave potentials ($E_{1/2}$) of the Pt-Ni-Co-Cu@CNF-5%PTP/GCE is shifted in the more noble direction. Pt-Ni-Co-Cu@CNF-5%PTP/GCE shows an onset potential (E_{onset}) of 0.91 V vs. RHE, and a half-wave potential ($E_{1/2}$) of 0.84 V vs. RHE, which are almost identical to that of 20 wt.% Pt/C under alkaline conditions [252]. Table 3.10 below summarized the ORR activity performance for the different catalysts.

Table 3.10. *Onset potentials (*E_{onset}*), half-wave potentials (*$E_{1/2}$*), and limiting current densities (LCD) at 0.2 V for different catalysts at 1600 rpm in an alkaline media.*

Catalyst	E_{onset} (V)	$E_{1/2}$ (V)	LCD (mA cm^{-2})
Glassy carbon electrode RDE(blank)	0.64	0.52	1.3
Ni-Co-Cu@CNF-3%S/GCE	0.77	0.64	2.2

Ni-Co-Cu@CNF-5%PTP/GCE	0.78	0.67	2.3
Pt-Ni-Co-Cu@CNF-5%PTP/GCE	0.91	0.84	4.1

The durability of the Pt-Ni-Co-Cu@CNF-5%PTP/GCE catalyst investigated by ORR polarization curves for diferent rotation speeds using the 30 minutes - electrodeposited Pt-Ni-Co-Cu in O_2-saturated 1 M NaOH electrolyte (Figure 3.72B). The catalyst showed good stability up to 3500 RPM.

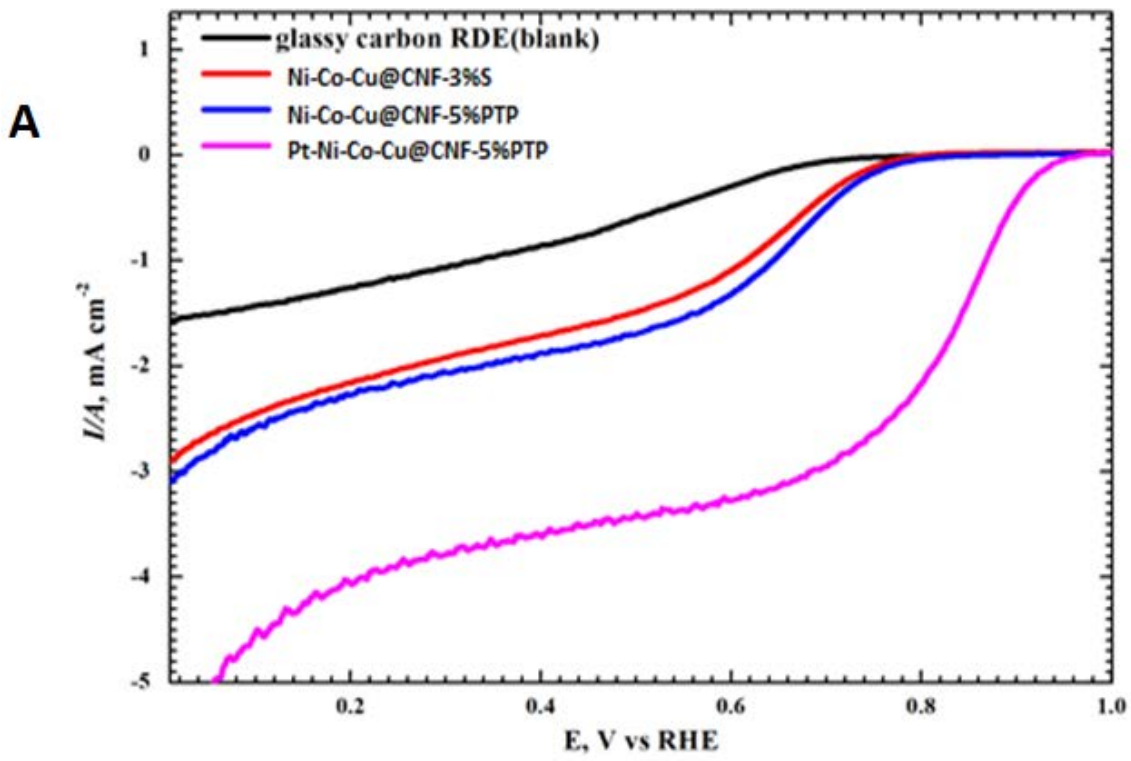

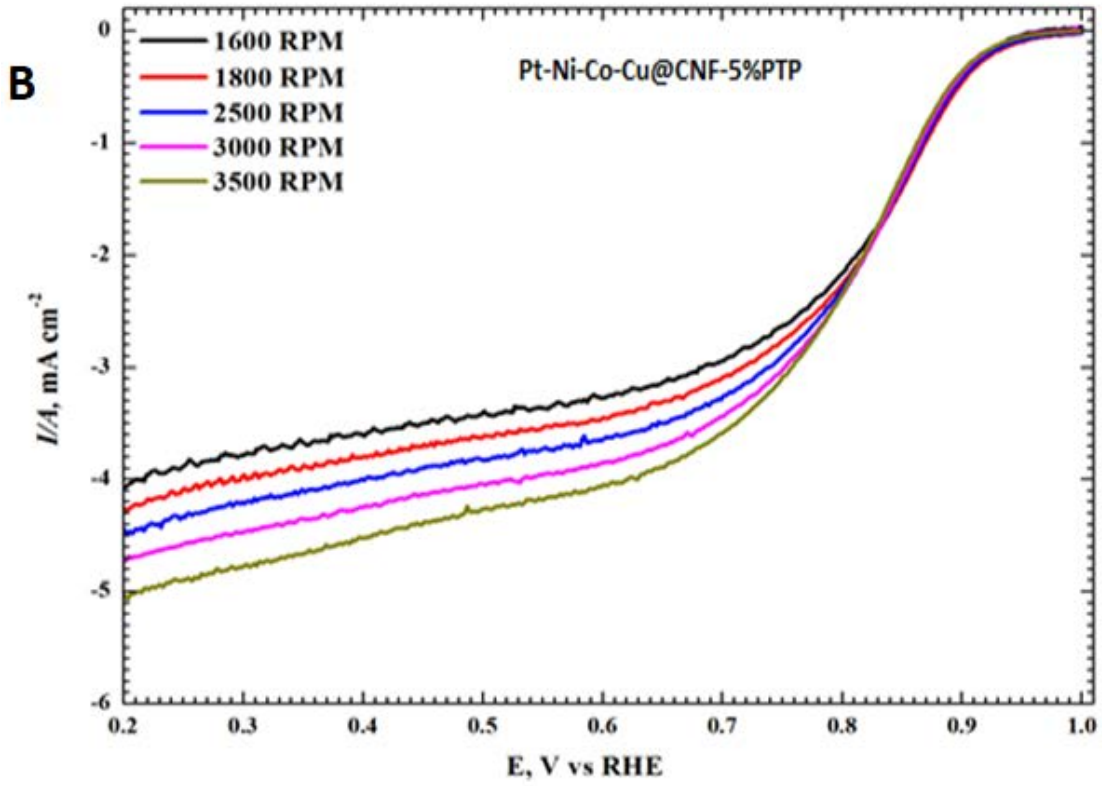

Figure 3.72. LSVs of different electrodes in oxygen-saturated 1M NaOH solution at room temperature at (A) 1600 and (B) 1600, 1800, 2500, 3000 and 3500 rpm.

In order to determine the overall electrons number (*n*) involved in the ORR process, a plot of (j^{-1}) vs ($\omega^{-1/2}$) known as the Koutcky-Levich (K-L) plot obtained from the LSV-RDE curves is applied at different potentials, where *j* is the current density, and ω is the rotation speed in rpm [253][254][128]. From the slope of the straight lines, we can determine the number of electrons from the Koutcky-Levich equation. The equation is written as the following [119][255] :

$$\frac{1}{j} = \frac{1}{j_k} + \frac{1}{j_d} = \frac{1}{j_k} + \frac{1}{0.2nFAD^{2/3}\nu^{-1/6}C\omega^{1/2}} \qquad \textit{Equation 22}$$

where: *n* is the number of electrons, F is the Faraday's constant (F= 96485 C mol^{-1})[119], A is the electrode area (A=0.2 cm^2), D is the Diffusion coefficient of O_2 (D= $1.65X10^{-5}$ $cm^2.s^{-1}$ for 1 M NaOH at 25 ^{O}C), ν is the kinematic viscosity of the electrolyte (ν= 0.011 $cm^2.s^{-1}$ for 1 M NaOH), C is the concentration of dissolved oxygen (C= $8.4X10^{-4}$ $mol.cm^{-3}$ for 1M NaOH), and 0.2 is a constant applied when ω (rotating speed) is in rpm. j_d is the diffusion-limited current density and j_k is the kinetic current density[256][257].

Figure 3.73 below show the identical Koutecky-Levich (K-L) plots for the Pt-Ni-Co-Cu@CNF-5%PTP obtained at a potential of 0.3, 0.4, 0.5 and 0.6 V. Clearly, the straight lines displayed in the plot suggest the typical of first order reaction of O_2 kinetics [134][150]. From the slopes of the (K-L) plot, the number of electrons (*n*) was calculated by using equation (22) above. The calculated number of the electrons was in average of n≈ 3.5, with a highest value of n≈ 3.62 at 0.3 V. The calculated number of electrons is close to 4, indicating that the Pt-Ni-Co-Cu@CNF-5%PTP is able to catalyze ORR via the $4e^-$ pathway mechanism with nearly complete reduction of O_2 to H_2O [150][258][68]. Table 3.11 represent the Koutecky–Levich slopes and average number of electron calculated.

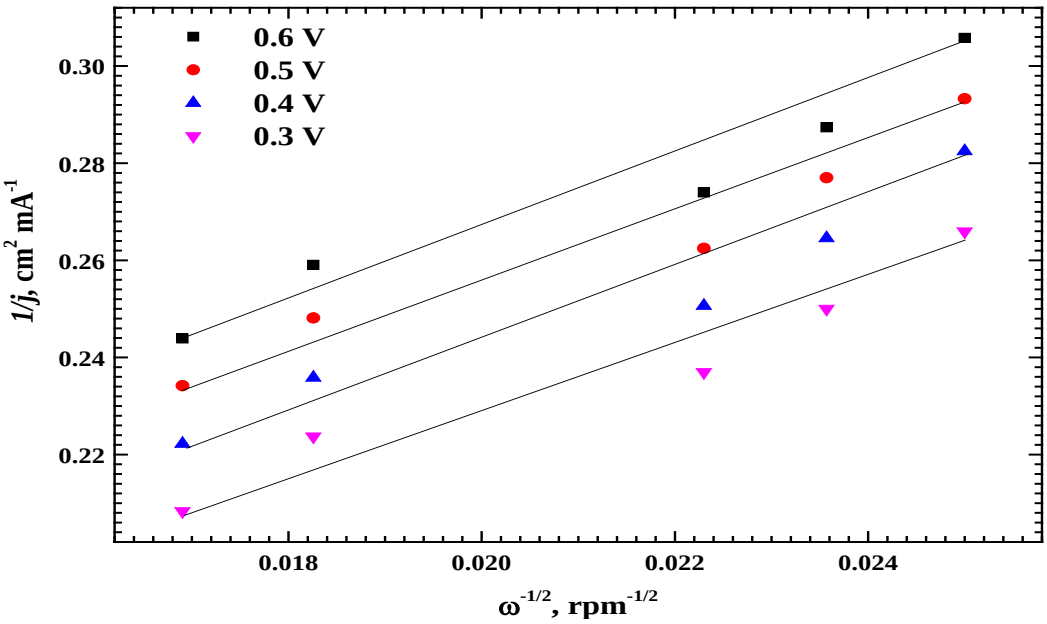

Figure 3.73. K-L plots for different potentials of ORR polarization curves recorded using an RDE in O_2-staurated 1 M NaOH electrolyte at room temperature. To obtain equidistant points, the adopted rpm rates are 1600, 1800, 2500, 3000, and 3500 rpms, respectively.

Table 3.11. *Koutecky–Levich slopes and the calculated average number of electron*

Potential, V	K-L slope	Number of electrons
0.6	6.71	3.35
0.5	6.60	3.40
0.4	6.51	3.45
0.3	6.20	3.62

3.5.3 The electrochemical impedance spectroscopy analysis (EIS)

EIS is an effective technique to characterize the electrocatalytic behavior and the interface properties of the prepared catalyst and the surface of the electrode[126][106].

The EIS analysis was performed at open circuit potential (OCP) within a frequency range of 0.1 Hz to 100 kHz with an AC amplitude of 10 mV. The analyses were done for CNF-3%S and CNF-5%PTP in absence (A) and presence (B) of oxygen.

Figure 3.74 and Figure 3.75, represent the EIS Nyquist spectra for the CNF-3%S and CNF-5%PTP, respectively in (A) absence and (B) presence of oxygen. It can be noticed that the semi-circle diameter decrease with the increase of the deposition time in presence or absence of oxygen. The semi-circle diameter is related to the "charge transfer resistance R_{ct}"[259]. The smaller semi-circles suggesting a faster charge-transfer kinetics[260][247]. Cao et al. [120] reported that the ORR process is including charge transfer process, mass transfer process, and the reaction on the catalyst. Therefore, lowering he R_{ct} means enhanced electron transfer, and thus, enhancing the ORR kinetics of the catalyst[261]. Accordingly, from the results, the activity of the (CNF-5%PTP) is higher than that of (CNF3%-S). The CNF-5%PTP semi-circles dimeter decrease from the range of 2000 $\Omega.cm^2$ after 60 seconds deposition time to 850 $\Omega.cm^2$ after 2400 seconds in presence of oxygen, while CNF-3%S show larger semi-circle diameter in the range of 4300-5400 $\Omega.cm^2$. The decrease of the charge transfer resistance increases the current density, and thus the ORR activity which was confirmed previously using the LSVs

Moreover, the EIS analysis was measured on the Pt-Ni-Co-Cu@CNF-5%PTP as represented in Figure 3.77 with different rotation speeds of 1600, 1800, 2500, 3000, and

3500 RPM. It can be noticed that the semi-circle dimeter increases with the increase on the rotation, and thus, the activity of the catalyst decrease. The resistance at 1600 RPM was 3400 $\Omega.cm^2$ while at 3500 RPM was 7000 $\Omega.cm^2$.

For more details, the EIS data was fitted using the equivalent circuit in Figure 3.76, and the fitted outcomes are shown in Table 3.12 and Table 3.13.

In the equivalent circuit, R_s, R_{ct}, and R_{po} are the solution, the charge transfer, and the pore resistances of the deposited layer respectively. Y_{po} and Y_{ct} are the constant phase elements of the electrodeposited layer and the double layer (*CPE1*) and *(CPE2)*, respectively. The non-ideal capacitance behavior of a double layer can be attributed to many reasons; e.g, surface roughness and a non-uniform (i) surface coverage, (ii) corrosion rate or (iii) current distribution. The impedance of the *CPE* is expressed by [48]:

$$Z_{CPE} = [\, Y_o^{-1} \; (j\omega)^{-n}] \qquad \textit{Equation 23}$$

where Z_{CPE} is *CPE* impedance (Ω cm^{-2}); Y_0 is the *CPE* constant, $j = (-1)^{1/2}$, which apparently is equivalent to the imaginary number; ω is the angular frequency in rad/s; and the *CPE* becomes a variable in calculating the double layer capacitance (C_{dl}) [48] because it can be measured from the equation:

$$C_{dl} = \frac{Y\,\omega^{n-1}}{sin(n(\pi/2))} \qquad \textit{Equation 24}$$

where ω is the angular frequency ($\omega = 2\pi f_{max}$), f_{max} is the frequency when the imaginary component of the impedance is maximum. The value of *n* ranges between 0 and 1. When n = 1, the *CPE* becomes equivalent to an ideal capacitor, and when n = 0, the *CPE* becomes a resistor[262].

From Table 3.12, we can notice that the R_s is independent of the deposition time, while the R_{po} increase as the deposition time increases due to the decrease of porosity when the deposited metals take place on the CNF surface[263], and the capacitance of the decreases. Moreover, the R_{ct} values decrease with the increase of the deposition time as the surface area of the catalyst increases. For the CNF-5%PTP in presence of oxygen, the R_{ct} is reduced from 4290 Ω.cm^2 before deposition to 1030 Ω.cm^2 after a deposition time of 2400 seconds. In addition, the capacitance of the double layer decreases from 295.6 $\times 10^{-6}$ sn Ω^{-1} to 155.5 $\times 10^{-6}$ sn Ω^{-1}.

For the Pt-Cu-Ni-Co@CNF-5%PTP from Table 3.13, we can notice that the R_{po} and R_{ct} values increase with the increase of the rotation speed, while the Y_{po} and Y_{ct} decrease. The increase of the R_{ct} of platinum-containing electrode may be due to structure change of the CNF, furthermore, the increase of platinum loading on the CNF leads platinum particles to aggregate and increase of the platinum particle size[264].

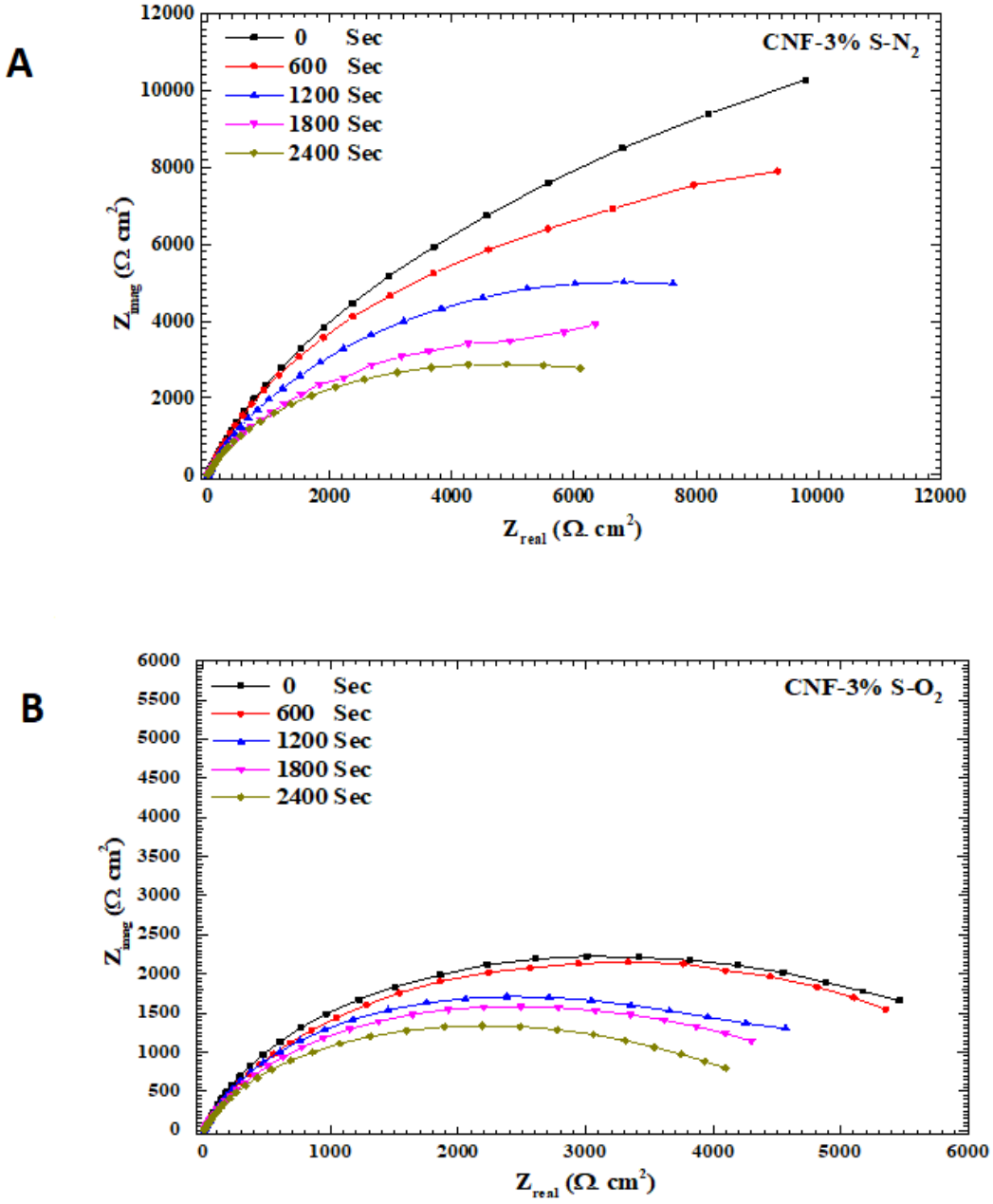

Figure 3.74. Nyquist spectra in 1 M NaOH solution in A) Nitrogen and B) Oxygen, of glassy carbon electrode with sulfur doped carbon fiber (CNF-3%S-CNF) with electrodeposited Ni-Co-Cu at different deposited time at 1600RPM.

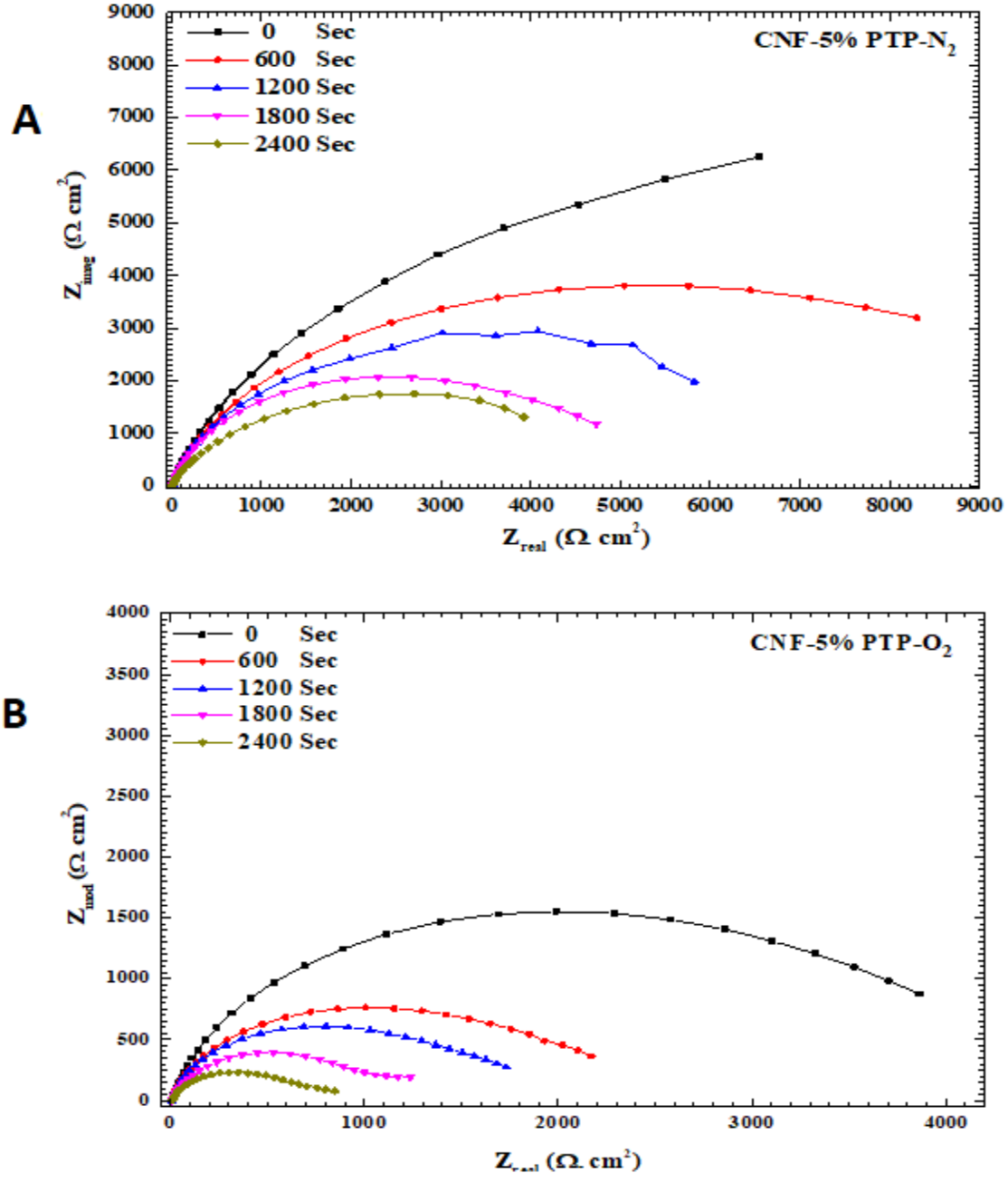

Figure 3.75. Nyquist spectra in 1 M NaOH solution in A) Nitrogen and B) Oxygen, of glassy carbon electrode with doped carbon fiber (CNF-5%PTP) with electrodeposited Ni-Co-Cu at different deposited time at 1600RPM.

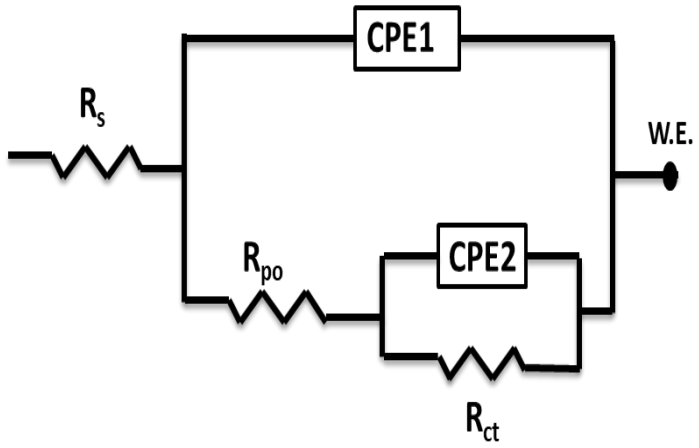

Figure 3.76. Equivalent circuits used for EIS analysis at OCP.

Table 3.12. *Dynamic EIS Parameters for CNF-5%PTP and CNF-3%S with electrodeposited Ni-Co-Cu at different deposited time at 1600RPM in presence of nitrogen and oxygen.*

Compound	**Deposition Time, Sec**	**R_s, Ω cm^2**	**R_{po}, Ω cm^2**	**Y_{po} $\times 10^{-6}$ sn Ω^{-1} cm^{-2}**	**n1**	**R_{ct}, KΩ cm^2**	**Y_{ct} $\times 10^{-6}$ sn Ω^{-1}**	**n2**	**Cdl µF**
CNF-5%	0	7.897	30.8	381.8	0.924	10.46	218.7	0.840	256.03
	600	6.380	90.42	314.1	0.599	9.65	202.2	0.845	228.57
PTP	1200	7.299	114.2	260.4	0.950	6.86	156.8	0.860	158.53
	1800	7.814	164.5	236.8	0.694	5.29	103.6	0.887	95.95

(N_2)	2400	7.938	211.5	149.2	0.841	4.36	64.25	0.891	54.97
CNF-5% PTP (O_2)	0	6.77	18.5	606.5	0.937	4.29	295.6	0.852	308.05
	600	8.14	49.27	554.2	0.647	2.61	254.1	0.870	239.49
	1200	6.48	59.32	543.7	0.877	2.11	217.4	0.871	193.70
	1800	4.48	69.72	515.7	0.589	1.38	187.7	0.849	147.61
	2400	5.97	90.42	492.8	0.738	1.03	155.0	0.864	116.11
CNF-3% S (N_2)	0	5.69	43.1	257.0	0.672	12.73	119.7	0.891	126.02
	600	6.00	128.2	211.7	0.489	10.59	82.57	0.928	81.71
	1200	4.41	169.8	194.5	0.830	9.76	76.85	0.917	74.87
	1800	8.49	253.0	161.4	0.465	8.86	59.51	0.928	56.62
	2400	6.47	341.6	105.95	0.812	7.65	67.91	0.869	61.52
CNF-3% S (O_2)	0	6.54	24.27	425.0	0.972	6.30	252.7	0.821	279.66
	600	4.34	64.8	405.7	0.679	6.05	231.0	0.823	248.24
	1200	5.87	89.0	390.3	0.962	5.72	185.7	0.832	187.97
	1800	7.18	112.2	377.0	0.557	5.29	141.9	0.852	135.00
	2400	6.25	145.8	331.4	0.839	4.87	124.6	0.856	114.55

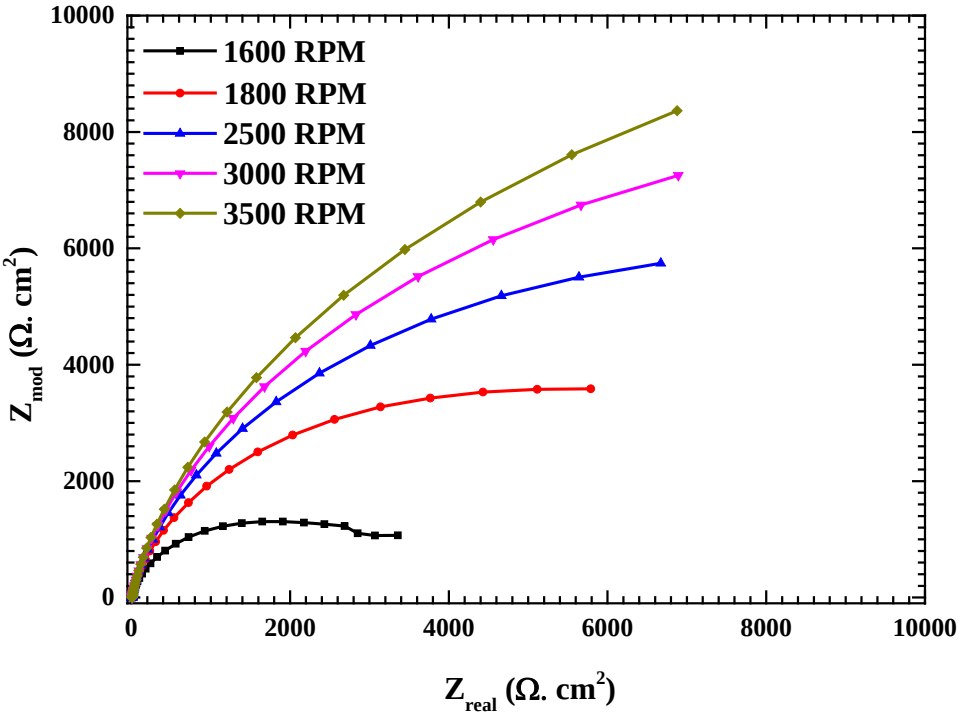

Figure 3.77. Nyquist spectra for glassy carbon in 1 M NaOH solution of sulfur doped carbon fiber (PAN+5%PTP-CNF) with electrodeposited Pt-Ni-Co-Cu at different rotation speed.

Table 3.13. *Dynamic EIS Parameters for CNF-5%PTP with electrodeposited Pt-Ni-Co-Cu at different rotation speed in presence of oxygen.*

Compound	**Rotation Speed, RPM**	**R_s, Ω cm^2**	**R_{po}, Ω cm^2**	**Y_{po} $\times 10^{-6}$ sn**	**n_1**	**R_{ct}, KΩ cm^2**	**Y_{ct} $\times 10^{-6}$ sn Ω^{-1}**	**n_2**	**Cdl µF**
Pt,CNF-5% PTP (O_2)	1600	7.27	689.3	2038	0.702	3.17	108.2	0.917	96.197
	1800	7.74	827.4	1863	0.749	8.76	96.1	0.815	92.44
	2500	6.98	1140	1531	0.842	12.82	87.3	0.862	88.88
	3000	7.32	1334	1267	0.886	16.33	72.5	0.956	73.02
	3500	7.31	1662	1022	0.884	20.12	62.8	0.772	67.29

4 Chapter 4: Conclusion and future work

In this work, we developed a novel low cost non-precious efficient catalyst based on nanostructure materials that are supported on modified carbon fibers to be used as electrodes for oxygen reduction at cathode side within PEMFCs. Electrospinning technique was used to prepare the sulfur-doped carbon nanofibers with few nanometer diameter as an effective and cheap method to prepare effective catalyst based nanocomposite material for use in fuel cell application.

The process was based on polyacrylonitrile (PAN) as the polymer material which doped with sulfur using two different sulfur sources. Pure sulfur and polythiophene were used as sulfur sources with various concentrations of sulfur to produce the nanofiber. Following this stage the fabricated nanofibers were thermally treated via two steps. The first step is stabilization in air and the second step is carbonization on the nanofibers to transfer the nanofibers to carbon nanofibers (CNFs). The produced materials were characterized by scanning electron microscopy (SEM), energy-dispersive X-ray spectroscopy (EDX), X-ray photoelectron spectroscopy (XPS), X-ray diffraction (XRD), and FTIR. In addition electrochemical characterization was carried out on the catalyst responsible for the ORR. Electrochemical deposition technique was used to load the different metals on the CNF/GCE surface.

The SEM and EDX results showed that the produced sulfur-doped CNF has continuous and beads free fibers with an average diameter of 500 nm and 1 wt. % sulfur doping. The mapping results observed a random distribution of sulfur atoms within the fibers. The chemical properties and structural of the resulting sulfur-doped CNFs demonstrated that

the sulfur doped as thiophene-like (-C-S-C-) form into the CNF networks.

The deposition for the metals on the sulfur-doped CNF surface was successfully achieved via the electrochemical deposition method. The electrochemical results exhibited better durability and excellent electrocatalytic activity towards ORR through a direct 4-electron reaction pathway mechanism. The coupling between Ni, Co, Cu and the sulfur-doped CNFs enhanced the kinetics of the ORR through the direct 4-electron reaction pathway mechanism. In terms of onset potential and half-wave potential, the addition of metals to the sulfur doped CNF shifted them in the more noble direction. The Pt free Ni-Co-Cu@CNF-5%PTP catalyst had onset potential of 0.78 V and half-wave potential of 0.67 V vs RHE, which is still good compared to the cost of the materials. The addition of Pt with a ratio of 1:1 with the metals in the Pt-Ni-Co-Cu@CNF-5%PTP electrocatalyzed the ORR performance as was proved by the positive shift in the onset potential to 0.91 V and the half-wave potential to 0.84 V vs RHE. The high electrocatalytic ORR performance of this electrode could be attributed to:

I. The high graphiticity degree of the prepared sulfur-doped CNFs structure.

II. The high surface area and the high conductivity of the CNFs.

III. Doping with sulfur creates more active sites to the CNFs and high spin density from the unpaired electrons.

IV. The metals deposition on the sulfur-doped CNFs electrocatalyzed the oxygen reduction at their interface.

Considering the low-cost and efficiency, the produced sulfur-doped CNF which have unique structure and excellent thermal and electrical properties held great promise as electrocatalyst for ORR in PEM fuel cells.

In future work, we could change the electrospinning conditions to improve the surface morphology and structure of the eletrospun PAN nanofibers. Moreover, we could increase the carbonization temperature to enhance the stability of the produced carbon nanofibers. Also, it would be great interest to involve other transition metals such as Fe and Ru and study the effect of using such metals with the S-doped carbon nanofibers towards ORR. It would be interesting to use the microwave irradiation-assisted method to synthesis of metals and deposition on the support materials. Furthermore, it is important to test the ORR activity and stability of the fabricated catalysts in both alkaline and acidic media as well. Finally, if possible, we will try test the ORR performance of the fabricated catalyst by using real PEM fuel cell.

REFERENCES

[1] A. K. Hussein, “Applications of nanotechnology in renewable energies - A comprehensive overview and understanding,” *Renew. Sustain. Energy Rev.*, vol. 42, pp. 460–476, 2015.

[2] BP, “BP Statistical Review of World Energy 2017,” *Br. Pet.*, no. 66, pp. 1–52, 2017.

[3] P. Kurzeil, “Fuel cells.,” *Elsevier*, pp. 579–595, 2009.

[4] S. Horizontal and V. T. Operation, “1 . Introduction,” pp. 1–16, 2008.

[5] R. W. Asplund, “Fuel Cells,” pp. 147–162, 2008.

[6] G. Kaur, *Solid oxide fuel cell components: Interfacial compatibility of SOFC glass seals*. 2015.

[7] S. Kartha and P. Grimes, “Fuel Cells for Energy Conversion,” *Physic Today*, vol. 13, pp. 54–61, 2012.

[8] Y. Wang, K. S. Chen, J. Mishler, S. C. Cho, and X. C. Adroher, “A review of polymer electrolyte membrane fuel cells: Technology, applications, and needs on fundamental research,” *Appl. Energy*, vol. 88, no. 4, pp. 981–1007, 2011.

[9] H. S. Han, C. Cho, S. Y. Kim, and J. M. Hyun, “Performance evaluation of a polymer electrolyte membrane fuel cell system for powering portable freezer,” *Appl. Energy*, vol. 105, pp. 125–137, 2013.

[10] J. Larminie and A. Dicks, *Fuel cell systems explained*. 2003.

[11] E. G. And and D. M SCHULZE, *Alkaline fuel cells*. Woodhead Publishing Limited, 2008.

[12] T. F. FULLER and K. G. GALLAGHER, *Phosphoric acid fuel cells 5.1*.

Woodhead Publishing Limited, 2008.

[13] S. McPHAIL, E. SIMONETTI, and A. MORENO, *Molten carbonate fuel cells*, vol. 8, no. 5. Woodhead Publishing Limited, 2008.

[14] K. Huang, *Solid oxide fuel cells*. Woodhead Publishing Limited, 2008.

[15] Y. Wang, J. Jin, S. Yang, G. Li, and J. Qiao, "Electrochimica Acta Highly active and stable platinum catalyst supported on porous carbon nano fi bers for improved performance of PEMFC," *Electrochim. Acta*, vol. 177, pp. 181–189, 2015.

[16] I. Maciejasz, "Synthesis and characterisation of nanofibre supports for platinum as electrodes for polymer electrolyte fuel cells Iuliia Maciejasz Délivré par l ' Université Montpellier 2 Sciences et Techniques du Languedoc Préparée au sein de l ' école doctorale," 2015.

[17] Y. J. Wang, B. Fang, H. Li, X. T. Bi, and H. Wang, "Progress in modified carbon support materials for Pt and Pt-alloy cathode catalysts in polymer electrolyte membrane fuel cells," *Prog. Mater. Sci.*, vol. 82, pp. 445–498, 2016.

[18] O. T. Holton and J. W. Stevenson, "The Role of Platinum in Proton Exchange Membrane Fuel Cells Evaluation of platinum's unique properties for use in both the anode and cathode of a proton exchange membrane fuel cell," *@BULLETPlatinum Met. Rev*, vol. 57, no. 4, pp. 259–271, 2013.

[19] L. Dai, Y. Xue, L. Qu, H.-J. Choi, and J.-B. Baek, "Metal-Free Catalysts for Oxygen Reduction Reaction," *Chem. Rev.*, vol. 115, no. 11, pp. 4823–4892, 2015.

[20] W. Sheng, H. A. Gasteiger, and Y. Shao-Horn, "Hydrogen Oxidation and Evolution Reaction Kinetics on Platinum: Acid vs Alkaline Electrolytes," *J. Electrochem. Soc.*, vol. 157, no. 11, p. B1529, 2010.

[21] S. Lu and Z. Zhuang, “Electrocatalysts for hydrogen oxidation and evolution reactions,” *Sci. China Mater.*, vol. 59, no. 3, pp. 217–238, 2016.

[22] S. Energy and F. Pemfcs, *Polymer electrolyte membrane fuel cells*, no. 3. Woodhead Publishing Limited.

[23] M. G. Santarelli and M. F. Torchio, “Experimental analysis of the effects of the operating variables on the performance of a single PEMFC,” *Energy Convers. Manag.*, vol. 48, no. 1, pp. 40–51, 2007.

[24] “A review on modelling of high temperature proton exchange membrane fuel cells (HT-PEMFCs),” *Int. J. Hydrogen Energy*, vol. 42, no. 5, pp. 3142–3165, Feb. 2017.

[25] “Porous polybenzimidazole membranes doped with phosphoric acid: Preparation and application in high temperature PEM fuel cells,” *Int. J. Hydrogen Energy*, Jul. 2017.

[26] “Proton exchange membrane from tetrazole-based poly (phthalazinone ether sulfone ketone) for high-temperature fuel cells,” *Int. J. Hydrogen Energy*, vol. 41, no. 28, pp. 12337–12346, Jul. 2016.

[27] J. Gao, J. Liu, W. Liu, Y. Xin, Y. Yin, and Z. Zou, “Proton Exchange Membrane Fuel Cell Working at Elevated Temperature with Ionic Liquid as Electrolyte,” *Int. J. Electrochem. Sci.*, vol. 6, no. 2011, pp. 6115–6122, 2011.

[28] J. Zhang, H. Zhang, J. Wu, and J. Zhang, “Fuel Cell Open Circuit Voltage,” *Pem Fuel Cell Test. Diagnosis*, pp. 187–200, 2013.

[29] J. Zhang, H. Zhang, J. Wu, and J. Zhang, *Design and Fabrication of PEM Fuel Cell MEA, Single Cell, and Stack*. 2013.

[30] M. A. R. S. Al-Baghdadi, “A parametric study of the natural vibration and mode shapes of PEM fuel cell stacks,” *Int. J. ENERGY Environ.*, vol. 7, no. 1, pp. 1–22, 2016.

[31] C. Kunusch, P. Puleston, and M. Mayosky, “Sliding-Mode Control of PEM Fuel Cells,” 2012.

[32] J. Zhang, J. Wu, H. Zhang, and J. Zhang, *PEM Fuel Cell Fundamentals*. 2013.

[33] C. Catalysis, “Handbook of Polymer Nanocomposites. Processing, Performance and Application,” pp. 361–390, 2015.

[34] M. Gasik, *Introduction: materials challenges in fuel cells*. Woodhead Publishing Limited, 2008.

[35] R. Othman, A. L. Dicks, and Z. Zhu, “Non precious metal catalysts for the PEM fuel cell cathode,” *Int. J. Hydrogen Energy*, vol. 37, no. 1, pp. 357–372, 2011.

[36] Samaneh Shahgaldi and J. Hamelin, “Improved carbon nanostructures as a novel catalyst support in the cathode side of PEMFC: a critical review,” *Carbon N. Y.*, vol. 94, pp. 705–728, Nov. 2015.

[37] M. V. Martínez-Huerta and M. J. Lázaro, “Electrocatalysts for low temperature fuel cells,” *Catal. Today*, vol. 285, pp. 3–12, 2017.

[38] Y. Sun, C. Li, and G. Shi, “Nanoporous nitrogen doped carbon modified graphene as electrocatalyst for oxygen reduction reaction,” *J. Mater. Chem.*, vol. 22, no. 25, p. 12810, 2012.

[39] J. Wu and H. Yang, “Platinum-based oxygen reduction electrocatalysts,” *Acc. Chem. Res.*, vol. 46, no. 8, pp. 1848–1857, 2013.

[40] S. Sui, X. Wang, X. Zhou, and Y. Su, “A comprehensive review of Pt

electrocatalysts for the oxygen reduction reaction : Nanostructure , activity , mechanism and carbon support in PEM fuel," pp. 1808–1825, 2017.

[41] J. K. Nørskov, J. Rossmeisl, A. Logadottir, L. Lindqvist, J. R. Kitchin, T. Bligaard, and H. Jónsson, "Origin of the overpotential for oxygen reduction at a fuel-cell cathode," *J. Phys. Chem. B*, vol. 108, no. 46, pp. 17886–17892, 2004.

[42] Q. Wei, X. Tong, G. Zhang, J. Qiao, Q. Gong, and S. Sun, "Nitrogen-Doped Carbon Nanotube and Graphene Materials for Oxygen Reduction Reactions," *Catalysts*, vol. 5, no. 3, pp. 1574–1602, 2015.

[43] H. Lv, D. Li, D. Strmcnik, A. P. Paulikas, N. M. Markovic, and V. R. Stamenkovic, "Recent advances in the design of tailored nanomaterials for efficient oxygen reduction reaction," *Nano Energy*, vol. 29, pp. 149–165, 2016.

[44] B. Zhang, F. Kang, J. Tarascon, and J. Kim, "Progress in Materials Science Recent advances in electrospun carbon nanofibers and their application in electrochemical energy storage," *Prog. Mater. Sci.*, vol. 76, pp. 319–380, 2016.

[45] M. Yaldagard, "Carbonaceous Nanostructured Support Materials for Low Temperature Fuel Cell Electrocatalysts—A Review," *World J. Nano Sci. Eng.*, vol. 2013, no. December, pp. 121–153, 2013.

[46] D. S. Su and R. Schlögl, "Nanostructured carbon and carbon nanocomposites for electrochemical energy storage applications," *ChemSusChem*, vol. 3, no. 2, pp. 136–168, 2010.

[47] B. Zhang, Y. Yu, Y. Liu, Z.-D. Huang, Y. He, and J.-K. Kim, "Percolation threshold of graphene nanosheets as conductive additives in Li4Ti5O12 anodes of Li-ion batteries," *Nanoscale*, vol. 5, no. 5, pp. 2100–2106, 2013.

[48] X. Li, F. Kang, X. Bai, and W. Shen, “A novel network composite cathode of LiFePO4/multiwalled carbon nanotubes with high rate capability for lithium ion batteries,” *Electrochem. commun.*, vol. 9, no. 4, pp. 663–666, 2007.

[49] Z. Wen, Q. Wang, Q. Zhang, and J. Li, “In situ growth of mesoporous SnO2 on multiwalled carbon nanotubes: A novel composite with porous-tube structure as anode for lithium batteries,” *Adv. Funct. Mater.*, vol. 17, no. 15, pp. 2772–2778, 2007.

[50] S. Paek, E. Yoo, and I. Honma, “Enhanced Cyclic Performance and Lithium Storage Capacity of SnO 2 / Graphene Nanoporous Electrodes with,” *Nano Lett.*, vol. 9, no. 1, pp. 72–75, 2009.

[51] G. Y. Zheng, Y. Yang, J. J. Cha, S. S. Hong, and Y. Cui, “Hollow Carbon Nanofiber-Encapsulated Sulfur Cathodes for High Specific Capacity Rechargeable Lithium Batteries,” *Nano Lett.*, vol. 11, no. 10, pp. 4462–4467, 2011.

[52] E. Antolini, “Carbon supports for low-temperature fuel cell catalysts,” *Appl. Catal. B Environ.*, vol. 88, no. 1–2, pp. 1–24, 2009.

[53] Y. J. Wang, N. Zhao, B. Fang, H. Li, X. T. Bi, and H. Wang, “Carbon-Supported Pt-Based Alloy Electrocatalysts for the Oxygen Reduction Reaction in Polymer Electrolyte Membrane Fuel Cells: Particle Size, Shape, and Composition Manipulation and Their Impact to Activity,” *Chem. Rev.*, vol. 115, no. 9, pp. 3433–3467, 2015.

[54] S. TANG, G. SUN, J. QI, S. SUN, J. GUO, Q. XIN, and G. M. HAARBERG, “Review of New Carbon Materials as Catalyst Supports in Direct Alcohol Fuel Cells,” *Chinese J. Catal.*, vol. 31, no. 1, pp. 12–17, 2010.

[55] Y. J. Wang, D. P. Wilkinson, and J. Zhang, “Noncarbon support materials for polymer electrolyte membrane fuel cell electrocatalysts,” *Chem. Rev.*, vol. 111, no. 12, pp. 7625–7651, 2011.

[56] G. A. Rimbu, C. L. Jackson, and K. Scott, “Platinum / carbon / polyaniline based nanocomposites as catalysts for fuel cell technology,” *J. Optoelectron. Adv. Mater.*, vol. 8, no. 2, pp. 611–616, 2006.

[57] J. P. Konell, J. A. King, and I. Miskioglu, “Synergistic Effects of Carbon Fillers in Nylon 6 , 6 and Polycarbonate Based Resins,” vol. 25, no. 2, 2004.

[58] J. Tang, J. Liu, N. L. Torad, T. Kimura, and Y. Yamauchi, “Tailored design of functional nanoporous carbon materials toward fuel cell applications,” *Nano Today*, vol. 9, no. 3, pp. 305–323, 2014.

[59] Z. Zhang, J. Liu, J. Gu, L. Su, and L. Cheng, “An overview of metal oxide materials as electrocatalysts and supports for polymer electrolyte fuel cells,” *Energy Environ. Sci.*, vol. 7, no. 8, pp. 2535–2558, 2014.

[60] H. Lv and S. Mu, “Nano-ceramic support materials for low temperature fuel cell catalysts,” *Nanoscale*, vol. 6, no. 10, pp. 5063–5074, 2014.

[61] E. Antolini, “Composite materials: An emerging class of fuel cell catalyst supports,” *Appl. Catal. B Environ.*, vol. 100, no. 3–4, pp. 413–426, 2010.

[62] X. Yu and S. Ye, “Recent advances in activity and durability enhancement of Pt/C catalytic cathode in PEMFC. Part II: Degradation mechanism and durability enhancement of carbon supported platinum catalyst,” *J. Power Sources*, vol. 172, no. 1, pp. 145–154, 2007.

[63] Y. Zhang, S. Chen, Y. Wang, W. Ding, R. Wu, L. Li, X. Qi, and Z. Wei, “Study of

the degradation mechanisms of carbon-supported platinum fuel cells catalyst via different accelerated stress test," *J. Power Sources*, vol. 273, pp. 62–69, 2015.

[64] J. Speder, A. Zana, I. Spanos, J. J. K. Kirkensgaard, K. Mortensen, M. Hanzlik, and M. Arenz, "Comparative degradation study of carbon supported proton exchange membrane fuel cell electrocatalysts - The influence of the platinum to carbon ratio on the degradation rate," *J. Power Sources*, vol. 261, pp. 14–22, 2014.

[65] J. Wang, G. Yin, Y. Shao, S. Zhang, Z. Wang, and Y. Gao, "Effect of carbon black support corrosion on the durability of Pt/C catalyst," *J. Power Sources*, vol. 171, no. 2, pp. 331–339, 2007.

[66] W. Li and A. M. Lane, "Electrochemistry Communications Investigation of Pt catalytic effects on carbon support corrosion of the cathode catalyst in PEM fuel cells using DEMS spectra," *Electrochem. commun.*, vol. 11, no. 6, pp. 1187–1190, 2009.

[67] P. T. Yu, W. Gu, J. Zhang, R. Makharia, F. T. Wagner, and H. A. Gasteiger, "Carbon-support requirements for highly durable fuel cell operation," *Polym. Electrolyte Fuel Cell Durab.*, pp. 29–53, 2009.

[68] K. Jukk, N. Alexeyeva, A. Sarapuu, P. Ritslaid, J. Kozlova, V. Sammelselg, and K. Tammeveski, "Electroreduction of oxygen on sputter-deposited Pd nanolayers on multi-walled carbon nanotubes," *Int. J. Hydrogen Energy*, vol. 38, no. 9, pp. 3614–3620, 2013.

[69] N. Mansor, T. S. Miller, I. Dedigama, A. B. Jorge, J. Jia, V. Brázdová, C. Mattevi, C. Gibbs, D. Hodgson, P. R. Shearing, C. A. Howard, F. Corà, M. Shaffer, D. J. L. Brett, and P. F. McMillan, "Graphitic Carbon Nitride as a Catalyst Support in Fuel

Cells and Electrolyzers," *Electrochim. Acta*, vol. 222, pp. 44–57, 2016.

[70] S. Basri, S. K. Kamarudin, W. R. W. Daud, and Z. Yaakub, "Nanocatalyst for direct methanol fuel cell (DMFC)," *Int. J. Hydrogen Energy*, vol. 35, no. 15, pp. 7957–7970, 2010.

[71] H. S. Thiam, W. R. W. Daud, S. K. Kamarudin, A. B. Mohammad, A. A. H. Kadhum, K. S. Loh, and E. H. Majlan, "Overview on nanostructured membrane in fuel cell applications," *Int. J. Hydrogen Energy*, vol. 36, no. 4, pp. 3187–3205, 2011.

[72] M. H. Seo, S. M. Choi, H. J. Kim, and W. B. Kim, "The graphene-supported Pd and Pt catalysts for highly active oxygen reduction reaction in an alkaline condition," *Electrochem. commun.*, vol. 13, no. 2, pp. 182–185, 2011.

[73] J. Lee, K. Kim, W. I. Park, B. H. Kim, J. H. Park, T. H. Kim, S. Bong, C. H. Kim, G. Chae, M. Jun, Y. Hwang, Y. S. Jung, and S. Jeon, "Uniform graphene quantum dots patterned from self-assembled silica nanodots," *Nano Lett.*, vol. 12, no. 12, pp. 6078–6083, 2012.

[74] L. Li, L. Hu, J. Li, and Z. Wei, "Enhanced stability of Pt nanoparticle electrocatalysts for fuel cells," *Nano Res.*, vol. 8, no. 2, pp. 418–440, 2015.

[75] S. Sharma and B. G. Pollet, "Support materials for PEMFC and DMFC electrocatalysts - A review," *J. Power Sources*, vol. 208, pp. 96–119, 2012.

[76] J. Huang, N. Zhu, T. Yang, T. Zhang, P. Wu, and Z. Dang, "Nickel oxide and carbon nanotube composite (NiO/CNT) as a novel cathode non-precious metal catalyst in microbial fuel cells," *Biosens. Bioelectron.*, vol. 72, pp. 332–339, 2015.

[77] A. Marinkas, R. Hempelmann, A. Heinzel, V. Peinecke, I. Radev, and H. Natter,

"Enhanced stability of multilayer graphene-supported catalysts for polymer electrolyte membrane fuel cell cathodes," *J. Power Sources*, vol. 295, pp. 79–91, 2015.

[78] A. Iwan, M. Malinowski, and G. Pasciak, "Polymer fuel cell components modi fi ed by graphene : Electrodes , electrolytes and bipolar plates," vol. 49, pp. 954–967, 2015.

[79] J.-S. Zheng, X.-S. Zhang, P. Li, J. Zhu, X.-G. Zhou, and W.-K. Yuan, "Effect of carbon nanofiber microstructure on oxygen reduction activity of supported palladium electrocatalyst," *Electrochem. commun.*, vol. 9, no. 5, pp. 895–900, 2007.

[80] A. M. Al-Enizi, M. A. Ghanem, A. A. El-Zatahry, and S. S. Al-Deyab, "Nickel oxide/nitrogen doped carbon nanofibers catalyst for methanol oxidation in alkaline media," *Electrochim. Acta*, vol. 137, pp. 774–780, 2014.

[81] A. M. Al-Enizi, A. A. Elzatahry, A. M. Abdullah, M. A. Almaadeed, J. Wang, D. Zhao, and S. Al-Deyab, "Synthesis and electrochemical properties of nickel oxide/carbon nanofiber composites," *Carbon N. Y.*, vol. 71, pp. 276–283, 2014.

[82] L. Feng, Y. Chen, and L. Chen, "Easy-to-operate and low-temperature synthesis of gram-scale nitrogen-doped graphene and its application as cathode catalyst in microbial fuel cells," *ACS Nano*, vol. 5, no. 12, pp. 9611–9618, 2011.

[83] L. Feng, L. Yang, Z. Huang, J. Luo, M. Li, D. Wang, and Y. Chen, "Enhancing Electrocatalytic Oxygen Reduction on Nitrogen-Doped Graphene by Active Sites Implantation," *Sci. Rep.*, vol. 3, no. 1, p. 3306, 2013.

[84] Z.-J. Lu, S.-J. Bao, Y.-T. Gou, C.-J. Cai, C.-C. Ji, M.-W. Xu, J. Song, and R.

Wang, “Nitrogen-doped reduced-graphene oxide as an efficient metal-free electrocatalyst for oxygen reduction in fuel cells,” *RSC Adv.*, vol. 3, no. 12, p. 3990, 2013.

[85] Z. Yan, M. Wang, B. Huang, R. Liu, and J. Zhao, “Graphene supported Pt-Co alloy nanoparticles as cathode catalyst for microbial fuel cells,” *Int. J. Electrochem. Sci.*, vol. 8, no. 1, pp. 149–158, 2013.

[86] J.-H. LEE, G.-S. KIM, Y.-M. CHOI, W. IL PARK, J. A. ROGERS, and U. PAIK, “Comparison of multiwalled carbon nanotubes and carbon black as percolative paths in aqueous-based natural graphite negative electrodes with high-rate capability for lithium-ion batteries,” *J. Power Sources*, vol. 184, no. 1, pp. 308–311.

[87] L. Gan, R. Lv, H. Du, B. Li, and F. Kang, “High loading of Pt-Ru nanocatalysts by pentagon defects introduced in a bamboo-shaped carbon nanotube support for high performance anode of direct methanol fuel cells,” *Electrochem. commun.*, vol. 11, no. 2, pp. 355–358, 2009.

[88] C. Yu, C. Masarapu, J. Rong, B. Wei, and H. Jiang, “Stretchable supercapacitors based on buckled single-walled carbon nanotube macrofilms,” *Adv. Mater.*, vol. 21, no. 47, pp. 4793–4797, 2009.

[89] G. Q. Zhang, J. P. Zheng, R. Liang, C. Zhang, B. Wang, M. Hendrickson, and E. J. Plichta, “Lithium–Air Batteries Using SWNT/CNF Buckypapers as Air Electrodes,” *J. Electrochem. Soc.*, vol. 157, no. 8, p. A953, 2010.

[90] L. Qie, W. M. Chen, Z. H. Wang, Q. G. Shao, X. Li, L. X. Yuan, X. L. Hu, W. X. Zhang, and Y. H. Huang, “Nitrogen-doped porous carbon nanofiber webs as

anodes for lithium ion batteries with a superhigh capacity and rate capability," *Adv. Mater.*, vol. 24, no. 15, pp. 2047–2050, 2012.

[91] A. Peigney, C. Laurent, E. Flahaut, R. R. Bacsa, and A. Rousset, "Specific surface area of carbon nanotubes and bundles of carbon nanotubes," *Carbon N. Y.*, vol. 39, no. 4, pp. 507–514, 2001.

[92] P. C. Ma, N. A. Siddiqui, G. Marom, and J. K. Kim, "Dispersion and functionalization of carbon nanotubes for polymer-based nanocomposites: A review," *Compos. Part A Appl. Sci. Manuf.*, vol. 41, no. 10, pp. 1345–1367, 2010.

[93] N. K. Mahanta, A. R. Abramson, M. L. Lake, D. J. Burton, J. C. Chang, H. K. Mayer, and J. L. Ravine, "Thermal conductivity of carbon nanofiber mats," *Carbon N. Y.*, vol. 48, no. 15, pp. 4457–4465, 2010.

[94] A. K. Geim and K. S. Novoselov, "The rise of graphene," *Nat. Mater.*, vol. 6, no. 3, pp. 183–191, 2007.

[95] Y. Zhu, S. Murali, W. Cai, X. Li, J. W. Suk, J. R. Potts, and R. S. Ruoff, "Graphene and graphene oxide: Synthesis, properties, and applications," *Adv. Mater.*, vol. 22, no. 35, pp. 3906–3924, 2010.

[96] E. Mayhew and V. Prakash, "Thermal conductivity of individual carbon nanofibers," *Carbon N. Y.*, vol. 62, pp. 493–500, 2013.

[97] "Bansal, R. C., Donnet, J. B., & Wang, M. J. (Eds.). (1993). Carbon black: Science and technology. Marcel Dekker."

[98] B. Zhang, F. Kang, J. M. Tarascon, and J. K. Kim, "Recent advances in electrospun carbon nanofibers and their application in electrochemical energy storage," *Prog. Mater. Sci.*, vol. 76, pp. 319–380, 2016.

[99] V. Thavasi, G. Singh, S. Ramakrishna, B. Liu, A. Kumar, S. Ramakrishna, M. Khayet, C. M. Lukehart, G. A. Olah, and D. H. Reneker, "Electrospun nanofibers in energy and environmental applications," *Energy Environ. Sci.*, vol. 1, no. 2, p. 205, 2008.

[100] S. M. Andersen, M. Borghei, P. Lund, Y. R. Elina, A. Pasanen, E. Kauppinen, V. Ruiz, P. Kauranen, and E. M. Skou, "Durability of carbon nanofiber (CNF) & carbon nanotube (CNT) as catalyst support for Proton Exchange Membrane Fuel Cells," *Solid State Ionics*, vol. 231, pp. 94–101, 2013.

[101] J. H. Park, Y. W. Ju, S. H. Park, H. R. Jung, K. S. Yang, and W. J. Lee, "Effects of electrospun polyacrylonitrile-based carbon nanofibers as catalyst support in PEMFC," *J. Appl. Electrochem.*, vol. 39, no. 8, pp. 1229–1236, 2009.

[102] Y. Wang, K. S. Chen, J. Mishler, S. C. Cho, and X. C. Adroher, "A review of polymer electrolyte membrane fuel cells: Technology, applications, and needs on fundamental research," *Appl. Energy*, vol. 88, no. 4, pp. 981–1007, 2011.

[103] W. Li, Q. Xin, and Y. Yan, "Nanostructured Pt-Fe/C cathode catalysts for direct methanol fuel cell: The effect of catalyst composition," *Int. J. Hydrogen Energy*, vol. 35, no. 6, pp. 2530–2538, 2010.

[104] P. Mukherjee, J. Bagchi, S. Dutta, and S. K. Bhattacharya, "The nickel supported platinum catalyst for anodic oxidation of ethanol in alkaline medium," *Appl. Catal. A Gen.*, vol. 506, pp. 220–227, 2015.

[105] D. P. Chem and A. C. Soc, "Oxygen Reduction at Pt(0.65)Cr(0.3)s, Pt(0.2)Cr(0.8) and Roughened Platinum," *J. Electrochem. Soc.*, vol. 135, no. 6, pp. 1431–1436, 1988.

[106] R. M. A. Hameed, “Microwave irradiated Ni-MnOx/C as an electrocatalyst for methanol oxidation in KOH solution for fuel cell application,” *Appl. Surf. Sci.*, vol. 357, pp. 417–428, 2015.

[107] W. Li and P. Haldar, “Supportless PdFe nanorods as highly active electrocatalyst for proton exchange membrane fuel cell,” *Electrochem. commun.*, vol. 11, no. 6, pp. 1195–1198, 2009.

[108] F. Bensebaa, A. A. Farah, D. Wang, C. Bock, X. Du, J. Kung, and Y. Le Page, “Microwave synthesis of polymer-embedded Pt-Ru catalyst for direct methanol fuel cell.,” *J. Phys. Chem. B*, vol. 109, no. 32, pp. 15339–15344, 2005.

[109] S. Dutta, C. Ray, S. Sarkar, A. Roy, R. Sahoo, and T. Pal, “Facile Synthesis of Bimetallic Au-Pt, Pd-Pt, and Au-Pd Nanostructures: Enhanced Catalytic Performance of Pd-Pt Analogue towards Fuel Cell Application and Electrochemical Sensing,” *Electrochim. Acta*, vol. 180, pp. 1075–1084, 2015.

[110] M. Shao, Q. Chang, J.-P. Dodelet, and R. Chenitz, “Recent Advances in Electrocatalysts for Oxygen Reduction Reaction,” *Chem. Rev.*, vol. 116, no. 6, pp. 3594–3657, 2016.

[111] a. Smirnova, *Novel fuel cells and materials*. Woodhead Publishing Limited, 2008.

[112] A. Hamza, S. El-Refaei, A. Elzatahry, and A. Abdullah, “High Electrocatalytic Performance of CuCoNi@CNTs Modified Glassy Carbon Electrode towards Methanol Oxidation in Alkaline Medium,” *Appl. Sci.*, vol. 7, no. 1, p. 64, 2017.

[113] L. Liu and E. Pippel, “Low-platinum-content quaternary PtCuCoNi nanotubes with markedly enhanced oxygen reduction activity,” *Angew. Chemie - Int. Ed.*, vol. 50, no. 12, pp. 2729–2733, 2011.

[114] C. Wang, W. Li, X. Lu, S. Xie, F. Xiao, P. Liu, and Y. Tong, “Facile synthesis of porous 3D CoNiCu nano-network structure and their activity towards hydrogen evolution reaction,” *Int. J. Hydrogen Energy*, vol. 37, no. 24, pp. 18688–18693, 2012.

[115] T. Rostami, M. Jafarian, S. Miandari, M. G. Mahjani, and F. Gobal, “Synergistic effect of cobalt and copper on a nickel-based modified graphite electrode during methanol electro-oxidation in NaOH solution,” *Cuihua Xuebao/Chinese J. Catal.*, vol. 36, no. 11, pp. 1867–1874, 2015.

[116] H. Liu, C. Song, L. Zhang, J. Zhang, H. Wang, and D. P. Wilkinson, “A review of anode catalysis in the direct methanol fuel cell,” *J. Power Sources*, vol. 155, no. 2, pp. 95–110, 2006.

[117] B. Molero-Sánchez, J. Prado-Gonjal, D. Ávila-Brande, V. Birss, and E. Morán, “Microwave-assisted synthesis and characterization of new cathodic material for solid oxide fuel cells: La0.3Ca0.7Fe0.7Cr0.3O3−δ,” *Ceram. Int.*, vol. 41, no. 7, pp. 8411–8416, 2015.

[118] C.-T. Hsieh, J.-L. Gu, Y.-C. Chen, and D.-Y. Tzou, “Pulse microwave synthesis of palladium catalysts on graphene electrodes for proton exchange membrane fuel cells,” *Electrochim. Acta*, vol. 98, pp. 39–47, 2013.

[119] A. Z. Al-Hakemy, A. B. A. A. Nassr, A. H. Naggar, M. S. Elnouby, H. M. A. E. F. Soliman, and M. A. Taher, “Electrodeposited cobalt oxide nanoparticles modified carbon nanotubes as a non-precious catalyst electrode for oxygen reduction reaction,” *J. Appl. Electrochem.*, vol. 47, no. 2, pp. 183–195, 2017.

[120] F. Cao, Z. Zang, S. Sun, X. Sun, X. Li, and T. Liu, “RSC Advances The in fl uence

of deposited potential on the ORR activity of Pt catalysts on glassy carbon electrode," *RSC Adv.*, vol. 7, pp. 25429–25436, 2017.

[121] S. B. Han, D. H. Kwak, Y. W. Lee, S. J. Kim, J. Y. Lee, S. Lee, H. J. Kwon, and K. W. Park, "Electrodeposited nanoporous PtY alloy electrodes with enhanced oxygen reduction reaction," *Int. J. Electrochem. Sci.*, vol. 11, no. 5, pp. 3803–3814, 2016.

[122] Y. I. Kim, D. Soundararajan, C. W. Park, S. H. Kim, J. H. Park, and J. M. Ko, "Electrocatalytic Properties of Carbon Nanofiber Web – Supported Nanocrystalline Pt Catalyst as Applied to Direct Methanol Fuel Cell," *Int. J. Electrochem. Sci.*, vol. 4, pp. 1548–1559, 2009.

[123] B. Li and S. H. Chan, "PtFeNi tri-metallic alloy nanoparticles as electrocatalyst for oxygen reduction reaction in proton exchange membrane fuel cells with ultra-low Pt loading," *Int. J. Hydrogen Energy*, vol. 38, no. 8, pp. 3338–3345, 2013.

[124] L. Wang, Y. Zheng, X. Lu, Z. Li, L. Sun, and Y. Song, "Dendritic copper-cobalt nanostructures/reduced graphene oxide-chitosan modified glassy carbon electrode for glucose sensing," *Sensors Actuators, B Chem.*, vol. 195, pp. 1–7, 2014.

[125] M. Yang, X. Jin, and Q. Huang, "Electrochemical glucose oxidation on dendritic cuprous oxide film fabricated by PSS-assisted electrochemical deposition," *Solid State Sci.*, vol. 13, no. 2, pp. 427–433, 2011.

[126] L. P. Xia, P. Guo, Y. Wang, S. Q. Ding, and J. B. He, "Multi-laminated copper nanoparticles deposited on conductive substrates for electrocatalytic oxidation of methanol in alkaline electrolytes," *J. Power Sources*, vol. 262, pp. 232–238, 2014.

[127] L. A. Hutton, M. Vidotti, A. N. Patel, M. E. Newton, P. R. Unwin, and J. V.

MacPherson, “Electrodeposition of nickel hydroxide nanoparticles on boron-doped diamond electrodes for oxidative electrocatalysis,” *J. Phys. Chem. C*, vol. 115, no. 5, pp. 1649–1658, 2011.

[128] M. Li, Y. Lei, N. Sheng, and T. Ohtsuka, “Preparation of low-platinum-content platinum-nickel, platinum-cobalt binary alloy and platinum-nickel-cobalt ternary alloy catalysts for oxygen reduction reaction in polymer electrolyte fuel cells,” *J. Power Sources*, vol. 294, pp. 420–429, 2015.

[129] Z. Liu, Q. Shi, F. Peng, H. Wang, H. Yu, J. Li, and X. Wei, “Enhanced methanol oxidation activity of Pt catalyst supported on the phosphorus-doped multiwalled carbon nanotubes in alkaline medium,” *Catal. Commun.*, vol. 22, no. 3, pp. 34–38, 2012.

[130] Z. Liu, J. Qu, X. Fu, Q. Wang, G. Zhong, and F. Peng, “Low Pt content catalyst supported on nitrogen and phosphorus-codoped carbon nanotubes for electrocatalytic O2 reaction in acidic medium,” *Mater. Lett.*, vol. 142, pp. 115–118, 2015.

[131] Y. Zhou, K. Neyerlin, T. S. Olson, S. Pylypenko, J. Bult, H. N. Dinh, T. Gennett, Z. Shao, and R. O’Hayre, “Enhancement of Pt and Pt-alloy fuel cell catalyst activity and durability via nitrogen-modified carbon supports,” *Energy Environ. Sci.*, vol. 3, no. 10, pp. 1437–1446, 2010.

[132] D. Yu, E. Nagelli, F. Du, and L. Dai, “Metal-free carbon nanomaterials become more active than metal catalysts and last longer,” *J. Phys. Chem. Lett.*, vol. 1, no. 14, pp. 2165–2173, 2010.

[133] W. J. Lee, U. N. Maiti, J. M. Lee, J. Lim, T. H. Han, and S. O. Kim, “Nitrogen-

doped carbon nanotubes and graphene composite structures for energy and catalytic applications," *Chem. Commun.*, vol. 50, no. 52, p. 6818, 2014.

[134] G. Panomsuwan, N. Saito, and T. Ishizaki, "Nitrogen-Doped Carbon Nanoparticle-Carbon Nanofiber Composite as an Efficient Metal-Free Cathode Catalyst for Oxygen Reduction Reaction," *ACS Appl. Mater. Interfaces*, vol. 8, no. 11, pp. 6962–6971, 2016.

[135] K.-Y. Chun, H. S. Lee, and C. J. Lee, "Nitrogen doping effects on the structure behavior and the field emission performance of double-walled carbon nanotubes," *Carbon N. Y.*, vol. 47, no. 1, pp. 169–177, 2009.

[136] D. Shin, B. Jeong, B. S. Mun, H. Jeon, H. J. Shin, J. Baik, and J. Lee, "On the origin of electrocatalytic oxygen reduction reaction on electrospun nitrogen-carbon species," *J. Phys. Chem. C*, vol. 117, no. 22, pp. 11619–11624, 2013.

[137] D. Bokach, S. ten Hoopen, N. Muthuswamy, M. E. M. Buan, and M. R??nning, "Nitrogen-doped carbon nanofiber catalyst for ORR in PEM fuel cell stack: Performance, durability and market application aspects," *Int. J. Hydrogen Energy*, vol. 41, no. 39, pp. 17616–17630, 2016.

[138] Y. Qiu, J. Yu, T. Shi, X. Zhou, X. Bai, and J. Y. Huang, "Nitrogen-doped ultrathin carbon nanofibers derived from electrospinning: Large-scale production, unique structure, and application as electrocatalysts for oxygen reduction," *J. Power Sources*, vol. 196, no. 23, pp. 9862–9867, 2011.

[139] S. Wang, C. Dai, J. Li, L. Zhao, Z. Ren, Y. Ren, Y. Qiu, and J. Yu, "The effect of different nitrogen sources on the electrocatalytic properties of nitrogen-doped electrospun carbon nanofibers for the oxygen reduction reaction," *Int. J. Hydrogen*

Energy, vol. 40, no. 13, pp. 4673–4682, 2015.

[140] D. C. Higgins, D. Meza, and Z. Chen, "Nitrogen-Doped Carbon Nanotubes as Platinum Catalyst Supports for Oxygen Reduction Reaction in Proton Exchange Membrane Fuel Cells," pp. 21982–21988, 2010.

[141] D. Yang, S. Chaudhari, K. P. Rajesh, and J. Yu, "Preparation of Nitrogen-Doped Porous Carbon Nanofibers and the Effect of Porosity, Electrical Conductivity, and Nitrogen Content on Their Oxygen Reduction Performance," *ChemCatChem*, p. n/a-n/a, Mar. 2014.

[142] W. A. Saidi, "Oxygen reduction electrocatalysis using N-doped graphene quantum-dots," *J. Phys. Chem. Lett.*, vol. 4, no. 23, pp. 4160–4165, 2013.

[143] J. D. Wiggins-Camacho and K. J. Stevenson, "Mechanistic discussion of the oxygen reduction reaction at nitrogen-doped carbon nanotubes," *J. Phys. Chem. C*, vol. 115, no. 40, pp. 20002–20010, 2011.

[144] L. Yang, S. Jiang, Y. Zhao, L. Zhu, S. Chen, X. Wang, Q. Wu, J. Ma, Y. Ma, and Z. Hu, "Boron-doped carbon nanotubes as metal-free electrocatalysts for the oxygen reduction reaction," *Angew. Chemie - Int. Ed.*, vol. 50, no. 31, pp. 7132–7135, 2011.

[145] Z. W. Liu, F. Peng, H. J. Wang, H. Yu, W. X. Zheng, and J. Yang, "Phosphorus-doped graphite layers with high electrocatalytic activity for the O2 reduction in an alkaline medium," *Angew. Chemie - Int. Ed.*, vol. 50, no. 14, pp. 3257–3261, 2011.

[146] L. Wang, W. Jia, X. Liu, J. Li, and M. M. Titirici, "Sulphur-doped ordered mesoporous carbon with enhanced electrocatalytic activity for the oxygen reduction reaction," *J. Energy Chem.*, vol. 25, no. 4, pp. 566–570, 2016.

[147] Z. Yang, Z. Yao, G. Li, G. Fang, H. Nie, Z. Liu, X. Zhou, X. Chen, and S. Huang, "Sulfur-doped graphene as an efficient metal-free cathode catalyst for oxygen reduction," *ACS Nano*, vol. 6, no. 1, pp. 205–211, 2012.

[148] W. Li, D. Yang, H. Chen, Y. Gao, and H. Li, "Sulfur-doped carbon nanotubes as catalysts for the oxygen reduction reaction in alkaline medium," *Electrochim. Acta*, vol. 165, pp. 191–197, 2015.

[149] H. Tavakol and F. Keshavarzipour, "A sulfur doped carbon nanotube as a potential catalyst for the oxygen reduction reaction," *RSC Adv.*, vol. 6, no. 67, pp. 63084–63090, 2016.

[150] J. Wang, R. Ma, Z. Zhou, G. Liu, and Q. Liu, "Magnesiothermic synthesis of sulfur-doped graphene as an efficient metal-free electrocatalyst for oxygen reduction.," *Sci. Rep.*, vol. 5, p. 9304, 2015.

[151] S.-A. Wohlgemuth, R. J. White, M.-G. Willinger, M.-M. Titirici, and M. Antonietti, "A one-pot hydrothermal synthesis of sulfur and nitrogen doped carbon aerogels with enhanced electrocatalytic activity in the oxygen reduction reaction," *Green Chem.*, vol. 14, no. 5, p. 1515, 2012.

[152] J. Park, Y. J. Jang, Y. J. Kim, M.-S. Song, S. Yoon, D. H. Kim, and S.-J. Kim, "Sulfur-doped graphene as a potential alternative metal-free electrocatalyst and Pt-catalyst supporting material for oxygen reduction reaction.," *Phys. Chem. Chem. Phys.*, vol. 16, no. 1, pp. 103–9, 2013.

[153] W. Kiciński, M. Szala, and M. Bystrzejewski, "Sulfur-doped porous carbons: Synthesis and applications," *Carbon N. Y.*, vol. 68, pp. 1–32, 2014.

[154] W. Li, D. Yang, H. Chen, Y. Gao, and H. Li, "Electrochimica Acta Sulfur-doped

carbon nanotubes as catalysts for the oxygen reduction reaction in alkaline medium," *Electrochim. Acta*, vol. 165, pp. 191–197, 2015.

[155] A. Hoque, F. M. Hassan, M. Seo, J. Choi, M. Pritzker, S. Knights, S. Ye, and Z. Chen, "Optimization of sulfur-doped graphene as an emerging platinum nanowires support for oxygen reduction reaction," *Nano Energy*, vol. 19, pp. 27–38, 2016.

[156] S. Inamdar, H. S. Choi, P. Wang, M. Y. Song, and J. S. Yu, "Sulfur-containing carbon by flame synthesis as efficient metal-free electrocatalyst for oxygen reduction reaction," *Electrochem. commun.*, vol. 30, pp. 9–12, 2013.

[157] C. Domínguez, F. J. Pérez-alonso, S. A. Al-thabaiti, S. Nassir, A. Y. Obaid, A. Obaid, J. L. Gómez, D. Fuente, and S. Rojas, "Electrochimica Acta Effect of N and S co-doping of multiwalled carbon nanotubes for the oxygen reduction," *Electrochim. Acta*, vol. 157, pp. 158–165, 2015.

[158] J. Liang, Y. Jiao, M. Jaroniec, and S. Z. Qiao, "Sulfur and nitrogen dual-doped mesoporous graphene electrocatalyst for oxygen reduction with synergistically enhanced performance," *Angew. Chemie - Int. Ed.*, vol. 51, no. 46, pp. 11496–11500, 2012.

[159] S. Wang, L. Zhang, Z. Xia, A. Roy, D. W. Chang, J. B. Baek, and L. Dai, "BCN graphene as efficient metal-free electrocatalyst for the oxygen reduction reaction," *Angew. Chemie - Int. Ed.*, vol. 51, no. 17, pp. 4209–4212, 2012.

[160] H. Zhang, Y. Niu, and W. Hu, "Nitrogen/sulfur-doping of graphene with cysteine as a heteroatom source for oxygen reduction electrocatalysis," *J. Colloid Interface Sci.*, vol. 505, pp. 32–37, 2017.

[161] L. Persano, A. Camposeo, C. Tekmen, and D. Pisignano, "Industrial Upscaling of

Electrospinning and Applications of Polymer Nanofibers : A Review," pp. 504–520.

[162] Q. Q. Ni, X. D. Jin, H. Xia, and F. Liu, "Electrospinning, processing and characterization of polymer-based nano-composite fibers," pp. 128–148, 2014.

[163] G. Sun, L. Sun, H. Xie, and J. Liu, "Electrospinning of Nanofibers for Energy Applications," 2016.

[164] N. Kaur, V. Kumar, and S. R. Dhakate, "Synthesis and characterization of multiwalled CNT – PAN based composite carbon nanofibers via electrospinning," *Springerplus*, 2016.

[165] M. Wei, M. Jiang, X. Liu, M. Wang, and S. Mu, "Graphene-doped electrospun nano fi ber membrane electrodes and proton exchange membrane fuel cell performance," *J. Power Sources*, vol. 327, pp. 384–393, 2016.

[166] P. Zamani, D. Higgins, F. Hassan, G. Jiang, J. Wu, S. Abureden, and Z. Chen, "Electrochimica Acta Electrospun Iron – Polyaniline – Polyacrylonitrile Derived Nanofibers as Non – Precious Oxygen Reduction Reaction Catalysts for PEM Fuel Cells," *Electrochim. Acta*, vol. 139, pp. 111–116, 2014.

[167] A. R. Unnithan, R. S. Arathyram, and C. S. Kim, *Electrospinning of Polymers for Tissue Engineering*. Elsevier Inc., 2015.

[168] D.-G. Yu, L.-M. Zhu, K. White, and C. Branford-White, "Electrospun nanofiber-based drug delivery systems," *Health (Irvine. Calif).*, vol. 1, no. 2, pp. 67–75, 2009.

[169] N. Bhardwaj and S. C. Kundu, "Electrospinning: A fascinating fiber fabrication technique," *Biotechnol. Adv.*, vol. 28, no. 3, pp. 325–347, 2010.

[170] A. Formhals, “Oct. 2, 1934- A," FORMHALS-,” 1934.

[171] A. F. O. R. Spinning, “W ,”,” 1939.

[172] T. Of and P. Sm, “Jan. 16, 1940- â€™ A. FORMHALS,” 1940.

[173] P. Of, A. Fibers, F. Fiber, and F. Liquids, “UNITED : STATES PATENT ’ OFFlCE .,” 1943.

[174] A. Formhals, “Mymm. 6%,” 1944.

[175] B. Vonnegut and R. L. Neubauer, “Production of monodisperse liquid particles by electrical atomization,” *J. Colloid Sci.*, vol. 7, no. 6, pp. 616–622, 1952.

[176] V. G. Drozin, “The electrical dispersion of liquids as aerosols,” *J. Colloid Sci.*, vol. 10, no. 2, pp. 158–164, 1955.

[177] A. Baji, Y. W. Mai, S. C. Wong, M. Abtahi, and P. Chen, “Electrospinning of polymer nanofibers: Effects on oriented morphology, structures and tensile properties,” *Compos. Sci. Technol.*, vol. 70, no. 5, pp. 703–718, 2010.

[178] R. Society and P. Sciences, “The Lattice Spacings of Solid Solutions of Different Elements in Aluminium Author (s): H . J . Axon and W . Hume-Rothery Source : Proceedings of the Royal Society of London . Series A , Mathematical and Physical Published by : Royal Society Stable URL :,” vol. 193, no. 1032, pp. 1–24, 2017.

[179] R. Society and P. Sciences, “Supercooling of Liquids Author (s): F . C . Frank Source : Proceedings of the Royal Society of London . Series A , Mathematical and Physical Published by : Royal Society Stable URL : http://www.jstor.org/stable/99132,” vol. 215, no. 1120, pp. 43–46, 2017.

[180] N. Fabrics, “Oct. 18, 1966’,” 1966.

[181] P. K. Baumgarten, “Electrostatic spinning of acrylic microfibers,” *J. Colloid Interface Sci.*, vol. 36, no. 1, pp. 71–79, 1971.

[182] T. Mitarai, A. Shander, M. Tight, N. Fabrics, F. N. Martin, and J. T. English, “An Introduction to electrospinning and nanofibres,” *J. Cardiothorac. Vasc. Anesth.*, vol. 27, no. 4 Suppl, pp. S1-2, 2013.

[183] J. Doshi and D. H. Reneker, “Electrospinning Process and Applications of Electrospun Fibers,” *Ind. Appl. Soc. Annu. Meet. 1993., Conf. Rec. 1993 IEEE*, vol. 3, pp. 1698–1703, 1993.

[184] M. Mirjalili and S. Zohoori, “Review for application of electrospinning and electrospun nanofibers technology in textile industry,” *J. Nanostructure Chem.*, vol. 6, no. 3, pp. 207–213, 2016.

[185] X. Hu, S. Liu, G. Zhou, Y. Huang, Z. Xie, and X. Jing, “Electrospinning of polymeric nanofibers for drug delivery applications,” *J. Control. Release*, vol. 185, no. 1, pp. 12–21, 2014.

[186] C. J. Angammana and S. H. Jayaram, “Fundamentals of electrospinning and processing technologies,” *Part. Sci. Technol.*, vol. 34, no. 1, pp. 72–82, 2016.

[187] Y. Si, X. Tang, J. Yu, and B. Ding, *Electrospun Nanofibers for Energy and Environmental Applications*. 2014.

[188] A. Greiner and J. H. Wendorff, “Electrospinning: A fascinating method for the preparation of ultrathin fibers,” *Angew. Chemie - Int. Ed.*, vol. 46, no. 30, pp. 5670–5703, 2007.

[189] C. Laurencin, S. Kumbar, S. Nukavarapu, R. James, and M. Hogan, “Recent Patents on Electrospun Biomedical Nanostructures: An Overview,” *Recent Patents*

Biomed. Eng., vol. 1, no. 1, pp. 68–78, 2008.

[190] B. Zhang, Y. Yu, Z. L. Xu, S. Abouali, M. Akbari, Y. B. He, F. Kang, and J. K. Kim, "Correlation between atomic structure and electrochemical performance of anodes made from electrospun carbon nanofiber films," *Adv. Energy Mater.*, vol. 4, no. 7, pp. 1–9, 2014.

[191] S. Y. Chew, J. Wen, E. K. F. Yim, and K. W. Leong, "Sustained release of proteins from electrospun biodegradable fibers," *Biomacromolecules*, vol. 6, no. 4, pp. 2017–2024, 2005.

[192] "Development of carbon nanofibers from aligned electrospun polyacrylonitrile nanofiber bundles and characterization of their microstructural, electrical, and mechanical properties," *Polymer (Guildf).*, vol. 50, no. 13, pp. 2999–3006, Jun. 2009.

[193] A. Mickova, M. Buzgo, O. Benada, M. Rampichova, Z. Fisar, E. Filova, M. Tesarova, D. Lukas, and E. Amler, "Core/shell nanofibers with embedded liposomes as a drug delivery system," *Biomacromolecules*, vol. 13, no. 4, pp. 952–962, 2012.

[194] B. Wang, Y. Wang, T. Yin, and Q. Yu, "Applications of electrospinning technique in drug delivery," *Chem. Eng. Commun.*, vol. 197, no. 10, pp. 1315–1338, 2010.

[195] F. Li, Y. Zhao, and Y. Song, "Core-Shell Nanofibers: Nano Channel and Capsule by Coaxial Electrospinning," *Nanofibers*, no. February, 2010.

[196] T. H. Hwang, Y. M. Lee, B. S. Kong, J. S. Seo, and J. W. Choi, "Electrospun core-shell fibers for robust silicon nanoparticle-based lithium ion battery anodes," *Nano Lett.*, vol. 12, no. 2, pp. 802–807, 2012.

[197] Y. Yu, L. Gu, C. Wang, A. Dhanabalan, P. A. Van Aken, and J. Maier, "Encapsulation of Sn@carbon nanoparticles in bamboo-like hollow carbon nanofibers as an anode material in lithium-based batteries," *Angew. Chemie - Int. Ed.*, vol. 48, no. 35, pp. 6485–6489, 2009.

[198] H. Jiang, L. Wang, and K. Zhu, "Coaxial electrospinning for encapsulation and controlled release of fragile water-soluble bioactive agents," *J. Control. Release*, vol. 193, pp. 296–303, 2014.

[199] G. Jiang and X. Qin, "An improved free surface electrospinning for high throughput manufacturing of core-shell nanofibers," *Mater. Lett.*, vol. 128, pp. 259–262, 2014.

[200] T. Spinneret, B. D. Li, A. Babel, and S. A. Jenekhe, "Nanofibers of Conjugated Polymers Prepared by Electrospinning with a," no. 22, pp. 2062–2066, 2004.

[201] Z. Sun, E. Zussman, A. L. Yarin, J. H. Wendorff, and A. Greiner, "Compound Core-Shell Polymer Nanofibers by Co-Electrospinning," *Adv. Mater.*, vol. 15, no. 22, pp. 1929–1932, 2003.

[202] Q. Yang, L. I. Zhenyu, Y. Hong, Y. Zhao, S. Qiu, C. E. Wang, and Y. Wei, "Influence of solvents on the formation of ultrathin uniform poly(vinyl pyrrolidone) nanofibers with electrospinning," *J. Polym. Sci. Part B Polym. Phys.*, vol. 42, no. 20, pp. 3721–3726, 2004.

[203] "Beaded nanofibers formed during electrospinning," *Polymer (Guildf).*, vol. 40, no. 16, pp. 4585–4592, Jul. 1999.

[204] J. Fang, H. Wang, H. Niu, T. Lin, and X. Wang, "Evolution of fiber morphology during electrospinning," *J. Appl. Polym. Sci.*, vol. 118, no. 5, 2010.

[205] P. Supaphol, C. Mit-Uppatham, and M. Nithitanakul, “Ultrafine electrospun polyamide-6 fibers: Effect of emitting electrode polarity on morphology and average fiber diameter,” *J. Polym. Sci. Part B Polym. Phys.*, vol. 43, no. 24, pp. 3699–3712, 2005.

[206] “Electrospinning of linear homopolymers of poly(methyl methacrylate): exploring relationships between fiber formation, viscosity, molecular weight and concentration in a good solvent,” *Polymer (Guildf).*, vol. 46, no. 13, pp. 4799–4810, Jun. 2005.

[207] C. Wang, C. H. Hsu, and J. H. Lin, “Scaling laws in electrospinning of polystyrene solutions,” *Macromolecules*, vol. 39, no. 22, pp. 7662–7672, 2006.

[208] “Beaded nanofibers formed during electrospinning,” *Polymer (Guildf).*, vol. 40, no. 16, pp. 4585–4592, Jul. 1999.

[209] “Biodegradable electrospun fibers for drug delivery,” *J. Control. Release*, vol. 92, no. 3, pp. 227–231, Oct. 2003.

[210] “Large-scale fabrication of two-dimensional spider-web-like gelatin nano-nets via electro-netting,” *Colloids Surfaces B Biointerfaces*, vol. 86, no. 2, pp. 345–352, Sep. 2011.

[211] N. T. Xuyen, E. J. Ra, H. Z. Geng, K. K. Kim, K. H. An, and Y. H. Lee, “Enhancement of conductivity by diameter control of polyimide-based electrospun carbon nanofibers,” *J. Phys. Chem. B*, vol. 111, no. 39, pp. 11350–11353, 2007.

[212] D. Li and Y. Xia, “Electrospinning of nanofibers: Reinventing the wheel?,” *Adv. Mater.*, vol. 16, no. 14, pp. 1151–1170, 2004.

[213] “Processing and microstructural characterization of porous biocompatible protein

polymer thin films," *Polymer (Guildf).*, vol. 40, no. 26, pp. 7397–7407, Dec. 1999.

[214] X. Y. Yuan, Y. Y. Zhang, C. Dong, and J. Sheng, "Morphology of ultrafine polysulfone fibers prepared by electrospinning," *Polym. Int.*, vol. 53, no. 11, pp. 1704–1710, 2004.

[215] C. L. Casper, J. S. Stephens, N. G. Tassi, D. B. Chase, and J. F. Rabolt, "Controlling surface morphology of electrospun polystyrene fibers: Effect of humidity and molecular weight in the electrospinning process," *Macromolecules*, vol. 37, no. 2, pp. 573–578, 2004.

[216] M. Inagaki, F. Kang, M. Toyoda, H. Konno, M. Inagaki, F. Kang, M. Toyoda, and H. Konno, "Chapter 8 – Carbon Nanofibers Via Electrospinning," in *Advanced Materials Science and Engineering of Carbon*, 2014, pp. 165–188.

[217] S. Peng, L. Li, J. Kong Yoong Lee, L. Tian, M. Srinivasan, S. Adams, and S. Ramakrishna, "Electrospun carbon nanofibers and their hybrid composites as advanced materials for energy conversion and storage," *Nano Energy*, vol. 22, pp. 361–395, 2016.

[218] M. Inagaki, F. Kang, M. Toyoda, and H. Konno, "Carbon Nanofibers Via Electrospinning," *Adv. Mater. Sci. Eng. Carbon*, vol. 4, pp. 165–188, 2014.

[219] M. S. A. Rahaman, A. F. Ismail, and A. Mustafa, "A review of heat treatment on polyacrylonitrile fiber," *Polym. Degrad. Stab.*, vol. 92, no. 8, pp. 1421–1432, 2007.

[220] C. Kim, K. S. Yang, M. Kojima, K. Yoshida, Y. J. Kim, Y. A. Kim, and M. Endo, "Fabrication of electrospinning-derived carbon nanofiber webs for the anode material of lithium-ion secondary batteries," *Adv. Funct. Mater.*, vol. 16, no. 18,

pp. 2393–2397, 2006.

[221] L. I. B. David and A. F. Ismail, “Influence of the thermastabilization process and soak time during pyrolysis process on the polyacrylonitrile carbon membranes for O2/N2separation,” *J. Memb. Sci.*, vol. 213, no. 1–2, pp. 285–291, 2003.

[222] L. Zhang, A. Aboagye, A. Kelkar, C. Lai, and H. Fong, “A review: Carbon nanofibers from electrospun polyacrylonitrile and their applications,” *J. Mater. Sci.*, vol. 49, no. 2, pp. 463–480, 2014.

[223] E. Fitzer, W. Frohs, and M. Heine, “Optimization of stabilization and carbonization treatment of PAN fibres and structural characterization of the resulting carbon fibres,” *Carbon N. Y.*, vol. 24, no. 4, pp. 387–395, 1986.

[224] R. B. Mathur, O. P. Bahl, and J. Mittal, “A new approach to thermal stabilisation of PAN fibres,” *Carbon N. Y.*, vol. 30, no. 4, pp. 657–663, 1992.

[225] J. Ye, F. He, J. Nie, Y. Cao, H. Yang, and X. Ai, “capacity cathode for lithium – sulfur batteries †,” *J. Mater. Chem. A Mater. energy Sustain.*, vol. 3, pp. 7406–7412, 2015.

[226] C. Shang, M. Li, Z. Wang, S. Wu, and Z. Lu, “Electrospun Nitrogen-Doped Carbon Nanofibers Encapsulating Cobalt Nanoparticles as Efficient Oxygen Reduction Reaction Catalysts,” *ChemElectroChem*, vol. 3, no. 9, pp. 1437–1445, 2016.

[227] X. Mao, T. Hatton, and G. Rutledge, “A Review of Electrospun Carbon Fibers as Electrode Materials for Energy Storage,” *Curr. Org. Chem.*, vol. 17, no. 13, pp. 1390–1401, 2013.

[228] I. S. Chronakis, *Micro- and Nano-fibers by Electrospinning Technology*, Second

Edi. Yi Qin, 2015.

[229] Y. Qiu, J. Yu, W. Wu, J. Yin, and X. Bai, “Fe-N/C nanofiber electrocatalysts with improved activity and stability for oxygen reduction in alkaline and acid solutions,” *J. Solid State Electrochem.*, vol. 17, no. 3, pp. 565–573, 2013.

[230] J. Guo, Q. Niu, Y. Yuan, I. Maitlo, J. Nie, and G. Ma, “Electrospun core–shell nanofibers derived Fe–S/N doped carbon material for oxygen reduction reaction,” *Appl. Surf. Sci.*, vol. 416, pp. 118–123, 2017.

[231] Q. Niu, J. Guo, B. Chen, J. Nie, X. Guo, and G. Ma, “Bimetal-organic frameworks/polymer core-shell nanofibers derived heteroatom-doped carbon materials as electrocatalysts for oxygen reduction reaction,” *Carbon N. Y.*, vol. 114, pp. 250–260, 2017.

[232] L. Deng, H. Fang, P. Zhang, A. Abdelkader, X. Ren, Y. Li, and N. Xie, “Nitrogen and Sulfur Dual-Doped Carbon Microtubes with Enhanced Performances for Oxygen Reduction Reaction,” *J. Electrochem. Soc.*, vol. 163, no. 5, pp. H343–H349, 2016.

[233] L. Xu, G. Pan, and X. Liang, “Nitrogen/sulfur co-doped non-noble metal material as an efficient electrocatalyst for the oxygen reduction reaction in alkaline media,” *RSC Adv.*, vol. 4, no. 38, p. 19756, 2014.

[234] L. Zhang, J. Niu, M. Li, and Z. Xia, “Catalytic mechanisms of sulfur-doped graphene as efficient oxygen reduction reaction catalysts for fuel cells,” *J. Phys. Chem. C*, vol. 118, no. 7, pp. 3545–3553, 2014.

[235] H. Wang, X. Bo, Y. Zhang, and L. Guo, “Sulfur-doped ordered mesoporous carbon with high electrocatalytic activity for oxygen reduction,” *Electrochim.*

Acta, vol. 108, pp. 404–411, 2013.

[236] S. Eşsiz, B. Sarı, and N. Eldemir, "Effect of synthetic route on structural and morphological properties of poly(thiophene-co-indole)," *Polym. Sci. Ser. B*, vol. 56, no. 5, pp. 593–602, 2014.

[237] A. Gök, M. Omastová, and A. G. Yavuz, "Synthesis and characterization of polythiophenes prepared in the presence of surfactants," *Synth. Met.*, vol. 157, no. 1, pp. 23–29, 2007.

[238] T. H. Hwang, D. S. Jung, J. S. Kim, B. G. Kim, and J. W. Choi, "One-dimensional carbon-sulfur composite fibers for Na-S rechargeable batteries operating at room temperature," *Nano Lett.*, vol. 13, no. 9, pp. 4532–4538, 2013.

[239] D. B. Kamble, A. K. Sharma, J. B. Yadav, V. B. Patil, R. S. Devan, A. A. Jatratkar, M. A. Yewale, V. V. Ganbavle, and S. D. Pawar, "Facile chemical bath deposition method for interconnected nanofibrous polythiophene thin films and their use for highly efficient room temperature NO2 sensor application," *Sensors Actuators B Chem.*, vol. 244, pp. 522–530, 2017.

[240] A. Acharya, R. Mishra, and G. S. Roy, "CHARACTERIZATION OF CdSe/POLYTHIOPHENE NANOCOMPOSITE BY TGA/DTA, XRD, UV-VIS SPECTROSCOPY, SEM-EDXA AND FTIR," *Armen. J. Phys.*, vol. 3, no. 3, pp. 195–202, 2010.

[241] B. X. Valderrama-García, E. Rodríguez-Alba, E. G. Morales-Espinoza, K. M. Chane-Ching, E. Rivera, S. Reed, and M. Resendiz, "Synthesis and characterization of novel polythiophenes containing pyrene chromophores: Thermal, optical and electrochemical properties," *Molecules*, vol. 21, no. 2, 2016.

[242] P. He, H. R. Cheng, Y. Le, and J. F. Chen, “Preparation and characterization of nano-sized Sr0.7Ca0.3TiO3 crystallines by low temperature aqueous synthesis method,” *Mater. Lett.*, vol. 62, no. 14, pp. 2161–2164, 2008.

[243] S. F. Fennessey, “Continuous carbon nanofibers prepared from electrospun polyacrylonitrile precursor fibers .,” no. February, 2014.

[244] T. N. L. Doan, M. Ghaznavi, Y. Zhao, Y. Zhang, A. Konarov, M. Sadhu, R. Tangirala, and P. Chen, “Binding mechanism of sulfur and dehydrogenated polyacrylonitrile in sulfur/polymer composite cathode,” *J. Power Sources*, vol. 241, pp. 61–69, 2013.

[245] M. Wu, Q. Wang, K. Li, Y. Wu, and H. Liu, “Optimization of stabilization conditions for electrospun polyacrylonitrile nanofibers,” *Polym. Degrad. Stab.*, vol. 97, no. 8, pp. 1511–1519, 2012.

[246] A. Konarov, D. Gosselink, T. N. L. Doan, Y. Zhang, Y. Zhao, and P. Chen, “Simple, scalable, and economical preparation of sulfur-PAN composite cathodes for Li/S batteries,” *J. Power Sources*, vol. 259, pp. 183–187, 2014.

[247] Y. Liu, X. Zhao, G. S. Chauhan, and J. H. Ahn, “Nanostructured nitrogen-doped mesoporous carbon derived from polyacrylonitrile for advanced lithium sulfur batteries,” *Appl. Surf. Sci.*, vol. 380, pp. 151–158, 2016.

[248] J. Li, K. Li, M. Li, D. Gosselink, Y. Zhang, and P. Chen, “A sulfur-polyacrylonitrile/graphene composite cathode for lithium batteries with excellent cyclability,” *J. Power Sources*, vol. 252, pp. 107–112, 2014.

[249] a. Mahapatra, B. G. Mishra, and G. Hota, “Electrospun Fe2O3-Al2O3 nanocomposite fibers as efficient adsorbent for removal of heavy metal ions from

aqueous solution," *J. Hazard. Mater.*, vol. 258–259, pp. 116–123, 2013.

[250] A. Megherbi, R. Meghabar, and M. Belbachir, "Preparation and Characterization of Clay Composites," *J. Surf. Eng. Mater. Adv. Technol.*, vol. 3, no. January, pp. 21–27, 2013.

[251] M. Hatamzadeh and M. Jaymand, "Synthesis and characterization of polystyrene-graft-polythiophene via a combination of atom transfer radical polymerization and Grignard reaction," *RSC Adv.*, vol. 4, no. 32, pp. 16792–16802, 2014.

[252] T.-N. Tran, M. Y. Song, K. P. Singh, D.-S. Yang, and J.-S. Yu, "Iron–polypyrrole electrocatalyst with remarkable activity and stability for ORR in both alkaline and acidic conditions: a comprehensive assessment of catalyst preparation sequence," *J. Mater. Chem. A*, vol. 4, no. 22, pp. 8645–8657, 2016.

[253] Z. Wang, S. Peng, Y. Hu, L. Li, T. Yan, G. Yang, D. Ji, M. Srinivasan, Z. Pan, and S. Ramakrishna, "Cobalt nanoparticles encapsulated in carbon nanotube-grafted nitrogen and sulfur co-doped multichannel carbon fibers as efficient bifunctional oxygen electrocatalysts," *J. Mater. Chem. A*, vol. 5, pp. 4949–4961, 2017.

[254] T. Liu, Y. F. Guo, Y. M. Yan, F. Wang, C. Deng, D. Rooney, and K. N. Sun, "CoO nanoparticles embedded in three-dimensional nitrogen/sulfur co-doped carbon nanofiber networks as a bifunctional catalyst for oxygen reduction/evolution reactions," *Carbon N. Y.*, vol. 106, pp. 84–92, 2016.

[255] J. C. B. Vera, "ScienceDirect EIS analysis of oxygen reduction reaction of Pt supported on different substrates," vol. 2, pp. 0–9, 2017.

[256] C. W. Chen, Y. S. Hsieh, C. C. Syu, H. R. Chen, and C. L. Lee, "Displacement preparation-induced effects on structure of Ag-Pd nanobrushes for catalyzing

oxygen reduction," *J. Alloys Compd.*, vol. 580, no. SUPPL1, pp. S359–S363, 2013.

[257] C. L. Lee, H. P. Chiou, C. M. Syu, and C. C. Wu, "Silver triangular nanoplates as electrocatalyst for oxygen reduction reaction," *Electrochem. commun.*, vol. 12, no. 11, pp. 1609–1613, 2010.

[258] I. L. Alonso-Lemus, M. Z. Figueroa-Torres, A. B. García-Hernández, B. Escobar-Morales, F. J. Rodríguez-Varela, A. F. Fuentes, D. Lardizabal-Gutierrez, and P. Quintana-Owen, "Low-cost sonochemical synthesis of nitrogen-doped graphene metal-free electrocatalyst for the oxygen reduction reaction in alkaline media," *Int. J. Hydrogen Energy*, vol. 2, pp. 0–8, 2017.

[259] R. K. Singh, R. Devivaraprasad, T. Kar, A. Chakraborty, and M. Neergat, "Electrochemical Impedance Spectroscopy of Oxygen Reduction Reaction (ORR) in a Rotating Disk Electrode Configuration: Effect of Ionomer Content and Carbon-Support," *J. Electrochem. Soc.*, vol. 162, no. 6, pp. F489–F498, 2015.

[260] X. G. Sun, X. Wang, R. T. Mayes, and S. Dai, "Lithium-sulfur batteries based on nitrogen-doped carbon and an ionic-liquid electrolyte," *ChemSusChem*, vol. 5, no. 10, pp. 2079–2085, 2012.

[261] Y. Zhang, Y. Zhao, Z. Bakenov, A. Konarov, and P. Chen, "Preparation of novel network nanostructured sulfur composite cathode with enhanced stable cycle performance," *J. Power Sources*, vol. 270, pp. 326–331, 2014.

[262] Z. Gong, G. Zhang, and S. Wang, "Electrochemical reduction of oxygen on anthraquinone/carbon nanotubes nanohybrid modified glassy carbon electrode in neutral medium," *J. Chem.*, 2013.

[263] M. Abidian and D. Martin, “Experimental and theoretical characterization of implantable neural microelectrodes modified with conducting polymer nanotubes,” *Mater. Sci.*, vol. 29, no. 9, pp. 1273–1283, 2009.

[264] L. Niu, Q. Li, X. Chen, F. Wei, H. Wang, and H. Zhang, “Study on the impedance characteristic and electrocatalytic activity of platinum-modified polyaniline film,” *J. Chinese Chem. Soc.*, vol. 50, no. 6, pp. 1165–1170, 2003.